Experimental and Numerical Aeroacoustic Investigation of Impinging Flows at Low Mach Number

Von der Fakultät für Luft- und Raumfahrttechnik und Geodäsie der Universität Stuttgart zur Erlangung der Würde eines Doktors der Ingenieurwissenschaften (Dr.-Ing.) genehmigte Abhandlung

Vorgelegt von

Marco Zucchini

aus Padua (Italien)

Hauptberichter:	Prof. Dr. rer. nat. habil. C.-D.Munz
Mitberichter:	Prof. Dr.-Ing. F.Thiele

Tag der mündlichen Prüfung: 3. April 2007

Institut für Aerodynamik und Gasdynamik der Universität Stuttgart

2007

Preface

I would like to thank here many people who contributed on their own way to the success of this work. I start with the people at Robert Bosch GmbH corporate research where I am employed in the department of applied physics in Gerlingen-Schillerhöhe (Germany). First of all I am enormously indebted to my industrial supervisor Dr.-Ing. Martin Fischer: more than a 'simple' supervisor, he was always open for every discussion and creative process and finally a good friend. I am indebted as well to Dr. Barbara Heine and to the department chief Dr. Ralf Bergmann for the continuous confidence in me, the valuable suggestions and the incredible freedom I was granted in the work. I would like to show my appreciation also to all the collegues and other Ph.D. students, particularly of the groups fluid-mechanics (CR/ARF1) and acoustics (CR/ARP3) at corporate research, for the valuable scientific exchanges and friendly atmosphere and of course to the practicants Pachara Niumsawatt, Jean-Philippe Coulet, Tiago Vieira and Birte Schrader who worked intensivly with me.

I would like to thank my university supervisor Prof. Dr. Claus-Dieter Munz, in particular for having introduced me in his highly competent team in the institute of aerodynamics and gasdynamics (IAG) in Stuttgart and in mathematical international workshops. Part of this work was matured thanks to these exchanges. Among his former assistents, my special thanks to Dr.-Ing. Michael Dumbser, whose extraordinary work I have had the chance to learn a little bit. I am also grateful to co-examiner Prof. Dr. Frank Thiele for the proof-reading of this work.

During this period I have had the chance to work and exchange ideas, at different intensity levels, with many professionals from external companies and research intitutes. I would like therefore to thank all those people, whishing myself a long-term cooperation:

- at EXA Corp. in Stuttgart, Germany: Dr. Bernd Crouse, Mr. Guillaume Mercier and Dr. Stephane Cyr
- at DLR in Braunschweig, Germany: Dr. Roland Ewert
- at TNO in Holland: Mr. Eric Vedy
- at AUDI in Ingolstadt, Germany: Mr. Hans Miehling and Dr. Wickern

Un riconoscimento straordinario e' riservato ai miei genitori che grazie al loro affetto mi hanno continuamente sostenuto e motivato. Questo lavoro e' interamente dedicato alla mia ragazza Claudia per la pazienza, il conforto ed il sacrificio che ha saputo dimostrare, accompagnandomi in questa avventura.

Contents

Abstract

This work presents the development of methods for the experimental and numerical investigation of flow-induced noise. Moreover it offers a systematic validation and comparison of various numerical prediction techniques for small Mach number aeroacoustics. The work is motivated from the need to validate all the calculation steps of aeroacoustic simulations beyond pure analytical solutions. This encompasses the fluid dynamics and source calculations up to the propagation of sound for problems of technical interest.

The configurations investigated are chosen to ensure geometrical simplicity, given the limitations associated with the numerical calculations of complex geometries, in addition to geometrical relevance with respect to technical problems. The investigation concentrates on the numerical calculations of a low subsonic jet impinging on flat inclined plates with various downstream obstacles. Particular focus is placed on broad band noise contributions.

The first numerical approach analysed consists of extracting sources from unsteady detached eddy simulations of incompressible flow, performed with a commercial finite volume solver, and describes the sound propagation within an existing finite element code. The coupling between the two codes is part of this work. Differences in the intensity and spectra of the turbulence exist between simulations and experiments and are influenced by the topology of the numerical domains in the incompressible solution. The sound propagation calculated with a 2D code is corrected successfully to a 3D field.

The second approach of deriving sound sources is based on steady state flow simulations. The stochastic modeling of the velocity fluctuations using the SNGR (Stochastic Noise Generation and Radiation) approach is investigated with a commercial implementation as well as the author's own implementation. The length scales of the turbulence play a larger role in the sound pressure level than the magnitude of the turbulence. A parametric study indicates the sensitivity of these scales. An approach based on Lagrange multiplicators is presented in order to reduce the spurious source terms which arise from the generation of stochastic turbulence (divergence of the turbulent field).

As a third approach for aeroacoustics the Lattice-Boltzmann method is investigated. In this approach, the acoustic perturbations are part of the solution of the compressible fluid dynamics equations. At present, we judge the numerical efficiency and the accuracy of the acoustic solution of this method as superior compared to the other methods for this class of aeroacoustic problems.

In this work a number of experimental methods and facilities are selected, set up and in part developed for the validation of the numerical approaches. These include the design of a small aeroacoustic wind tunnel and of a traversing unit for automatic positioning of measurement probes. Fluid dynamic validations are conducted with laser Doppler anemometry and hot-wire anemometry. Within this work we develop laser interferometry for acoustic measurements. Our investigations indicate that laser interferometry is a very precise technique in the localisation of aeroacoustic sound sources and that the sound waves propagation can be validated qualitatively. However quantitative local informations, obtained by laser focusing, are still not satisfactory.

This work classifies essential physical phenomena of aeroacoustic sound generation for the investigated test cases: The main sound sources are located at the obstacle itself

and in the region where the flow reattaches to the wall. The latter causes more intense emission in the higher frequency range, the former in the lower frequency range. Nevertheless, the sound can be considered globally as broadband. Moreover, an obstacle with wiper-like shape is slightly quieter than with rectangular shape. We assume that the difference depends on the turbulent structure in the wake. We found numerical and experimental confirmation of the effect of the obstacle shape on the separation length and the turbulent wake behind the objects.

Furthermore, this work presents two concepts to reduce the emitted sound by changing the obstacle geometry. The first concept is based on the idea that an 'air pillow', generated from an air jet under the obstacle, energises the recirculation region and reduces the buffeting in the impinging region. The second concept is based on the spatial decorrelation of the sound sources by modulating the obstacle height.

Finally, investigations of a real windscreen wiper in the full-scale aeroacoustic windtunnel of AUDI AG reveals the role of the wiper struts on the sound emission of windscreen wiper systems and supports the idea of the sound generation mechanisms investigated previously in this work on simplified geometries.

Zusammenfassung

In dieser Arbeit werden experimentelle und numerische Methoden für die Untersuchung von strömungsinduzierten Geräuschen entwickelt. Darüber hinaus werden unterschiedliche numerische Ansätze für die aeroakustische Vorhersage bei niedrigen Machzahlen systematisch vergliechen und validiert. Die Notwendigkeit dieser Arbeit ergibt sich aus dem Bedarf, neue numerische Verfahren über analytische Lösungen hinaus zu validieren und alle Berechnungsschritte, von der Strömungsmechanik über die Schallquellendefinition bis hin zur Schallausbreitung, zu berücksichtigen.

Die Wahl der untersuchten geometrischen Konfigurationen unterliegt folgendem Kompromiss: Zum einen muss die Anordnung wegen der zurzeit existierenden Begrenztheit der numerischen Verfahren einfach aufgebaut sein, zum anderen muss sie ausreichend komplex sein, um die Ergebnisse auf reelle Konfigurationen übertragen zu können. In der vorliegenden Arbeit werden Unterschall-Anströmungen auf schräge Platten ohne oder mit zusätzlichen Hindernissen im Hinblick auf breitbandiges Geräusch untersucht.

Der erste untersuchte numerische Ansatz besteht in der Ableitung der Schallquellen aus instationären Simulationen von inkompressiblen Strömungen (DES) mit einem kommerziellen *finiten Volumen* Code und anschließend in der Berechnung der Schallausbreitung mit einem *finiten elementen* Code. Die 2D-Kopplung der Codes wird im Rahmen dieser Arbeit realisiert. Die berechneten Turbulenzpegel und -spektren zeigen teilweise große Abweichung von den Messungen. Dies ist zum Teil auf die Kopplung der numerischen Domänen im DES-Ansatz zurückzuführen. Die mit dem 2D Code berechnete Schallausbreitung wird für symmetrische Konfigurationen erfolgreich auf 3D übertragen.

Der zweite Ansatz für die Ableitung der Schallquellen basiert auf stationären Strömungssimulationen. Die anschließende stochastische Modellierung der Schallquellen mit dem SNGR Ansatz (Stochstic Noise Generation and Radiation) wird sowohl mit einer kommerziellen als auch mit einer eigenen Implementierung untersucht. Die akustischen Ergebnisse scheinen mehr von den Längenskalen als von den absoluten Werten der Turbulenz beeinflusst zu werden. Parametrische Untersuchungen zeigen die Sensitivität der Ergebnisse auf diese Faktoren. Darüber hinaus können unphysikalische Schallquellen wegen prinzipbedingter Schwächen des Verfahrens (Nichterfüllung der Divergenzfreiheit des Turbulenzfeldes) entstehen. Ein auf Lagrange-Multiplikatoren basierter Ansatz wird beispielhaft vorgestellt, um diesen letzten Einfluss zu reduzieren.

Als dritter Ansatz für die Strömungsakustiksimulation wird das Lattice-Boltzmann Verfahren (LBM) untersucht. Bei diesem direkten Ansatz werden die akustischen Schwankungen gleichzeitig mit der kompressiblen Strömung aufgelöst. Gegenwärtig ist LBM bezüglich der numerischen Effizienz und Genauigkeit der akustischen Lösung bei den untersuchten strömungsakustischen Problemstellungen den vorherigen Ansätzen überlegen.

In dieser Arbeit werden verschiedene experimentelle Verfahren und Einrichtungen zur Validierung der numerischen Ansätze aufgebaut und zum Teil weiterentwickelt. Zum

einen wurde ein aeroakustischer Windkanal mitentwickelt und eine Taversierungseinheit für die automatisierte Positionierung von Mess-Sonden realisiert, zum anderen werden Strömungsuntersuchungen mit Laser-Doppler-Anemometer und Hitzdrathanemometer durchgeführt. Die laserinterferometrische Vermessung von aeroakustischen Druckschwankungen wird im Rahmen dieser Arbeit weiterentwickelt. Die experimentellen Untersuchungen zeigen, dass die Laser-Interferometrie strömungsakustische Quellen genauer als andere Verfahren lokalisiert und insgesamt akustische Phänomene qualitativ validieren kann. Der Versuch, punktuelle Informationen durch Laser-Fokusierung mittels optischen Verfahren zu gewinnen, liefert jedoch noch nicht ausreichende Ergebnisse.

Für die ausgewählten Testfälle werden die wesentlichen physikalischen Ursachen für die Schallentstehung identifiziert: die Hauptschallquellen sind sowohl am Hinderniss als auch stromabwärts in der Region lokalisiert, wo die Strömung wiederaufsetzt. Die erste Schallquelle emittiert hauptsächlich bei niedrigen Frequenzen, die letztere bei höheren Frequenzen. Dennoch kann der Schall im Fernfeld als breitbandig betrachtet werden. Die untersuchten Hindernissgeometrien zeigen kleine Unterschiede in der Schallemission. Bei seitlich uneingeschränkter Strömung ist ein scheibenwischerähnliches Profil leiser als ein rechteckiges. Numerische und experimentelle Untersuchungen weisen darauf hin, dass die Ablöselänge und der turbulente Nachlauf maßgeblich beeinflusst sind.

Zwei Konzepte für die Reduzierung des vom Hindernis strömungsinduzierten Schalles werden vorgestellt. Das erste Konzept basiert auf der Idee eines 'Luftkissens', das von einer Strömung generiert wird und unter das Hinderniss selbst eingeleitet wird. Dies verstärkt die Rezirkulation hinter dem Hindernis und reduziert die Intensität der Druckschwankungen im Wiederauflegengebiet. Das zweite Konzept basiert auf einer räumlichen Dekorrelation der Schallquellen durch Modulation der Höhe des Hindernisses.

Zum Abschluss werden reale Scheibenwischer auf einem Serienfahrzeug im strömungsakustischen Windkanal der Fa. AUDI AG experimentell untersucht. Dies zeigt den Einfluss des Scheibenwischerarmes auf den Schallentstehungprozess und eine gute qualitative Analogie zu den Mechanismen, die im vorherigen Teil dieser Arbeit untersucht wurden.

Symbols

Roman Symbols

c	Speed of Sound
$\frac{D}{Dt}$	Substantial Time Derivative
Kn	Knudnsen Number
M	Mach Number
p	Pressure
Re	Reynolds Number
T	Temperature
Tu	Turbulence Level
$\vec{\mathcal{U}}$	Vector of variables for the fluid governing equations

Greek Symbols

γ	Ratio of Specific Heats
λ	Wave Length
Λ	Integral Correlation Length
μ	Dynamic Viscosity
ν	Kinematic Viscosity
ρ	Density

The symbols not listed here have multiple meaning in this work, therefore they are defined each time new in the text when necessary.

Abbreviations

BEM	Boundary Element Method
CAA	Computaional Aero Acoustics
CFD	Computational Fluid Dynamics
CFL	Courant-Friedrichs-Levy
CPU	Central Processing Unit
DES	Detached Eddy Simulation
DG	Discontinuous Galerkin
EIF	Expansion about Incompressible Flow
EOS	Equation of State
FD	Finite Difference
FE	Finite Element
FV	Finite Volume
HWA	Hot-Wire Anemometry
LBM	Lattice-Boltzmann Method
LASER	Light Amplification by Stimulated Emission of Radiation
LDA	Laser Doppler Anemometry
LEE	Linearised Euler Equation
LES	Large Eddy Simulation
N-S	Navier-Stokes
OASPL	Overall Sound Pressure Level
PC	Personal Computer
PDE	Partial Differential Equation
PPW	Point per Wave Length
RANS	Raynols Averaged Navier-Stokes
SNGR	Stochastic Noise Generation and Radiation
SPL	Sound Pressure Level
TKE	Turbulent Kinetic Energy

Chapter 1

Introduction

What is aeroacoustics ? Aeroacoustics is the branch of physics which deals with airflow-generated sound. The first theory was proposed by Sir Lighthill in 1952 [1] and became the basis of a series of so-called 'acoustic analogies' [2]. The name 'analogy' was derived from the fact that the fluid dynamics and the acoustics were solved separately. Although the numerical simulation of aeroacoustic problems is very recent, in the past decade, the scientific community of computational aeroacoustics has achieved impressive results for high subsonic and supersonic free jets, supported from the civil and military aircraft industry. More recently aeroacoustic noise became a concern for the automotive industry because of the increasing importance placed on the acoustic comfort. This increased awareness leads to tightened requirements on sound design in the product development. Within this framework the noise generated from turbulent flows plays a major role. In fact, fluid turbulent flows are common in technical applications (i.e. heat exchange, internal and external aerodynamics) and build, under certain operating conditions, the most intense sound source.

The aeroacoustic numerical simulation imposes high requirements on numeric methods due to the diversity of scales between fluid dynamics and acoustics. Therefore the development of validated, robust and efficient simulation methods is a focus of advanced research throughout the world.

Most numerical approaches consist of separating the computational domains and the governing equations (hybrid approach) in order to better model this scale diversity. At present few commercial applications based on acoustic analogies (i.e Ffowcs-Williams and Hawkings Analogy) exists. A major drawback to these implementations is that the sound propagation is described by the linear wave equation. Therefore, this approach is only capable of predicting the sound propagation in the acoustic far field in a homogeneous medium at rest. Acoustic phenomena like sound wave reflections and refractions due to moving media can not be predicted. The understanding and prediction of these phenomena together with the identification of aeroacoustic sources is a basic condition for a good prediction in the far field. Therefore this work is oriented towards methods which recover these phenomena.

Aim of this work In this work we aim to understand the generation mechanism of airflow-generated sound and predict the sound emission for selected configurations. The configurations investigated should ensure geometrical simplicity, given the limitations

associated with the numerical calculations of complex geometries, but allow geometrical relevance with respect to technical problems. The investigation is therefore centered on the numerical calculations of a low subsonic jet impinging on flat inclined plates with various downstream obstacles, particular focus being placed on broad band noise contributions. The aim of this work is to select, define, validate experimentally and, where necessary, develop numerical methods for these applications.

Outline In section 2.1 we describe the experimental facilities which have been designed and realised during this work for aeroacoustic investigations.

We review the fundamentals and the specific implementation of the measurement techniques used in this work in sections 2.2 and 2.3. Results of own developments are illustrated here as well.

In section 3 we analyse the theory behind the aeroacoustic numerical approaches used in this work and several aspects of their implementation: a hybrid approach based on large eddy simulation (3.2), a hybrid approach based on stochastic techniques (3.3) and a direct approach based on lattice-Boltzmann method (3.4).

The numerical results and the experimental validations are discussed in section 4 for a free jet and a jet impinging on inclined plates and in section 5 for a jet impinging on obstacles.

Finally, in section 6 real screen wipers on a vehicle are investigated in a full-scale wind tunnel.

Chapter 2

Experimental Approach

Extensive experimental investigations for the validation of numerical methods constitute a fundamental part of this work. Therefore it was necessary, within thin work, to design and develop new experimental facilities at Bosch Corporate Research. This includes the complete design of an aeroacoustic wind tunnel and an automatic traversing unit. Besides that it was necessary to set up measurement systems for fluid dynamic and acoustic investigations. Among the former: hot-wire anemometer and laser-doppler anemometer. Among the latter: laser interferometer, acoustic camera and near field holography. The wind tunnel belongs to the category 'small wind tunnel', as the design leaded to a nozzle cross-sectional area of about $100\,\mathrm{cm}^2$ by an operative maximal speed of 50 m/s. The wind tunnel was manufactured by the company 'Siegle + Epple' in Stuttgart under the technical supervision of M. Fischer [1] and the author.

2.1 Aeroacoustic Windtunnel

2.1.1 Requirements

For fluid dynamics purposes, the windtunnel should produce an homogeneous low turbulent flow within a wide velocity range (10–50 m/s). It should be possible however to change the turbulence level in order to reproduce real inflow conditions. For acoustic investigations, the test room must be sufficiently isolated from external or windtunnel internal noise. This noise should be lower than the free jet noise with a gap of at least 10 dB over a wide frequency range. Moreover the test room should have low sound reflections in order to reproduce an acoustic open field. The open field condition allows the comparison with numerical data and with experimental data from different facilities. Tables 2.1 and 2.2 synthetise the requirements to the windtunnel and to the traversing unit. A major geometrical constraint was the integration of the wind tunnel in a pre-existing semi-anechoic[1] chamber and its limited room size, the floor surface being $10\,\mathrm{m}^2$, the height 3.5 m.

Although many of the measurements reported here have been performed manually, during this work there was the need for automatic measurements in order to increase ef-

[1] Bosch Corporate Research, Applied Physics, Robert Bosch GmbH.

[1] The chamber is defined semi-anechoic because not every wall is covered with sound absorbing material(the floor is excluded).

ficiency and repeatability. For this purpose we added the requirement to develop a computer controlled 3-axis traversing system.

Table 2.1: *Design requirements for the aeroacoustic Bosch windtunnel*

Requirements	
Nominal volume flow	$0.5\,\mathrm{m}^3/\mathrm{s}$
Max turbulence[a]	1 %
Temperature range	20 – 30 °C
Temperature tolerance	±1°C
Background noise[b]	≤ 30 dB(A)
Useful acoustic frequency range at nominal speed[c]	200 – 20000 Hz

[a]Outside shear layer.

[b]Noise inside the anechoic chamber without free jet

[c]Range in which the difference of sound pressure level between free jet and background noise + windtunnel noise is larger than 10 dB.

Table 2.2: *Design requirements for traversing unit*

Requirements	
Probe types	1D–3D HWA and 1D compact laser unit
Measuring volume	$0.8 \times 0.5 \times 0.5$ m
Background noise with traversing unit	≤ 40 dB(A)
Repeatability	0.1 mm
Properties	low vibrations

2.1.2 Design

Windtunnel Wind tunnel technology is dealt with in detail in standard works such as Pankhurst and Holder [3] and Pope [4]. Two main types exist and are distinguished by the air guidance type: open loop (Eiffel type) and closed loop (Goettingen type) as visible in Figure 2.1(labeled a and b respectively). Due to the aeroacoustic requirements and geometrical constraints of section2.1.1, a combination of both types is used here (labeled c in the same figure): closed loop wind tunnel with open vein test chamber. However, differently from a conventional closed loop, the velocity at the end of the test section is almost equal to zero and the static pressure is close to the atmospheric pressure. This is due to the fact that the test chamber corresponds to the pre-existing semi-anechoic room and has open vents to the outside. This concept has been widely adopted for aeroacoustic wind tunnels (i.e. in Germany: Institute ITSM in Stuttgart [7]).

The semi-anechoic chamber features wedge-shaped noise absorber (25 cm deep) on all surfaces, except for the floor. Moreover the chamber is decoupled from the rest of the building by springs and dampers. This design concept has the acoustic advantage to isolate the test chamber well and the possibility to use noise absorber throughout the closed loop. Even if the wind tunnel has a closed refeeding, the power needed is high as the whole velocity must be recovered in form of a pressure increment from the engine (fan) $\Delta p = \frac{K}{2}\rho U_\infty^2$ with K = 1. The total pressure loss is even larger because the flow experiences pressure drops in the closed conduct up to the nozzle. For simplification one

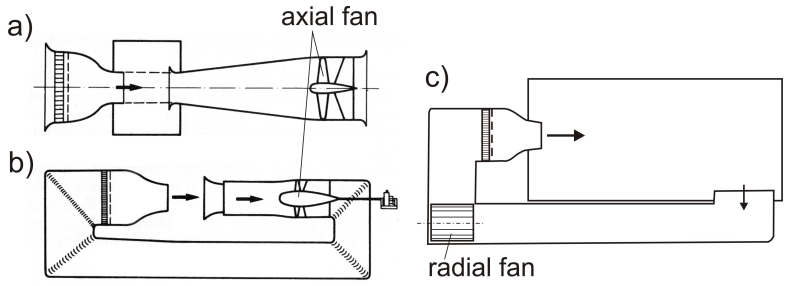

Figure 2.1: *Wind tunnel types: a) open loop, b) closed loop, c) present wind tunnel. Picture a) and b) are taken from [6].*

accounts each single losses in the conduct as concentrated and expresses them similarly with individual factors K_i estimated empirically. The total pressure loss calculates as sum of these factors, leading for the windtunnel to a global factor K= $\sum K_i \sim 1.2$.

The fan data sheet reports the emitted sound power levels at nominal flow rate for both sides of the fan (suction and compression side) separately. The requirements of table 2.1 impose a sound pressure level in the anechoic room lower than the free jet noise level (deduced from [8]). Therefore, on each side of the fan, noise absorbers have been added in order to reduce the sound power emitted. The required noise reduction is obtained by a combined strategy: a plate resonator designed for the 125 Hz octave in order to reduce very low frequencies, and a diffuser silencer for broadband noise reduction, with peak reduction being centered at 2000 Hz-octave.

As the wind tunnel should be operated also with lower flow rates, it was important in the design phase to investigate also the effect on the emitted noise from the fan. The estimation of the noise increase beyond the nominal flow rate is deduced from the German standard norm VDI 3731 [5].

The nozzle is removable and manufactured by rapid prototyping with plastic material in two geometries: cylindrical and rectangular. The cylindrical nozzle has a diameter of 120 mm, while the rectangular one has an opening of 200 by 50 mm. This corresponds to a contraction ratio[1] of 5 allowing a good reduction of the (longitudinal) turbulence level. In addition to the contraction ratio, the contour of the nozzle ensures the quality of flow. It is manifest that smooth curves with first and second derivatives being equal to zero at the ends prevent from flow separations and reduce the contractions of the open vain (so-called 'Design by eye' [9]). For axisymmetric nozzles the smooth curves by Witoszynski [13] are commonly used, which however does not allow to control the nozzle length. Some authors [10] use the solution of the Stokes-Beltrami partial differential equation which is valid for steady irrotational flow, or iterative methods considering the boundary layer [11] in addition and thus leading to slight widening of the contour at the nozzle outlet, or even polynomial curves [12] for 2D nozzles. In this work we used contours according to Witoszynski for both nozzles. See Appendix B.1 for details on the nozzle contour.

Figure 2.2 gives an overview of the windtunnel, while figure 2.3 sketches the components within the nozzle. The flow is rectified by an aramidic honeycomb panel(A). Between nozzle outlet (F) and honeycomb (A) an additional grid (E) with different mesh size can be inserted in order to change the turbulence level of the flow. In order to carry out

[1]Ratio of the nozzle inlet to the nozzle outlet cross-sectional areas.

flow field measurements with tracers (i.e. with Laser Doppler Anemometry), the tracer droplets can be introduced from a nebuliser (B) positioned between the honeycomb (A) and the nozzle outlet (F). An additional honeycomb panel (C) placed in front of the rectangular room (D) rectifies the flow.

A filter unit, placed in the outflow duct, captures the tracer droplets contained in the outflow, thus preventing from contamination of the mechanical parts of the fan. The pressure drop caused from the filter yields, at nominal fan volume flow, about 100 Pa (which corresponds to a value for the previously encountered factor K of about 0.07). In case of the LDA measurements we experienced that the filter must be replaced every 20 working hours (at maximum flow rate) in order to prevent more significant pressure loss.

A state of the art centrifugal fan (Pollrich VR40S10UM, 1.5 kW nominal power, 6 blades) with lowest noise 89 dB(A) produces the required pressure increase (2500 Pa) for nominal volume flow of 0.5 m^3/s. This fan is 4 dB quieter than the reference value given in the German standard norm VDI 3731). The acoustic blade passing frequency at nominal 3200 RPM yields to 320 Hz. A smaller volume flow, down to about 0.1 m^3/s, can be obtained by voltage reduction (from 690 down to 400 V) using transformers.

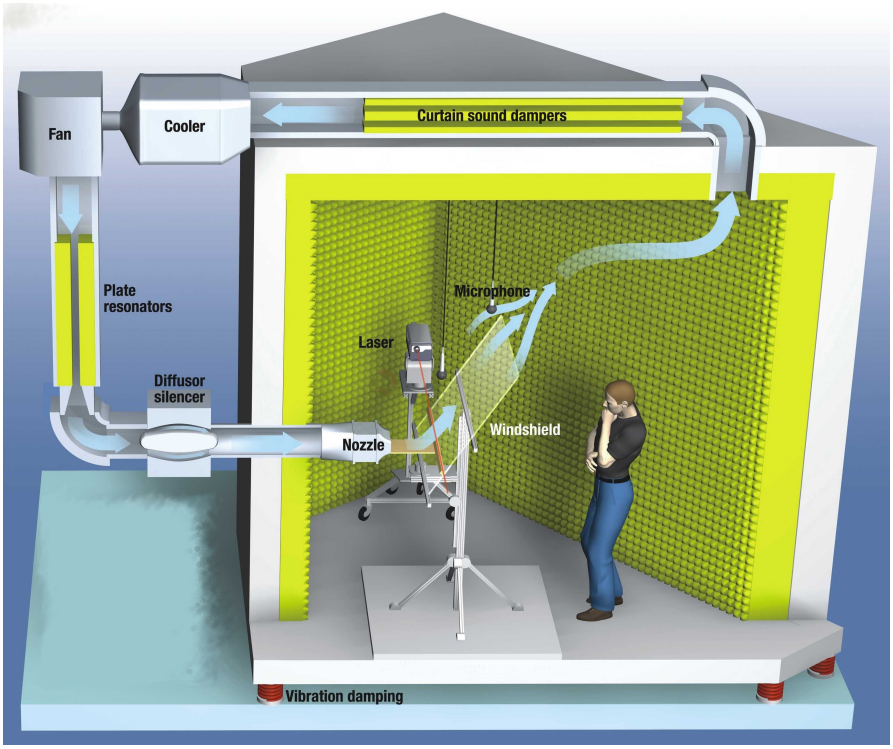

Figure 2.2: *Overview of the aeroacoustic wind-tunnel facility.*

Traversing Unit Figure 2.4 shows the CAD model (PTC Pro/Engineer) of the traversing unit version developed for high accurate laser measurements (see section 2.3.3.3 for further information). It consists of a rigid base made of steel (about 100 kg) which is moved by four wheels and fixed in place by four extensible vibration damping feet. The feet feature vibration absorbers, which are designed for very low eigenfrequency (10 Hz), to damp vibrations induced from the ground and from the traverse itself. On the top of the base, there are three rigid linear guides defined in a Cartesian reference system.

Figure 2.3: *Sketch of the nozzle. Honeycomb (A), removable pipe for particle seeding (B), honeycomb (C), rectangular room (D), grid (E), nozzle outlet(F).*

Three computer-controlled stepping motors drive different types of sensors along these guides. In order to compensate orientation errors towards the reference system of the wind tunnel (nozzle) or of testing geometries three angles can be adjusted manually. One angle can be changed by moving the base, one (α) by swinging the vertical guide on the vertical rigid bar $\pm 2°$ to compensate perpendicularity errors and the last one (β) by rotating the arm carrying the measurement equipment and probes ($\pm 45°$).

The response of the probes to the vibration induced from the movement of the traversing unit has been assessed after construction. Vibrations at the probe reach amplitude of $5\,\mathrm{m/s^2}$ already at speeds of 5 mm/s. We found out however, that the whole traversing unit behaves like a first-order system with a time constant of about 0.15 s for both, vertical and horizontal movements (at speed of 5 mm/s). That means that after the probe reaches a new position, 99.9 % of the vibration is damped down within 0.45 s. The persistence of the disturbing vibration after a stopping increases with increasing speed of the stepping-motors because of the increasing excitatory impulse. This will be considered as a dead-time in the definition of automatic measurements, during which no measurements should take place.

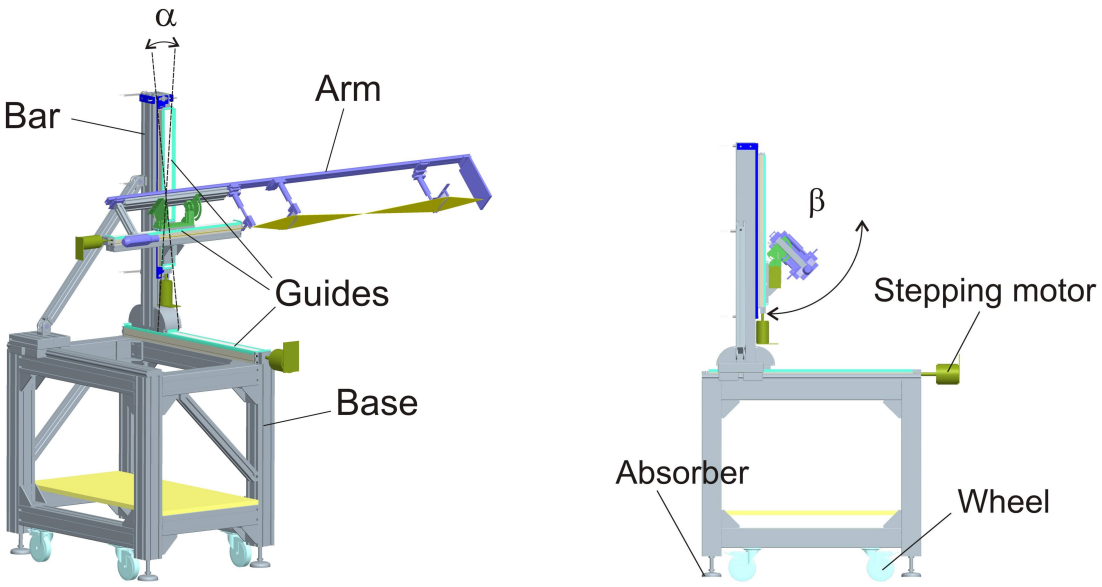

Figure 2.4: *CAD models of the traversing unit and mount for laser interferometer: assonometric view (left), orthogonal side-view (right).*

2.1.3 Performances

The minimum turbulence level at the nozzle section is 0.7%[1]. This level can be increased using the previously described grids (marked E in Figure 2.3) to about 1.5 % at maximum fluid velocity.

The velocity in the nozzle section remains constant within a tolerance of ±2% showing typical accelerations at the edges due to the constriction (See Figure B.1 in Annex B.1).

Local sound pressure measurements in the test chamber without flow show a background noise lower than 30 dB(A) which is low enough to investigate even free jets at low speeds (10 m/s). Figure 2.5 shows the overall pressure level increase for a free jet and plot that in comparison to other aeroacoustic windtunnels (The OASPL scales about with the power of six of the outflow mach number). Moreover the sound spectrum of the free jet shows the characteristic shape [15] and is not affected from the blade passing frequency (BPF) of the fan.(U_{out}=40 m/s, $f_{BPF} \sim 320Hz$ would lead to a peak at St $\sim$ 0.4). The lower cut-off frequency is about 150 Hz.

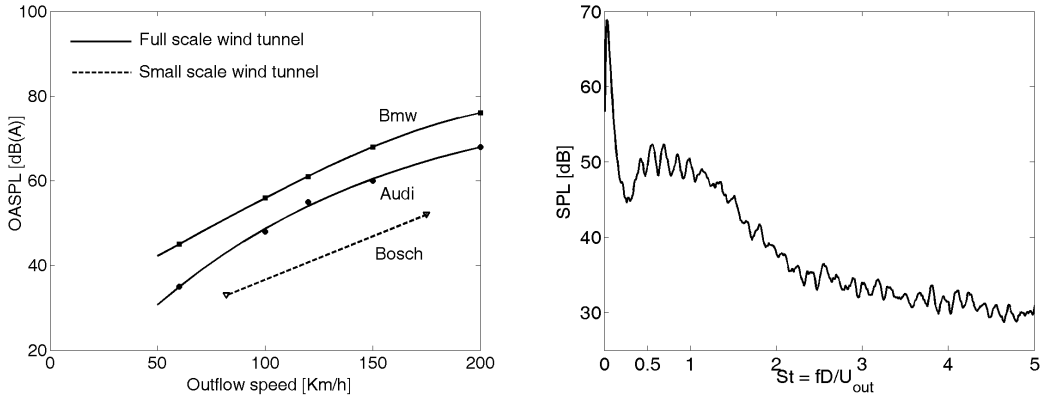

Figure 2.5: *Acoustic performances of windtunnels (left) and sound pressure spectrum for the free jet (right) measured in the Bosch windtunnel at the nozzle outlet plane 0.5 m above and perpendicular to the free jet. Data for Audi and BMW are taken from [14]. St = Strouhal number, f = frequency, D = nozzle hight, U_{out}= velocity at nozzle outlet.*

2.2 Fluid Dynamics Techniques

2.2.1 Flow Visualisation

Among various visualisation techniques for subsonic flow we choose a traditional one in this work: the oil visualisation technique. In this way one obtains informations at the wall which is otherwise hardly accessible with other techniques, i.e. with laser Doppler anemometry. This technique reveals in particular regions of flow separation and reattachment which, as we will see later, play also a role in acoustics.

The oil visualisation technique is based on colour pigments mixed with oil and painted onto the surface to investigate. During the wind tunnel test the oil will be blown away or evaporates leaving the colour behind. The colour forms streak lines on the surface of

[1]Measurement with 1D Hot-Wire Anemometry (HWA). See section 2.2.2 for details on HWA

the model. Moreover characteristic regions can be identified: the shear stress is defined as $\tau = \mu \frac{du}{dn}$ with u being the velocity parallel to the wall, n the normal to the wall and μ the fluid viscosity. At the wall the shear stress is zero only in places where the fluid separates because there $\frac{du}{dn} |_{separation} = 0$, In these regions the time needed to blow away or evaporate the oil becomes longer. More pigments aggregate in the streak and thus the streaks are more distinct. These streaks also visualize the direction of the flow close to the solid walls. Moreover regions of separation or reattachment may be identified from convergent or divergent streaks.

However streak lines coincide with streamlines only for steady flows. That means that this method is not accurate for highly unsteady flows and that the evaporation time should be long enough to average unsteadiness. On the other hand it should be short enough, so that the oil can be blown off or evaporate completely before the steady testing conditions in the windtunnel cease and the flow conditions begin to change. If this is achieved the pattern will remain visible after the flow has stopped. It is the art of the experimentalist to create a pigment-oil mixture in such a way that the oil sticks to the wall sufficiently. In this work a mixture of benzene and motor oil with higher evaporation temperature has been chosen. Titanium dioxide (TiO_2) powder served as color pigment. Photographs are used to record the final pattern.

2.2.2 Hot-Wire Anemometry

Fundamentals Hot-Wire Anemometry (HWA) is a fundamental experimental method in the study of low bis medium (less than $\sim$ 30%) turbulent gas flows. It is based on the convective heat transfer from a heated wire (sensor) placed in the flow. Therefore any flow variable which affects the heat transfer of the wire, like velocity, temperature and composition of the flow, can be measured with this approach. In this work the velocity field is measured as the temperature and the composition of the gas flow can be considered constant, not only during a single measurement but also, unless otherwise noted, throughout the whole measurement campaign. Turbulence information can be then obtained as statistical moments from the measured velocity field. This technique is well-developed and documented in numerous contributions since the early fifties. For a comprehensive description the author refers to the valuable work of Bruun [18]. In the following the principle is given.

Except for small fluid velocities, the heat from a electrically heated wire is drawn off mainly by convection, while radiation at the typical wire temperatures (150-300°C) and conduction through the supports of the wire are negligible. King (1914) derived an equation for the heat transfer for an infinite cylinder (approximation of the sensor) in an incompressible low Reynolds number flow, for equilibrium, where the released heat is only drawn off by convection. With the Reynolds number being related to the sensor diameter Re_{wire} and if extremely thin wires (5 μm is a typical value for tungsten hot-wires) are used as sensor for HWA, King's equation is a good fit over a moderate velocity range and valid for speeds of even more than 100 m/s[1].

[1]Measurements of higher velocities with HWA are however possible, using the vortex shedding method which is based on the relationship of vortex shedding frequency at the sensor for Re_{wire} of up to about 2000: $St = 0.212Re - 2.7$ [19]

King's equation reads:

$$Q_{elect} = \frac{E^2}{R_{T_{wire}}} = Q_{flow} = (a + b\sqrt{U})(T_{wire} - T_{flow}) \tag{2.1}$$

where Q_{elect} is the electrical power delivered to the sensor, Q_{flow} is the heat loss, E is the voltage drop across the sensor, R is its (electric)resistance, T is the temperature of wire or flow, U the unknown flow speed, and a and b are constants. The wire resistance is a function of the temperature:

$$R_{T_{wire}} = R_{T_{flow}}(1 + \alpha(T) \cdot (T_{wire} - T_{flow})) \tag{2.2}$$

with α being the temperature resistive coefficient, which also is (slightly) dependent on the temperature itself.

It follows that, by keeping the temperature of the sensor constant(that also means constant electric-resistance), the voltage drop at the sensor is a measure of the flow velocity. This approach is called constant temperature anemometry (CTA).

Similar relationship to Eq.2.1 has been introduced for extended velocity range: the so-called extended power law equation.

$$E^2 = A + B\sqrt{U} + CU \tag{2.3}$$

Calibration Many investigations in the past were dedicated to obtain the best calibration curves. An alternative to the extended power law equation (Eq.2.3) is the power law equation with a different exponent proposed by Collis and Williams [20]:

$$E^2 = A + BU^n \tag{2.4}$$

here n is a variable parameter which, also with respect to the velocity range to be measured, lies usually in the range 0.4–0.45. Nowadays, more general polynomial curve-fits are used due to improved computation capabilities, making the uncertainties of curve fitting the smallest uncertainty in the measurement chain. For velocities ranging from 5 to 50 m/s a normalised standard deviation ϵ_U [2] of less than 0.5 % is typical [18]. In this work the calibration data obtained from a TSI calibration unit up to about 50 m/s was extrapolated to 66 m/s by a 2nd order polynomial curve and fitted globally by 4th order polynomial curves resulting in a standard deviation ϵ_U of $\sim 1\%$.

Since no universal calibration is available, each sensor must be calibrated separately. To do this, a low turbulence flow of known velocity must be used. Ideally, the probe should be placed into the flow in the same way as it will be used for the actual measurement. In practice, the value of the exponent n changes with the sensor and velocity as do the values of A and B. Therefore it is necessary to calibrate each sensor individually, and to check this calibration frequently.

Major uncertainties linked to HWA arise due to probe disturbances (like vibrations or deposits on the wire) and to signal analysis at high turbulence, whereas a inappropriate sampling rate and measurement duration are common concern for every measurement technique.

[2] $\epsilon_U = \sqrt{\frac{1}{N}\sum(1 - \frac{U_R}{U_C})^2}$ with U being the speed corresponding to a given reference voltage (U_R) or derived from a best fit curve (U_C)

A fixed probe can only measure one velocity component. Therefore it is important that the wire element is placed orthogonal to the mean flow direction. If the flow is not orthogonal to the wire or if it is turbulent, an effective velocity (U_{eff}) should replace the velocity U in the equations 2.3 and 2.4:

$$U_{eff}^2 = U^2 + k^2V^2 + h^2W^2 \tag{2.5}$$

with k and h being the heat-transfer coefficients with respect to the velocity components V and W (See Figure 2.6 for localisation of velocity directions). For high turbulence intensities (Tu)[3] there is an uncertainty in the time-averaged velocity measurement even when the probe is placed correctly. Assuming that k is much smaller than h[4], and decomposing the velocity in time-averaged and fluctuating terms $U = \bar{U} + u, V = \bar{V} + v$ and $W = \bar{W} + w$, it follows:

$$\bar{U_{eff}^2} = \bar{U}^2 + \bar{u^2} + h^2\bar{w^2} \tag{2.6}$$

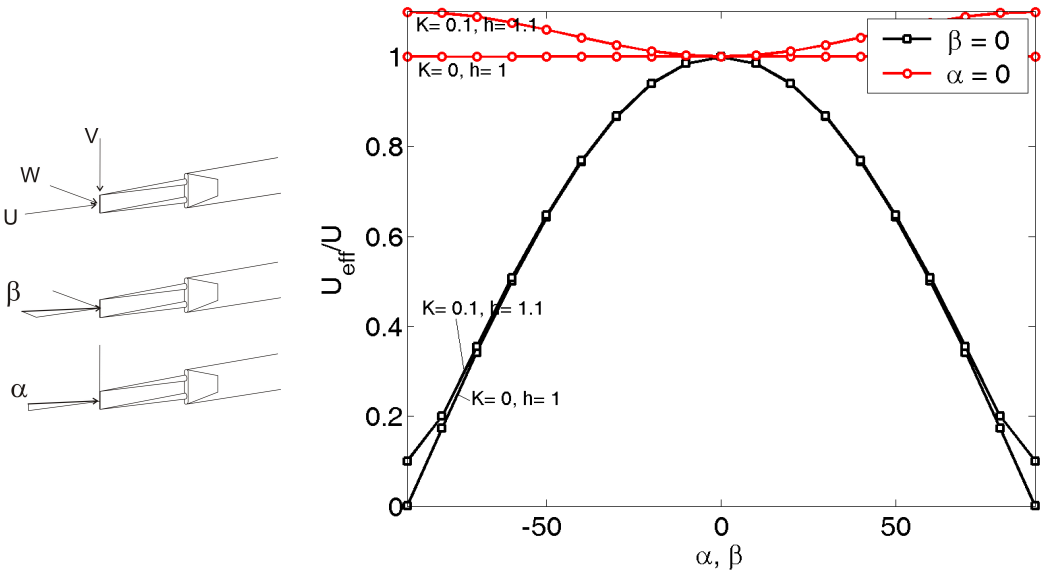

Figure 2.6: *Signal dependency of single HWA probe on velocity direction: α is the angle in the vertical plane, β is the angle in the orthogonal plane. k and h are the heat-transfer coefficients. U and U_{eff} are the velocities defined in eq. 2.5.*

The uncertainty increases with the turbulence level but can be reduced with correction factors for pre-defined turbulence types: Table 2.3 sums up the correction factor to use in order to compensate these errors, assuming isotropic turbulence ($\bar{u^2} = \bar{v^2} = \bar{w^2}$).

Higher statistical moments of the velocity (as variance, skewness and flatness) are even more affected from the turbulence. Especially for these Swaminathan (1986) [18] suggests to calculate them from the row voltage signals instead as usual, after that the electric signal has been converted into velocity by one of the calibration curves (i.e.

[3] $Tu \stackrel{\text{def}}{=} \frac{\sqrt{\bar{u^2}}}{|\vec{U}|}$ with u being the velocity fluctuation.

[4] Typical ranges are k = [0 – 0.2] and h = [1.05 – 1.2], where k = 0, h = 1 are the limit values for an infinite cylinder without supports.

with Eq.2.4). Two or three wire sensors are however much more appropriate. In this work both single and double wire sensors have been used.

Table 2.3: *Correction factors ($\frac{\bar{U_{eff}}}{\bar{U}}$) for the velocity measured with single probe HWA depending from the turbulence level (Tu) [18].*

Tu (%)	$\frac{\bar{U_{eff}}}{\bar{U}}$
10	1.006
20	1.02
30	1.05

Summarising, the advantages of HWA are: it has a high frequency response, does not need any fluid tracers, is quick applicable, accurate and is relatively cheap compared, for instance, to Laser Doppler Anemometry (LDA). The drawbacks are: it is invasive, produces values averaged over the wire size, the determination of the velocity direction is ambiguous and it is inaccurate at low velocities (less than about 4 m/s) and for highly turbulent flows (particularly in the intermittence region).

2.2.3 Laser Doppler Anemometry

Through laser doppler anemometry (LDA) the velocity of a fluid flow can be measured by measuring the velocity of particles which are seeded in the fluid. For the measured velocity approximates the velocity of the fluid, the particles should be small enough to be convected with the same velocity. In this work Di-Ethyl-Hexyl-Sebacate ($C_{26}H_{50}O_4$) particles with diameter $\oslash \sim 1\,\mu$m have been used for seeding. LDA systems can measure all velocity components of the particles. The fundamentals of this technique are given by Durst in [21], while practical suggestions are given, among others, in the review of Jensen [22].

Figure 2.7 shows the construction schema for a typical 1D LDA system. A laser beam is splitted (BS) into two beams, lying in the plane of the figure, and focused through a lens (L) at point P in the measuring volume. The measuring principle is based on the Doppler effect: the light reflected from the particles crossing the measuring volume experiences a frequency shift proportional to the velocity of the particles. The reflected light is amplified by a photo-multiplier (detector D), which can be located either opposite to the generated beam (*Forward scattering LDA* as in the picture) or integrated in the same transmitting optics now provided with an orifice to avoid the reception of the newly generated beam (*backward scatter LDA*).

Forward scattering LDA was used at the beginning, and still now when high velocity flow are measured or high particle rates are requested, because the amount of light scattered forwards is much larger than backwards[5]. The backscatter LDA allows, however, for the integration of transmitting and receiving optics in a common housing, saving the user a lot of tedious and time-consuming work aligning separate units. This latter approach has been used in this work.

Whatever the scattering modus is, the electrical signal at detector D is then transformed in an A/D converter for data processing which consists of signal filtering and fringe counting. Thanks to interferometry the extremely small Doppler frequency shift (f_D)

[5]Especially for particles bigger than the wavelength of laser light, according to earliest calculation by Mie (1908).

can finally be detected. Moreover if the frequency of one of the interfering laser beams is shifted (f_B) in the so-called Bragg cell[6], the so-called *fringe bias* decreases. That means to increase the probability to generate a measurable signal also for particles moving almost parallel to the fringes (small velocity component V in figure). This causes optical fringes in the measurement volume to move in the direction from the shifted beam (higher frequency) to the unshifted beam at a frequency equal to the shift width. Therefore the direction of the particle velocity is not ambiguous anymore and the velocity direction can be identified now. The frequency detected in D is $f_B + f_D$ if the particle moves in a direction against the fringes, $f_B - f_D$ in the opposite case.

LDA measurements are intrinsically local measurements because interferences exist only where the laser beams cross each other. A small well-shaped crossing volume and high flow rate of small highly reflective particles are fundamental requirements for good measurements [21]. Interferometry will be focused on later in this work, therefore we also refer to chapter 2.3.3 for fundamentals of interferometry and comparison to laser vibrometry.

In order to measure all three velocity components the laser beam is first splitted into three and then their frequencies shifted to obtain three monochromatic beams[7] before they are splitted again and pass the Bragg cells, being positioned on different planes and finally focused in the same point P.

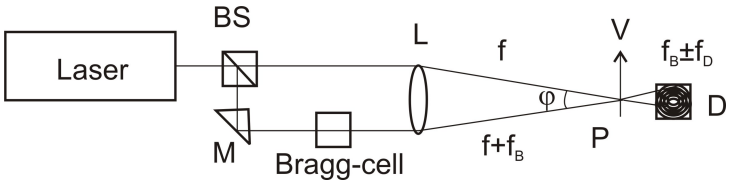

Figure 2.7: *Implementation of 1D LDA: the laser beam is splitted into two beams which interfere in point P. Detector (D), lens (L), mirror (M), beam splitter (BS). Original laser frequency (f), shifted from Bragg cell (f_B) and from Doppler effect (f_D).*

Nowadays LDA is widely used for velocity measurements either exclusively or together with other techniques, i.e. HWA like in this work, in order to integrate and corroborate the results. Advantages of LDA are: it is non-invasive, measures flow reversal and large velocity ranges, has no limits on turbulence levels, is independent from fluid temperature and no calibration is needed. Drawbacks of LDA are: time consuming optical adjustments and necessity of flow seeding. The latter is often a major limitation of closed loop wind tunnels because mechanical parts of the tunnel quickly become contaminated due to the seeding particles.

2.3 Acoustic Techniques

2.3.1 Near Field Holography

Near Field Holography (NAH) is nowadays a popular measurement technique based on Fourier acoustics (See Annex A) developed by E.G.Williams [23].

[6] A Bragg cell is a acoustooptic modulator which uses the interaction of laser light and high frequency ultrasound in a transparent medium to shift the frequency (early prediction from Brillouin, 1922).

[7] Different frequencies assure that the beams do not interfere with each other.

A pressure hologram represents a measurement of a coherent pressure field (phase and amplitude) in two spatial dimensions. The hologram is decomposed into a Fourier series and can be propagated to different but parallel two-dimensional surfaces by altering the amplitude and phase of each element of the series. Provided that no sound sources lie between both surfaces the homogeneous wave equation can be used for this purpose. Furthermore the pressure on this new surface can be converted into velocity by multiplication with a different amplitude and phase using the Eulers equation.

Williams demonstrated that the Fourier series approach to NAH applies basically to any 2D geometry. Assuming the propagation of planar acoustic waves and that the equation of the plane where the pressure signal is known (i.e. measured with microphones) is z=0, the two-dimensional Fourier transformation of the pressure signal for that plane reads:

$$P(k_x, k_y) = \int_{-\infty}^{\infty}\int_{-\infty}^{\infty} p(x, y, 0) \cdot e^{-i\cdot(k_x x + k_y y)}\, dk_x\, dk_y \tag{2.7}$$

where $k = \frac{2\pi f}{c}$ is the wave vector, c is the speed of sound, f the investigated frequency, and $P(k_x, k_y)$ is a complex amplitude called the angular spectrum.

Once the angular spectrum is known, the pressure field in a parallel plane ($z \neq 0$) is derived from a planar integral of the Fourier transformation of the pressure in the measured plane ($z = 0$), multiplied by a complex transformation functions:

$$p(x, y, z) = \frac{1}{4\pi^2} \cdot \int_{-\infty}^{\infty}\int_{-\infty}^{\infty} P(k_x, k_y) \cdot e^{i\cdot k_z \cdot z} \cdot e^{i\cdot(k_x x + k_y y)}\, dk_x\, dk_y \tag{2.8}$$

The extrapolation of the wave field can be either towards the sources, allowing their localisation, or away from them, allowing the calculation of the pressure level in the far field.

The derivation and the limitations of this transformation are listed in the Annex A.4.

2.3.2 Time-reversal Acoustic Source Localisation

In the work of Fink [25] it was experimentally shown that if the sound signal recorded by microphones is played backwards respecting all original time delays from the microphone locations, the original signal at the emittance is obtained per interference (time-reversal mirror). The essential property that makes time-reversed acoustics possible is that the underlying physical processes of sound waves are unaltered if time is reversed. The two functions f(x,t) and f(x,-t) are in fact both solution of the wave equation. That is true only in linear acoustics for waves propagating in a medium at rest with constant physical properties. The interference (time-)transformation developed by Heinz [24] in neurocomputing field works similar. It is the fundament of a measurement instrument called *acoustic camera*. Here the sound field is measured simultaneously with several microphones with known relative positions and the sound sources are subsequently reconstructed per interference.

This time, however, the interference does not take place in real space but in the field of view of a camera. For each pixel on the screen the interference values are calculated with respect to the time delays measured from the microphones. The microphones are localised on the screen and the distances calculated on a plane in the field of view of the camera (See Figure 2.8). A map of sound sources arise where the waves have maximum

positive interference. The name 'acoustic camera' derives from the unique feature to see the localised sound sources overlapped to the image of the environment in real time, captured with a video camera.

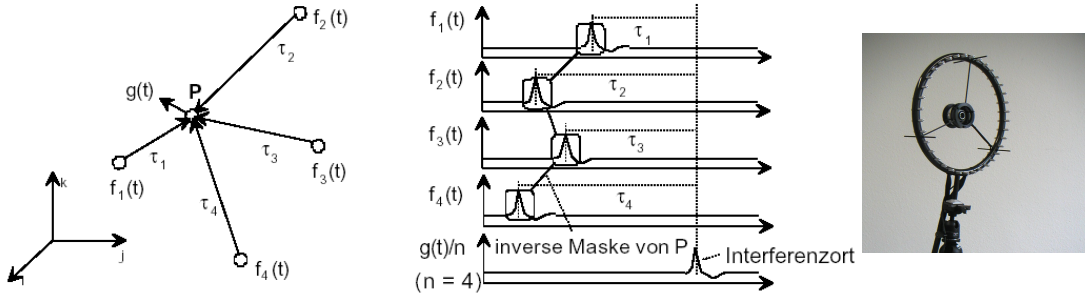

Figure 2.8: *Interference principle (left) by Heinz [24] and acoustic camera (right). $f_i(t)$ are the pressure signals measured in different locations (i=1..4) in order to reconstruct the signal g(t) per interference.*

Figure 2.8 shows the measuring system used in this work (developed and manufactured by the 'Gesellschaft zur Förderung angewandter Informatik' (GFaI)). It consists of an array of 32 equally spaced microphones placed on the circumference of a circle with diameter of 75 cm. The lower cut-off frequency, due to array size, is about 100 Hz. Limits of the measuring systems are: the reconstruction theory assumes planar sound waves emitted towards a microphone-array plane located parallel to it. The mapping quality depends on the type of the incoming pressure signal: discrete tones cause a blurred localisation, because constructive interferences take place periodically in space. In contrast impulse signals or broad band noise are focused best.

2.3.3 Laser Vibrometry

2.3.3.1 Fundmentals

Laser Vibrometry (LV) is an optical measuring method based on interferometry. Interferences emerge from superposing beams with same frequency (monochromatic) and same polarisation. Considering two superposing monochromatic beams E_1 and E_2 with time averaged intensities $I_1 =< E_1^2 >$ and $I_2 =< E_2^2 >$

$$E_1 = E_{01}\cos(\phi_1) \tag{2.9}$$
$$E_2 = E_{02}\cos(\phi_2) \tag{2.10}$$

the resulting beam is their sum:

$$E_{sum} = E_{01}\cos(\phi_1) + E_{02}\cos(\phi_2) \tag{2.11}$$

with the following intensity:

$$\begin{aligned} I_{sum} &= < E_{sum}^2 > \\ &= < E_{01}^2\cos^2(\phi_1) + E_{02}^2\cos^2(\phi_2) \\ &\quad + 2E_{01}E_{02}\cos(\phi_1)\cos(\phi_2) > \qquad (2.12) \\ I_{sum} &= I_1 + I_2 + 2\sqrt{(I_1 \cdot I_2)} \cdot \cos(\phi_1 - \phi_2) \qquad (2.13) \end{aligned}$$

Laser interferometry exploits the specific physical properties of Laser light[1], which are high intensity, polarisation, discrete frequency and high coherence of the light beam. Due to the high coherence, the phases of the monochromatic light beams (ϕ_1, ϕ_2) remain constant on distances larger than the length of the light path used in experiments unless it is altered along the optical path by external devices (i.e. Bragg-cells) or by medium or boundary properties. This latter, that is the phase change due to medium or boundary is used as principle for quantitative measurement of physical variables like distance, velocity, pressure, temperature and gas composition.

Figure 2.9 shows the measurement principle using the scheme of the first and easiest interferometer constructed by Michelson in 1881 [30]. Practical implementations differ from this basic scheme and will be discussed in the next section. Into the beam splitter (BS), the laser beam with frequency f is splitted into two beams: one is reflected by mirror (M) and comes across BS into the detector (D). It is called reference beam. The other beam crosses the pressure-perturbated medium (P) twice and is reflected by the vibrating object (V). Both, the perturbated medium and the vibrating object cause changes in the phase of the reflected beam. Time-dependent interferences with the reference beam are taking place and detected at detector (D).

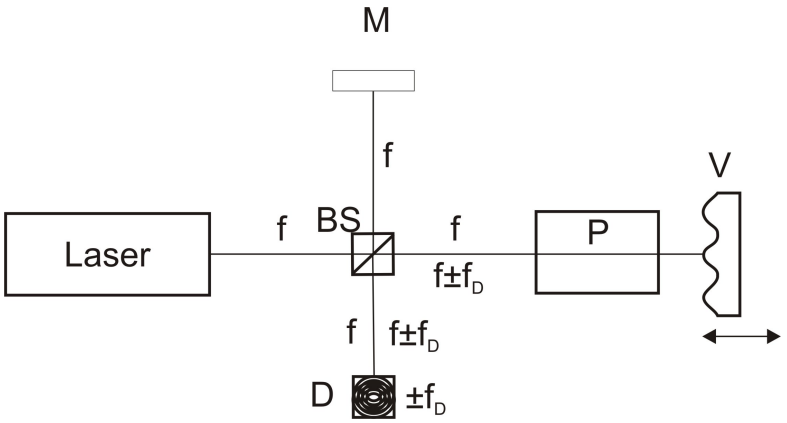

Figure 2.9: *Michelson interferometer. Detector (D), mirror (M), beam splitter (BS), laboratory medium (P), vibrating object (V). Original laser frequency (f) and shifted from Doppler effect (f_D).*

In the classic use of laser vibrometry the laboratory medium (P) is aimed to be at rest with constant temperature and pressure. Therefore interferences give a measure of the vibration frequency and amplitude of the object(V) in the spot of laser on the object. The signal from the detector generally consists of a signal with frequency f_D (due to Doppler effect of a vibration with velocity v), modulated on the carrier (incoming laser light with frequency f) (See Eq. 2.14).

$$f_D = \pm f \frac{2v}{c} \tag{2.14}$$

here is c the speed of light in the laboratory medium at rest.

The quality of the interference can be expressed as modulation deepness m

$$m = \frac{I_{max} - I_{min}}{I_{max} + I_{min}} = \frac{2 * \sqrt{I_1 I_2}}{I_1 + I_2} \tag{2.15}$$

[1]Laser: Acronym of Light Amplification by Stimulated Emission of Radiation

The best interference quality (m=1) is obtained when the two superposing beams have same intensity because just in this case one can have complete signal cancellation.

On the other hand, if the object (V) is replaced by a mirror or back scattering reflector and one cares for not vibrating conditions, one can use the modification of interference pattern as a measure for the temperature and pressure variation in the medium (P) along the laser beam. Therefore, one speaks here more appropriately of laser interferometry instead of laser vibrometry. In this work both terms will be used.

Mayrhofer (2001) [27] measured hydrodynamic pressure fluctuations in compressors by this approach. Vibration and pressure fluctuations could be separated in frequency domain according to their particular flow condition [28]. Moreover Zipser et al. [26] published the same approach for measurement of acoustic pressure fluctuations.

Both, measurements of hydrodynamic and acoustic pressure fluctuations, rely on variations of the refraction index of light within a medium. This can be expressed as a function of the local density as follows:

$$n \stackrel{def}{=} \frac{c}{c_0} \tag{2.16}$$

$$(n-1)_\rho = \sum_{i=1}^{N} (G_i \rho_i) \tag{2.17}$$

with n being the refraction index of a gas with density ρ. c and c_0 are respectively the speed of light in the medium and in vacuum for a given monochromatic light frequency. G_i the Gladstone-Dale constant for the same monochromatic light frequency and ρ_i are the partial density of each of N gas components.

In our case the temperature and the medium composition can be considered constant for times larger than the time needed for the measurement. So, when considering dry air and the adiabatic transformation of an ideal gas, the refraction index changes as follows:

$$\Delta n = (n_1 - n_0) = (n_0 - 1) \cdot \left(\left(\frac{p_1}{p_0} \right)^{\frac{1}{\kappa}} - 1 \right) \tag{2.18}$$

The reference refraction index for a Helium-Neon laser (He-Ne) beam with wavelength 633 nm in air at standard atmospheric pressure is given as $n_0 = 1.00029$ [29]. Therefore, for standard atmospheric pressure condition and very small pressure fluctuations ($\delta p \ll p_0$), the derivative of the refraction index can be approximated as follows:

$$\frac{\delta n(t)}{\delta p(t)} \approx \frac{n_0 - 1}{\kappa p_0} \approx 2.1 \cdot 10^{-9} [Pa^{-1}] \tag{2.19}$$

By integration of the refraction index over the laser beam length (L) one obtains an equivalent optical length. This optical length changes by changing the refraction index as follows:

$$\Delta l(t) \approx L \Delta n(t) \approx \frac{(n_0 - 1)\Delta p(t)}{\kappa p_0} \tag{2.20}$$

On the other hand the optical length for the reference path inside the interferometer remains the same. The difference between the integration along the measurement path

and the reference path can be expressed as phase difference $\Delta\phi$. Changes in the pressure cause a movement of the interferometric fringes. These are finally detected by the electronic circuits.

$$\Delta\phi(x,y,t) = \frac{2\pi}{\lambda}\int_L n(x,y,z,t)\,dz - \frac{2\pi}{\lambda}\int_{L_{ref}} n(x,y,z)\,dz \tag{2.21}$$

with z the beam axis.

Therefore it is possible to measure pressure fluctuation averaged over the laser beam length. It can be expressed as equivalent velocity (also called *effective* velocity)

$$v_{eff}(x,y,t) \;=\; 2\cdot\frac{dn}{dp}\int_L \frac{dp(x,y,z,t)}{dt}\,dz \tag{2.22}$$

with L being the length of geometrical path covered by the laser beam between laser head and reflector (z direction).

On the other side, in classical vibrometry, the refraction index is also constant on the measurement path, therefore the phase-change reads:

$$\phi(t) \;=\; \frac{4\pi}{\lambda}z(t) \tag{2.23}$$

$$v \;=\; \frac{dz}{dt} = \frac{\lambda}{4\pi}\frac{d\phi}{dt} \tag{2.24}$$

Even though laser vibrometry exploits, similar to the LDA (Section 2.2.3), interference fringes to obtain a signal, the measuring principle is quite different: LDA does not measure pressure fluctuations because the change in the interference fringes can only occur in a small measurement volume and only if light-reflecting particles cross it. Laser vibrometry, on the other hand, can not directly measure the flow velocity as in the flow there are no particles[8]. The measurement volume corresponds to the whole length of the laser beam.

2.3.3.2 Implementation

After having reviewed the interferometric principle and the application for both vibrometric and pressure measurements, now two commercial implementations of this principle (Polytec) are introduced. They have been used in this work for aeroacoustic measurements. The first implementation is based on the Mach-Zehnder Interferometer and is on the market under the name Polytec Scanning Vibrometer (PSV). It consists of an interferometric system whose He-Ne laser beam can be tilted through internal mirrors. The tilting mechanism is used to scan a whole region from the same fixed position. Figure 2.10 shows the working principle. In the following, P and V denote the two possible applications as described in the previous sections: classic vibrometry (V) or density measurement (P).

The laser beam with frequency f is splitted into a reference and a measurement path with same polarisation by BS1. The measure path experiences a frequency shift due

[8]Commonly, the density of the particles naturally contained in the air, i.e. dust, is not sufficient and the size of the particles too large and not uniform to serve for LDA measurements.

to the Bragg cell (f_B). The initial linear polarisation of the beam (i.e. horizontal) is converted into a circular one when passing the $\lambda/4$ plate[9].

The light reflected by V has still circular polarisation but reversed rotation. Therefore, after passing the same plate again, the light is now vertically polarised. The different polarisation avoids interferences on the same path. On the other side, interferences take place at detector D1 where the first beam meets the reference beam whose polarisation is changed to vertical by a $\lambda/2$ plate inclined 45°. The second detector D2 is not compulsory but allows a better signal-to-noise ratio. Namely, one can cross-correlate the output of both detectors and use it as new signal; Due to the fact that the noise at two separated detectors is uncorrelated, the only coherent contribution comes from the signal.

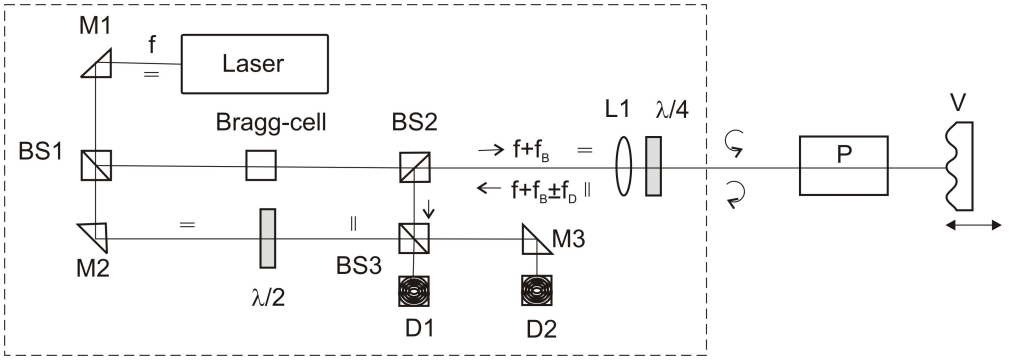

Figure 2.10: *Implementation of PSV interferometer following the Mach-Zehnder principle: mirrors (M), lens (L1), beam splitters (BS), detectors (D), polarisation filters ($\lambda/2, \lambda/4$), measurement volume affected by pressure changes (P), reflecting object (V). The direction of light polarisation is indicated with two parallel horizontal or vertical lines. The dashed line groups parts belonging to the same physical unit.*

The second implementation is known as Compact Laser Vibrometer (CLV). CLV is classified as one-point vibrometer as the axis of the laser beam remains fixed. It consists of two separated units: a laser unit with decoder modules and a Bragg cell with lenses. The two units are connected by a fiberglass cable. The working principle differs from the PSV because here the measurement beam and the reference beam are routed on the same optical fiber (fiberglass cable). Figure 2.11 shows the principle: The generated beam passes the beam splitter (BS) and, after a 45° polarisation change at the $\lambda/2$ plate, reaches the Bragg-cell, the lens (L1) and further down the measurement domain (P,V). The fiber ends in point E causing a partial reflection of the original beam. This reflected beam will be called 'reference beam' further on. This reflection property at the fiber-end is exploited in the measuring principle: by passing the $\lambda/2$ plate again, the reference beam and the beam reflected in V have now the same polarisation and can therefore interfere with each other, but not with the originally generated beam, even though they are transmitted on the same optical path. In the figure 2.11 the ideal case of a perfect interference (m=1) is sketched: that is the amplitude of interfering beams with frequency f is the same. In reality the reference beam will have a smaller intensity than

[9]Circular polarisers are made of bi-refracting crystals which have different refractive indices, and therefore different propagating velocities, depending on the polarisation of the incident light. If linear polarised light crosses those crystals inclined 45° to the major axis, the phase changes. This produces for instance phase differences of $\pi/2(\lambda/4$ plate) or $\pm\pi$ ($\lambda/2$ plate).

the measurement one. Therefore, the signal with frequency f will not complete cancels out at the detector D. Nevertheless commercial detection software (Polytec PSV) is capable to cope with this allowing a very high detection rate even by different reflection index of the object surface (V).

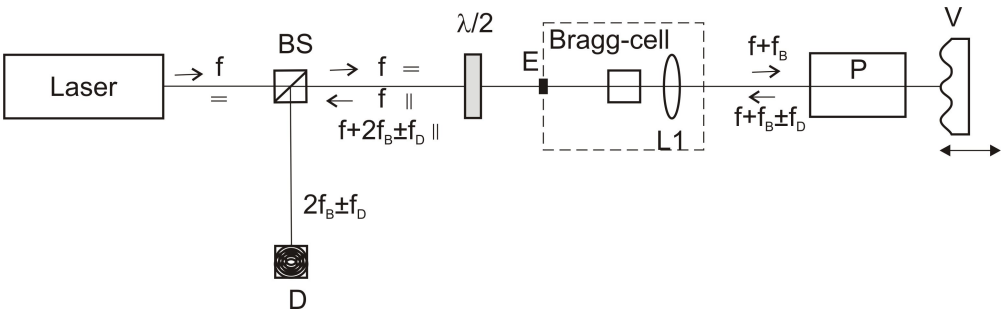

Figure 2.11: *Implementation of CLV interferometer (Compact Laser Vibrometer).*

For aeroacoustic purposes we replace the object (V) by a mirror or a back scattering reflector. By using a back scatting reflector instead of a mirror the light is reflected in all directions. Thus the reflector is not required to be positioned exactly orthogonal to the laser beam anymore. However, the scanning motion of the beam of PSV requires the reflector to be at least as big as the domain to be scanned. This can cause spurious reflections of acoustic waves at the reflector which are a drawback for measurements of acoustic pressure fluctuations. Moreover the laser beam crosses the measurement domain at different angles introducing an additional spatial averaging of pressure fluctuations in the measuring volume which is a drawback for sound source localisation.

2.3.3.3 Progresses

Localisation Enhancement of Acoustic Pressure Fluctuation

Hydrodynamic near fields are characterised from the fact that both types of pressure fluctuations (hydrodynamic and acoustic) occurs [10].

For better acoustic experiments, it is convenient to separate these contributions.

With Laser interferometry it is possible to detect the acoustic pressure fluctuations inside a hydrodynamic near field much better than with other conventional acoustic techniques (i.e. microphones).

We demonstrate that, with a simple numerical simulation, by assuming a planar sound wave and a coherent pressure fluctuation representing the hydrodynamic fluctuation. The amplitudes are taken equal to ($\sim$ 50 dB) and 60 dB respectively. If the pressure were locally measured with microphones, it would have lead to a sound signal completely

[10]The word *pseudo sound* is used in this work, following the example of Ffowcs-Williams [34] to indicate the pressure fluctuations convected with the eddy structures of the flow. This distinguish from the typical acoustic pressure fluctuations , which propagate with speed of sound. In general acoustics, pseudo sound is often described with the term 'wind noise'. This is due to the fact that it can be detected through a microphone and designates exactly what a microphone located in the flow measures. More correctly, pseudo sound exists because of the balance of inertial forces in the flow and can be detected also by not-invasive probes (laser). In this work, the region where pseudo sound is defined will be called *the* hydro-dynamic near field.

perturbed from pseudo sound, coherent pressure fluctuation representing the hydrodynamic fluctuation. The amplitudes are taken equal to ($\sim$ 50 dB) and 60 dB respectively. If the pressure were locally measured with microphones, it would have lead to a sound signal completely perturbed from pseudo sound, while with laser interferometry in many cases we can preserve almost the original sound pressure level. Figure 2.13 shows the result of this simulation: one can estimate the measurement precision, which can be obtained with laser interferometry for a given flow width and amplitude of the hydrodynamic pressure. Through the integration of changes in the light index along the path L_A, the laser interferometry is less sensitive than microphones to hydraulic fluctuations. In fact, the effect of the sound pressure on the signal measured with laser interferometry (v_{eff}) prevails over those of pseudo sound by increasing the ratio between laser beam length (L_A) and the extension of turbulence (L_F). It follows that the quality of sound measurements depends also on the extension of the turbulence region.

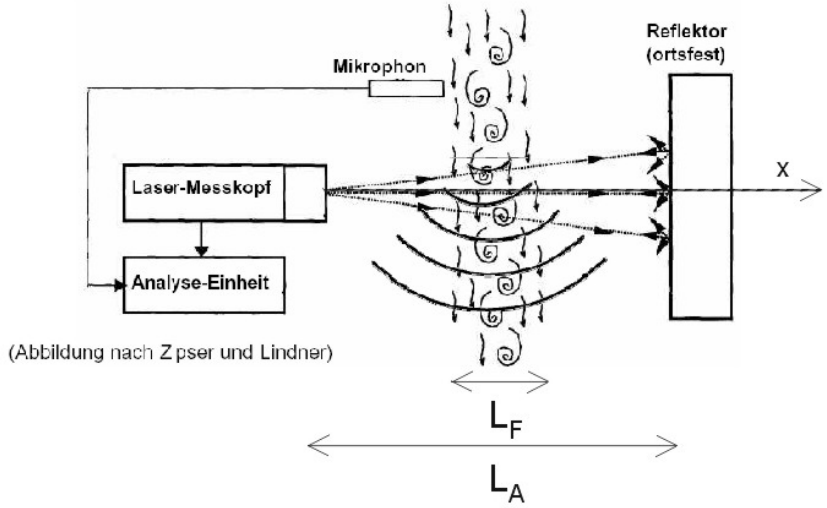

Figure 2.12: *Application schemata of Laser interferometry for aeroacoustics [26]. L_F is the extension of the turbulent flow along the laser ray and L_A is the distance from laser to the fixed (back)reflector.*

Localisation of sound sources

Further in this work it is attempted to localise sound sources with laser interferometry. Already in the work of Zipser [26] the sound sources were qualitatively localised by visualisation of the time evolution of the pressure field. Here we follow to same extent the same approach: the acoustic sound pressure has been measured in the far field and used as reference for the visualisation of the propagation of sound waves. Hereby, the phase measured in far field has been subtracted from the phase measured, with the laser vibrometer, in near field. The phase is calculated with fast Fourier transformation technique (FFT). When the phase difference between two points remains constant, it shows a correlation and therefore indicates either sound waves or turbulent structures. The formers can be distinguished from the latters depending on the length between minima and maxima of the pressure signal.

Furthermore a new approach is tried in this work: inside a turbulent region the acoustic pressure fluctuations are much smaller than the hydrodynamic one and can be therefore neglected. In particular, as the Mach number considered in this work is small, the

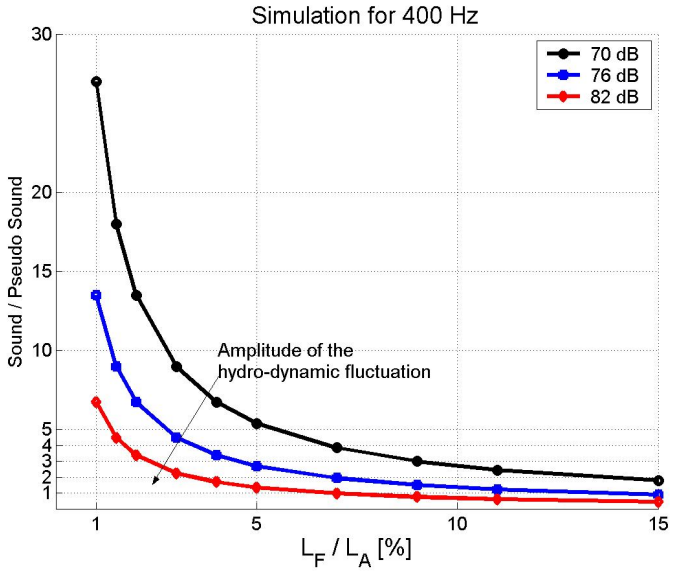

Figure 2.13: *Flow influence in sound measurement with laser interferometry. the measured variable (v_{eff} is influenced by the hydraulic pressure perturbation. Reference value for the sound without hydraulic perturbation is 0.2 $\mu m/s$ (laser interferometry measurement) or $\sim$ 50 dB (microphone measurement).*

hydrodynamic pressure fluctuations can be modelled as incompressible. Using the same expansion about incompressible flow (EIF) [43] used for numerical prediction (section 3.2.2), the substantial derivative of the hydrodynamic pressure is identified, as acoustic source term. Therefore, a part of the velocity gradient which is the difference between partial and substantial derivative, the square mean root of the detected signal (v_{eff}) is a measure of the strength of aeroacoustic sound sources.

$$rms(v_{eff}) = 2|\frac{dn}{dp}| \cdot \sqrt{\frac{1}{T}\int_0^T (\int_B \frac{dp(z,t)}{dt}\, dz)^2\, dt} \tag{2.25}$$

Localisation Enhancement of Hydraulic Pressure Fluctuation The measurements in this work are conducted on configurations with particular symmetry: i.e. cylindrical geometries with the laser beams being parallel to its axis. The derivative of the refraction index with respect to the pressure is constant throughout the measurement field, therefore the measured variable can be easily defined with the integral formulation in Eq.2.22. For measurements not respecting this symmetry or for more general geometries, in order to remove the effect of spatial averaging, it is necessary to measure the pressure fluctuations locally. Mayrhofer [27] reviewed some possible approaches: correlation of two laser beams, laser tomography and so-called laser with small 'depth of sharpness'. In this work we investigated the latter. From [27] it seems that the previous author has not achieved satisfactory results with a similar approach. We aimed here to reduce the integration length used in equation 2.22. In particular, by widening the laser beam over a region larger than the local turbulence correlation length (Λ) we aim to have a negligible space-averaged signal over a large part of the integration length. Further in this work we call this approach 'Small Sharpness Depth Laser Vibrometer' (SSD-LV). Figure 2.14 shows the principle. The laser beam from a CLV unit with di-

ameter d crosses three cylindrical lenses L0, L1, L2 before being reflected at mirror M. The relative positioning of the lenses (a, b) is related to their focal length f. From the theory of thin lenses it follows:

$$\frac{1}{a} + \frac{1}{b} = \frac{1}{f} \tag{2.26}$$

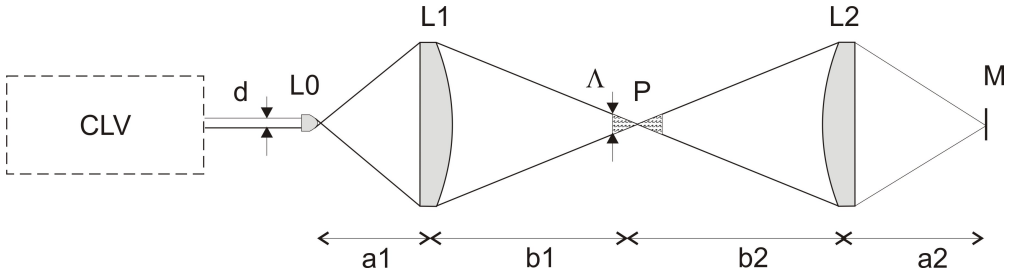

Figure 2.14: *Principle of the Small Sharpness Depth Laser Vibrometer(SSD-LV). Turbulence correlation length Λ, lenses L0, L1, L2, focal point P, laser beam width d, mirror M.*

The shear layer of the windtunnel nozzle has been used as test case for initial measurement with laser interferometry. The previously defined variable v_{eff} has been measured with PSV, CLV and SSD-LV within the same region (grey in figure 2.17-a) and same outflow speed (U=40 m/s). For CLV and SSD-LV the reflector is built from the small mirror (M) of figure 2.15 while for PSV a larger retro-reflector is positioned behind the nozzle. In all the three cases the laser beam was focused on the middle plane of the nozzle.

We could separate spatially the frequency content of the turbulence. In figure 2.16, for instance, one can see the intensity of v_{eff} for different frequencies (a, b, c) and as overall (d).

Figure 2.17 shows the spectra of v_{eff} for different longitudinal distances from the nozzle outlet and transversal distances from the nozzle symmetry plane. In general one can see a good capability of this technique, in all three realisations, to localise hydrodynamic pressure fluctuations (and as previously showed, also acoustic sources) and separate spatially according to its frequency. In fact one observes high frequency perturbations near the outlet (≈500–1500 Hz) and stronger low-frequency perturbations with increasing distance, with maximum at about d/H=2 (≈400–500 Hz). The levels measured from CLV and SSD-LV are similar but inferior to those of PSV. The reason is unclear but probably dependent from the laser spot size in the turbulence region.

If the focus point of the laser beam (SSD-LV) is moved outside the flow while keeping the length of the laser beam crossing the flow constant, one observes a reduced signal as expected. However, the focusing properties of SSD-LV are not sufficient for investigation of pressure fields which are subject to large gradients in the laser axis direction.

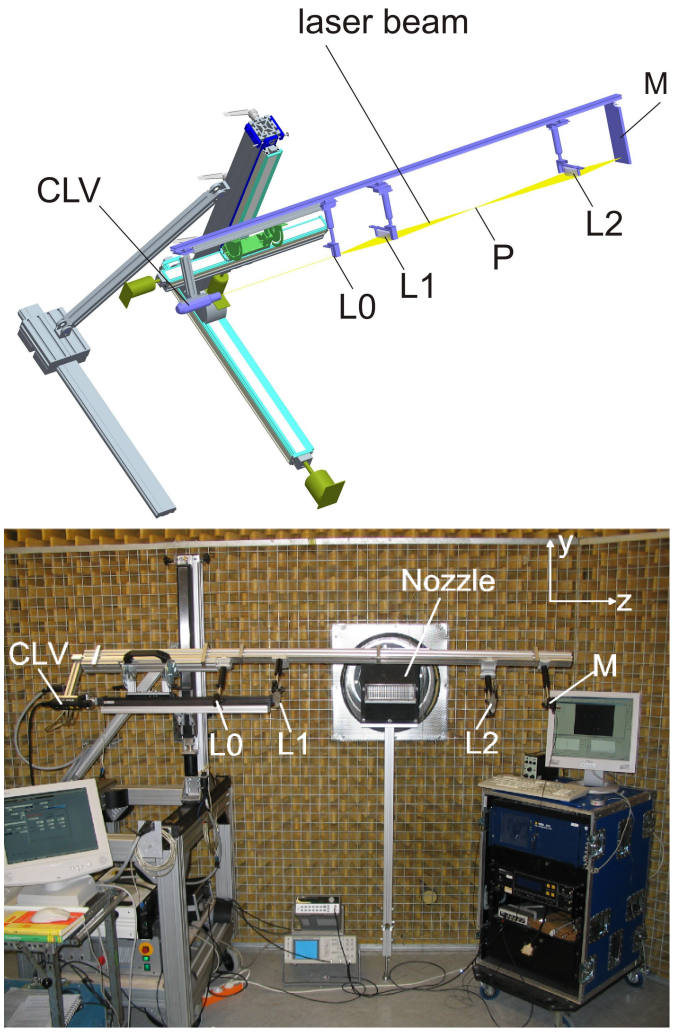

Figure 2.15: *SSD-LV configuration: detail of CAD model (above) and overview of the wind-tunnel with the traversing unit (underneath). Compact Laser Vibrometer (CLV), Lenses (L0, L1, L2), focal point (P), mirror (M).*

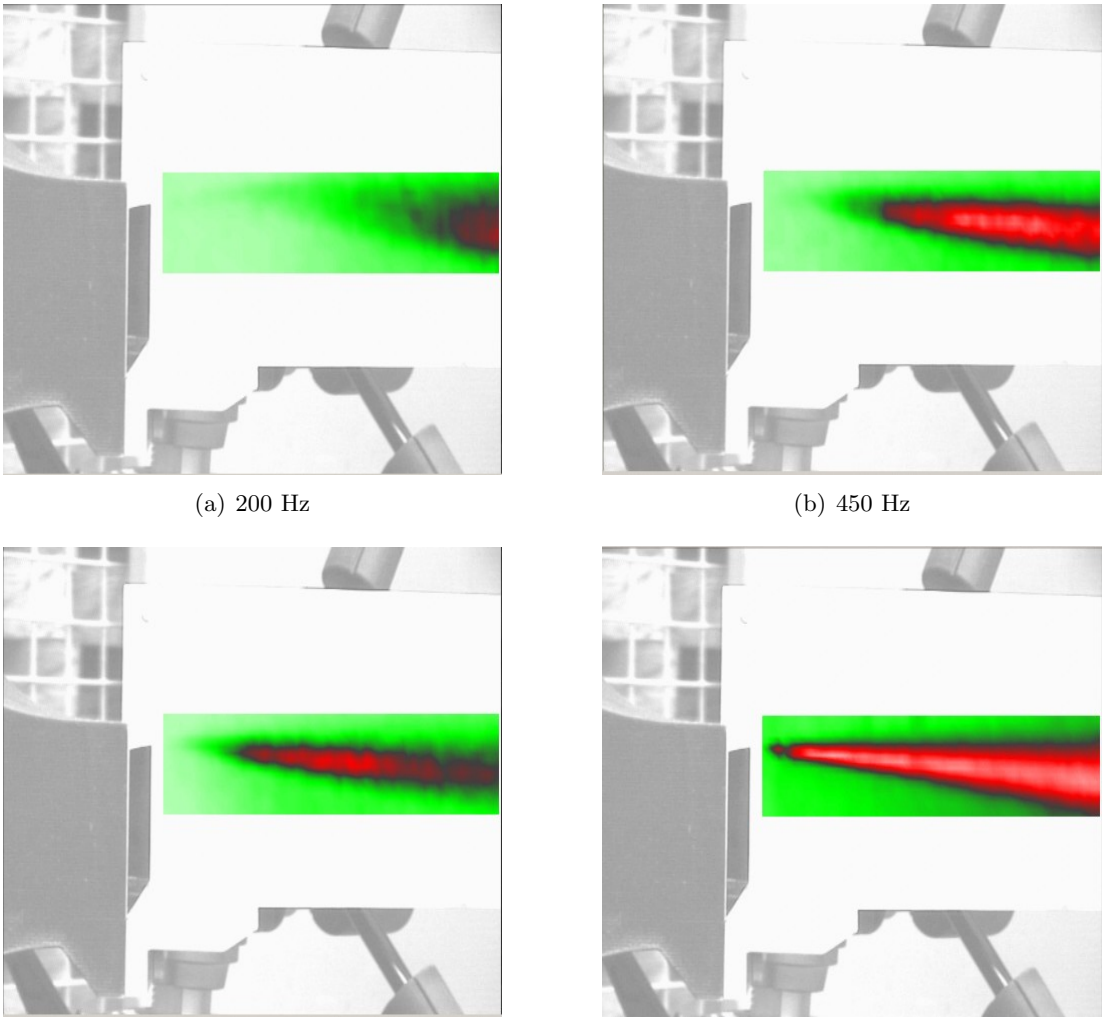

(a) 200 Hz

(b) 450 Hz

(c) 700 Hz

(d) all frequencies

Figure 2.16: *Shear layer measurement with PSV for outflow speed 40 m/s. Map of root mean square of v_{eff}. Maximum = 150 μm/s (red).*

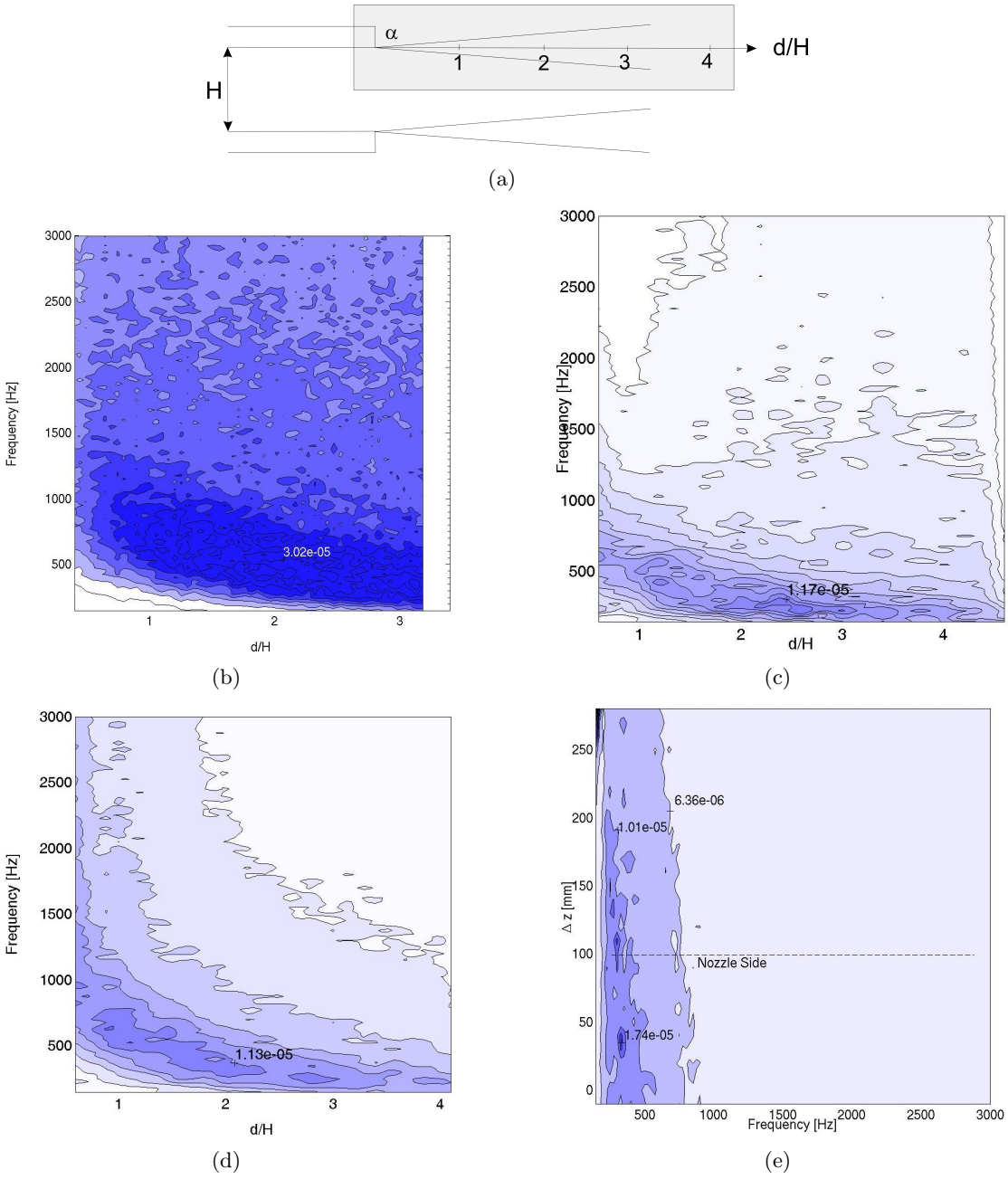

Figure 2.17: *Shear layer measurement: a) region measured (in gray) at nozzle outlet of the wind tunnel. Opening angle of shear layer $\alpha \approx 15°$. Spectra of v_{eff} measured with laser interferometry along the shear layer for outflow speed 40 m/s. b) with PSV c) with CLV, d) CLV with lenses (SSD-LV). e) Spectra of v_{eff} with SSD-LV, for the same longitudinal position (d/H) with shift of the focusing points in transversal direction (Δz). Amplitude range = 0.2 – 3·10^{-5} m/s.*

Chapter 3

Analytical and Numerical Approach

In this chapter we present the governing equations for the dynamics of a gas, the model simplifications for the aeroacoustic problem and details of the implementation in commercial and own code. We first recall briefly the fundamentals of governing equations for compressible gas (Navier-Stokes and Euler equations) and the discretisation techniques (finite difference, finite elements and finite volume method). Than we present three approaches for aeroacoustics which have been used in this work: two of them are hybrid approaches and one is a direct one. The hybrid approach solves the fluid dynamic and the acoustic problems separately. The sound sources are extracted from the turbulence solved in the fluid dynamic simulation (here with RANS, DES). As shown further, the goal is to reduce the numerical complexity by adapting the governing equation and the numerical discretisation to each problem. The direct approach, on the other side, solves both problems at the same time and captures, differently from the hybrid approach, the reciprocal physical interaction. In this work we used the direct approach according to the Lattice-Boltzmann Method (LBM). In all these methods the turbulence is either completely (RANS) or partially modeled (DES, LBM).

3.1 Fundamentals

3.1.1 Conservation Laws

The general laws of conservation of mass, momentum and total energy for a fluid continuum, under the assumption that the variables are sufficiently smooth to allow differentiation, read

$$\rho_t + \nabla \cdot (\rho\vec{u}) = 0 \tag{3.1}$$

$$(\rho\vec{u})_t + \nabla \cdot [\rho\vec{u} \otimes \vec{u} + pI - \Pi] = \rho\vec{g} \tag{3.2}$$

$$E_t + \nabla \cdot \left[(E+p)\vec{u} - \vec{u} \cdot \Pi + \vec{Q}\right] = \rho(\vec{u} \cdot \vec{g}) \tag{3.3}$$

where $\vec{u}$ is the velocity vector, $\vec{g}$ is a body force vector (i.e. electromagnetic or gravity force), Π is the viscous stress tensor, $\vec{Q}$ the energy flux vector[1], I is the identity tensor and E is the total energy per unit mass.

[1] I.e. conduction, convection or radiation of heat due to temperature gradients.

The thermodynamic pressure p is related to other thermodynamic variables, density and temperature, through the thermal equation of state (EOS) $p = p(T, \rho)$. For thermally perfect gas it reads for instance:

$$p = \rho RT \tag{3.4}$$

where R is the specific gas constant.

Considering p the thermodynamic pressure, two viscosity coefficients (shear and bulk viscosity coefficients) are necessary in oder to define Π. Normally[2] only the shear coefficient is retained and called μ, the (dynamic) viscosity.

The viscous stress tensor Π is linearly related to the derivative of the velocity field under the hypothesis of *Newtonian* isotropic fluid, which is valid for a large number of gas and fluids (i.e air and water).

$$\Pi_{ij} = \mu \left(\frac{\delta u_i}{\delta x_j} + \frac{\delta u_j}{\delta x_i} \right) - \frac{2}{3} \left(\mu \frac{\delta u_i}{\delta x_i} \right) \tag{3.5}$$

Moreover, E is obtained from the specific kinetic energy and the specific internal energy e as follows:

$$E = \rho(\frac{1}{2}\vec{u^2} + e) \tag{3.6}$$

The specific internal energy is defined from the caloric equation of state, which for a thermally ideal gas, has the simple expression

$$e = \frac{p}{\rho(\gamma(T) - 1)} \tag{3.7}$$

Defining the speed of sound c

$$c = \sqrt{(\frac{\delta p}{\delta \rho})_s} \tag{3.8}$$

for constant entropy, from the 2nd law of thermodynamics for thermally ideal gas follows:

$$c = \sqrt{\frac{\gamma p}{\rho}} \tag{3.9}$$

Setting the body force to zero and considering a Newtonian fluid the equation system 3.1 is usually referred to as the compressible Navier-Stokes equations (1827; 1845). The Navier-Stokes equations build the model for fluid dynamic simulations. The viscous stresses (Eq.3.5) build the mechanism for turbulence and are important where the velocity gradient are large i.e. in shear or boundary layers.

The homogeneous Euler equations are then obtained from 3.1 by neglecting viscous stresses and heat flux[3]. They still represent a non-linear system of partial differential equations (PDE), however of first instead of second order:

$$\rho_t + \nabla \cdot (\rho \vec{u}) = 0 \tag{3.10}$$

$$(\rho \vec{u})_t + \nabla \cdot [\rho \vec{u} \otimes \vec{u} + pI] = 0 \tag{3.11}$$

$$E_t + \nabla \cdot [(E + p)\vec{u}] = 0 \tag{3.12}$$

[2]For mono-atomic or bi-atomic gas with relative small volume dilatation rate. When this is not satisfied either p does not represent the thermodynamic pressure anymore, but just the isotropic part of the stress tensor, or a second coefficient (bulk) for the viscosity is necessary. See [31] for a historical review.

[3]Although, strictly speaking, the Euler equation is just the momentum conservation equation

By considering smooth solutions of this system (no shock waves) the system entropy is conserved. It follows that the equation for E is redundant.

In this work, the conservation laws will be also expressed in the compact notation. The 2D Euler equation now reads:

$$\vec{\mathcal{U}}_t + F(\vec{\mathcal{U}})_x + G(\vec{\mathcal{U}})_y = 0 \tag{3.13}$$

with $\vec{\mathcal{U}}$ the variable of conserved quantities $(\rho, \rho u, \rho v, E)$ and $F(\vec{\mathcal{U}}), G(\vec{\mathcal{U}})$ their *flux*:

$$\vec{\mathcal{U}} = \begin{bmatrix} \rho \\ \rho u \\ \rho v \\ E \end{bmatrix}, F(\vec{\mathcal{U}}) = \begin{bmatrix} \rho u \\ \rho u^2 + p \\ \rho uv \\ u(E+p) \end{bmatrix}, G(\vec{\mathcal{U}}) = \begin{bmatrix} \rho v \\ \rho uv \\ \rho v^2 + p \\ v(E+p) \end{bmatrix}$$

The Euler equation system is called *quasi-linear* as the flux matrices F, G are function of the vector $\vec{\mathcal{U}}$. It can be expressed in the following form:

$$F(\vec{\mathcal{U}})_x = A(\vec{\mathcal{U}})\vec{\mathcal{U}}_x,\ G(\vec{\mathcal{U}})_y = B(\vec{\mathcal{U}})\vec{\mathcal{U}}_y \tag{3.14}$$

where A and B are called the Jacobian matrix of the system. For an overview of further properties of Euler equations and modern techniques of numerical solution we refer to the work of Toro [32].

In classical acoustics, the homogeneous Euler equations build the model for sound propagation as long as one can neglect the dissipation of sound waves. This is commonly the case when the travelling distance of sound waves in air is smaller than typically few hundreds wave lengths. Under these circumstances the effect of viscous stresses in the fluid due to acoustic waves is negligible.

In aeroacoustics, the viscous stress plays a major role because the turbulence is the source of sound. Nevertheless it is still open the question if it is important also in the propagation. In fact the role of viscosity in aerodynamic sound generation has long been an area of controversy [34]. The more evident case is represented from the dependence of sound intensity from the velocity in the boundary layer of an infinite plate [35]. Only recently (2003), Morfey [36] highlighted that an additional radiation mechanism, for turbulence in contact with a boundary, is the viscous scattering of incident vorticity into sound. In this work the classical acoustic approach with Euler equations has been used.

For small perturbations, the Euler equations can be further simplified: the non-linear system can be linearised around the local, even inhomogeneous, fluid properties (LEE). Developing the solution as

$$\vec{\mathcal{U}} = \vec{U} + \vec{u\prime} \tag{3.15}$$

with $\vec{U}$ the time-averaged solution and $\vec{u\prime}$ the perturbation one.

The compact form of Eq.3.13 can be still maintained. However, when writing the flux using the Jacobian matrices, additional terms, linear in $\vec{\mathcal{U}}$ arise:

$$\vec{u\prime}_t + A(\vec{u\prime})\vec{u\prime}_x + B(\vec{u\prime})\vec{u\prime}_y + D(\vec{u\prime}) = 0 \tag{3.16}$$

According to the conventional terminology (i.e. [32]) we call the form of Eq.3.16 inhomogeneous, nevertheless we stress that the vector D is still a function of the solution $\vec{u\prime}$ and not of an external source.

For simple inhomogeneous background flow, the continuity equation can be combined with the impulse conservation equation into one equation of higher order, which has the character of a third-order wave equation. We call it further convective wave-equation. Assuming that the background velocity is a function of one variable only (i.e.$U = U(y)$) and that constant background density and pressure exist, the convective wave equation reads [2]:

$$\frac{D}{Dt}\left(\nabla^2 p\prime - \frac{1}{c_0^2}\frac{D^2}{Dt^2}p\prime\right) - 2\frac{\delta U}{\delta y}\frac{\delta^2 p\prime}{\delta x \delta y} = 0 \tag{3.17}$$

The convective wave equation 3.17 allows to capture the refraction of sound waves due to the inhomogeneous medium and the enhancement of sound due to the moving medium, similar to the Doppler effect for moving sources.

The so-called acoustic analogies build up exactly at this level. The source term at the right-hand side is not zero but is derived from the solution of inhomogeneous turbulent fluid. The inhomogeneous Euler equations serve then to the propagation of sound in the medium. In particular, the acoustic analogy of Lilley [38] yields from this convective wave equation.

For propagation of sound waves in an homogeneous field, which means with time and space-constant background velocity U_0, V_0 and density ρ_0 the homogeneous LEE is recovered and its (constant) Jacobian matrix reads, for example, in primitive variables (ρ, u, v, p):

$$A = \begin{bmatrix} U_0 & \rho_0 & 0 & 0 \\ 0 & U_0 & 0 & \frac{1}{\rho_0} \\ 0 & 0 & U_0 & 0 \\ 0 & \rho_0 c_0^2 & 0 & U_0 \end{bmatrix}, B = \begin{bmatrix} V_0 & \rho_0 & 0 & 0 \\ 0 & V_0 & 0 & 0 \\ 0 & 0 & V_0 & \frac{1}{\rho_0} \\ 0 & 0 & \rho_0 c_0^2 & V_0 \end{bmatrix}, D = \begin{bmatrix} 0 \\ 0 \\ 0 \\ 0 \end{bmatrix} \tag{3.18}$$

This simplified model still allows to capture the enhancement of sound due to the moving medium.

A further, more extreme simplification is represented from the well-known homogeneous linear second-order wave equation which yields from a global linearisation of the Euler equations around a medium at rest.

$$p\prime_{tt} - c_0^2 \nabla^2 p\prime = 0 \tag{3.19}$$

The equivalent in frequency domain is the Helmholtz equation (Eq.A.11 in Appendix). The famous acoustic analogy of Sir Lighthill [1] yields from this homogeneous wave equation.

3.1.2 Numerical Discretisation

Before introducing the aeroacoustic approaches in the next sections, let us remind here the numerical methods which can be applied for the solution of PDE like Euler or N-S equations.

Finite Difference If the fluid dynamic variables are smooth functions in space, the system of conservation laws can be solved in the differential form of Eq. 3.1. The spatial derivatives are approximated with finite differences at the nodal points of a discretised space domain using values at neighboring points. Figure 3.1 exemplifies

the discretisation in two dimensions. The approximation for the derivative of the one variable (u) of the solution vector $\vec{\mathcal{U}}$ in two dimensions for the node at position i,j reads for instance:

$$u_x(i,j) \approx \frac{1}{\Delta x_i} \sum_{l=-L}^{M} a_l u_{i+l,j}, \quad u_y(i,j) \approx \frac{1}{\Delta y_j} \sum_{l=-L}^{M} a_l ui, j+l, \tag{3.20}$$

where a_l, L, M are geometrical coefficients and parameters which depends on the number and location of neighbours for the node i,j,k [4]. Higher order approximation of the derivatives are obtained using more points (i.e $L, M > 1$ in Eq.3.20) and derivatives of neighbours as well (compact schemes). It leads to a system of equations for all the grid points

$$\sum_{l=-L}^{M} a_l u_{i+l,j} + \sum_{m=-L}^{M} b_m u_{i,j+m} + \sum_{o=-L}^{M} d_o u_{i,j} = 0 \tag{3.21}$$

where now, the coefficients a,b,d arise from the previous geometrical parameters and the physical coefficients of the Jacobian matrix from Eq.3.16.

See further [37, 42] for instance for storage techniques, errors analysis and treatment of boundary conditions.

Finite Element The conservation laws are here multiplied by test functions and then integrated over each element Ω_i. The solution itself is approximated as series of basis functions $\Phi_i(\vec{x})$. Using eq. 3.13 it reads:

$$\vec{\mathcal{U}}(\vec{x},t) = \sum c_i(t)\Phi_i(\vec{x}) \tag{3.22}$$

$$\int_{\Omega_i} \left(\vec{\mathcal{U}}_t + F(\vec{\mathcal{U}})_x + G(\vec{\mathcal{U}})_y\right) \Phi_i \, d\Omega = 0 \tag{3.23}$$

This formulation of the problem is called *variational*, and the solution $\vec{\mathcal{U}}$, *weak* solution. Due to the variational formulation (integral) the requirements of regularity for the solution are less strict. However, possible discontinuities of the solution (i.e. in the density due to shock waves) can be captured only if the numerical method supports these discontinuities (i.e. discontinuous basis functions between the grid elements).

Finite Volume Also the finite volume method uses the integral form of the conservation equation. For the i-th element ω_i

$$\int_{t_n}^{t_{n+1}} \int_{\Omega_i} \vec{\mathcal{U}}_t + F_x + G_y \, d\Omega = 0 \tag{3.24}$$

leads to evolution equations for integral mean values

$$\vec{\mathcal{U}}_{i,j}^{n+1} = \vec{\mathcal{U}}_{i,j}^{n} - \frac{\Delta t}{\Delta x}(f_{i+1/2,j} - f_{i-1/2,j}) - \frac{\Delta t}{\Delta x}(g_{i,j+1/2} - g_{i,j-1/2}) \tag{3.25}$$

[4] i.e. for upwind scheme 1st Order $L = 0, M = 1, a_0 = 1$ and $a_1 = 1$, for central scheme $L = 1, M = 1, a_{-1} = 1, a_0 = 0, a_1 = 1$.

with

$$\vec{\mathcal{U}}^n_{i,j} \overset{\text{def}}{=} \frac{1}{\Delta x \Delta y} \int_{\Omega_i} \vec{\mathcal{U}}(x, y, t_n)\, \delta\Omega \tag{3.26}$$

$$f_{i+1/2,j} \overset{\text{def}}{=} \frac{1}{\Delta t} \int_{\Delta t} F(\vec{\mathcal{U}}(x_{i+1/2}, y_j, t_n))\, \delta t \tag{3.27}$$

$$g_{i,j+1/2} \overset{\text{def}}{=} \frac{1}{\Delta t} \int_{\Delta t} G(\vec{\mathcal{U}}(x_i, y_{j+1/2}, t_n))\, \delta t \tag{3.28}$$

where the numerical flux (f,g) can be derived analytically or approximated numerically. See further [32] for a comprehensive comparison of numerical schemes under the finite volume framework.

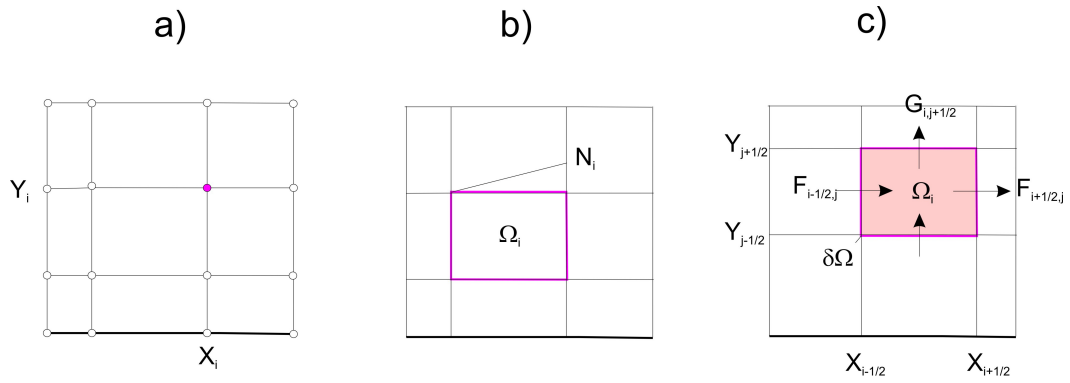

Figure 3.1: *Discretisation approaches on a 2D cartesian grid: a) FD, b) FE, c) FV. Ω_i is the i-th element of the discretisation.*

3.2 Hybrid Approach based on Large Eddy Simulation

One approach to derive the acoustic sources from a subsonic flow consists in the 'Expansion about Incompressible Flow' (EIF). In this approach the sound sources are derived in the limit of incompressible flow field. In particular in the following section it will be shown that the substantial derivative of the fluid pressure field calculated as *incompressible* acts as volume sound source for the acoustic equations (Euler equations).

Obviously, the condition for accurate acoustic results is a 'precise' unsteady solution of the turbulent flow field. This requires that the velocity fluctuations are expression of the real turbulence of the flow and that the velocity field satisfies the kinematic requirement of incompressibility (the divergence of the velocity field equals zero).

The most direct approach consists in the solution of the Navier Stokes equations (DNS) with a discretisation of the computational domain enough fine to capture all turbulent scales up to the smallest(Kolmogorov scale) [37]. The computational effort is almost linear with the characteristic Reynolds number of the flow. For instance the number of element necessary in each space dimension is estimated in [40] for a channel flow as follows:

$$N \approx 0.05 \cdot Re^{0.9} \tag{3.29}$$

which leads for middle-high Reynolds number (i.e. Re = 10^5) for 3 dimensions to $N^3 \approx 4 \cdot 10^{10}$ elements, which corresponds to a calculation time of about 84 years by using a computational power of 150 Mflops[5].

In oder to reduce this, at present inaccessible, computational effort it is looked to solve only for the largest eddies. The physical motivation is that the largest scales carry the maximum energy and therefore can transmit also more energy acoustically. This approach is known in the literature as large eddy simulation (LES) and consists in the spatial filtering of the velocity field in the Navier-Stokes equations: turbulence structures whose scale are larger then the scale length associated with the filter (Δ) are solved directly with the unsteady Navier Stokes equations.

The spatial filtering is obtained by applying a localised function $G(x, x\prime)$ called filter kernel to the velocity field $\vec{u} = (u_1, u_2, u_3)$. For instance, for a top-hat filter it reads:

$$\overline{u_i}(x_i) \stackrel{\text{def}}{=} \int G(x_i, x_i\prime) u_i(x_i\prime) dx_i\prime \tag{3.30}$$

$$G(x_i) \stackrel{\text{def}}{=} \begin{cases} \frac{1}{\Delta} & for \mid x_i \leq \frac{\Delta}{2} \mid \\ 0 & otherwise \end{cases} \tag{3.31}$$

Deriving from equations 3.1, the N-S equations in incompressible form read :

$$\nabla \cdot \vec{u} = 0 \tag{3.32}$$

$$\vec{u}_t + \vec{u} \cdot \nabla \vec{u} + \frac{\nabla p}{\rho} = \nu \nabla^2 \vec{u} \tag{3.33}$$

therefore the space averaged incompressible N-S equations yield:

$$\nabla \cdot \overline{\vec{u}} = 0 \tag{3.34}$$

$$\overline{\vec{u}_t} + \overline{\vec{u}} \cdot \nabla \overline{\vec{u}} + \frac{\nabla \overline{p}}{\rho} = \nu \nabla^2 \overline{\vec{u}} - \nabla \cdot \tau^s \tag{3.35}$$

[5] with the assumption of 1000 operations pro element and 10000 time steps.

where τ^s, the so-called subgrid Scale (SGS) Reynolds stress, is defined as follows:

$$\tau^s = \overline{\vec{u} \otimes \vec{u}} - \overline{\vec{u}} \otimes \overline{\vec{u}} \tag{3.36}$$

and represents the momentum flux caused by the action of the small turbulent scales. Only by using a model for the subgrid scales, the equations 3.34 and 3.35 are closed and can be solved.

As the small turbulent structures tend to be homogeneous and isotropic they are adapt to be easily modelled. Most commonly used subgrid models, i.e. proposed by Smagorinsky (1963), are well documented in the literature [37].

In this work a multi-zonal variant of LES has been used (DES, detached eddy simulation). This ansatz has been used in the implementation of CFX (Ansys). The principle will be explained in the following section. For the subsequent simulation of sound propagation the linearised Euler equation have been used in the finite element implementation of the university code Hydsol (IAG). A file-based approach has been implemented here for the data exchange between the codes and it will be described further in the following sections.

3.2.1 Detached Eddy Simulation

Detached eddy simulation (DES) is a hybrid approach which combines classical RANS (Section 3.3.1) and LES models. It bases on the idea to cover boundary layers by a RANS model and to switch to LES model in separated flow regions, which are typically characterised by larger turbulent structures. In other words, it allows a much coarser domain discretisation than LES and therefore a reduced computational time, but still offers some of the advantages of an LES method in separated regions. In figure 3.2 the discretisation strategy of DES is illustrated with respect to RANS and LES. For simplicity one identifies three turbulent structures with decreasing size; the largest ones being anisotropic(1,2) and the smallest(3) being isotropic. A mesh is adequate for LES when it discretises all anisotropic structures (1,2). The isotropic subgrid scales (SGS) are modelled with, for instance, simple algebraic turbulence model (Smagorinsky). On the other hand, the coarser mesh used by DES leaves more scales unresolved. These should be modeled with a turbulence model more complex than the algebraic one with constant scale: neglecting the effect of the flow anisotropy, two-equation models like turbulence viscosity models as k-ϵ [37] or SST [103] (see section 3.3.1) are therefore used. On the other side more equations (Reynold-Stress) models are used for taking into account anisotropy. On the other hand, in RANS simulations, the turbulence is completely modeled and not resolved therefore a much coarser domain discretisations can be used.

The implementations of the DES formulation differ in the following points:

- switching mechanism between RANS and LES
- how quickly the turbulent structures develop after that the model has switched from RANS to LES mode

The effects of the different implementation can be seen for separated flows at the separation and at the reattachment points. In particular a typical problem is the grid-induced

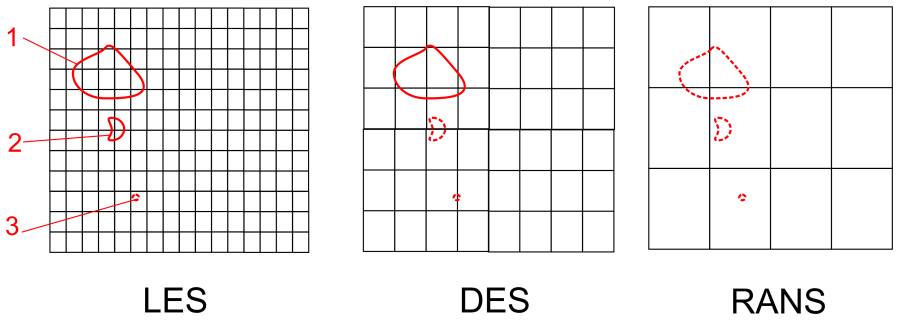

Figure 3.2: *Example of turbulence scales (1, 2, 3) and grid discretisation. For each method (LES, DES, RANS) the resolved turbulent scale (red solid line) are distinguished from the modelled turbulent scale (dashed red line).*

flow separation for increasing mesh refinements [103]. In contrast to the implementation of Strelets [45], the implementation of CFX leads to a more accurate result [103], therefore the latter has be chosen in this work.

The implementation of CFX bases on a zonal formulation, that is, it switches from SST-RANS model to LES model where the turbulent length, predicted by the RANS model is larger than a scale based on the local grid spacing. The length scale used then in RANS is replaced by the local grid spacing therefore the DES model returns to the RANS formulation in attached boundary layers. The switch occurs locally and is updated at each time step. Two variants are implemented: the first one (called after the name of a parameter, F1) takes the grid scale as the mean value of the local element edge length, while the second one (F2) takes the grid scale as the maximal value of the local element edge length. The choice of the second scale factor (F2) is more conservative.

For LES and DES, the integral flow quantities like the turbulent kinetic energy (K), are sum of two parts: one part is due to the fluctuation of the velocity ($\vec{u}$) resolved in the discretisation grid while the other part is derived from the modeling of the subgrid scales K_{SGS}.

$$K \overset{\text{def}}{=} \frac{1}{2}\sum_i \overline{u_i^2} + K_{SGS} \tag{3.37}$$

3.2.2 Expansion about Incompressible Flow

The 'Expansion about Incompressible Flow'(EIF) is an approach, due to Hardin and Pope [43], which splits the aeroacoustic problem into an incompressible flow problem and an acoustic perturbation problem. Once the unsteady incompressible flow problem has been resolved, the sound sources can be derived[6].

In order to show that, one starts from the governing equation for acoustics (Euler equations 3.13, 3.14).

Than the solution $\vec{\mathcal{U}}$ is split into incompressible $\vec{\mathcal{U}}_{inc}$ and compressible $\vec{u}$

$$\vec{\mathcal{U}} = \vec{\mathcal{U}}_{inc} + \vec{u} \tag{3.38}$$

[6]In case of DES, only the resolved perturbations can lead to sound sources.

The Euler equations are first linearised around the incompressible flow $\vec{\mathcal{U}}_{inc}$. The linearisation consists of using the Jacobian matrix written for $\vec{\mathcal{U}}_{inc}$ instead of $\vec{\mathcal{U}}$. In two dimensions:

$$\vec{\mathcal{U}}_t + A(\vec{\mathcal{U}}_{inc}) \cdot \vec{\mathcal{U}}_x + B(\vec{\mathcal{U}}_{inc}) \cdot \vec{\mathcal{U}}_y = 0 \tag{3.39}$$

$\vec{\mathcal{U}}_{inc}$ is generally not constant in time and space but known and independent from the solution of the acoustic problem ($\vec{u}$). This is acceptable as long as the acoustic perturbations are smaller than the fluid turbulence. The fluid state in which the acoustic wave propagates is therefore fully determined.

Then the variable splitting (3.38) is introduced and all incompressible terms are grouped on the right end side, constituting the source term $\vec{S}$ of the LEE equation for the acoustic problem:

$$\vec{u}_t + A(\vec{\mathcal{U}}_{inc}) \cdot \vec{u}_x + B(\vec{\mathcal{U}}_{inc}) \cdot \vec{u}_y = -(\vec{\mathcal{U}}_{inc,t} + \vec{\mathcal{U}}_{inc,x} + \vec{\mathcal{U}}_{inc,y}) \tag{3.40}$$

In the original formulation of Hardin and Pope, a correction to the incompressible density was introduced in order to consider the compressibility of the flow for high subsonic Mach numbers. Later, Shen and Sorensen [44] demonstrated that there is no need to introduce a hydrodynamic density correction. In this work we follow this last approach.

For non-vibrating surfaces the source term vector reduces to a source term for the energy equation and embodies the substantial derivative of the hydrodynamic pressure.

$$\vec{S} = \begin{bmatrix} 0 \\ 0 \\ 0 \\ -(\frac{\partial P_{inc}}{\partial t} + \vec{U_{inc}} \cdot \nabla P_{inc}) \end{bmatrix} \tag{3.41}$$

3.2.3 Discontinuous Galerkin Method

The Discontinuous Galerkin (DG) Method is a new and particular finite element method (equation 3.22) for the solution of hyperbolic equations (Euler equations). Differently to many continuous finite element schemes, the degrees of freedom do not correspond to the displacement of nodes in the domain discretisation, rather to element averages, and higher order curvature slopes. The numerical solution is represented, on each element m, with a polynom whose time-dependent coefficients are called degrees of freedom $\hat{\vec{\mathcal{U}}}_{ij}$:

$$\vec{\mathcal{U}}_i(\vec{x}, t)^{(m)} = \sum_{j=1}^{n} \hat{\vec{\mathcal{U}}}_{ij}^{(m)}(t) \Phi_j(\vec{x}) \tag{3.42}$$

The basis functions Φ_j used here are orthogonal and of the same type of those (Φ_i) used in Eq. 3.22. This scheme is very compact as the solution is expressed distinctly for each element and it is allowed to be discontinuous at the element interfaces. That is very suitable for parallelisation of the algorithm and for discretisation of complex geometries with unstructured grids.

For a efficient implementation, each element is usually transformed to a canonical reference element (orthogonal triangle in 2D or tetrahedron in 3D) in order to compute all integrals beforehand in the reference system. The integral is calculated with quadrature formula on each element of the unstructured grid. The locations where the functions are

evaluated are called Gauss-points (Integration weights and gauss points coordinates for triangular, rectangular, tetrahedral and hexahedral elements can be found in [46] and [47]).

In this work two realisations of DG have been used. They differ in the discretisation order and in the time discretisation method. The first one is due to Dumbser [47] and implemented in the code of the institute IAG in Stuttgart. It is a finite element scheme of arbitrary high order of accuracy in space and time for two-dimensional hyperbolic systems, including the linearised Euler equations, on unstructured grids. This scheme bases on ADER approach [48] where the calculation of time derivatives is replaced, by re-using the conservation equations, by space derivatives. The main advantage of this approach compared to the more classical Runge-Kutta time discretisation is that it is faster and the numerical efficiency is not limited by the so-called 'Butcher' barrier [47]. This numerical scheme has been used for the own implementation of both the EIF and SNGR methods.

The second one is implemented in the commercial code *Fire* and has been used for SNGR investigations (see chapter 5.1). It is a more classical DG implementation where the order of the space discretisation is limited to the 4th order and the time discretisation follows the Runge-Kutta scheme.

3.2.4 Implementation Aspects

3.2.4.1 Programs Interface

Advantage and consequence of a hybrid approach is that both time and domain discretisation can be chosen, and optimised, with respect to each sub-problem (fluid dynamic and acoustic). It is therefore necessary to interpolate the data between the different time and space discretisations. Moreover, in this work different codes are used for both problems, therefore an interface between both programs was also needed.

In this work a stand alone export user function was developed to export the CFD data (CFX). Secondly a build-in Fortran routine was developed to interpolate this data on the CAA broader mesh. The interface works with every mesh type and mesh type combination because only nodes co-ordinates are requested regardless of the topology (structured or unstructured).

Following interpolation strategies have been used:

Space interpolation Figure 3.3 gives an example of mesh combinations. The basis functions and their derivatives within the DG approach are calculated on each element on three or more Gauss points (2D). At these points, the input data for EIF approach (pressure and velocity field) should be known. The first step is to search at each Gauss point for the three nearest nodes of the CFD-Mesh, to calculate a weight factor according to the relative distance and to save it in computer memory. This occurs just once at the beginning of the acoustic calculation. During the calculation, the input sources are linear interpolated through these factors at each time step. This approach is, strictly speaking, not conservative. Nevertheless, the interpolation error can be controlled in two ways: on the one hand, the interpolation error decreases, even though only linearly, with the element size of the CFD grid. This approach is convenient because the grid needs anyhow to be very fine, due to the DES requirements. On the other hand, a higher order in the DG scheme reduces, with the same order, the error as well, by increasing

the number of gauss points. This approach, however is limited by instabilities in the LEE calculation as it will be shown later.

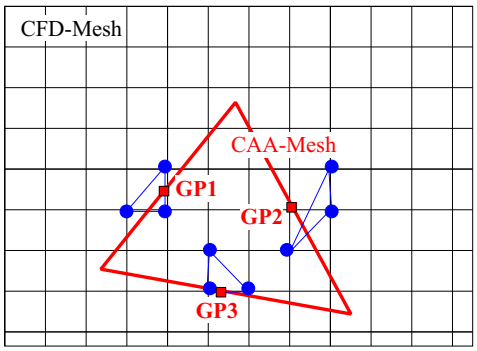

Figure 3.3: *Example of mesh-interpolation: the three nodes of CFD-Mesh (blue dots) nearest to the Gauss-points of the CAA-Mesh (red squares) are used for the data interpolation.*

Time interpolation Although one is interested, within the acoustic simulation, only in frequencies up to few kHz (about 3 kHz in this work), the sampling rate of the CFD data can not be reduced to those low levels. The reason is that it would aliase the much higher frequencies present in the turbulence. Only with a low pass filtering of CFD data that would be correct. However, in this work that has been not used in order to reduce the post processing effort. Therefore the sampling frequency has been chosen equal to a 'relatively' high frequency threshold, dependent from the fluid situation [7]. However, the CFD data are sampled before the CAA calculation with a time step which is a priori different and in general larger then the time step used for the CAA calculation itself, in order to reduce the size of stored data. A time interpolation of data is therefore necessary.

According to the type of interpolation, spurious frequencies in the source term for CAA can arise. We investigated this effect, comparing the spectra of a test signal (DES) containing discrete frequencies (500, 1000, 2000 and 4000 Hz) and its different time interpolations. Figure 3.4 shows the result: one notices spurious peaks at high frequency (i.e. 6000, 8000 Hz). Nevertheless a third-order natural-spline time interpolation reduces this effect considerably (10 dB in this test case) with respect to the case without interpolation . Therefore in this work this interpolation type has been implemented in the CAA code.

[7] For the velocity in the present test cases the simulations showed max velocity frequencies less than 5 kHz in the shear layer, therefore a sampling frequency of 10 up to 20 kHz has been judged sufficient.

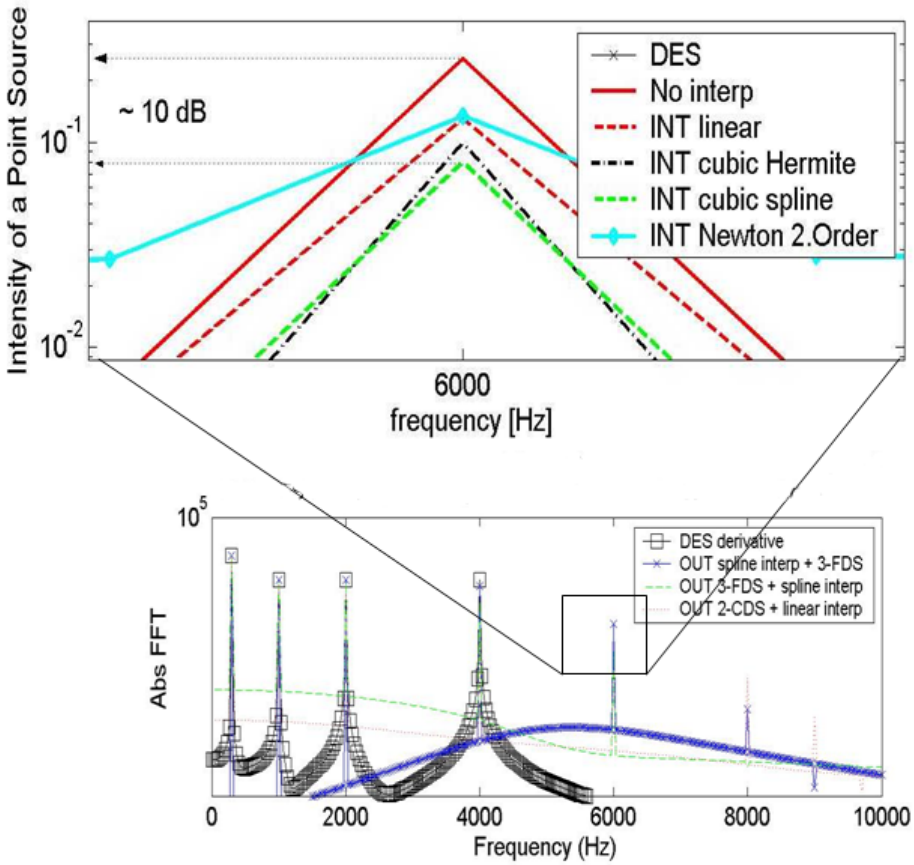

Figure 3.4: *Effect of time interpolation of CFD source signal on acoustic signal for CAA code. Ratio LES time step to LES output = 10, ratio LES output to LEE time step = 20. A spline interpolation (INT cubic spline) reduces the spurious frequencies up to 10 dB.*

3.3 Hybrid Approach based on Stochastic Techniques

The stochastic noise generation and radiation (SNGR) method is a hybrid approach for aeroacoustics initially developed in France by Bechara, Bailly and Lafon (1994) [54] and now further improved and differently implemented in a few codes, among others the commercial code *Fire* by AVL. This section resumes the basic principles and presents own developments and implementation in the university code *Hydsol*.

Like every other hybrid approach for aeroacoustics, the aeroacoustic calculation of SNGR splits in two steps: firstly the underlying flow should be calculated with conventional CFD calculations, secondly, the sound sources are derived from the hydrodynamic flow field and used for a separate calculation using different discretisation and governing equation, more suitable for the propagation of sound waves. The terminology 'SNGR' has been used in the past either for the whole process or for the second of the two steps creating misunderstanding. Further we prefer to use the word 'SNGR' only for the part of the second step where the sound sources are modeled as that is the main characteristic of this method and to decouple it from the numerical method used for the resolution of the sound propagation.

The main difference to the other approaches for aeroacoustics, consists in the form and in the derivation of the sound sources from the CFD. First because the sound sources are expressed just using velocity fluctuations and their gradients instead of pressure fluctuations. Second because the velocity fluctuations are not directly calculated like in LES and DES but synthetically modeled from a steady CFD solution around a time averaged flow field (Reynolds Averaged Navier-Stokes Equations (RANS)).

3.3.1 Reynolds averaged Navier-Stokes Equations

By averaging the N-S equations over the time rather than in space, one obtains the so-called Reynolds Averaged Navier Stokes equations (RANS) instead of the previously introduced LES (Section 3.2).

For an incompressible flow, it leads to the following form:

$$\frac{\partial \overline{U_i}}{\partial t} + \frac{\partial \overline{U_i U_j}}{\partial x_j} = -\frac{1}{\rho}\frac{\partial \overline{P}}{\partial x_i} - \frac{\partial(\tau_{ij} + \overline{u_i u_j})}{\partial x_j} \tag{3.43}$$

where u_i are the velocity fluctuations around the time averaged velocity $\overline{U_i}$, ρ is the (constant) flow density and τ_{ij} are the viscous shear stresses. The whole turbulence dynamics is represented by $\rho\overline{u_i u_j}$. They are called Reynolds stresses and should be modeled for the closure of the eq. 3.43. This is the common practice for RANS calculation. In this work two eddy-viscosity turbulence models (two-equations) have been used within the implementation of commercial codes: the classical $k-\epsilon$ in the code Fire and the SST by Menter [49] in the code CFX. The latter is known from the literature and Bosch internal benchmarks as well, to be more indicated for separated flows. However, for the investigated impinging jets, only small differences in the quantitative prediction of turbulence are present (Figures 5.16). Both models assume the turbulence to be isotropic, therefore the turbulence is represented as a single time-averaged integral quantity: the turbulent kinetic energy (TKE).

In the CAA stochastic approach, the dynamic of the turbulence is modeled on statistical basis. In this way the fluctuations, which have been filtered out with RANS, are introduced synthetically using integral RANS data as starting point. The key advantage is a

strong reduction of CPU effort, because algebraic equations are used instead of solving the N-S differential equations on a fine grid (like before with DES). In particular the turbulence energy (k) and the dissipation rate (ϵ) are used for the source generation 3.3.3.

3.3.2 Source Term Formulation

Differently from the EIF approach (section 3.2.2), the variables of the homogeneous system of equations are here splitted into a time averaged part and a fluctuation part. The original formulation of stochastic techniques for CAA relies on linearised Euler equations. Here the linearisation is done around a stationary mean flow (known from the RANS solution) with local solution $\vec{U_0}$. This is actually valid as long as the (turbulent) fluctuations are small compared to the time averaged flow properties. In this case the Jacobian matrices A and B (Eq.3.44) depends on the time averaged part $\vec{U_0}$ instead of the instantaneous $\vec{U}$. We then regroup the remaining terms in a vector $\vec{H}$ or in a vector $\vec{S}$ depending if they are respectively linear on non-linear in the perturbation. $\vec{S}$ is then called the vector of the sound sources and is synthetically created starting from the RANS numerical solution.

$$\vec{U_t} + A(\vec{U_0}) \cdot \vec{U_x} + B(\vec{U_0}) \cdot \vec{U_y} + \vec{H} = \vec{S} \tag{3.44}$$

The derivation of $\vec{H}$ and $\vec{S}$ presents in the literature many differences. In some literature ([64]) the unknown variable vector $\vec{U}$ is decomposed in time averaged and perturbation quantities($\prime$), while in some other literature ([58],[60],[69],[66]) one decompose further the perturbation quantities ($\prime$) into an acoustic ($_a$) and a turbulent part($_t$).

Further in order to linearise the Euler equation, one subtracts the time average from the initial Euler equations.

In the first case, all terms which contains more than one perturbation variables are neglected except for $\rho u' \nabla u'$. This term consist mostly of turbulent velocity fluctuation as the velocity induced from the sound is considerably smaller. If the turbulent flow field is known, this term is also known and is used as a source in the Euler equation system. Because the (turbulent) pressure perturbation is of order two with the velocity fluctuations, all terms containing the perturbated pressure and other perturbated variables (i.e. $p' \nabla \cdot \vec{u'}$) are smaller in comparison with $\rho u' \nabla u'$ and are neglected in the linearised Euler equation. This source term is put on the right hand side of the system while on left hand side one considers the perturbation variable as unknown, as unprecised sum of acoustic and (new) turbulent perturbations. The solution of the Euler equations has been shown in the past to contain rotation-affected perturbations. The Euler equations system contains in fact three modes (acoustic, vortical and entropic) which can be excitated from the source term [65].

In the second case, one decomposes the perturbations in acoustic and turbulent one. These terms can be than regrouped, depending on the interactions, as follows:

1. acoustic-acoustic
2. turbulence-turbulence
3. acoustic-turbulence

4. mean flow-turbulence

We compare now the formulations, putting the terms in the vectors $\vec{H}$ and $\vec{S}$ as indicated previously (Eq. 3.44). Originally, these formulations have been written in different ways (conservative, primitive [61],[69], or using the derived variable $\pi = \ln p$ [58]), therefore we re-write them in the same primitive vectorial form.

From the formulation of Bailly [57],[61] it reads:

$$\vec{H} = \begin{bmatrix} 0 \\ (u' \cdot \nabla)U_0 + \frac{\rho'}{\rho_0}(U_0 \cdot \nabla)U_0 \\ (u' \cdot \nabla)P_0 + \gamma(p') \cdot \nabla U_0 \end{bmatrix}; \vec{S} = \begin{bmatrix} 0 \\ (\vec{u_t} \cdot \nabla)\vec{u_t} - \overline{(\vec{u_t} \cdot \nabla)\vec{u_t}} \\ 0 \end{bmatrix} \tag{3.45}$$

which can be further simplified (H) if the mean flow is considered to be incompressible. Longatte ([58])) considers the source term for the pressure equation as negligible. Moreover, as long as the acoustic fluctuations are many order of magnitude smaller than the turbulent fluctuations, one can neglect also the interactions 1 and 3. The term 4 is considered not as a source but part of the operator itself, as already seen for the convective wave equation 3.17, demonstrating an equivalence to the Lilley equation.

$$\vec{H} = \begin{bmatrix} 0 \\ -\frac{p'}{\rho_0^2 c_0^2}\nabla P_0 + u' \cdot \nabla U_0 \\ -u_t \cdot \vec{\nabla} P_0 \end{bmatrix}; \vec{S} = \begin{bmatrix} 0 \\ (\vec{u_t} \cdot \nabla)\vec{u_t} \\ 0 \end{bmatrix} \tag{3.46}$$

TNO [69] follows the same approach, neglect however the second order terms in acoustic perturbations and cross terms in the acoustic and turbulent perturbations.

$$\vec{H} = \begin{bmatrix} 0 \\ -\frac{p'}{\rho_0^2 c_0^2}\nabla P_0 + u' \cdot \nabla U_0 \\ -\vec{u'} \cdot \nabla P_0 \end{bmatrix}; \vec{S} = \begin{bmatrix} -\vec{u_t} \cdot \nabla \rho_0 \\ -(U_0 \cdot \nabla)\vec{u_t} + (\vec{u_t} \cdot \nabla)(\vec{U_0} + \vec{u_t}) \\ -\vec{u_t} \cdot \nabla P_0 \end{bmatrix} \tag{3.47}$$

Two main differences are observed:

- The terms containing time averages of second order perturbations arise from the subtraction of averaged Euler equations, but are neglected due to the reason that they are small compared to the rest ([58],[64]). We consider this reason irrelevant as long as the equation structure is linear. In fact the terms containing time averages act like an offset to the turbulent perturbations. Indeed an offset in the source term of the equation does not change the propagation as long as the offset does not influence the state of the medium (Jacobi Matrix). This operation is allowed because these terms do not enter in the state equation of the fluid therefore the background medium behave at the same way: not the time average of the sources but its fluctuation has influence on the acoustic problem. Moreover the main advantage by neglecting that term consist in a significant reduction in the implementation effort (data storing).

- The terms containing the product of the perturbation with the gradient of the mean flow (shear terms) are used either as know source or as part of the unknown variable on the left hand side. A quite arbitrary separation origins this separation. These terms (i.e. $(\vec{u} \cdot \nabla)\vec{U_0}$) are responsible for the coupling between acoustic and turbulent mode [58],[62]. The linearisation of the Euler equations around the mean flow is therefore not perfectly adapt for the acoustic propagation in shear flows. If the mean flow were uniform ($\vec{U_0}$ constant), is $\vec{H} = 0$ and the equation system is stable.

  In order to preserve the stability, a reduced formulation, in which the gradient of the mean velocity is removed, has shown however interesting results for subsonic shear flows as long as the Mach number is small. Without these terms, one still considers the Doppler effect but neglects the refraction and reflection of the sound waves due to the mean flow. In this work a heuristic approach was additional used for the stability of the LEE in the shear layers (also with EIF): reduction of the discretisation order in the numerical scheme[8].

3.3.3 Synthetic Source Generation

In the previous section 3.3.2, the source terms have been analysed. Part of the SNGR approach consists now in the synthetic generation of these source terms. As long as just the turbulent velocities appears in the source terms, one needs only to model the turbulent velocity field. All models of the literature follow the decomposition of the velocity field in a Fourier space proposed by Kraichnan [51] and Karweit [53][9]. Its basic form reads:

$$\vec{u}(\vec{x}, t) = \sum_{n=1}^{N} \hat{u}_n \cos(\vec{\alpha}_n(\vec{x} - \vec{U_0}t) + \Psi_n)\vec{\sigma_n} \tag{3.48}$$

with $\hat{u}_n$ the (complex) velocity amplitude, $\vec{\alpha}_n$ the wave vector, Ψ_n the phase angle and $\vec{\sigma_n}$ a unit vector.

A synthetic velocity perturbation can be therefore seen as a sum of N linear independent Fourier modes defined through the parameters above. The choice of these parameters precises the characteristic of the turbulent field generated.

Each mode contribute differently to the turbulence kinetic energy (K in Eq.3.37) according to the spectrum of the turbulence ($E(\alpha)$ with α the wave number). Imposing that $K = \int_0^\infty E(\alpha)d\alpha$, it results from 3.48 a constraint for the velocity amplitude: $\hat{u_n} = \sqrt{E(\alpha_n)\Delta\alpha_n}$. In order to obtain the amplitude of each single mode, the energy spectrum is modeled using typically algebraic equation for the spectral energy density based on physical experiments. Moreover another integral property (the turbulence dissipation rate) should be satisfied: $\varepsilon = 2\nu \int_0^\infty \alpha^2 E(\alpha)d\alpha$.

The spectrum is subdivided usually with a logarithmic [53],[59] or a linear [66] wave number distribution. For the same amount of modes, the logarithmic distribution shapes better the energy peak region but it has the side effect that the highest wave numbers are amplified. First of all, the generated turbulence field should satisfy basic statistical

[8] I.e. second order instead of larger order discretisation. See also section 5.1.6.

[9] only very recently Ewert proposed a new approach for the velocity perturbations [70]

requirements, in particular the first statistical moments, as defined in annex B.2 for the isotropic turbulence.
Each mode of the Fourier-Serie 3.48 is defined through a set of random parameters (α, Ψ). The values assumed from these parameters, in time and space domain, determine the coherence or incoherence of the synthetic sources.

Spectrum for Isotropic Turbulence

Three spectra are known to characterise the homogeneous turbulence: the von Karman spectrum, the Saffman-Pao spectrum and the Liepmann spectrum. The first two spectra have been used in the codes used in this work without noticeable differences in the acoustic solution. See Annex A.5 for the equations and the application to the impinging jet. Few differences in the overall sound pressure level between von Karman and Liepmann spectrum have been reported from Bauer [64] within wing noise investigations. More important seems to be the location of the maximum of the turbulence spectrum (section 5.1.4.3).

Time Coherence

The equation 3.48 is valid only for frozen turbulence, that is a turbulence without dynamic which is simply convected with the mean flow. In order to reproduce the time correlation, a time dependent term is added to the Fourier modes

$$\vec{u}(\vec{x},t) = \sum_{n=1}^{N} \hat{u_n} \cos(\vec{\alpha_n}(\vec{x} - \vec{U_0}t) + \Psi_n + 2\pi f_n t)\vec{\sigma_n} \tag{3.49}$$

with f_n the natural frequency of the mode, chosen randomly with Gaussian probability [59]. Although the single-point statistical moments are satisfied correctly, the two-points are not (a time decorrelation take place as shown by Billson [66]).
To resolve this problem, Billson et al.[66] proposed a method to control the time correlation by introducing a causal filter, directly when the velocity field is generated. At each time step m a turbulent velocity field $\vec{u}$ is generated like in equation 3.48, however, it is modified ($\vec{v}$) by using following one-step causal filter (Markov-chain):

$$\vec{v}^m(\vec{x}) = a \cdot \vec{v}^{m-1}(\vec{x}) + b \cdot \vec{u}^m(\vec{x}) \tag{3.50}$$

$$a = e^{\frac{-\Delta t}{\tau}} \tag{3.51}$$

$$b = \sqrt{1 - a^2} \tag{3.52}$$

where Δt is the time step and τ is the time scale derived from the RANS calculation [10].
For $\tau \to \infty$ one gets back frozen turbulence while with $\tau \to 0$ one gets uncorrelated turbulence (white noise).
Two shortcomings of this approach appear already from his work [66]. Firstly, the divergence of the synthetic turbulence field is not constant to zero , as required for an incompressible flow, and acts as a spurious sound source. Secondly, the correlation length plays a large role on both OASPL and sound spectrum.

[10] $\tau \propto \frac{k}{\epsilon}$ from dimensional considerations, where k is the turbulence kinetic energy $[\frac{m^2}{s^2}]$ and ϵ the eddy dissipation energy $[\frac{m^2}{s^3}]$.

3.3.4 Implementation Aspects

In this work we evaluate the impact of both previous methods for synthetic turbulence on low-subsonic impinging jets (section 5.1.4.3). From one side, the 3D commercial implementation in Fire has been used; From the other side a own implementation in 2D university code has been carried out[11] and stand-alone investigations have been carried out.

We anticipate here that similar shortcomings, as cited before, have been found out. Two improvements are therefore suggested and tried.ted before, have been found out. Two improvements are therefore suggested and tried.

Lagrange Multiplicator

In order to reduce the divergence, the random flow generation technique of Smirnov [72] has been applied to RANS data. Even though the turbulence field could be divergence free, we object that the spectrum of isotropic turbulence can be reproduced.

On the other side, the divergence of the turbulence field ($\vec{u}$) can be reduced at a price of higher numerical effort by using Lagrange multiplicators. We apply an hyperbolic correction following the approach proposed from Kemm et al.[71]. The divergence error (err_2) is transported with a constant speed (c) outside of the discretisation domain.

$$\nabla \cdot \vec{u} + err_2 = 0 \tag{3.53}$$

$$\frac{\delta^2 err_2}{\delta t^2} - c^2 \nabla^2 err_2 = 0 \tag{3.54}$$

Figure 3.3.4 shows the results for a 1D exemplar application. Starting from a divergence error distributed randomly on the X axis, the hyperbolic correction reduces the error to zero after few iterations. In this case, the rms value of the divergence was reduced about 100 times (from rms = 0.39 to rms = 0.003) in 40 iterations.

This ansatz is therefore promising for reducing the error introduced from SNGR based on Billson approach.

[11] Only original approach of Bailly

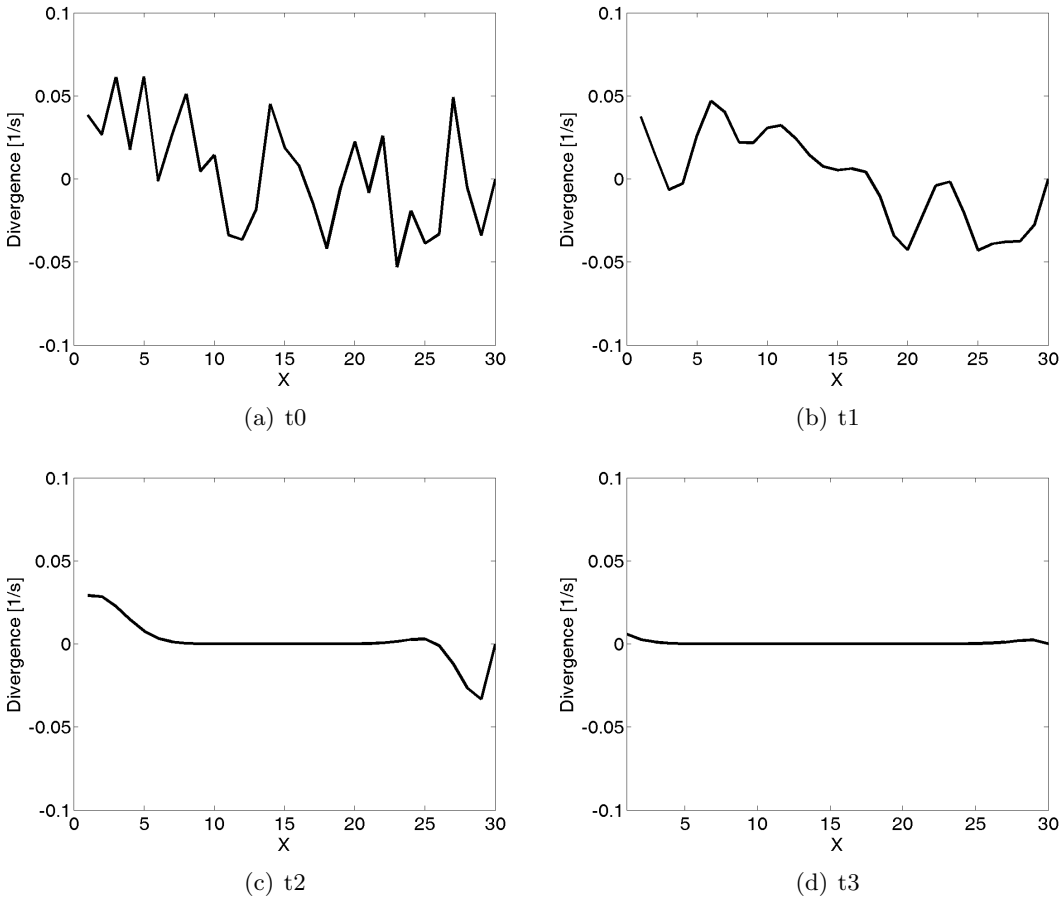

(a) t0 (b) t1

(c) t2 (d) t3

Figure 3.5: *Time evolution of the divergence of a 1D synthetic turbulence field with hyperbolic divergence correction. 10 iteration steps between pictures.*

3.4 Direct Approach based on Lattice-Boltzmann Method

The macroscopic conservation equations[12], represented for instance by the Euler equation or the Navier-Stokes equation, build a fluid dynamic model written from Eulerian point of view and valid in the approximation of fluid continuum. A more general approach is the Lagrangian one where the conservation equations are written for *each* particle of the fluid. However, only through the statistical formulation it is possible to reduce the complexity of the problem. The fundamental equation for the kinetic gas theory was derived by Ludwig Boltzmann (1872) and is known as Boltzmann-equation. This approach is compulsory when the hypothesis of fluid continuum is not satisfied, that is, for large Knudsen[13] numbers like in highly rarefied gases. On the other hand it can be used for fluid continuum as well. The discretisation of this approach is known as 'Lattice-Boltzmann Method' (LBM) and became more and more popular in the 90's. A similar discretisation approach was used already in the 70's and 80's for cellular automata. The latter will not be described here but can be found in the comprehensive work of Succi [74]. LBM recovers, for small Mach numbers, the transient, compressible and viscous Navier-Stokes equations and is capable of capturing the hydro-dynamics as well as acoustics. In the following section the theory is revisited, pointing out the implementation aspects and the limitations of the method.

3.4.1 Fundamentals

3.4.1.1 Boltzmann Equation

Considering a fluid constituted only by one type of particles[14], Boltzmann described the status of the particles using a probability function f. The probability function $f(\vec{x}, \vec{\xi}, t)$ is defined as the probability for a particle at time t to occupy the position $\vec{x}$ and to have the (microscopic) velocity $\vec{\xi}$. Therefore its integration over a volume element Ω and a, for the moment still to be defined, velocity element Ξ gives the mass of the fluid, in the neighbourhood of position $\vec{x}$ with size $d\Omega$ and with velocity $\vec{\xi}$ with range $d\vec{\xi}$ at time t. The density ρ of the fluid is a macroscopic quantity and it follows directly from this definition:

$$\rho(\vec{x}, t) = \int_{\vec{\Xi}} f \, d\xi \tag{3.55}$$

The density is therefore the zeroth order moment of the probability function f with the microscopic velocity $\vec{\xi}$. Moments of larger order are the momentum vector $\rho\vec{u}$ and the momentum-flux tensor Π. They read, always under the hypothesis of particles of the same type [78]:

$$\rho(\vec{x}, t)\vec{u}(\vec{x}, t) = \int_{\Xi} \vec{\xi} f \, d\xi \tag{3.56}$$

$$\Pi_{\alpha\beta}(\vec{x}, t) = \int_{\Xi} \vec{\xi}_\alpha \vec{\xi}_\beta f \, d\xi \tag{3.57}$$

$$D_{\alpha\beta}(\vec{x}, t) = \Pi_{\alpha\beta}(\vec{x}, t) - \rho u_\alpha u_\beta \tag{3.58}$$

[12] Mass conservation, momentum conservation and energy conservation

[13] The Knudsen number $Kn = \frac{\lambda}{l}$ is defined as the ratio between mean free path of gas molecules ($\lambda \, \mathcal{O}(10^{-8}\text{m})$ for standard pressure and temperature) and a characteristic macroscopic length L

[14] Dry air *can* be considered for instance like that, as long as the composition remains constant

The macroscopic velocity $\vec{u}$ represents the weighted average of the microscopic velocities $\vec{\xi}$ and D is the pressure tensor.
The particles can change their state due to external volume forces (i.e. gravity, magnetic, electrostatic forces) or to collisions (due to their enthalpy and speed). The evolution equation for the probability function f can be therefore generally expressed in the form of an integral-differential equation, *the Boltzmann equation*:

$$\left(\frac{\partial}{\partial t} + \vec{\xi} \cdot \nabla\right) f(\vec{x}, \vec{\xi}, t) = C(f, f) \tag{3.59}$$

where $C(f, f)$ is the collision operator, f is a function of 7 variables and the space where it is defined is called the phase-space[15].

3.4.1.2 Collision Operators

Further one discerns global equilibrium from local equilibrium. The former take place when all thermodynamic variables are spatially and temporally constant, the latter when it exists only within small length scale. This length scale corresponds to the particle mean free path, that is the mean distance traveled by molecules between two subsequent collisions. The collision operator $C(f, f)$ is typically modelled under the following hypothesis:

- only two-particle collisions[16]
- the collisions process is instantaneous
- velocity uncorrelation of the colliding particles (molecular chaos)
- volume forces smaller than the collision forces

It can be shown, that 5 functions ψ_k exist which satisfy:

$$\int_{\vec{\Xi}} (C(f, f) \cdot \psi_k)\, d\xi = 0 \tag{3.60}$$

they are:

$$\psi_k = \begin{cases} 1 & : \quad k = 1 \\ \vec{\xi}_k & : \quad k = 2, 3, 4 \\ \vec{\xi}^2 & : \quad k = 5 \end{cases} \tag{3.61}$$

and are called *collision invariants*.
Bhatnagar, Gross and Krook (1954) modelled the collision operator using a single parameter: the relaxation time τ necessary to bring the fluid particles from a state f to the local equilibrium state $f^{(0)}$. In this model the same relaxation time applies for density, velocity and energy in the same way.
This model is the simplest one and known under the name BGK:

$$C(f, f) = -\frac{1}{\tau}(f(\vec{x}, \vec{\xi}, t) - f^{(0)}) \tag{3.62}$$

[15]The phase-space is a $\Re^7$ space in time, dimension and velocity.
[16]The hypothesis of two particle collisions seems to be reasonable even for continuum fluids with small Knudsen numbers [76]

The role of the Knudsen number becomes evident with the adimensional version of the BGK equation [77]. Its derivation is simple. Starting from Eq.3.59 and 3.62 each variable and operator is normalised as following:

$$\hat{f} = \frac{f}{f_n}; \hat{\vec{\xi}} = \frac{\vec{\xi}}{c_n}; \hat{\vec{x}} = \frac{\vec{x}}{L_n}; \hat{t} = t\frac{c_n}{L_n} \tag{3.63}$$

$$\frac{\partial}{\partial \vec{x}} = \frac{1}{L_n}\frac{\partial}{\partial \hat{\vec{x}}}; \frac{\partial}{\partial t} = \frac{c_n}{L_n}\frac{\partial}{\partial \hat{t}} \tag{3.64}$$

where f_n, c_n, L_n are reference variables, respectively: distribution, microscopic speed and macroscopic length. With$\hat{}$it is indicated the (adimensional) variable after normalisation. Finally it leads to the BGK equation in adimensional form:

$$\frac{\partial \hat{f}}{\partial \hat{t}} + \hat{\vec{\xi}} \cdot \nabla \hat{f} = -\frac{1}{\epsilon}(\hat{f} - \hat{f}^{(0)}) \tag{3.65}$$

where the dependence of τ from the Knudsen number ϵ become now evident:

$$\epsilon = \frac{c_n \tau}{L_n} \tag{3.66}$$

Despite of the apparent simplicity, non-linearities are implicit in the expression of the local equilibrium $f^{(0)}$. The Maxwell distribution function $f^{(0)}$ is solution of the Boltzmann equation. In d space dimensions it reads [77]:

$$f^{(0)} = \frac{\rho}{(2\pi c_s^2)^{(d/2)}} e^{(-\frac{(\vec{\xi}-\vec{u})^2}{2c_s^2})} \tag{3.67}$$

with c_s the speed of sound. The dependence from space and time is indirect and comes from ρ and $\vec{u}$.

Having only one parameter (τ), all numerical and physical requirements on this model reduce the possible values it can assume. On one side a numerical limitation is given from the linear stability analysis: the dispersion relation[17] for BGK derived by Succi [74] requires

$$0 < \frac{1}{\tau} < 2 \tag{3.68}$$

for linear stability. On the other side a physical limitation will be shown in the section 3.4.1.4: in order to approximate the Navier-Stokes equations τ is required to be function of the kinematic viscosity. The conclusion is that the BGK method becomes instable for small viscosity or equivalently for large Reynolds numbers.

Different approaches have been investigated in the literature to overcome this limitation. Higuera and Jimenez (1988) propose a more complex operator C using a so-called scattering matrix [74], which can be seen as basis for a the multiple-time relaxation method (MRT) of d'Humieres. In the latter, velocity-moments of higher order are introduced: additional to mass density(zeroth-order moment), momentum (first-order moment) and energy (second-order moment), there are also energy square, energy cubic and components of heat flux. In this approach many relaxation times exist. This respects much

[17] With 'dispersion relation' is usually meant the Fourier transform of the considered equation system. By that, the amplitude and the phase are considered separately and the phase shift (dispersion) depending from system parameters can be identified.

more the physical intuition that, for instance, thermal exchange requires longer time than density propagation. An investigation of stability condition for the different relaxation time can be found in [90]. Lallemand and Luo [90] assessed the stability improvement of MRT over BGK and pointed out that BGK can be recovered as special case from MRT.

On the other hand, Zhang et al. [97] proposed a fractional volumetric scheme where the improvement over BGK is more in the mathematical rather than in the physical side: unlike the (standard) BGK method which transports all particle in a streaming step to the neighbouring site (see next section), the fractional volumetric scheme propagates only a fraction of the density. The Navier-Stokes equation can be still recovered. Moreover, as the particle effective evolution time step is practically reduced, the stability limit can be increased to much higher (i.e. 100 times larger) Reynolds number. This scheme is implemented in the code used for our investigation.

3.4.1.3 Discretisation

The numerical solution of the Boltzmann equation and in particular of its derivation (i.e. BGK equation 3.62), requires a discretised formulation. Cubic elements are normally used for the space discretisation. However, different to the Navier-Stokes equations, not only time and space but also the velocity is discretised. At each node in the space discretisation, the velocity vector can have, therefore, only a limited number of well-defined directions. The particles can be transported and collide only in these directions. If we sketch these onto the cubic elements used for the space discretisation, a sort of crystal pattern (lattice) arises. The Boltzmann equation after the discretisation on the lattice is called Lattice-Boltzmann equation. A systematic classification of discretisation patterns is first proposed by Qian et al. [86](1992). With the nomenclature $DnQm$ they proposed to identify a lattice in n dimensions with m possible velocity states (degrees of freedom) including the zero velocity. The D3Q15 is for instance a crystal made up by the center of the cell, the six face-centers and the 8 vertices. Therefore, it can support 15 different states: the velocity zero (element centre) and 14 velocities different from zero.

Basic properties of the Navier-Stokes equations are translational and rotational invariance. Lattices which do not support this symmetry are therefore not suited. Figure 3.6 shows some of the most used discretisation patterns using the classification of Qian. The 2D and 3D lattices illustrated in the figure retain the symmetry required above. On the other side, an example of not suitable lattice would be the D2Q5, used in the 70's from Hardy, Pomeau and de Pazzis for lattice gas cellular automata [74].

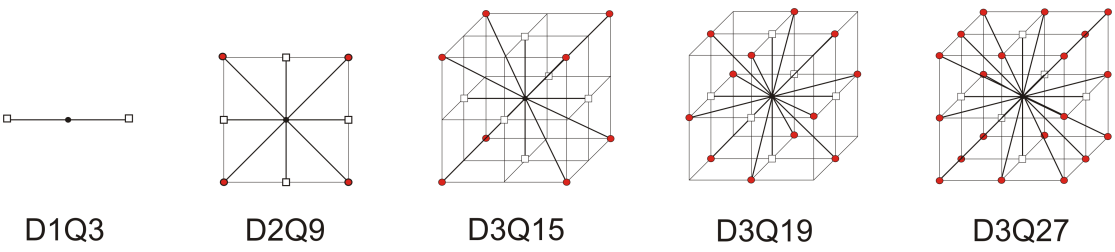

Figure 3.6: *Example of lattices for Lattice-Boltzmann Method. The solid lines connecting the element centre (black dot) with collocation points on the cube (white squares and red dots) show the possible directions for the velocity vector. One differentiates orthogonal extremities (white squares) from corner extremities (red dots).*

The integrals used for obtaining the macroscopic variables (Eq.3.55, 3.56) are now calculated with numerical quadrature formula. It follows respectively:

$$\rho(\vec{x},t) = \sum_{i=0}^{m-1} w_i \hat{f}_i = \sum_{i=0}^{m-1} f_i \tag{3.69}$$

$$\rho(\vec{x},t)\vec{u} = \sum_{i=0}^{m-1} w_i \vec{\xi}_i \hat{f}_i = \sum_{i=0}^{m-1} \vec{\xi}_i f_i \tag{3.70}$$

$$\Pi_{\alpha\beta} = \sum_{i=0}^{m-1} w_i \vec{\xi}_{i\alpha} \vec{\xi}_{i\beta} \hat{f}_i = \sum_{i=0}^{m-1} \vec{\xi}_{i\alpha} \vec{\xi}_{i\beta} f_i \tag{3.71}$$

with m the degrees of freedom, and $\alpha, \beta = 1, \cdots, n$ with n the space dimension and m the The weighting coefficients (w_i) are defined in order to obey the conservation of macroscopic variables, depending on the lattice type and on the collocation point. The probability function $f(\vec{x}, \vec{\xi}, t)$ is replaced from m defined probability at the m collocation points. If the fluid is not very rarefied, (small Knudsen number ϵ), the deviation from the equilibrium $f^{(0)}$ is small [77], therefore the probability function f can be approximated only with few degrees of freedom for the microscopic velocity. $f(\vec{x}, \vec{\xi}, t) = \hat{f}_i(\vec{x}, t)$ at $i = 1, \cdots, n$ collocation points.

Table 3.1: *Weighting coefficients of some DnQm lattices [74]. The position in the lattice are: element origin (o), orthogonal extremities (e) and corner extremities (c). See also Figure 3.6.*

Lattice	Weight	Position
D1Q3	2/3	o
	1/6	e
D2Q9	4/9	o
	1/9	e
	1/36	c
D3Q19	1/3	o
	1/18	e
	1/36	c

The Boltzmann-equation 3.59 discretised in the velocity space can be written therefore as:

$$\frac{\partial f_i}{\partial t} + \vec{\xi}_i \cdot \frac{\partial f_i}{\partial \vec{x}} = C(f_i, f_i) \tag{3.72}$$

In the following the BGK formulation for the collision operator C is used. Its discretisation has the following form [73, 84]:

$$\frac{\partial f_i}{\partial t} + \vec{\xi}_i \cdot \frac{\partial f_i}{\partial \vec{x}} = -\frac{1}{\tau}(f_i - f_i^{(0)}) \tag{3.73}$$

with $\vec{\xi}_i = c \cdot \vec{e}_i$, $\vec{e}_i$ the collocation vector (adimensional) and $i = 1, \cdots, m$ Setting an anti-clockwise numbering of the collocation points in the unit lattice and starting from the lattice centre, the coordinates $\vec{e}_i$ of the collocation points, for instance for D2Q9, read:

$$\vec{e}_i = \begin{pmatrix} x_i \\ y_i \end{pmatrix} = \begin{pmatrix} 0 & 1 & 1 & 0 & -1 & -1 & -1 & 0 & 1 \\ 0 & 0 & 1 & 1 & 1 & 0 & -1 & -1 & -1 \end{pmatrix} \quad (3.74)$$

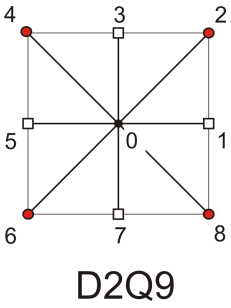

The system 3.73 is a set of m hyperbolic partial differential equations consisting of m linear independent equations where the matrix coefficient is constant and diagonal. The space and time discretisation can be done with every numerical scheme (An overview from finite-difference up to finite-volume is given by Succi in [74]). Within the framework of the finite differences and having set mesh size $\Delta x = c \cdot \Delta t$, one obtains:

$$f_i(\vec{x} + \vec{e}_i \Delta x,\, t + \Delta t) - f_i(\vec{x}, t) = -\frac{\Delta t}{\tau}(f_i(\vec{x}, t) - f_i^{(0)}) \quad (3.75)$$

The left side of equation 3.75 approximates the particle advection, while the right side represents the interaction of the particles (collision). This is implemented in two steps:

$$f_i^*(\vec{x}, t) = f_i(\vec{x}, t) - \frac{\Delta t}{\tau}(f_i(\vec{x}, t) - f_i^{(0)}) \quad \text{collision} \quad (3.76)$$

$$f_i(\vec{x} + e_i \vec{\Delta} x, t + \Delta t) = f_i^*(\vec{x}, t) \quad \text{propagation} \quad (3.77)$$

3.4.1.4 Multiscale Analysis

Chapman and Enskog (1910-1920) derived the Navier-Stokes equation with a multiscale analysis from the Boltzmann equation. The first step towards the derivation of the macroscopic conservation equations is to multiply the Boltzmann equation by the collision invariants ψ_k (Eq.3.61) and to integrate that on the velocity space. Using Eq.3.60 one obtains:

$$\int_{\vec{\xi}} \left(\frac{\partial f}{\partial t} + \vec{\xi} \cdot \nabla f \right) \cdot \psi_k \, d\vec{\xi} = 0 \quad (3.78)$$

One recovers the continuity equation directly by writing Eq.3.78 for the invariant ψ_0=1. The other conservation equations are obtained only after a multiscale decomposition of the probability function.

The probability function is written as a series of the Knudsen number (Kn), for simplicity renamed ϵ here, around the local equilibrium:

$$f = f^{(0)} + \epsilon f^{(1)} + \epsilon^2 f^{(2)} + \cdots \quad (3.79)$$

Similarly, the collision operator and derivatives are formed into a series with the Knudsen number. In the following only the results are reported and it is refered to [78, 77] particularly for a revisited derivation. The first order expression $^{(0)}$ for the impulse conservation equation leads to the (viscosity-free) Euler equation. Considering $\epsilon f^{(1)}$ additionally, second order expressions are obtained. The shear tensor yields for instance:

$$S_{\alpha\beta} = \tau c_s^2 \rho \left(\frac{\partial u_\alpha}{\partial x_\beta} + \frac{\partial u_\beta}{\partial x_\alpha} \right) + \mathcal{O}(\epsilon^2) \quad (3.80)$$

Navier-Stokes equation are now recovered only when $\nu = \tau c_s^2$.
In the discretisation form the kinematic viscosity yields:

$$\nu = \frac{1}{6} c^2 (2\tau - \delta t) \tag{3.81}$$

with $c = \frac{\delta x}{\delta t}$
Higher order truncation in the Chapman-Enskog expansion (ϵ^2) yields the so-called Burnett equation (Burnett, 1935). Succi [74] pointed out that the Chapman-Enskog expansion is not convergent, that is truncating the expansion at higher terms the Navier-Stokes equation is not obtained anymore. Moreover it introduces instabilities which violates the second law of thermodynamic [98].

On the other side, the limitation of the Lattice-Boltzmann equation to low Mach number results only from its discretisation in the velocity space. Krafczyk [77] showed the role of the probability function used for the local equilibrium $f^{(0)}$. Using a finite number of collocation points in the lattice, the expression for $f^{(0)}$ must be expanded as function of Mach number. In particular, Shan (1998) [79] pointed out that the truncation of the probability function has negligible effects on the conservation equations *only* at small Mach numbers, and that a higher Mach number limit can be reached with more collocation points in the discretisation of the velocity space. It is to observe that the discretisation so far correspond to a isothermal fluid dynamic model. This is independent from the model of the collision operator (BGK or MRT) and can be overcome with different approaches: for instance using a larger set of discrete velocities and high order truncation in the probability function expression or decoupling the flow simulation from the solution of the temperature equation. For a theoretical comparison of these approaches is hereby refered to the work of Lallemand and Luo [90](2003).

Finally the advantages of LBM for fluid dynamic can be summarised as follows:

- unconditional linear stability [74]
- good efficiency (no need to solve Poisson problem for pressure, simple algorithm)
- local computational scheme allows easy parallelisation

3.4.2 Implementation aspects of commercial code (PowerFlow)

The code PowerFLOW (Exa corp.) is a commercial application of LBM. The simulations in this work were performed with the 19 state version of the code (D3Q19), based on the BGK collision model[18]. LBM is implemented isothermal but a energy equation is solved at the same time. In this way the temperature can effect indirectly the LBM by changing the density. Therefore the code is also capable to simulate the heat exchange. The spatial discretisation is done within the finite volume approach [96]. Moreover, using a fractional volumetric scheme [97] flows with high Reynolds numbers can be solved. The code has been validated in the past for a wide variety of engineering flow applications [81, 82]. Moreover, Exa's unpublished test on the propagation of planar acoustic wave reports that the minimal required spatial resolution yields 6 up to 8 ppw [87].

[18] PowerFLOW Version 3.5a

An additional feature of this code is the ability to define arbitrarily shaped regions of varying resolution. Recently Crouse [76] proposed an efficient approach for cartesian and hierarchic grid where the size-ratio of different refinement levels between neighbouring cells is two. A similar approach is implemented in PowerFlow. Neighbouring domains with different refinement levels overlap over a width which is equal to the largest element of the neighboring domains. The mass between the domain is conserved but rapid fluctuations of stochastic nature arise (i.e. in $f^{(1)}$). This can cause small waves with wavelength comparable to the voxel size [87] and propagation speed equal to the sound speed.

The Cartesian structure of the computational grid (cubic cells) enables a fully automatic grid generation. The simulator requires all surface elements to be in form of a facet model consisting of triangles. So-called *surfels* are generated where the voxels cut the surface. The interface between fluid and boundary condition is captured with the surfels and the wall-near voxels as shown in a simplified way in figure 3.7. In each time step the surfels gather and scatter particle distributions and alter their momentum according to the boundary conditions. The surface forces depend on the momentum exchange and are realized with a combination of the specular and the bounce-back reflection [93]. While the bounce-back reflection realizes a momentum balance in normal and tangential direction the specular reflection balances only normal forces.

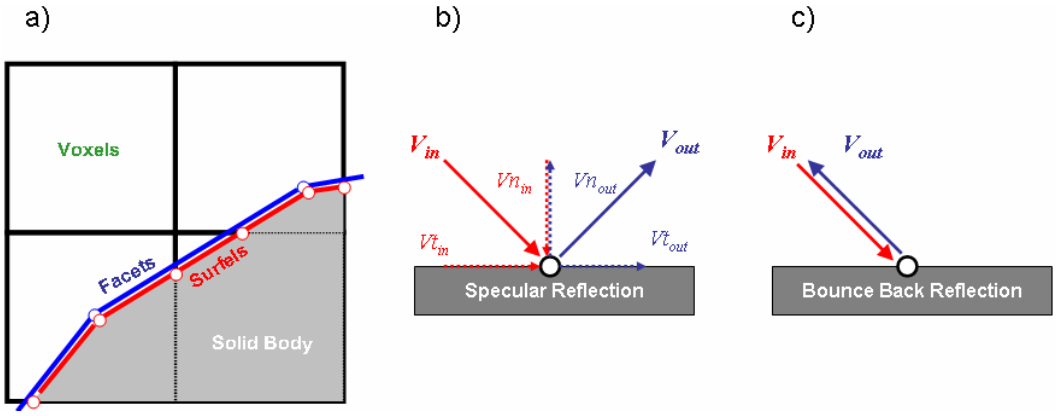

Figure 3.7: *Domain discretisation at boundaries with surfels and wall-near voxels a). A combination of specular reflections b) and bounce-back reflection c) for the distribution function is applied on the boundary depending on the orientation of the surfels. V_{in} and V_{out} are the velocities before and after the collision with the boundary (Picture Courtesy EXA).*

The implemented turbulence model is based on the two equation RNG $k-\epsilon$ formulation developed in [85],[92] for LBM.

$$\rho\frac{Dk}{Dt} = \frac{\partial}{\partial x_j}\left[\left(\frac{\rho\nu_0}{\sigma_{k_0}} + \frac{\rho\nu_T}{\sigma_{k_r}}\right)\frac{\partial k}{\partial x_j}\right] + \tau_{ij}S_{ij} - \rho\epsilon \tag{3.82}$$

$$\rho\frac{D\epsilon}{Dt} = \frac{\partial}{\partial x_j}\left[\left(\frac{\rho\nu_0}{\sigma_{S_0}} + \frac{\rho\nu_T}{\sigma_{S_r}}\right)\frac{\partial \epsilon}{\partial x_j}\right] + C_{S_1}\frac{\epsilon}{k}\tau_{ij}S_{ij} + \tag{3.83}$$
$$-\left[C_{S_2} + C_\mu\frac{\tilde{\eta}^3(1-\frac{\tilde{\eta}}{\eta_0})}{1+\beta\tilde{\eta}^3}\right]\rho\frac{\epsilon^2}{k}$$

All dimensionless coefficients are the same as in the original models [94]. The above

equations are solved on the same lattice using a modified Lax-Wendroff-like explicit time marching finite difference scheme. The turbulent eddy viscosity is defined as:

$$\nu_t = C_\mu \frac{\frac{k^2}{\epsilon}}{1 + \tilde{\eta}^2} \tag{3.84}$$

Where $\tilde{\eta}$ is a combination of a local strain parameter $\eta = \frac{k}{\epsilon} \mid S \mid$, local vorticity parameter $\eta_\omega = \frac{k}{\epsilon} \mid \Omega \mid$, and local helicity parameters. This so-called swirl-correction is introduced in order to deal with the large scale vortices adequately, whose spatial-temporal dynamics are to be resolved. This technique is referred to as Very Large Eddy Simulation (VLES).

The eddy viscosity ν_t is incorporated in the LBM approach via

$$\nu = \nu_0 + \nu_t \tag{3.85}$$

where ν_0 is the molecular kinematic viscosity. The new kinematic viscosity ν is then used in equation 3.81 for the Lattice-Boltzmann equation 3.73. It means that the relaxation time τ is normally neither constant in space nor in time.

Chapter 4

Preliminary Investigation

In this chapter subsonic free jets and jets impinging on large inclined plates are investigated experimentally and numerically. The aim of the numerical investigation is to verify the 2D implementation of the hybrid approach described in section 3.2 and in particular the coupling strategy between the codes used. On the other side the aim of the experimental investigation is to validate 2D and 3D fluid dynamic simulations used for the hybrid approach and to identify the most suitable experimental technique for the localisation of the sound sources.

The experiments of this chapter have been carried out in the facility of ITSM (Institut fur Thermische Strömungsmaschinen und Machinenlaboratorium) at the Stuttgart University (Germany). This facility consists of a low speed wind tunnel (open type) located in a semi-anechoic room. Detailed aeroacoustic properties of this wind tunnel are documented in [7].

The CFD calculations are carried out with the finite volume code '*CFX*' (Ansys) and the acoustic one with the finite element code '*Hydsol*' (IAG) (See also section 3.2).

These investigations are preparatory for following ones, where small obstacles are placed additionally onto the inclined plate. This will be presented in Chapter 5.

In the next sections two configuration for high Reynolds (Re=$2 \cdot 10^5$) number are investigated for different Mach numbers (M):

1. free round jet (M=0.15)
2. round jet impinging on an inclined plate (M=0.15, 0.30)

In both configurations the diameter of the round jet yields 30 mm.

4.1 Free Jet

A test case with axial symmetry has been chosen to be investigated with a 2D numerical approach. The simulation method follows the CAA hybrid approach described in 3.2.

4.1.1 Computational Models

Two domains have been defined to fulfill different requirements: The smallest element size of the CFD model should solve the turbulence on the shear layers. The CAA domain

is bigger in order to show low frequency sound waves and its element size is prescribed to resolve acoustic waves up to 3000 Hz but bigger than CFD one, in order to reduce the calculation time. See tables 4.1 and 4.2 for more details and Fig.4.1 for an overview of calculation domains.

Table 4.1: *DES model data for the free jet*

Jet speed	103m/s with block profile
Jet outlet dimension	D=30 mm; L=60mm
Element quantity	$2 \cdot 10^5$
Element form and size	Hexahedron 1–10mm
Domain size	60cm · 120cm · 1mm
Time step	20 μs
Export time step	0.1 ms

Table 4.2: *CAA model data for the free jet*

Element quantity	$2 \cdot 10^4$
Element form and size	Triangular 10–30 mm
Domain size	$150 \cdot 200$ cm
Discretisation Order	2
Time step	~ 7 μs

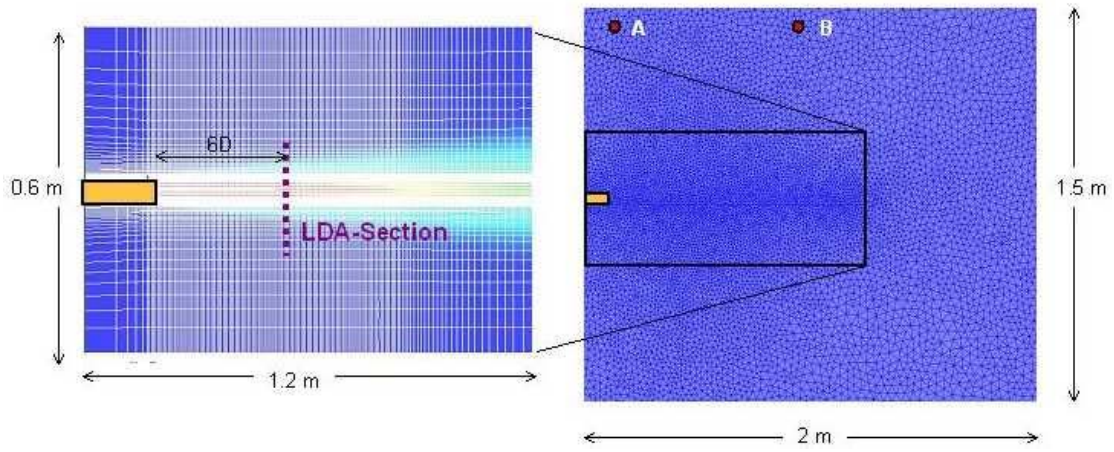

Figure 4.1: *Calculation domains: CFD-Mesh (left), CAA-Mesh (right). The dotted violet line and the points A and B are used for comparison with experiments. The jet outlet is indicated in yellow.*

4.1.2 CFD Simulation and Interpretation of Results

A fully developed turbulent flow should occur before recording pressure and velocity fields. The recording time was 35 ms with 10 kHz sampling rate to shorten the CPU time but enough to achieve good statistical results. The present calculations last about 500 CPU hours on a Pentium processor with a clock frequency of 1.8 GHz (250h for LES

and 250h for LEE). The LES calculation could be performed on parallel CPUs allowing a reduction of the computation time.

The calculated velocity has been compared with velocity measurements of a 3D axial-symmetrical free jet with same boundary conditions (speed, outlet profile velocity and initial turbulence). Differences are expected due to the fact that real turbulence is a fully 3D phenomena while 2D simulations of turbulences intrinsically presents physical artefacts like the *inverse* energy cascade[41]. Measurements were done with 3D LDA in the aeroacoustic windtunnel at ITSM prior to this work. Additionally, best-fit curves obtained in self similar regions of the jet are used as reference (from [33]). Figure 4.2 shows the comparison of integral quantities (time averaged velocity and turbulent kinetic energy (TKE)) at a distance of six diameters (6D) from the jet outlet.

At this distance the present flow is fully turbulent over the section and (therefore) the maximum axial velocity is smaller than the outlet velocity ($U/U_0 < 1$). This means that in the present flow the potential region is shorter than 6D. The LDA measurement agrees good with reference measurement, where however the potential region begins later. In conclusion, for a 2D CFD simulation there is a relative good agreement of the CFD results with the measurements, therefore it seems acceptable to use it for further (acoustic) simulations.

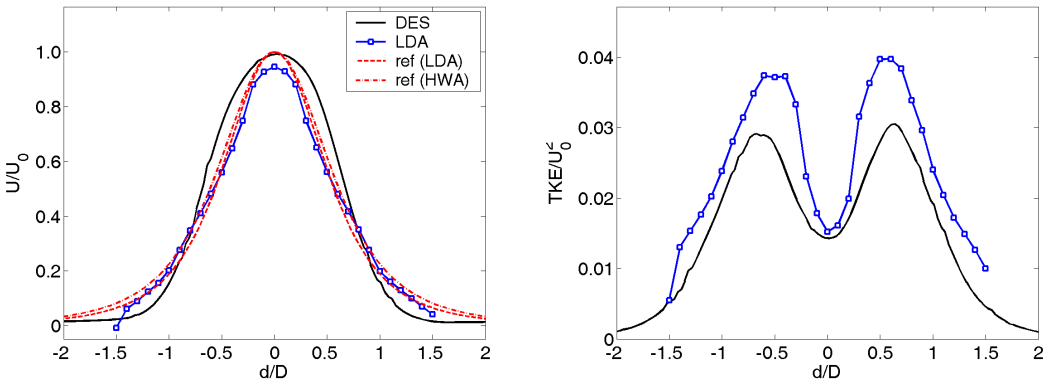

(a) (b)

Figure 4.2: *Comparison between CFD results and LDA measurements at a distance of 6D from the jet outlet. Best-fit curves on self-similar regions from measurements from Hussein et al.(1994) from [33] as reference. a) Speed on jet axis direction (U) normalised to the outlet speed (U_0). b) Turbulent kinetic energy (TKE) normalised to the square of outlet speed. Distance (d) from the centerline normalised to the jet diameter (D). DES data averaged over 350 time steps.*

To evaluate the frequency content of the 2D LES unsteady simulation, a Fourier analysis was done (See Figure 4.3). A dominant value around 400 Hz is found. This correlates well to the later generated acoustic main frequency from the CAA calculation.

4.1.3 CAA Simulation and Interpretation of Results

Figure 4.4-a gives a snapshot of the perturbated pressure field and of the source intensity at a given instant. The pressure at two observation points A and B (see Fig.4.1 for location) is analysed. The calculated overall sound pressure levels (138-141 dB) appears

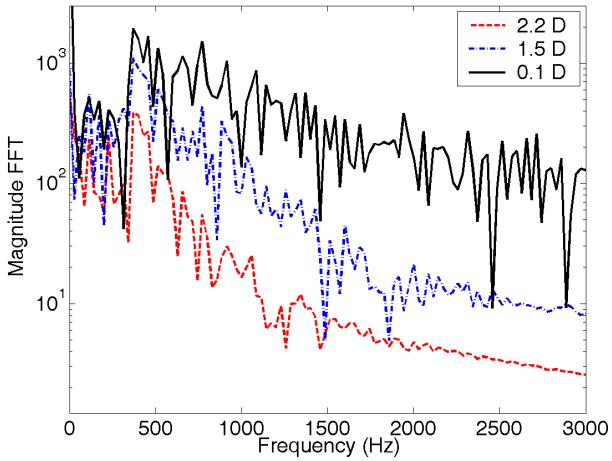

Figure 4.3: *Velocity spectra on a line situated 6D downstream (=180 mm) from the jet outlet with distance from the jet axis equal to 0.1 D, 1.5 D and 2.2 D. Numerical Simulation with DES.*

evidently much too high but the cause should be found in the intrinsic nature of a two dimensional simulation: from one side the 2D CFD simulation, from the other side the sound propagation in 2D. Concerning the CAA simulation, an approach for correcting the OASPL from 2D into 3D will be shown in the section 5.1.2. Another important feature for the validation of the calculation is the spectral distribution of the pressure fluctuations. Figure 4.4-b shows the spectrum profile (trend in red) and the maximum at 400 Hz (Strouhal number = 0.2). The frequency peak matches very well the experimental data from the literature [15]. In particular the experimental spectra for Point B corresponds to the curve for high Y/D ratio in the picture 4.8.

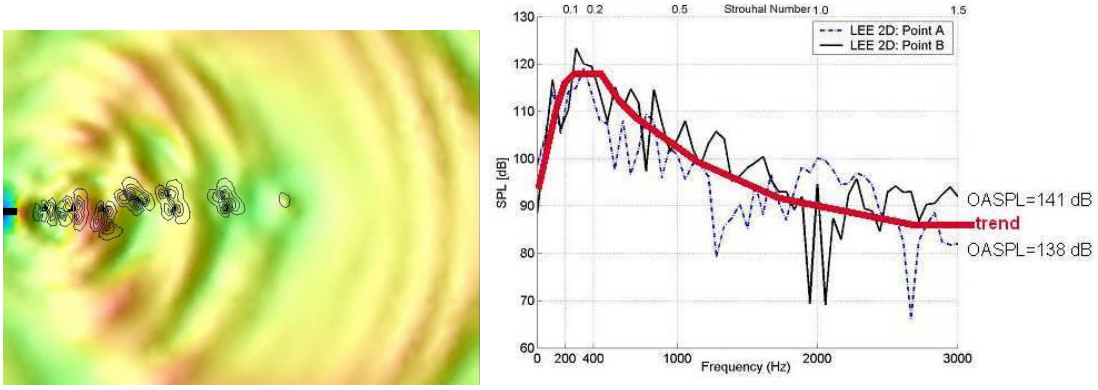

(a) (b)

Figure 4.4: *Instantaneous pressure field (coloured background) and instantaneous source intensity distribution (iso-lines) (a). Spectrum of the sound pressure at the two points, indicated in figure 4.1 (b).*

4.2 Inclined Plate

In this section the capability of experimental techniques to localise the sound sources of subsonic impinging flows is investigated. In the introduction it was pointed out that turbulence is the source of sound in aeroacoustics and that the acoustic and hydrodynamic near field are particularly of interest because of the sound generation process. Microphones located in (hydrodynamic) near field however capture also pseudo sound. As a consequence of that, the charts of overall pressure sound provide not only a picture of the sound pressure distribution but also a picture of the turbulence itself. Of particular interest is the question how much the hydrodynamic near field influences the measurements and the localisation of acoustic sound sources. Two techniques have been used to analyse the sound properties in near field: planar near field holography and one dimensional laser interferometry as described in the sections 2.3.1 and 2.3.3.

Furthermore in this section should be analysed which turbulence model and discretisation strategy can be used for impinging jets. In particular, concerning the SNGR hybrid approach, it is important to quantify how good RANS calculations are, because the sound sources are here derived from it. 3D RANS calculations are therefore validated with 3D LDA experiments. From the other side we continued the validation of the coupling for the CAA hybrid approach seen in Section 4.1 looking for effective interpolation strategies.

For all investigations the impinging flow has a mean velocity of about 50 and 100 m/s. The plate is inclined 25° and 50° against the nozzle direction.

4.2.1 Experimental Investigation

Figure 4.5 shows the interior of the facility used for this investigation.

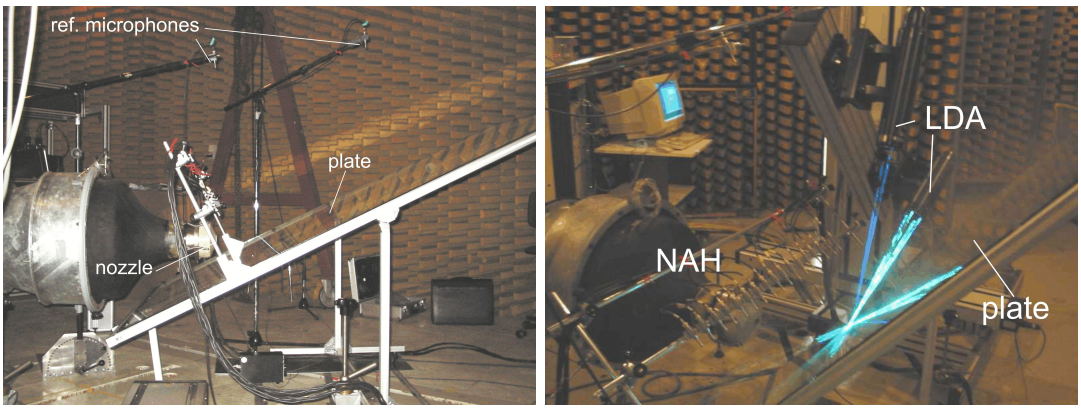

Figure 4.5: *Internal views of aeroacoustic windtunnel of ITSM with 3D LDA and NAH measurement systems. The section diameter of the nozzle used here yields 30 mm.*

4.2.1.1 Planar Near Field Holography

In the followings we discuss measurements obtained with planar near field holography (NAH). The pressure near field is measured through an array of equally spaced microphones. After each measurement the microphone array is moved forward parallel to the

plane in order to scan a planar area of 80 cm × 80 cm with a total of 289 points. Two extra microphones are placed more distantly as reference for the far field. (See geometry of the measurement facility in Figure 4.6)[1].

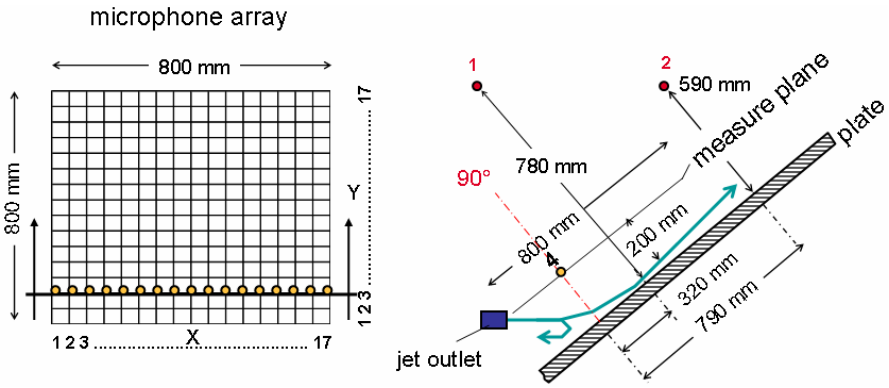

Figure 4.6: *Measurement grid and position of microphones (yellow circles) for planar near field holography and position of reference microphones (red circles 1,2). The distances refers to the configuration of the plate inclined 25°.*

Pseudo Sound Sound spectra show very high levels at low-middle frequencies (0-1000 Hz) (see figure 4.7) which are caused from turbulence intermittence at the free flow boundary (pseudo-sound). This assumption is confirmed from the observation at reference microphones or at array microphones situated 40 cm aside from the symmetry plane. These microphones are situated away from the main flow and show indeed much less SPL for low frequencies then at higher frequencies.

A frequency threshold can be seen in the flexion point of the sound spectra. Its position ranges from 100 Hz for distant points (reference microphones) and small speed (M=0.15) and about 700-1000 Hz for the nearest measured points at highest speed (M=0.3). A similar behaviour was found in [15] for the pseudo sound influence in a subsonic free jet. (See Figure 4.8).

Non dimensional Analysis Outside the frequency region dominated from pseudo-sound, one notices slight maxima in the spectrum, for instance at about 700 Hz for M=0.3. For comparison with literature data we use the modified Strouhal number proposed for the impinging jet in [16] :

$$St = \frac{f \cdot D}{U_J} \cdot \sqrt{\sin \alpha} \tag{4.1}$$

with St = Strouhal number, f = Frequency, D = Diameter, $U_J = 0.6 \cdot U$, U = Outlet Jet Speed, α = impinging angle. One obtains a maximum for St = 0.27 which matches quite well the Strouhal range (0.1 - 0.3) of impinging jets with speed between M=0.4 and M=0.9 [16].

After a constant rate of reduction of SPL, an additional slight increase then takes place. The frequency at which this slight increase takes place depends on the observer position: from about 3200 Hz until some 4600 Hz for the points measured here (See Fig. 4.7).

[1]Measurement software: Lms CADAX. Hardware: omni directional condenser microphones ICP TMS 130A10.

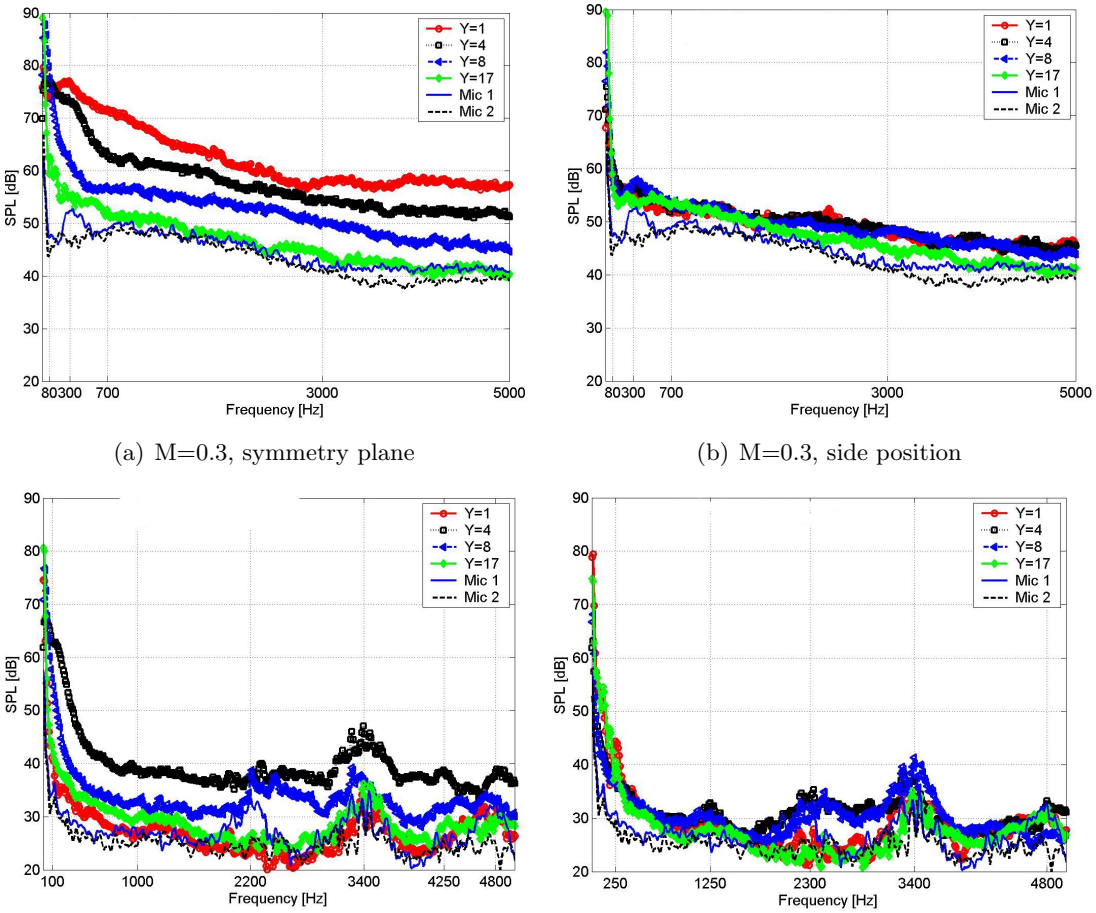

(a) M=0.3, symmetry plane

(b) M=0.3, side position

(c) M=0.15, symmetry plane

(d) M=0.15, side position

Figure 4.7: *Sound pressure level spectrum for plane angle = 50°. M=0.3 (a,b) M=0.15 (c,d). 6 measurement points (4 microphones in near field and 2 reference microphones). Points placed on symmetry plane (a,c) and 40 cm aside from symmetry plane (b,d).*

Turbulent Structures High frequency peaks, located around 2300, 3400 and 4800 Hz are visible for the lower speed test case (M=0.15) at every measurement point. These peeks are not observed at higher speed and it is here anticipated that they have been measured also with other techniques (laser interferometry). To the present knowledge of the author, there are no experimental data for this slow speed available in the literature to compare with. We assume that these peaks can not be caused from pseudo sound because they persist in far field (Mic 1 in figures 4.7-c and -d).

A selective mapping of the measuring plane should help in finding the cause: the chart of the overall sound pressure level (OASPL) integrated around these frequency peaks, (See Fig. 4.9), shows high values in two regions. The first region is located at the jet outlet; the second one looks like an arc of a circle whose radius changes with the frequency.

As these peaks do not occur at sharp tonal frequencies one can exclude that they are generated from fan noise. As this frequency pattern in the sound disappears at higher outflow speed, we assume finally that it is caused from the flow itself and in particular from the turbulent structure generated at the inlet. No evidence exists for the interaction of these turbulent structures with the plate to be the cause of the peaks.

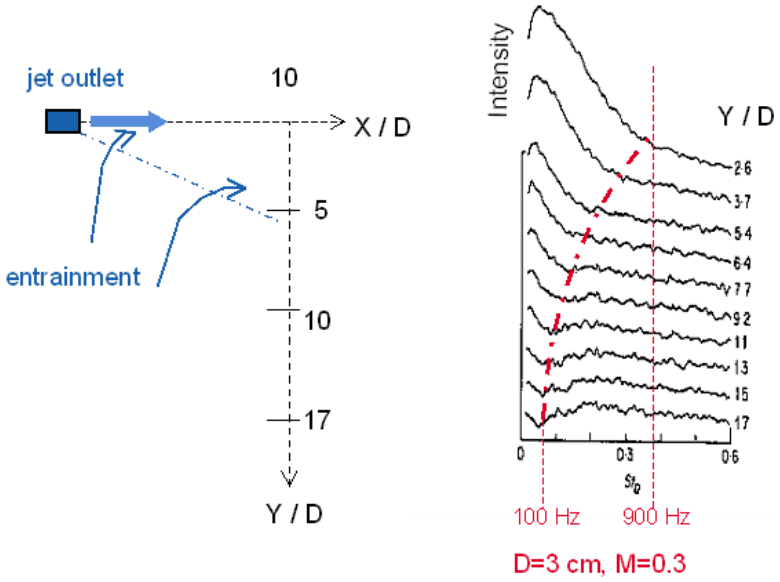

Figure 4.8: *Spectra of the near field pressure fluctuation for a free jet at distance = 10 diameter with different transverse locations (Y) from [15]. The red dashed line indicates the influence limit of the pseudo sound and the frequency are derived from Strouhal number for D=3 cm and M=0.3.*

Finally a ray-tracing simulation [2] of a single frequency emitted at the outlet and reflected from a plate shows a very similar interference pattern. This supports the assumption that these frequencies are of acoustic nature, generated from turbulence structures at the nozzle and intensified from reflections on the plate.

Sound-like pressure fluctuations decay slowly with the distance and with a known function (1/r in free field) while the pseudo sound due to a free jet streaming in a quiet environment decays more strongly with the distance (outside the mean stream). In order to emphasize the sound-like pressure perturbations a cross correlation of pressure levels between observation points situated in the near field (array microphones) and points in the far field (reference microphones) has been calculated. The bigger the distance of the reference microphone is (Ref 1), the more significant should be the result, because pseudo sound effects can be completely excluded. On the top of figure 4.11 one sees the cross power spectrum for 250 Hz. Although it has already be seen that pseudo sound is predominant at this frequency, we can appreciate the clear localisation of sound sources near the impinging point. The disadvantages of this method are the sensitivity from the position of the reference microphone (Ref 1 and Ref 2) and the fact that the calculated entity has no clear physical meaning and can not be directly compared to real sound pressure levels. The first effect can be considered however also as an advantage, as it allows a spatial separation of the sources according to the importance for the receiver. In fact even though the level for 1000 Hz at both reference microphones is the same (Fig. 4.7) the correlation of near field microphones with reference microphones shows different contribution of the source regions (Fig. 4.11 e, g).

Once the pressure field has been measured on a plane, with the assumption of planar wave propagation the sound pressure field can be calculated on another parallel plane using equation 2.8. The parallel plane is chosen to be 30 mm above the solid plate. Figure

[2] own implementation in Matlab

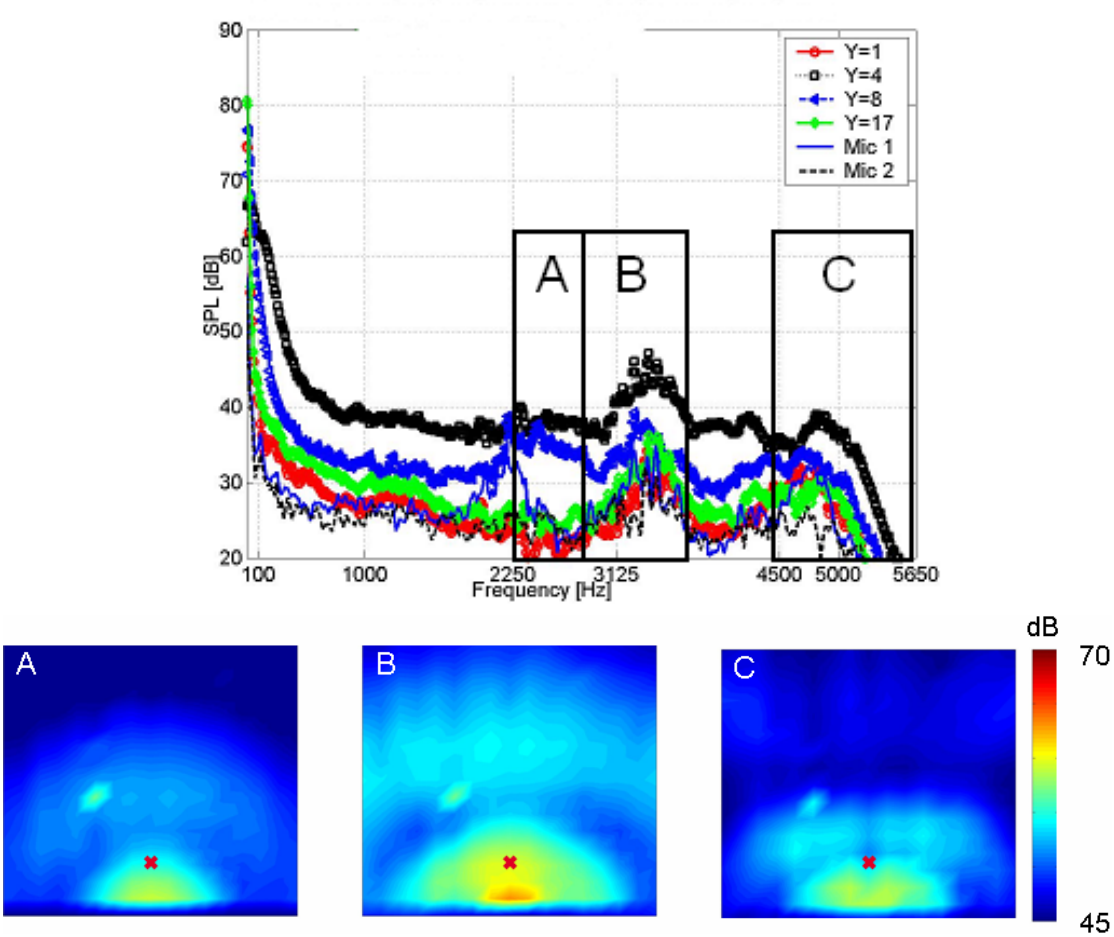

Figure 4.9: *Sound pressure level spectrum for M=0.15, plane angle = 50° on the symmetry plane. Map of third octave SPL in near field for M=0.15, angle=50°. Third octave are centered at 2500 Hz (A), 3150 Hz (B), 5000 Hz (C). The red cross shows the nominal impinging point on the plate.*

4.11 (b, d, f, h) shows however less precise localisation of the sound sources compared to the measurement on the plane (a, c, e, g). This is probably due to violations in the assumptions used for the NAH reconstruction. In particular there are sound sources between measurement plane and reconstructed planes due to the turbulence at the outlet and near the plate. No significant improvement is found with a change of the location of the plane between measurement plane and solid plate. We conclude that the localisation of aeroacoustic sources with NAH is not well determined and unequivocal.

4.2.1.2 Sound Wave Propagation with Laser Interferometry

The hydro-dynamic and acoustic field near the impinging jet has been scanned using the approach of section 2.3.3. Two positions of the laser relative to the solid plate have been used: side view and top view (Figure 4.12). From the side view one can see the turbulent flow field and sound pressure waves generated. Figures 4.13 and 4.14 show the results filtered for 600 and 1500 Hz. Observing the direction of the sound waves, the sound source can be localised around the impinging point. Although the sound source can not

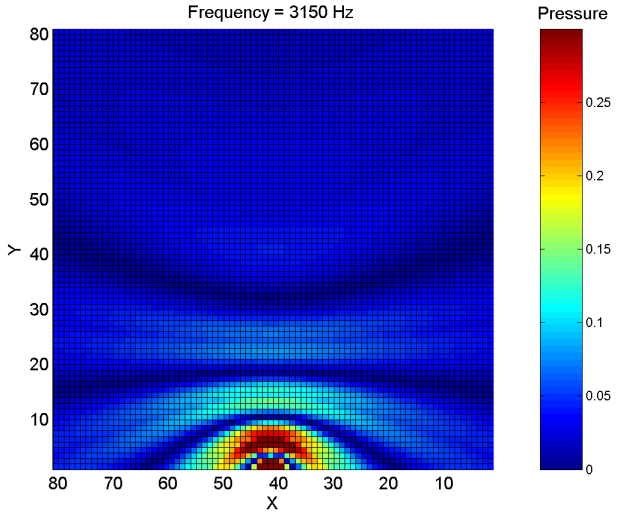

Figure 4.10: *Simulated pressure map resulting from the interference of sound generated at the jet-outlet and reflected from the plate. The simulation analyses the frequency 3150 Hz, and calculate its propagation as ray tracing. A pattern similar to the measured one (Figure 4.9-B) is visible.*

be localised more precisely then with NAH, the source location is unequivocal. Moreover this technique allows the visualisation of propagation-related sound mechanism. One sees, for instance, sound interferences due to the scattering at the plate, particularly visible for inclination of 50°. By measuring the distance between maxima and minima of the pressure fluctuations for a certain frequency, it is possible to deduce the velocity of propagation of the fluctuations. For subsonic flows, this allows to distinguish sound waves from hydro-dynamic turbulence. The firsts being propagated with local velocity of sound c, the second being convected with local flow velocity $U \ll c$. As consequence it is possible to localise very well regions (not)influenced from pseudo-sound.

Concerning hydro-dynamic turbulence, the top view (Fig. 4.15) shows ring structures embedded into the flow, impinging the plate and being deviated from it. This reveals that extremely correlated structures, and therefore highly energetic, are included in the impinging flows. Through these examples it has been shown that laser interferometry gives an insight into the physics of flows and therefore very suitable for aeroacoustic investigations.

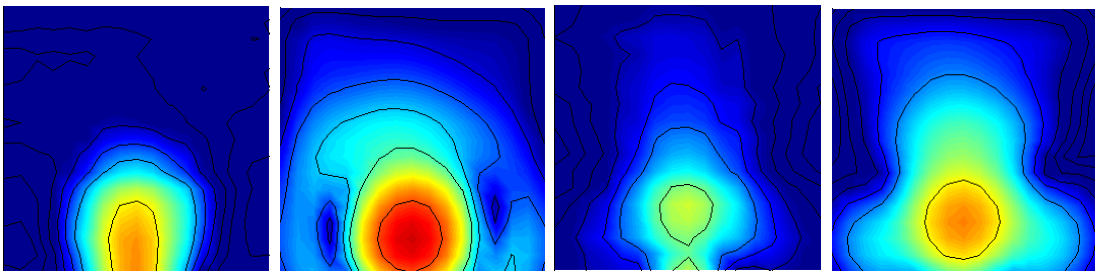

(a) P0, Ref1 (b) P1, Ref1 (c) P0, Ref2 (d) P1, Ref2

250 Hz

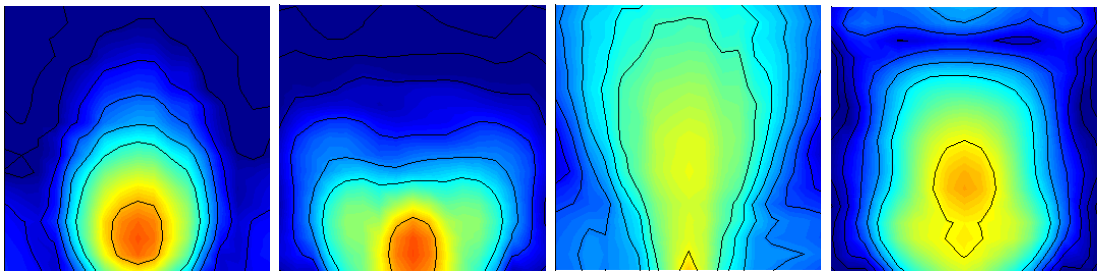

(e) P0, Ref1 (f) P1, Ref1 (g) P0, Ref2 (h) P1, Ref2

1000 Hz

Figure 4.11: *Plot of cross power spectrum of sound pressure between microphone array and two reference microphones (Ref1, Ref2) (M=0.3, angle=50°), for 250 Hz (above) and 1000 Hz (underneath). The cross spectrum is calculated at the measured plane (P0) and projected 170 mm nearer to the solid plate with planar holographyic transformation (P1). Plot size corresponds to 800 × 800 mm.*

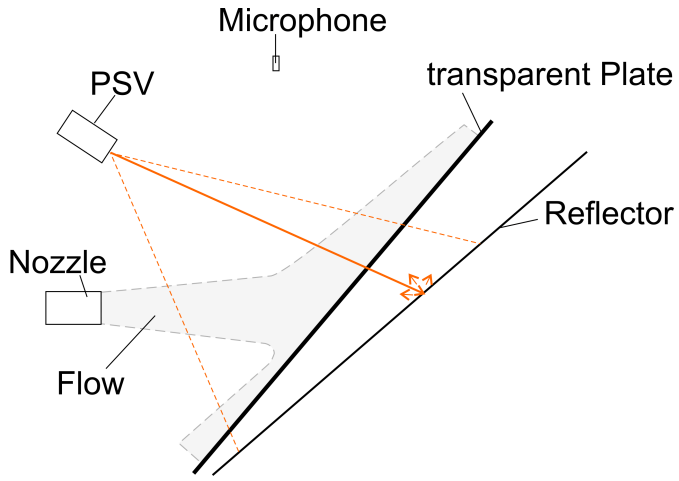

Figure 4.12: *Experimental set up of laser scanning interferometry (PSV) for the top view of a jet impinging a plate. The plate is transparent and the laser beam is reflected from a back-reflector placed behind the plate.*

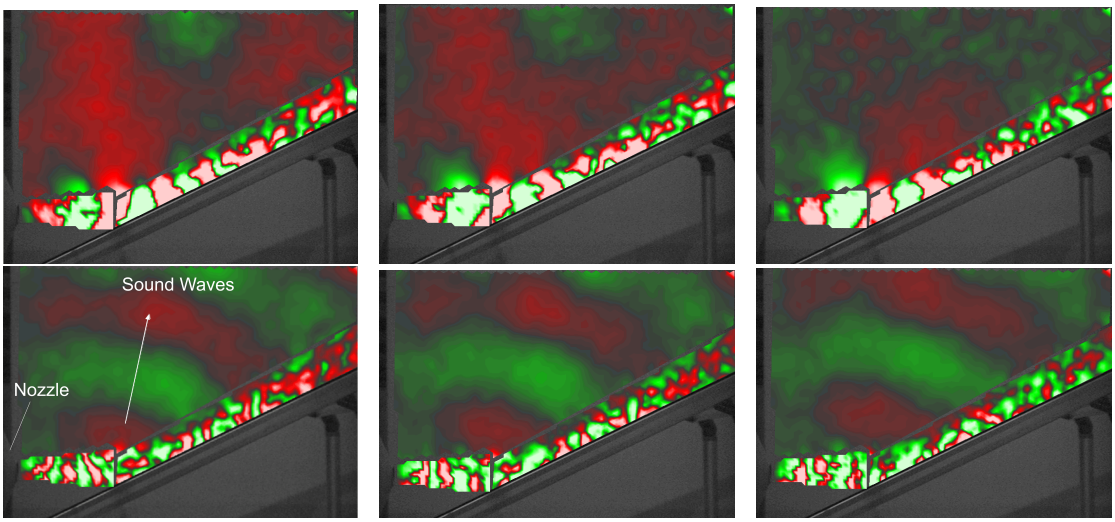

Figure 4.13: *Propagation of sound waves with laser interferometry for impinging speed 100 m/s and plane inclination 25° for 600 Hz (above) and 1500 Hz (underneath). The pictures show a sequence of three time steps. Color range ±1 μm/s.*

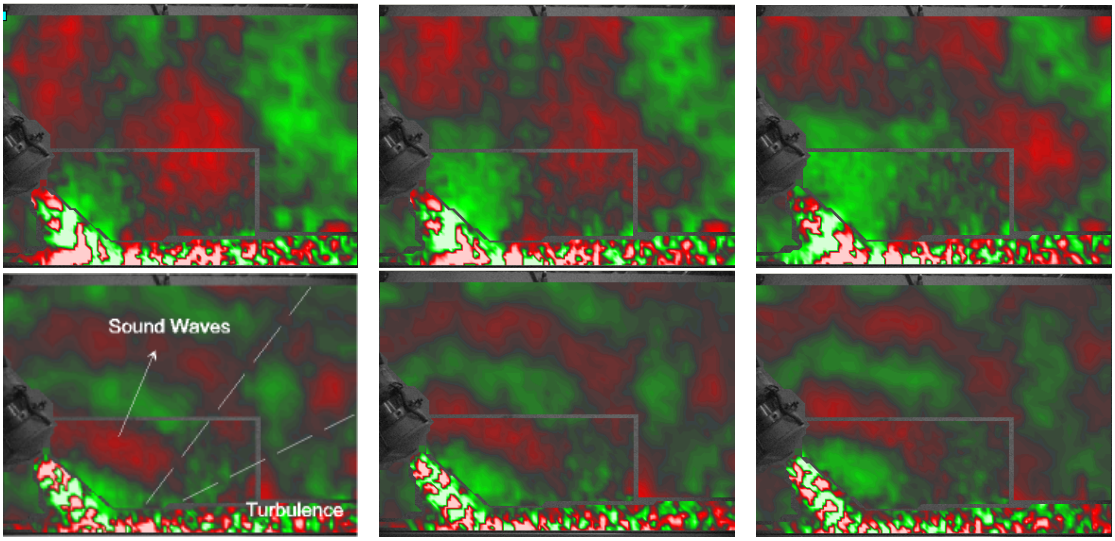

Figure 4.14: *Propagation of sound waves with laser interferometry for impinging speed 100 m/s and plane inclination 50° for 600 Hz (above) and 1500 Hz (underneath). The pictures show a sequence of three time steps. Color range ±1 μm/s.*

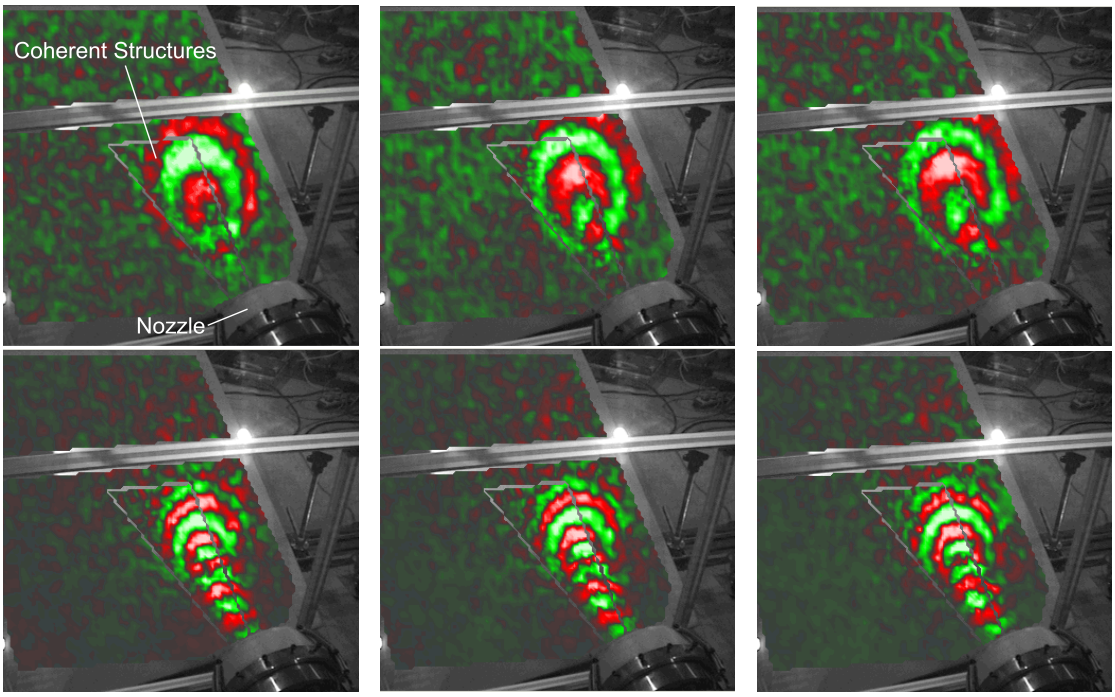

Figure 4.15: *Convection of coherent turbulent structures with laser interferometry for impinging speed 100 m/s and plane inclination 50° for 400 Hz (above) and 900 Hz (underneath). The pictures show a sequence of three time steps. Color range* $\pm 5\,\mu$m/s. *Reflector positioned as in figure 4.12.*

4.2.2 Numerical Investigation

4.2.2.1 3D RANS Validation

In this section we investigate the effect of the numerical discretisation and turbulence methods on a 3D RANS solution for the impinging jet and compare it with 3D LDA measurements. Table 4.3 gives details on the models used and figure 4.16 shows one of the discretisations (grid B). One can see the effect of the discretisation and turbulence model by comparing the turbulence kinetic energy on a jet section upstream of the impinging point, where the jet becomes fully turbulent. By using the same measurement position of the free jet (figure 4.2) one sees in figure 4.17 that, also for these 3D simulations, the level is globally smaller than the measurements[3]. The reasons can be the rough discretisation of the shear layer that retards the transition to turbulence (C) and the mesh elements inclined with respect to the jet axis that dissipate turbulence (A). For the same discretisation no improvement is obtained with a Reynold stress turbulence model (SSG) instead of a turbulence viscosity one (SST).

Grid	A	B	C
Element quantity	$1.9 \cdot 10^5$	$8.7 \cdot 10^5$	$4.6 \cdot 10^5 K$
Turbulence Model	SST	SST	SST, SSG
Half Model	yes	no	no

Table 4.3: *3D RANS models for impinging jet*

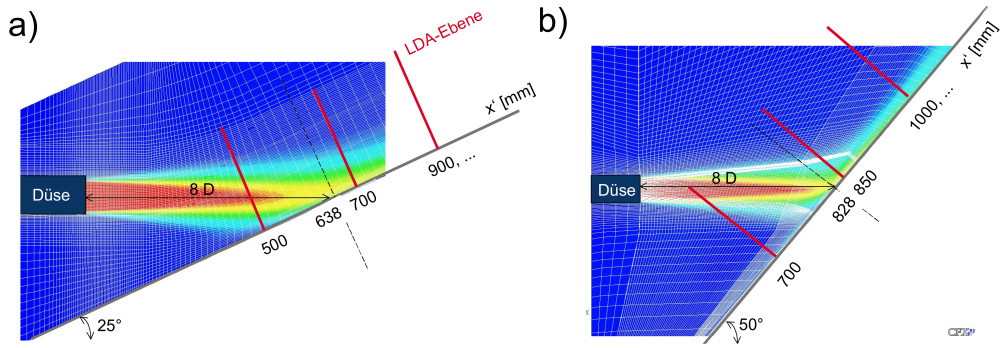

Figure 4.16: *Numerical discretisation for impinging jet on a plane inclined* 25° *(a) and* 50° *(b). Measurement planes are perpendicular to the plate and indicated with red solid lines.*

The complete comparison with experiments is therefore here illustrated using the more resolved discretisation (B) and turbulence model SST. Figures 4.18 show globally a relative good, up to very good, agreement of the profiles of velocity and turbulent kinetic energy on all sections. This demonstrates that the RANS model is robust and therefore suitable for a coupling, within a CAA hybrid approach, with the stochastic sound source generation model (SNGR).

[3]Number of samples at each measurement point is about 6K

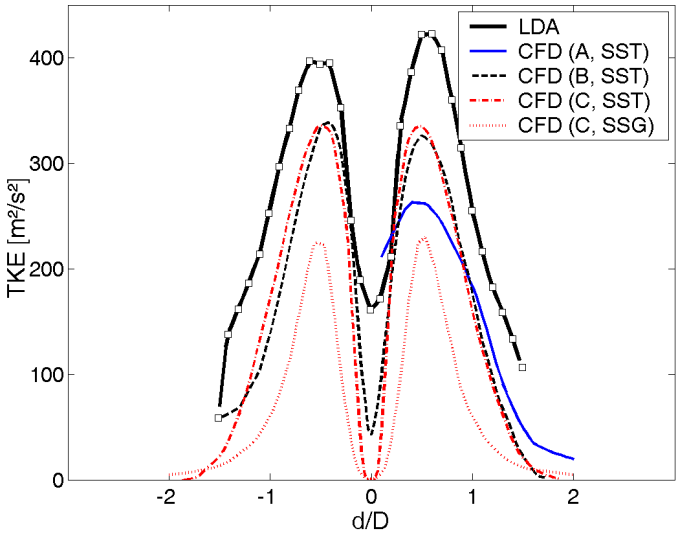

Figure 4.17: *Turbulence kinetic energy calculated with different grids (A, B, C) and turbulence models (SST, SSG) and measured with LDA on a section placed at 6 diameter (D) from the nozzle. Distance (d) from the centerline normalised to the nozzle diameter (D).*

4.2.2.2 2D CAA Hybrid Method

Tables 4.4 and 4.5 give details on the models used. Figures 4.19 and 4.20 give an overview of calculation domains and instantaneous results. The CAA mesh is real 2D, while the CFD mesh is a pseudo 2D: it is a 3D mesh with thickness equal one element (1mm).

Table 4.4: *CFD 2D Model Data*

Jet speed	103m/s with block profile
Plate angle	$\alpha = 50°$
Element quantity	$1 \cdot 10^5$
Element form and size	Hexahedron 1–10mm
Time step	20 μs
Export time step	0.1 ms

Table 4.5: *CAA 2D Model Data*

Element quantity	$8 \cdot 10^3$
Element form and size	Triangular 10–50 mm
Numerical Order	2
Time step	~ 7 μs

Because of different meshes an interface was needed. Similar to the previous section, CFD data have been interpolated on the CAA broader mesh. Moreover here is investigated the effect of time interpolation of CFD data on the acoustic result. Missing interpolation causes additional high frequency numerical noise (8-10 kHz). Figure 4.21

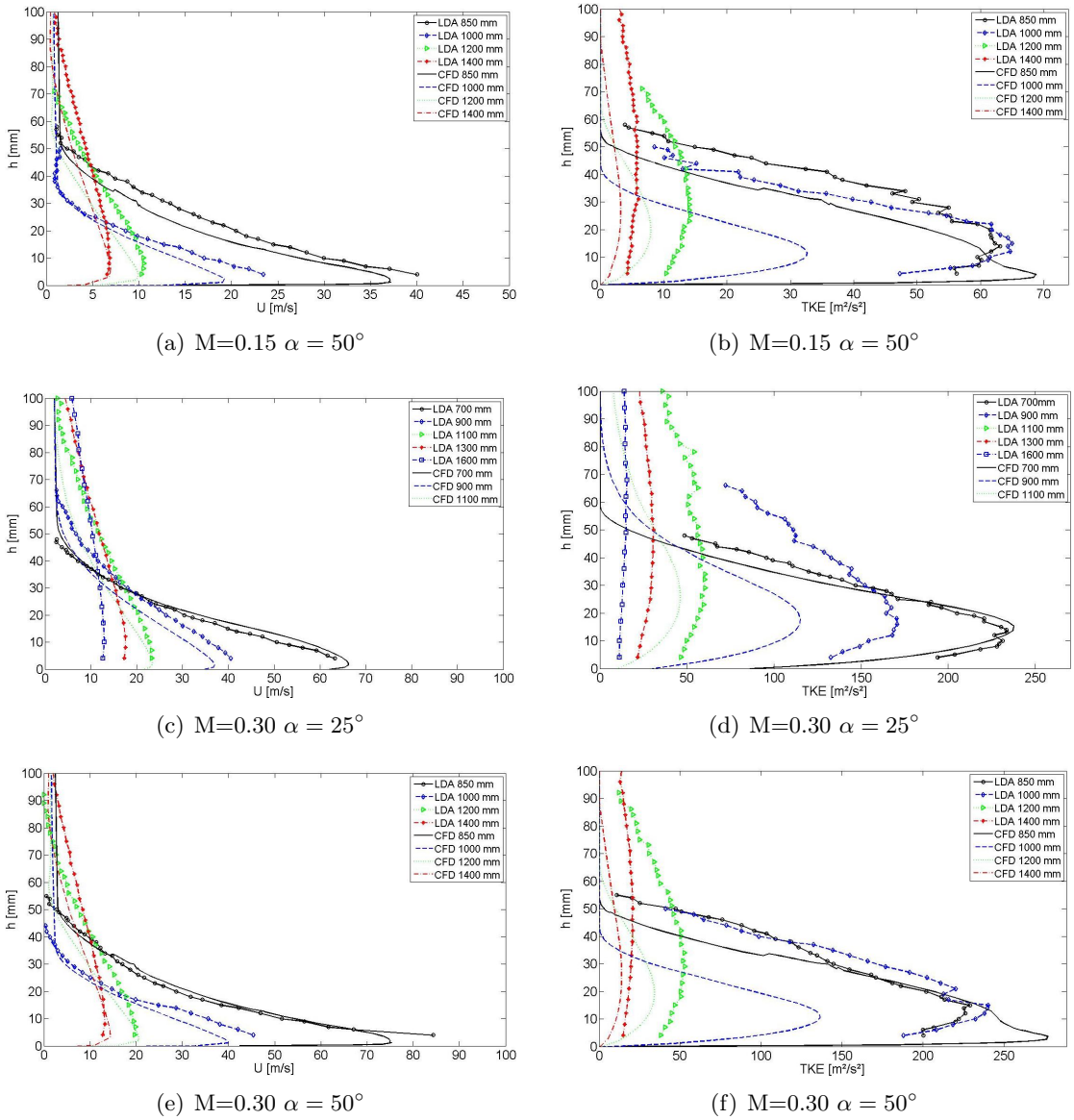

(a) M=0.15 $\alpha = 50°$ (b) M=0.15 $\alpha = 50°$

(c) M=0.30 $\alpha = 25°$ (d) M=0.30 $\alpha = 25°$

(e) M=0.30 $\alpha = 50°$ (f) M=0.30 $\alpha = 50°$

Figure 4.18: *Comparison of the time-averaged velocity (left) and TKE (right) for jet impinging on a plate at different locations. h = distance from the plate. Calculation (3D RANS) and measurement (3D LDA). Locations in the legend refer to figure 4.16.*

shows the improvement in the results thanks to the time interpolation between LES time steps. The source term in the EIF approach consists of the time partial derivative of pressure and of convective terms of pressure space gradients. These terms have different relevance according to the flow type and the speed. For very low speed the time partial derivative of pressure seems to be predominant. Figure 4.22 shows a snapshot of the source term distribution near the impinging point and figure 4.23 gives the ratio between the source terms. The effect of the flow convection on the stretching of sound sources is clearly visible. However, the effect on SPL-spectrum seems to be relevant only at high frequencies as one can see from figure 4.25.

Figure 4.24 shows the SPL spectrum calculated for the impinging jet (M=0.3, α =

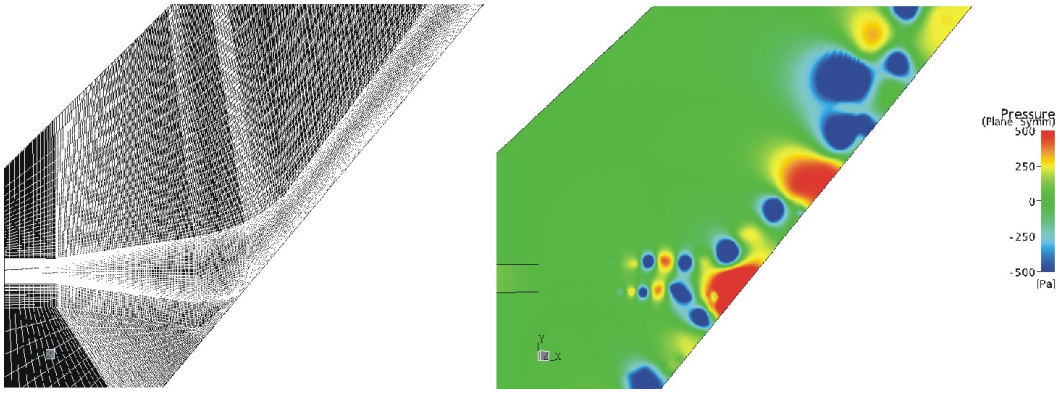

Figure 4.19: *Detail of LES domain topology (left) and instantaneous hydro-dynamic pressure field (right)*

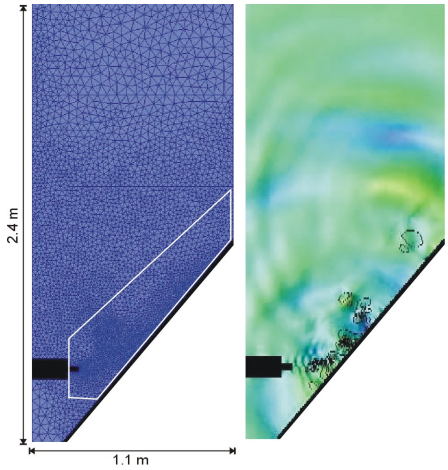

Figure 4.20: *LEE domain (left) and instantaneous result (right): pressure field (coloured background) and source intensity distribution (iso-lines). The polygon (white) shows the limits of LES-calculation domain.*

50°). One can see that the 2D decay-law is respected: ∼10 dB difference are expected and found between point P4 and the far field situated point, whose distance from the impinging point is ten times the distance to P4.

4.3 Conclusions

A complete computational aero acoustic method has been succesfully implemented in two dimensions: unsteady pressure and velocity fields calculated with a commercial CFD code (Ansys CFX) can be interpolated in time and space on (un)structured meshes for LEE computation, which can be much broader than the CFD one, saving calculation time.

The numerical result for noise generation of a plane jet is qualitatively confirmed from literature data. Moreover a qualitative comparison with laser interferometry has been sketched from the author in [99]. At this stage a quantitative comparison is still not possible because of the 2D acoustic simulation. In fact, due to the 2D propagation, the pressure intensity is overestimated intrinsically. Aeroacoustic sound sources have been

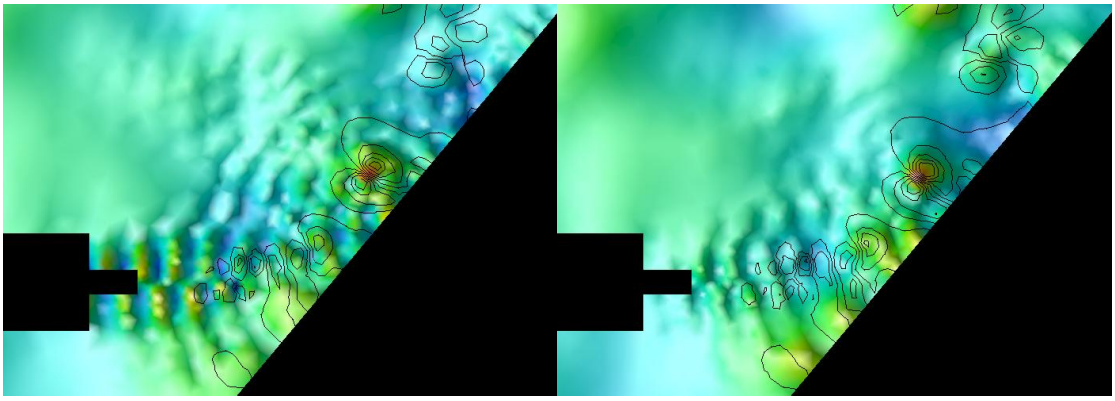

Figure 4.21: *Detail of an instantaneous pressure field near the impinging point calculated with LEE without time interpolation between LES-generated sound sources (left) and with a first order time interpolation (right): the high frequency numerical noise still exists but is damped.*

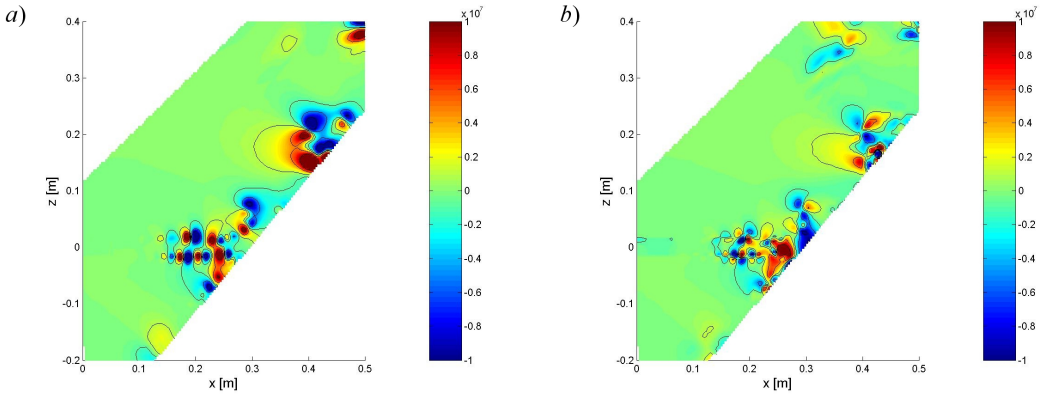

Figure 4.22: *Instantaneous distribution of acoustic sources with EIF-Method for M=0.30. a) source term $\frac{\delta p}{\delta t}$, b) source term including fluid convection. Iso-lines have the same value for both cases and are plotted at the same instant. The nozzle is not plotted*

localised with microphone array and laser interferometry as well. The localisation with microphone array is possible only trough cross correlation with reference microphones in far field and allows a rough localisation of the source. NAH could not improve the source localisation due to the turbulence originated in the impinging jet. On the other hand sound waves and turbulent structures can be visualised with laser interferometry, therefore the presence of sound sources, sound interferences and reflections can be effectively derived from it. Laser interferometry is therefore preferred for the investigation in the next section.

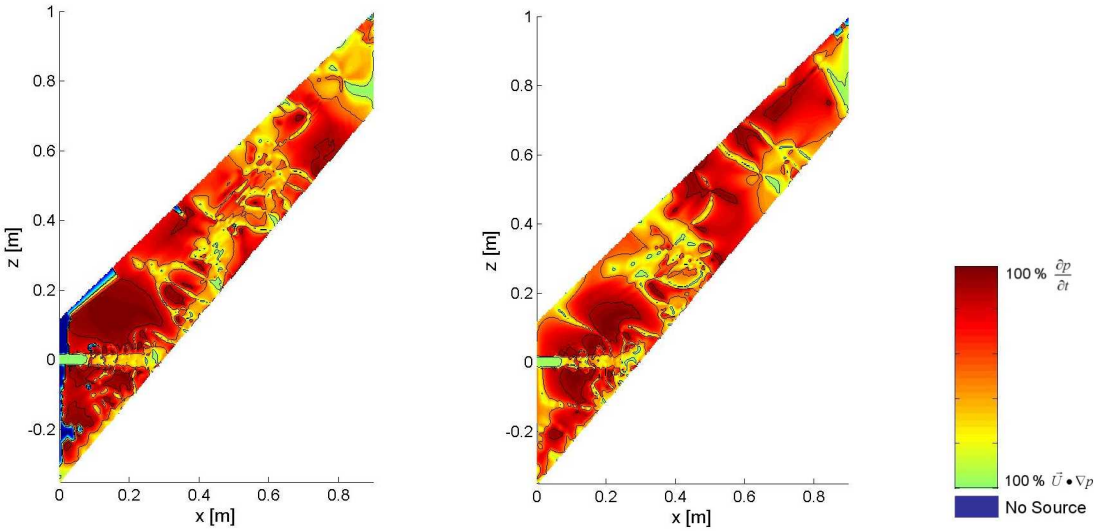

Figure 4.23: *Relative importance of source terms in EIF-Method at M=0.15 (left) and M=0.3 (right): only source term dp/dt (red), only convection term (green), no sources at all (blue). dp/dt is predominant away from the plate especially at the slowest speed. Pictures represent snapshots of the flow.*

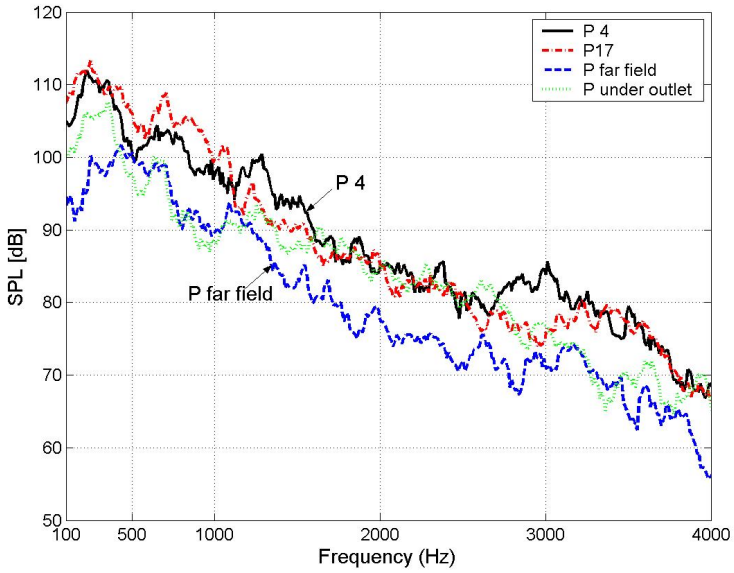

Figure 4.24: *SPL calculations with LEE for impinging jet (M=0.3,angle=50°) at four locations (based on 3872 LEE-outputs) (left). Only dp/dt is considered as source term. Spectra are plotted as moving average over 100 Hz width. P4 and P17 refers to the Y microphone location from Fig.4.6.*

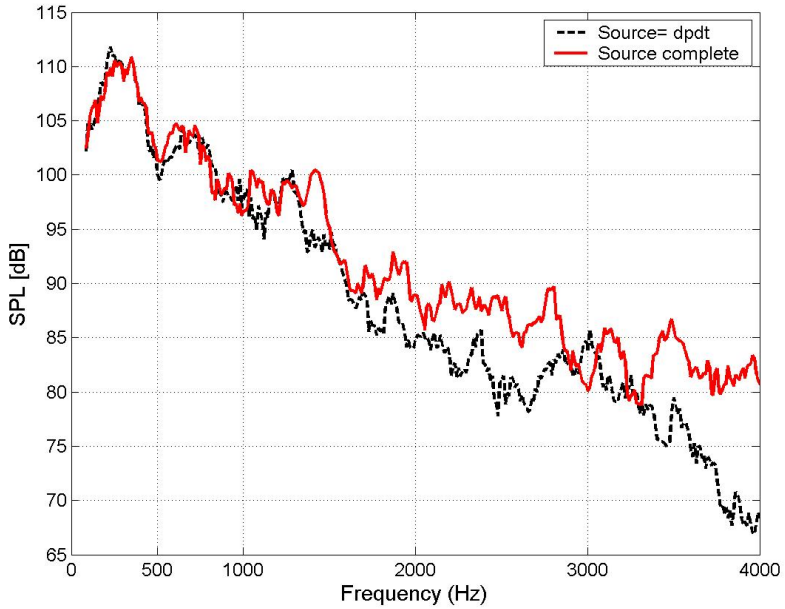

Figure 4.25: *Comparison between SPL spectra with different sources for the same Point (P4): with convection effects (solid line), without convection effects (dashed line). Plot with moving average over 100 Hz width.*

Chapter 5

Investigation of Impinging Jets on Obstacles

At the beginning of aeroacoustics in the fifties, investigations have been motivated from the application to aircraft jet engines due to the enormous acoustic impact on the population and on the aircraft structures as well. Since then, free jets at different Mach numbers have been largely investigated.

When a free jets impinges obstacles, it enhances the sound generation even more: very intense, dipole like, sound sources are generated [100],[101]. The sound produced is either tonal or broad band according to the Reynolds number of the flow, the threshold being dependent from the shape of the obstacle as well.

Example of impinging jets can be largely found even far outside the aircraft industry. We can classify these examples depending if the jet flows are functional or not: the first case occurs either in subsonic regime, for the convective cooling of surfaces like alternators-parts, cooling ribs, electronic units embedded in internal cooling flows or in supersonic regime, like for fluid injection in engines. The second case occurs in a more extended sense every time when components are embedded in an external flow. Examples from the automotive industry are, among others, bonnets, wind screen, screen wipers, rear mirrors and spoilers.

Since the acoustic comfort has assumed more and more importance for the customers, the aeroacoustic problems have assumed recently a central role in the industrial research. Therefore, since a few years, there is an increasing demand for reliable simulation methods for aeroacoustics.

Nowadays a large variety of numerical methods for computational aeroacoustics exist but they have been validated mostly only for academic purposes. Moreover, differently from free jets, the geometrical configuration of a impinging jets can be much more complex.

In this section we investigate the sound mechanism generation of impinging jets and perform comparison of numerical approaches for industrial application and extensive validation with experiments. We focus particularly the interest on broad band noise and attempt to understand the mechanism behind it, how to model it numerically and how to influence it.

Generally seen, one can distinguish flows according to the relative position of the observer (P) to the source and also with respect to the investigated geometry, as in figure 5:

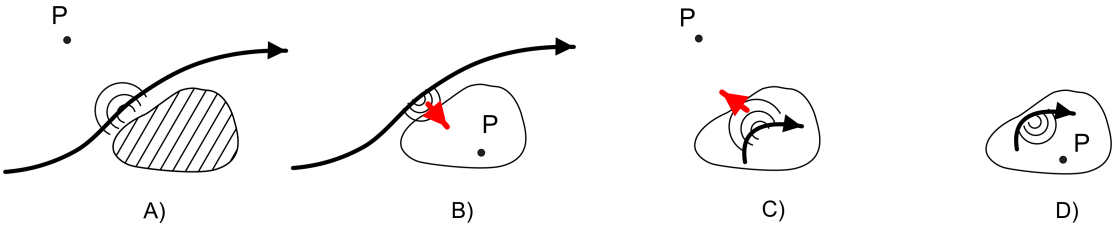

Figure 5.1: *Flow classification for aeroacoustic investigations. The red arrows shows a sound transmitting path through solid body.*

We distinguish first external flows (A, B) from internal flows (C, D). Moreover for flows of type B and C one needs the knowledge of the (sound) transmission function across the solid boundary. This is not the case for A and D. In this work we studied flows of type A because we aim to investigate the sound generation mechanism and not the transmitting properties of the environment.

The choice of the configuration to investigate in this work is motivated from a compromise: from one side geometrical simplicity due to the present limitation of numerical methods, from the other side possibility to extend the results to industrial configurations as previously indicated is looked forward.

In the next sections two configurations of a rectangular jet impinging an inclined plate with obstacles are investigated:

1. confined flow
2. unconfined flow

The flow is named 'confined' when the obstacle and the jet nozzle are partially enclosed in a channel. That is in oder to have a time averaged two-dimensional flow. the time averaged properties can be sufficiently considered two-dimensional. On the contrary the flow is named 'unconfined' when the flow is completely three dimensional and free to surround the obstacle on its sides. The confined case is investigated with a combination of 2D/3D numerical methods. Only in the second case a fully unsteady 3D CFD-CAA simulation was performed (LBM).

The choice of the obstacle geometries to be investigated and their position in the flow need to satisfy the following requirements:

- the geometry should be simple but idealise typical obstacles to be found in external flows of industrial interest
- the obstacle should be positioned on a surface and not isolated in a free infinite flow in order to reproduce typical industrial situation (wiper on a windshield or step in a channel)
- the geometry should be axial symmetric in order to allow both two and three dimensional computational modeling
- the air flow speed and the obstacle dimension should be compatible with the wind tunnel facility we set up (description in Chapter 2.1).

Our attention is therefore focused on small geometries with axial symmetry located on an inclined surface. Concerning the geometry we choose a basic shape (rectangular profile with sharp edges) and a profiled shape (wiper profile). The impinging flow has a mean velocity of 40 m/s and an environment temperature of 25°C. That corresponds to a Mach number of 0.12 and Reynolds number, related to the obstacle height, of about $4{\cdot}10^4$ (related to the nozzle height of $1.5{\cdot}10^5$).

Figure 5.2 shows the profiles and their idealised geometrical environment.

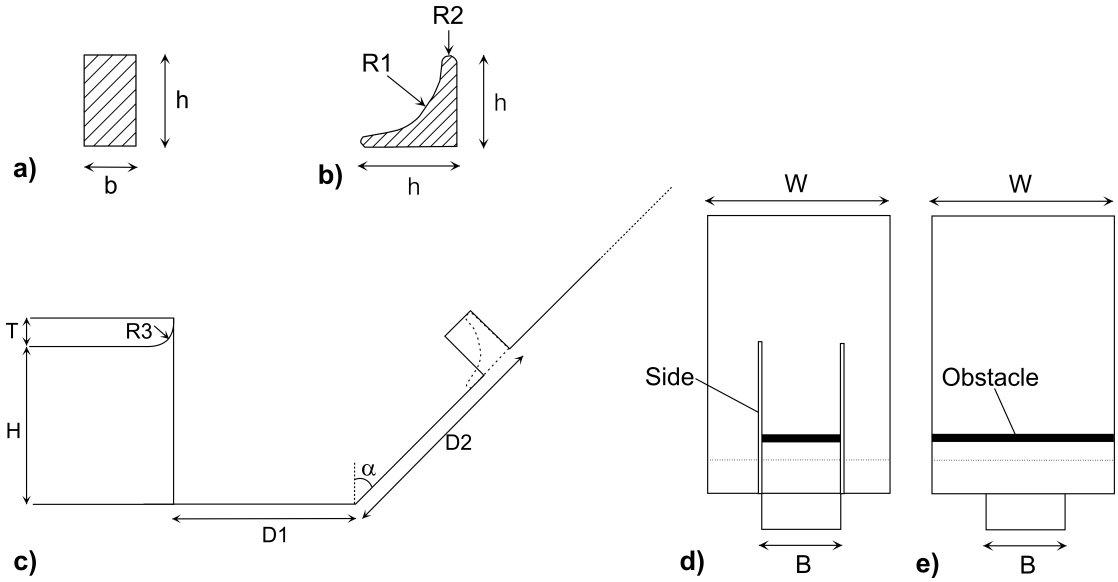

Figure 5.2: *a) rectangular profile, b) wiper profile, c) geometrical environment (profile), d) confined case and e) unconfined case (top view). h=15 mm, b=10 mm, R1=13 mm, R2=0.7 mm, R3=1.75 mm, D1=50 mm, D2=60 mm, H=50 mm, T=10 mm, B=200 mm, W=800 mm, $\alpha = 45°$.*

Choosing the length of the transition plane and the distance of the obstacles as indicated in Figure 5.2 (D1, D2), one recreates a complex impinging environment and reproduces the environment of the wind tunnel facility. The turbulence level of the impinging flow contains a thin shear layer from the nozzle and the boundary layer developing on the plate additionally to the uniform low turbulence level in background. Due the vicinity of the obstacle to the nozzle the impinging velocity and therefore the sound production are enhanced. This allows a better numerical and experimental investigation, because the ratio of useful signal to background disturbances is larger. On the other hand the outflow is perturbed from the obstacle itself. This last effect should be considered with care in the simulation and in the interpretation of the results. We refer therefore to chapter 5.1.4 to discuss how to handle this obstruction effect for aeroacoustic comparison of different configurations.

Figure 5.3 sumarises the numerical approaches that have been investigated and recall the conceptual calculation steps from the fluid dynamic field to the acoustic one.

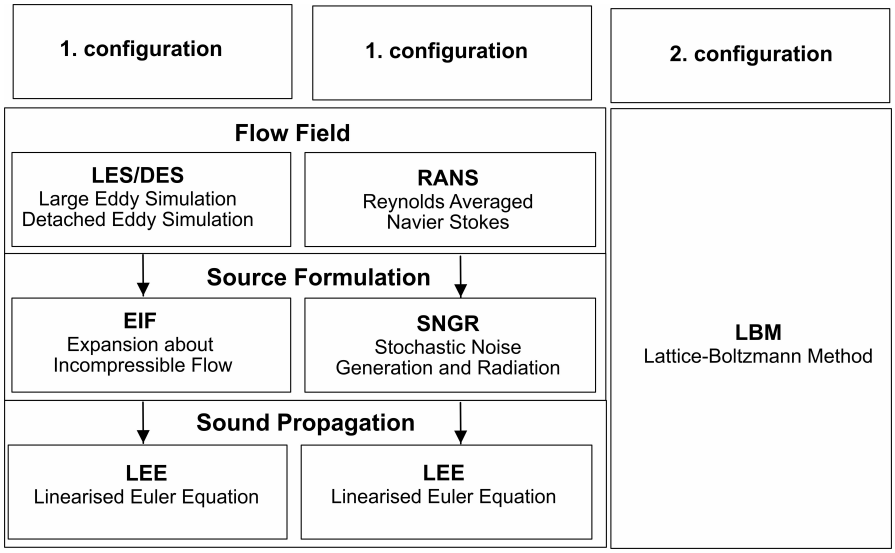

Figure 5.3: *Overview of CFD-CAA approaches and test-case configurations: 1= confined flow, 2= unconfined flow. DES + LEE (left), SNGR (centre), LBM (right).*

5.1 Inclined Plate with Obstacles (confined flow)

5.1.1 CFD Models

5.1.1.1 Domain

The discretisation of the domain depends on the chosen numerical methods. Due to the enormous computational effort for unsteady calculations, and profiting of the axial symmetry of the configuration, the numerical domain can be restricted to a thin slice of width L (Figure 5.4), the width being chosen larger than the characteristic length of the obstacle in order to model possible transversal flow correlations. The steady calculations have been performed in order to compare the mean properties of the unsteady calculation and to have data for the SNGR approach. The steady calculations are performed on the same domain or (for SNGR) on an even smaller thickness to reproduce a 2 dimensional calculation.

5.1.1.2 Mesh Properties

The topology of the mesh used for unsteady calculation consists of two parts: the inner, finely discretised mesh and the outer, coarsely discretised mesh. Table 5.1 gives the characteristic data, while figures 5.5 and 5.6 show the mesh overview and details of it. One notices different arts of interfacing the two mesh parts. By hanging nodes, the code interpolate linearly the solutions at the interface boundary. The purpose of this investigation is also to evaluate the effect of the interpolation.

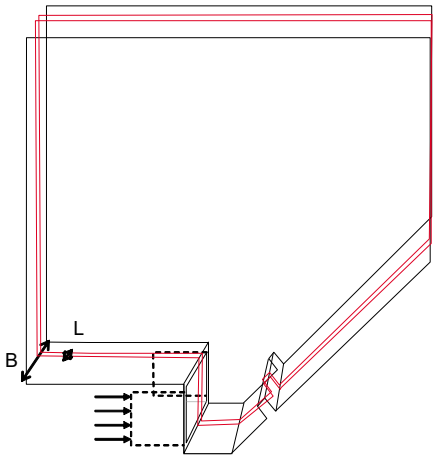

Figure 5.4: *Extension of the CFD domain(red) for the geometrical configuration (black). B=200 mm, L=20 mm. The inlet boundary condition is set before the nozzle outlet (arrows).*

Table 5.1: *Overview characteristic mesh data.*

obstacle	simulation	nTot[a]	nZ[b]	m_i[c]	m_o[d]	m_{type}[e]
rectangular	3D (un)steady	3 M	30	hexa	hexa	hanging nodes
rectangular	3D (un)steady	3.3 M	40	hexa	tetra	merged nodes
wiper	3D (un)steady	3 M	50	hexa	tetra	merged nodes
rectangular	2D steady[f]	0.1 M	1	hexa	hexa	-[g]
wiper	2D steady	0.1 M	1	hexa	hexa	-

[a]Total element number
[b]Element number in width direction (Z)
[c]Element type for inner mesh
[d]Element type for outer mesh
[e]mesh interface type
[f]for SNGR
[g]only one single mesh

5.1.1.3 Boundary Conditions

Inlet

The boundary conditions for the numerical model have been chosen to approximate the real experimental conditions. We anticipate here that the experimental inlet condition realised in the wind tunnel corresponds to a low turbulent flow (0.5-2%) with an undeveloped boundary layer (thinner than 2 mm). The previously anticipated obstruction at the outflow (Figure 5.11) should not be imposed but obtained from the numerical model. Therefore we impose as inlet boundary condition a simple velocity block profile (40 m/s) on a section located before the nozzle exit with a turbulence level of 2 %.

The location on the velocity block profile should not be too close to the nozzle exit in order to allow the obstruction effect to take place but also not too far away in order to reduce the domain extension and therefore the computational effort as much as possible and to avoid the growth of the boundary layer over the experimental expectation. Figure

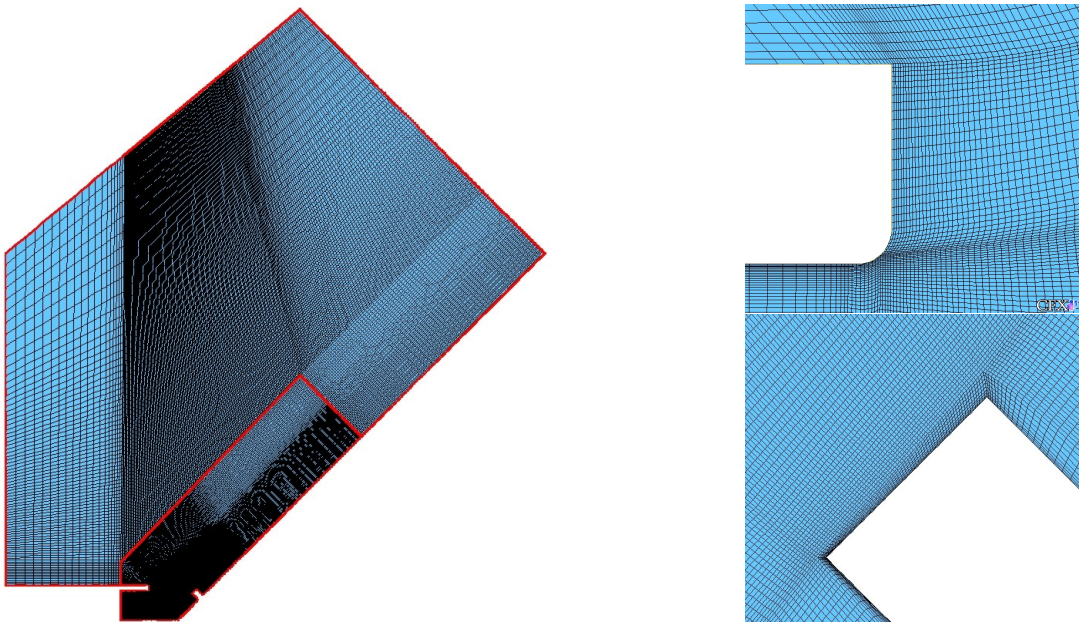

Figure 5.5: *Side view of the unstructured mesh used for the unsteady DES calculation (left). Two regions, which do not match, are interfaced along the inner red curve. Mesh details at the upper nozzle exit (right, above) and at the object top (right, below).*

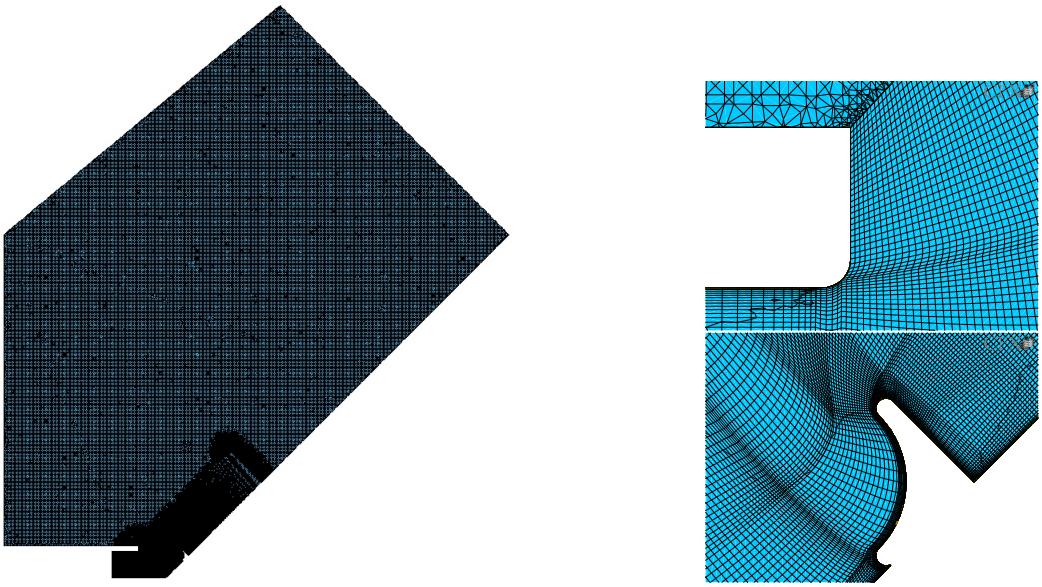

Figure 5.6: *Left: Side view of the unstructured mesh used for the unsteady DES calculation. The inner region with hexahedron elements is merged with the outer region with tetrahedron elements. Right: mesh details at the upper nozzle exit (above) and at the object top (below).*

5.7 shows this effect on the velocity profile at the nozzle exit setting a block profile at distance D=50 mm and D=100 mm. Due to the small effect we used the distance D=50 mm for further calculations.

Periodic or symmetry

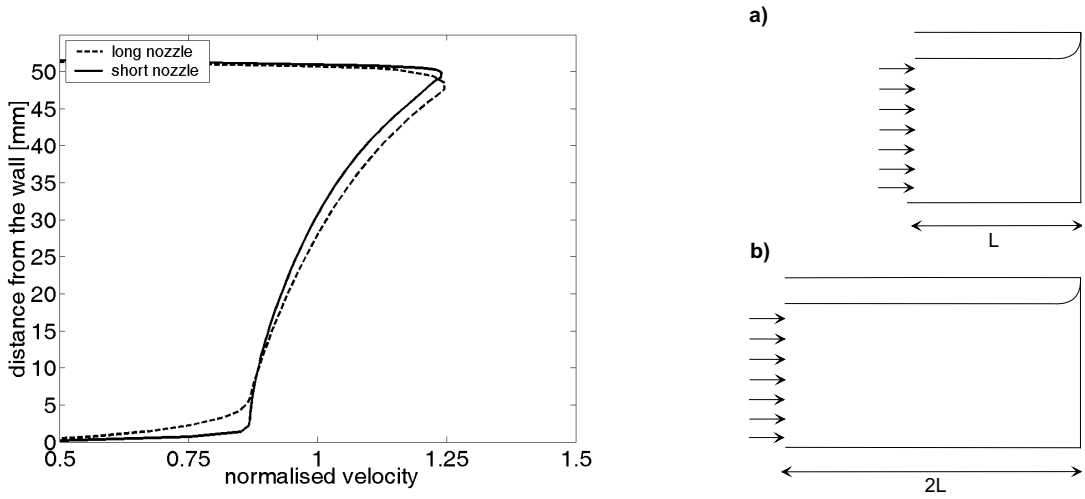

Figure 5.7: *Effect of the location of inlet boundary condition on the velocity profile at the nozzle exit. The short nozzle (a) has length L=50 mm before nozzle exit. The long nozzle (b) has length 2L=100 mm before the nozzle exit. The velocity is normalised to the velocity boundary condition set at the inlet (50 m/s).*

The steady calculations on the 2D domain use a symmetry boundary condition on the two sides. The unsteady calculations on the 3D domain use a periodic boundary condition.

Outlet or opening

The flow entrainment across the boundaries is simulated by setting opening conditions. This is implemented with total relative pressure = 0 for inflow condition and relative static pressure = 0 for outflow. Moreover for stability purpose the streamline direction is prescribed perpendicular to the boundary itself.

5.1.1.4 Turbulence Model

Unsteady calculation have been performed with the SST-DES zonal formulation implemented in the commercial code Ansys CFX 5.7.1 [102]. In the simulations, different settings of the DES switching parameter F (Section 3.2.1) have been analysed. The factor F1 promote a larger region where the turbulence is directly resolved (LES region) rather than modeled (SST-region) as one can see in Figure 5.8. Moreover, due to the non-uniform element size at mesh transition, local outgrowth of LES regions appears on the interface between hexahedron and tetrahedron elements.

A separation induced from the grid is not a concern for this geometrical configuration, because in the region of major interest near the obstacle, the flow separates anyhow due to the sharp edges. In this work we used the F2 factor for both geometries and additionally the F1 factor for the wiper-like obstacle in order to evaluate the effect of a more extended LES-region.

Steady calculations have been performed with the SST Model implemented in Ansys CFX 5.7.1 and with a classical k-ε Model implemented in Fire 8.31.

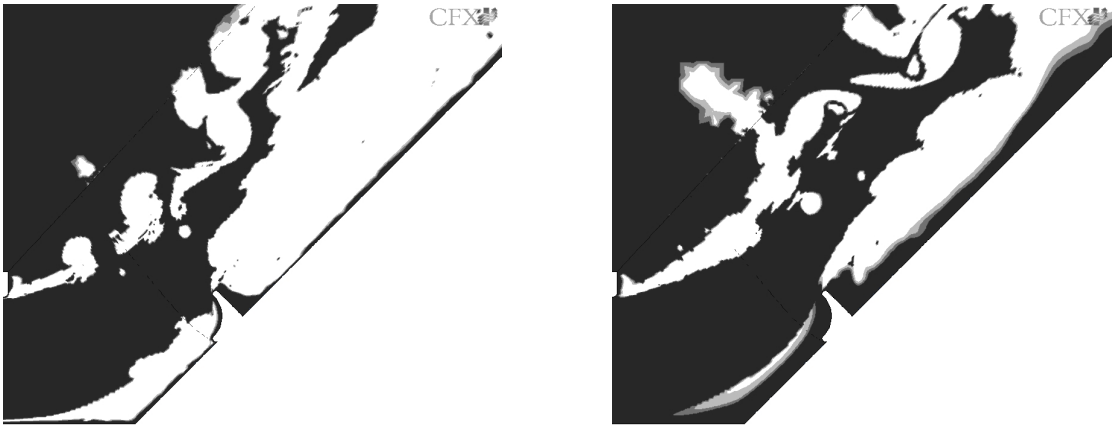

(a) (b)

Figure 5.8: *SST-DES Zonal formulation. Snapshot of domain splitting: LES region (white), SST region (black). The LES region obtained using the local grid scale factors F1 (a) is larger than that using F2 (b).*

5.1.1.5 Simulation Duration and Time Resolution

The time step of the calculation ranges around 10 μs (corresponding to a CFL-number of about 1.5). This can be increased, but up to 25 μs due to stability reasons. The unsteady flow needs time to develop after starting the calculation. We consider it completely developed after at least 10 vortices are shed and once the initial vortex are convected away from the obstacle (5-8 ms). The calculation is continued for a further 5 or 10 ms with a output data sampling frequency equal to 10 and 20 kHz respectively for the rectangular and wiper-like obstacle. The total computational effort corresponds to 1000 CPU-hours (wiper profile) on Linux-Cluster (Pentium 4 XEON, 2.8 GHz, 4 GB Ram).

5.1.2 CAA Models

Mesh

The discretisation for the acoustic calculation is chosen with the aim to resolve wave lengths up to about 3000 Hz. Two meshes of various refinement were used. Figure 5.9 shows them. Simple opening boundary conditions have been used, therefore multiple layers of coarse cells were necessary around the domain, in order to reduce reflections by increasing the local numerical dissipation.

Numerical Method

The acoustic pressure level calculated with 2D LEE code can not be directly compared with experiments due to the 2D instead of 3D propagation. The acoustic pressure perturbation have in two dimension bigger intensity than in a three dimensional free space and decay more slowly: the SPL-decay-law for a point source in 2D far field is $SPL_2 = SPL_1 - 10 \cdot \lg(\frac{d_2}{d_1})$ instead of $SPL_2 = SPL_1 - 20 \cdot \lg(\frac{d_2}{d_1})$ for 3D far field, being d_2 and d_1 the distances from the source. We subsequently use a correction strategy for trailing edge noise from Ewert et al.[104].

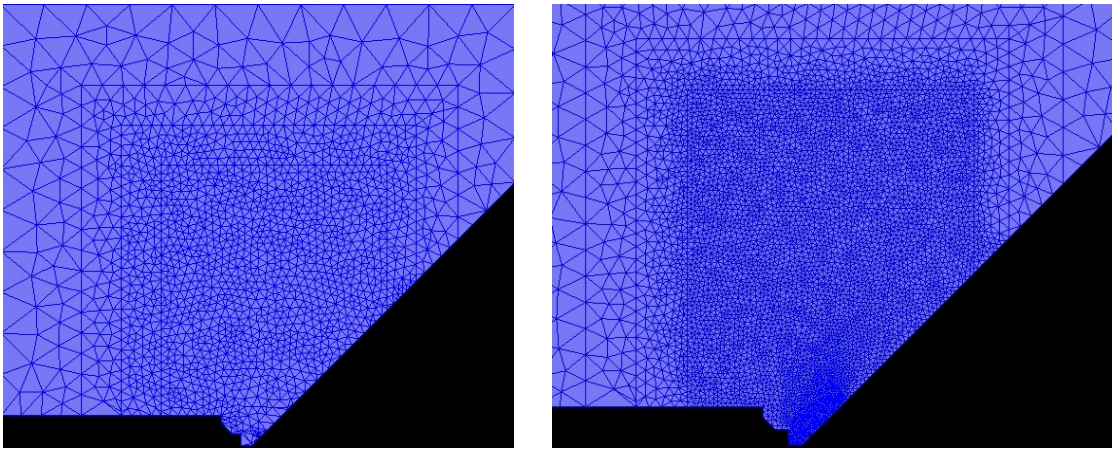

(a) coarse (b) fine

Figure 5.9: *2D acoustic meshes : a) 3K elements with size between 10 and 50 mm in the source region and 50 mm outside, b) 12K elements with size 8 mm in the source region and 20 mm outside. Both meshes present very big sized elements on the border to reduce waves reflections.*

Using a span-wise averaged acoustic source from the unsteady calculation on a full 3D domain slice, the sound pressure correction from 2D to 3D becomes according to Ewert et al. [104]:

$$SPL_{3D,L} = SPL_{2D} + 10\log(\frac{fL^2}{Rc_0}) \tag{5.1}$$

with f the frequency, L is the slice width calculated with DES (Figure 5.4), R the distance of the observer from the source and c_0 the sound speed at rest.

The correction is derived from a Green function for a distribution of correlated point-like sources along an infinitely long transversal direction compared to the acoustic solution for a point source in 2D.

Moreover, for a finite span-wise B (Figure 5.4) the correction given by Kato et al. (1993) is used where all slices of width L are supposed uncorrelated and therefore bring 3 dB SPL increment each doubling.

$$SPL_{3D,B} = SPL_{3D,L} + 10\log(\frac{B}{L}) \tag{5.2}$$

The author sees following shortcomings of this strategy:

- the Green function is derived, considering first the sources correlated on a infinite direction while later are supposed stepwise uncorrelated with each others
- the size of the resolved slice (L) influences the correction
- the correction is valid only for the acoustic far field .

SNGR Source Definition

Each point of the turbulent field contributes differently to the acoustic energy content. The value of the turbulent kinetic energy alone is not enough to estimate the contribution, as long as positive or negative interferences can occur. Within the SNGR approach, however we defined a threshold for the turbulent kinetic energy, under which we assume that the contribution to the total acoustic energy is negligible.

$$K_{threshold} = \alpha * K_{max} \tag{5.3}$$

The acoustic sources are then calculated only for the regions where the turbulent kinetic energy is larger than this threshold. By reducing in this way the extension of the significant stochastic velocity field, one reduce considerably the calculation effort.

5.1.3 Experimental Setup

Figure 5.10 shows the investigated geometrical configuration. The plexiglass sides confines the flow and make it accessible to optical measurement systems.

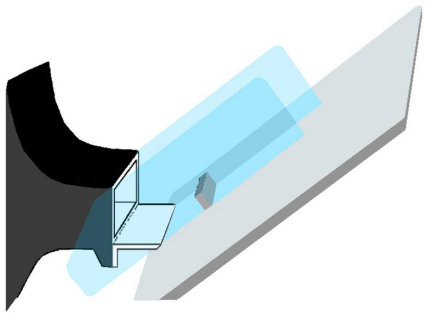

Figure 5.10: *Configuration with rectangular obstacle.*

Figure 5.11 shows experimentally the obstruction effect at the nozzle exit: the outflow mean velocity is strongly reduced from the inclined plane and from the object. The shape of the obstacle does not change significantly the mean velocity profile at the nozzle outlet as the differences of the averaged profiles are smaller than the measurement deviation. On the other hand, once the flow is confined, the outflow velocity is slight reduced in the lower part of the nozzle section (till -3%).

Hot Wire Anemometry

The measurements are carried out with a single probe hot wire[1] used in cross-flow mode, constant temperature, with a working temperature of 250°C. The calibration curve (obtained with environment temperature of 24°C) was not corrected with the flow temperature of the wind-tunnel because the temperature excursion is limited to ±1 °C thanks to the wind-tunnel heat-exchanger and the warm-up and cool-down phases before measurements begin. The positioning of the probe is manual with an absolute

[1] platined miniature probe DISA type 55P11 and 55P15

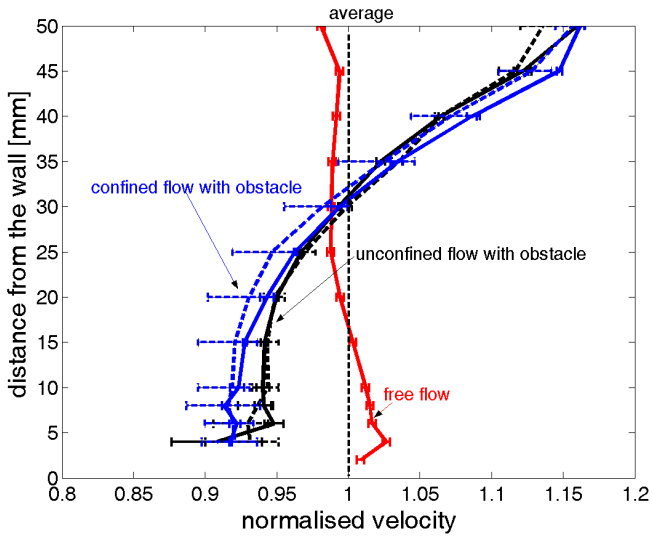

Figure 5.11: *Obstruction effect on the nozzle outflow due to obstacles measured with single probe hot-wire anemometry (DISA probe type 55P11). The velocity is normalised with the mean free flow velocity which would produce the same mass flow (vertical dashed line). The outflow without obstacles (free flow, red solid line) shows deviation from the ideal block profile (vertical dashed line) of ±2.5%. The measurements for flow with obstacles are repeated 4 times with manual positioning of the probe and on different days for each geometry: rectangular shape (solid line), wiper shape (dashed line) for confined flow (blue lines) or unconfined one (black lines). The horizontal error bars show the maximal deviation between measurements (±3%).*

location error of ±1 mm. Probes are positioned in the main flow with an angle error with respect to the calibrated flow direction, of ±10 % compared to estimated time averaged streamlines. See figure 5.12 for details. The signal is acquired with Dactron RT pro 5 (sampling frequency f_s= 24 kHz). The measurements were repeated at least 3 times for each section with independent repositioning of the probe during different days.

Laser Doppler Anemometry

The measurement are carried out with a two-channel LDA[2], with a nominal Power of 400 mW. The output power at the probe amounts to about 10 mW for the green beam and about 20 mW for the blue one. In order to scatter the laser light, the flow is seeded with small particles ($\oslash 1\mu m$) of Di-Ethyl-Hexyl-Sebacate ($C_{26}H_{50}O_4$) generated from an atomising seeder and introduced inside the flow with two pipes some 60 cm before the nozzle exit (Figure 2.3). The purpose of the measurement with LDA is mainly the determination of the turbulence kinetic energy of the flow but also the supplementary validation of the velocity measurements with hot wire anemometry.

The two beams are positioned to measure velocity components on the symmetry plane of the test case. The measured turbulence kinetic energy can only be determined from the velocity fluctuations in x and y. Therefore the measured turbulence kinetic energy is an underestimation of the actual physics. The underestimation depends largely from

[2]Digital burst correlator TSI IFA 755, Beam separator TSI 9201

the local turbulence type. In isotropic regions (far away from the obstacle or between shear layers) the mean square fluctuation is, by definition, equal in all space direction. Therefore the underestimation is maximum and reaches 50 % of the measured value. On the other hand, in strongly anisotropic regions (e.g. near the wall or free shear layer) the limit is a two component turbulence so that the perturbation transversal to the plate tends to zero. In this case there would be no underestimation. The measurement results, plotted in figure 5.17, are done so using only the raw data without any assumptions on the turbulence type.

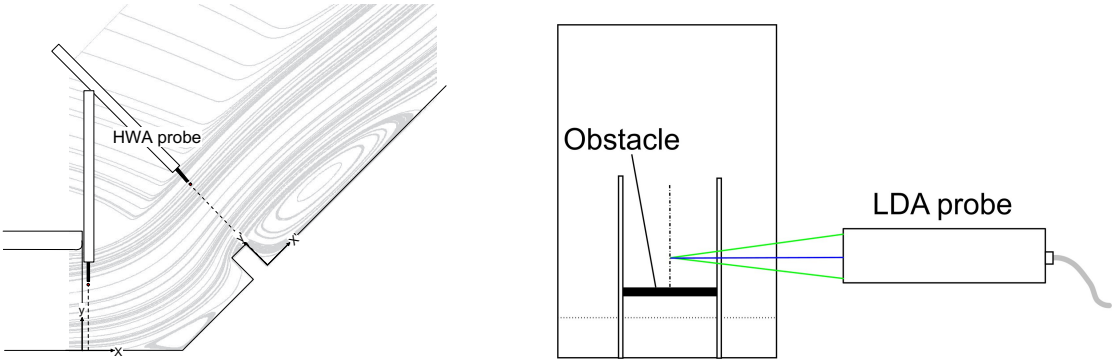

Figure 5.12: *Positioning of the measuring techniques: single probe HWA (left) and two-component LDA (right). The time averaged streamlines calculated with SST model are plotted in gray on the background as reference.*

5.1.4 Results

As previously introduced, the obstruction effect at the nozzle exit due to the obstacles represents an increase in the complexity of the the geometrical configuration. Before we extensively compare the calculation results to the measurements, we want to assure that at the nozzle exit the mass flow and velocity profiles correspond to the expected ones. Figure 5.13 demonstrates that: The obstacle shape has no effect on the velocity profile. The measured mass flow differs from the calculated one (0.40 m^3/s) by less then 2% that is within the experimental accuracy.

5.1.4.1 Velocity and Turbulence Fields

A first impression of the velocity field around the obstacle is given in figure 5.14 for the rectangular test case. Here one notices a qualitative global good agreement between the time-averaged unsteady solution with the steady one but also few differences in the separated region behind the obstacle.

For a detailed comparison, the flow mean properties are investigated at several sections before and after the obstacle as indicated in the figure 5.45.

Figures 5.16 compare the velocity profiles for both test cases on the previously described sections. The agreement of steady numerical results to the experiments is excellent, typically less than 2 % in the low turbulence region. The calculation with the k-epsilon model in the code shows overly entrainment outside the main flow. The reason seems to be the implementation of the boundary condition. Although the number of samples for the unsteady calculation is small (100) the profile follows the measured profile quite

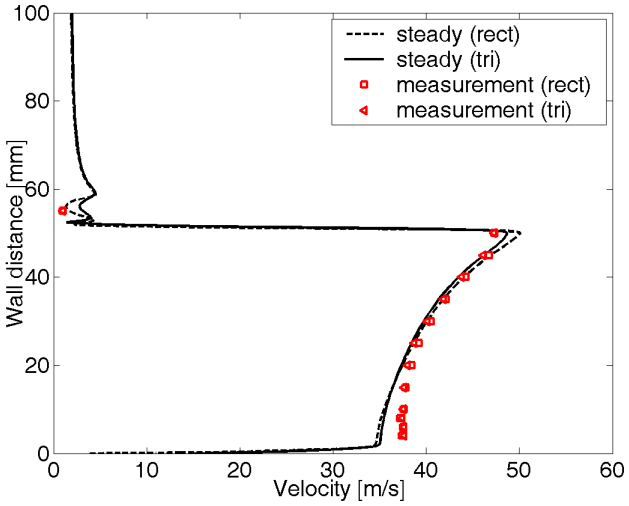

Figure 5.13: *Comparison of the velocity profiles for rectangular (rect) and wiper-like (tri) obstacle on the symmetry plane at the nozzle exit. Measurement with single probe hot wire anemometry. CFD steady calculation with SST turbulence model.*

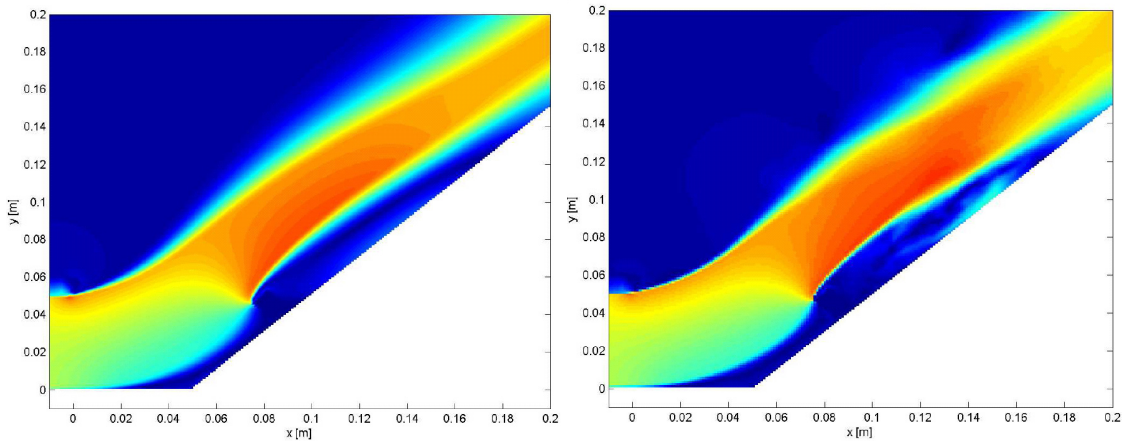

Figure 5.14: *Field of velocity magnitude around the rectangular obstacle calculated with RANS-SST (left) and average of 100 time steps with DES (right). The post processing with Matlab shows the obstacle and the regions with zero velocity in darkest blue.*

well. Only the section 100 mm after the wiper-like obstacle shows an unexpected shift of the velocity profile by about 1 cm in the direction perpendicular and away from the plate. By using different parameters for the DES zonal formulation F1 and F2 one notices differences in the splitting between solved and modeled regions (5.8) but this seems not to influence the shifting significantly (Figure 5.16).

Figures 5.17 compare the profiles of turbulent kinetic energy for both test cases on the previously described sections. The unsteady calculation shows much more turbulence than that measured especially in the numerical configuration for the wiper geometry. On the other hand, the unsteady calculation shows more realistic diffusive behavior between the shear layers.

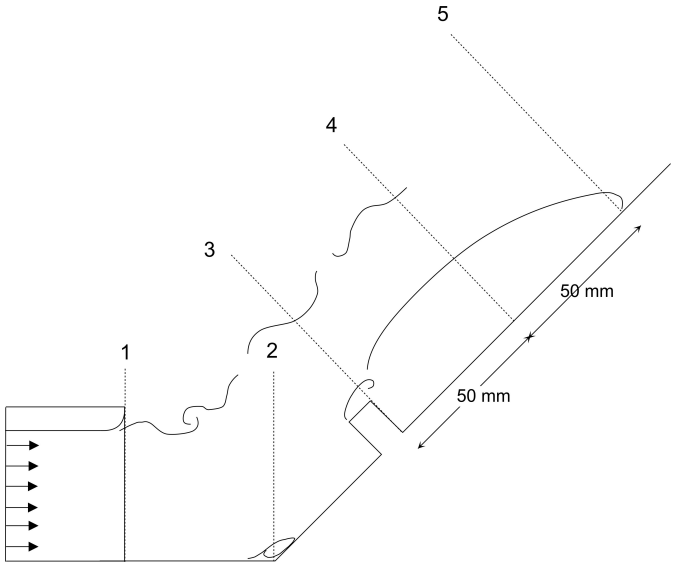

Figure 5.15: *Sections used for the comparison of the velocity field and turbulent kinetic energy between calculations and experiments. The separation regions of interest are sketched overlapped.*

DES

The vortex shedding at the nozzle edge gives information about the dynamic accuracy of the unsteady simulation. We distinguish a forced shedding from a natural one, depending on whether external causes trigger the separation at the nozzle edge. For a natural shedding one expects a non-dimensional shedding frequency of around St=$\frac{fD}{U_\infty}$ = 0.25, which is approximately f= 200-250 Hz for our test case. A more precise value and dependency on Reynolds number can not be derived from the literature due to our particular nozzle configuration (rectangular one with only one edge not confined).

A forced shedding can be induced in a wide frequency range for instance from an external or self produced strong sound wave. Experimentally (with Laser Interferometry) a trigger from flow-induced sound waves is not noticed. Figure 5.18 compares the experimental[3] and numerical [4] power spectral densities of the velocity signal at several points in the nozzle shear layer.

The nozzle vortex shedding should not depend on the obstacle form but the position of the shear layer could be influenced from it. That is experimentally shown. On the other hand, the calculated shedding frequency presents large differences between them and, particularly for the rectangular obstacle, compared to the experiment. We assume that the mesh topology is the cause because, although the domain extension is exactly the same, a grid interface near the nozzle is present for the calculation with rectangular obstacle. To demonstrate that, the rectangular profile has been further calculated with a perfectly merged grid like in the wiper case. Figure 5.19 shows that the shedding frequencies are different from the previous calculation and this time much similar to the wiper-case.

[3]HWA measurement with single cross flow probe TSI 1212-20 and a separate thermocouple in the back-stream.

[4]Absolute PSD values of experiments and calculations can not be directly compared as different sampling frequency have been used.

Changing the parameter for the DES domain splitting has no effect on the vortex shedding. As already noticed (Figure 5.8) the domain decomposition near the nozzle is unchanged. The frequency analysis in Figure 5.20 confirms this, the main frequency localised at around 250 Hz. A better accuracy in the comparison can not be discussed due to the relative small amount of samples.

As long as the fluid can be considered incompressible we expect that velocity spectra and pressure spectra exhibit the same behavior and, particularly, the same maxima location (that is strictly correct only for irrotational inviscid flow). For that reason we use the laser-scanning interferometry to compare the frequency content of the pressure fluctuations over the whole domain.

Figure 5.21 shows a relative wide frequency spectrum for the vortex shedding behind the nozzle and obstacle. As expected, the frequency of hydrodynamic structures decreases downstream. Moreover the shear layer from the nozzle shows large amplitudes only for low frequencies (225-700 Hz). These results with laser-scanner interferometry support the previously shown spectra of Figure 5.18.

An analysis of the vortex structures calculated with DES shows vortex shedding from the nozzle and collapsing into bigger coherent structures. The recirculating bubble where the plane changes slope generates turbulence which is convected and impinges on the obstacle. Moreover one sees fine scales structures interacting with the plate after the object, each one with its own rotational direction. The whole region than rotates almost like a rigid body and is slowly convected (at few meters per second) along the plate.

Figure 5.22 shows a snapshot of these vortex structures. The vortex structures generated at the nozzle are very coherent and almost two dimensional. No difference is noticed with changes in the local grid size, discretisation time or number of elements in the width direction. On the contrary the vortex structure induced from the separation at the obstacle features typical longitudinal and transversal small scales structures with highly rotational component (Z-Vorticity in Figure 5.22). Moreover the vortex structures behind the rectangular shape are extremely elongated and not compact as those behind the wiper. That agrees also with the separation length simulated with RANS (Table 5.4).

No difference is qualitatively noticed using the two parameters for domain splitting with DES.

rectangular profile

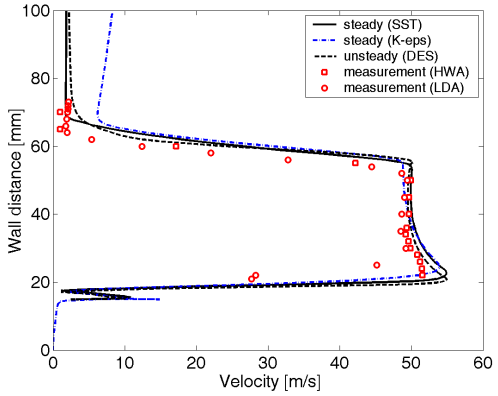

wiper profile

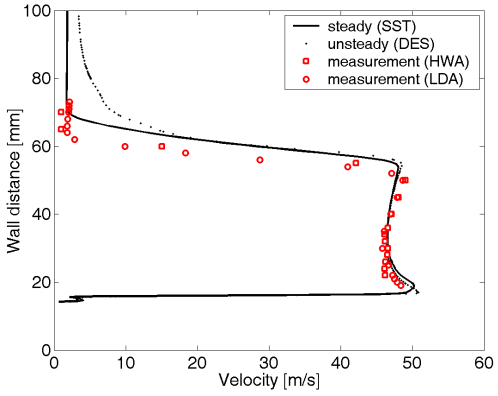

Section 3

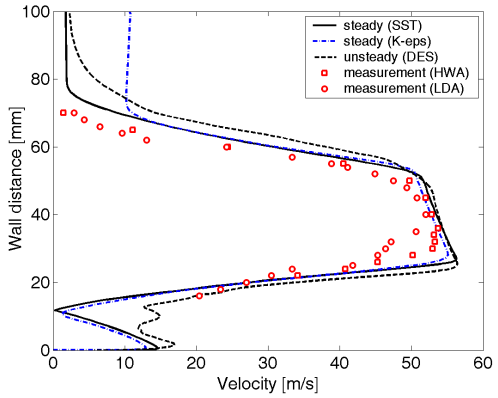

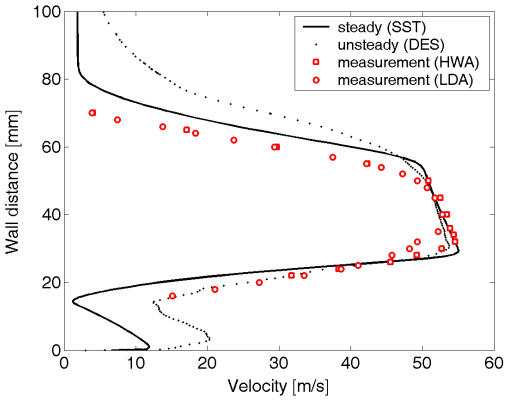

Section 4

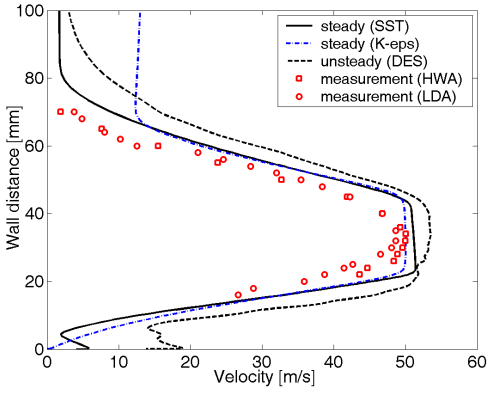

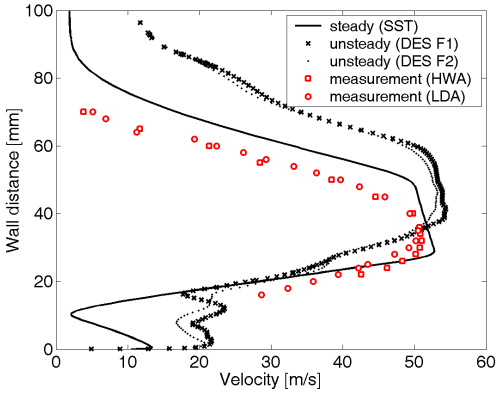

Section 5

Figure 5.16: *Comparison of velocity profiles, for the rectangular obstacle (left) and the wiper-like one (right) on the symmetry plane at sections 3-5 of Figure 5.45. Measurements with single probe hot wire anemometry (HWA) and two-component (in-plane) laser Doppler anemometry (LDA) (samples number $\geq$ 5000). DES averaged on 100 samples.*

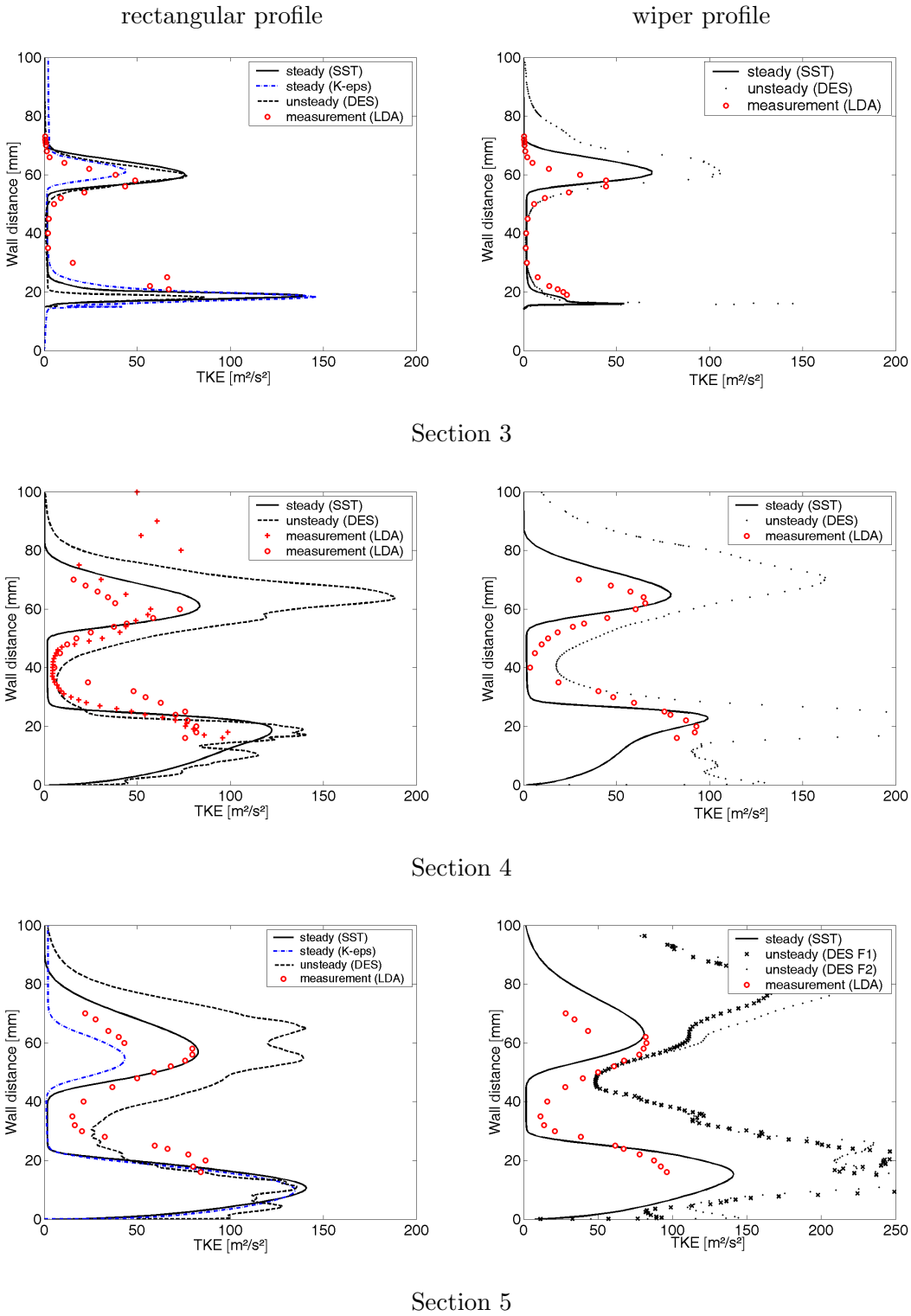

Figure 5.17: *Comparison profile of turbulent kinetic energy for rectangular obstacle (left) and wiper-like one (right) on the symmetry plane at sections 3-5 of Figure 5.45. Measurements with two-component (in-plane) laser Doppler anemometry (LDA) (number samples $\geq$ 5000), DES averaged on 100 samples with sampling frequency f_s= 20 kHz (rectangle) or 10 kHz (wiper)).*

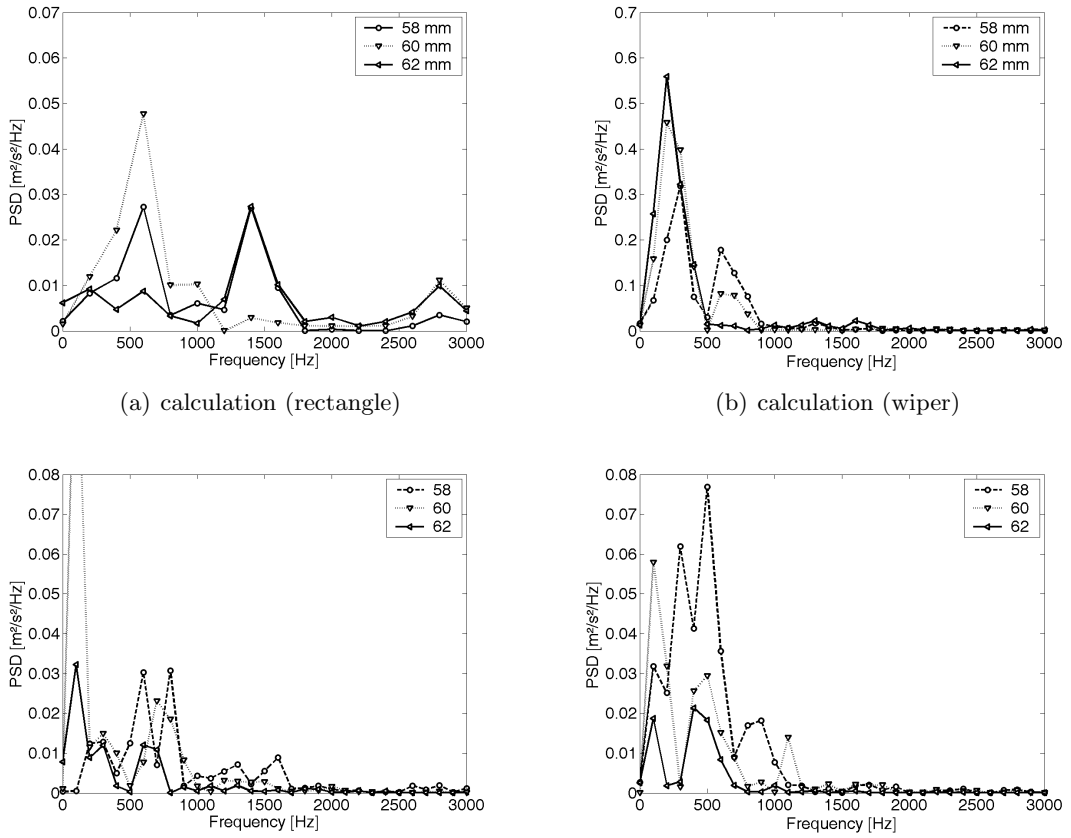

(a) calculation (rectangle)

(b) calculation (wiper)

(c) experiment (rectangle)

(d) experiment (wiper)

Figure 5.18: *Power spectral density (PSD) of the velocity in the nozzle shear layer calculated with DES-F2 Model (above) and measured with HWA (underneath) for rectangular geometry (left) and wiper-like one (right). Hanning window over complete recording time (5-10ms for DES, 1s experimentally). Experimental frequency resolution reduced to the numerical one for comparison with constant frequency band $\Delta f = 100$ Hz. PSD calculated with periodogram.*

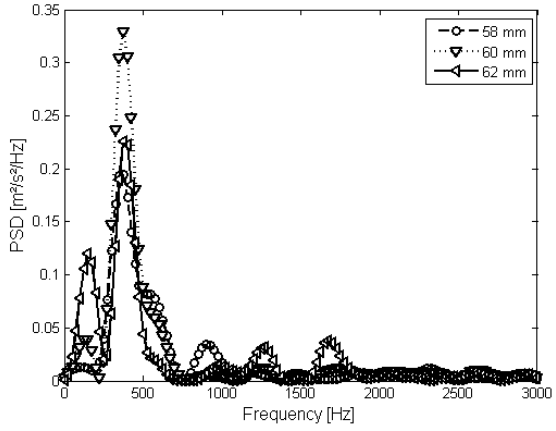

Figure 5.19: *Power spectral density (PSD) of the velocity in the nozzle shear layer for rectangular profile calculated with a perfectly merged grid.*

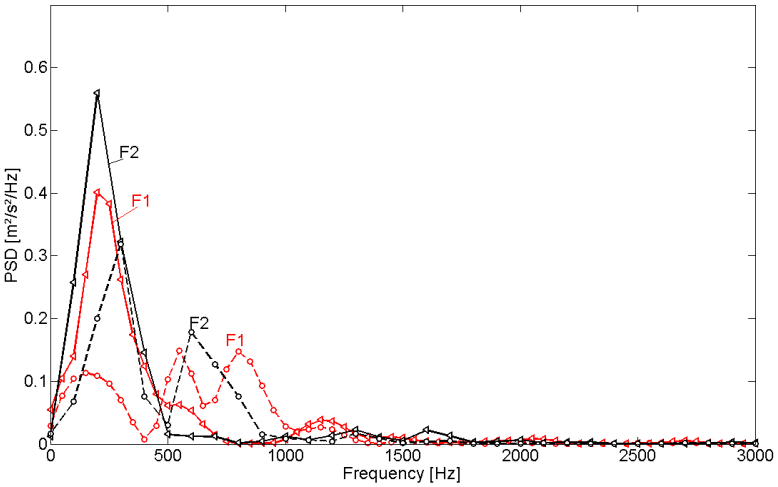

Figure 5.20: *Comparison between the velocity spectra calculated with DES in the region of vortex shedding. The curves show the effect of both parameters (F1,F2) at respectively two positions near the top of the nozzle. Number of samples/sampling frequency : 180/20kHz (F1), 100/10 kHz (F2). Hanning windowing.*

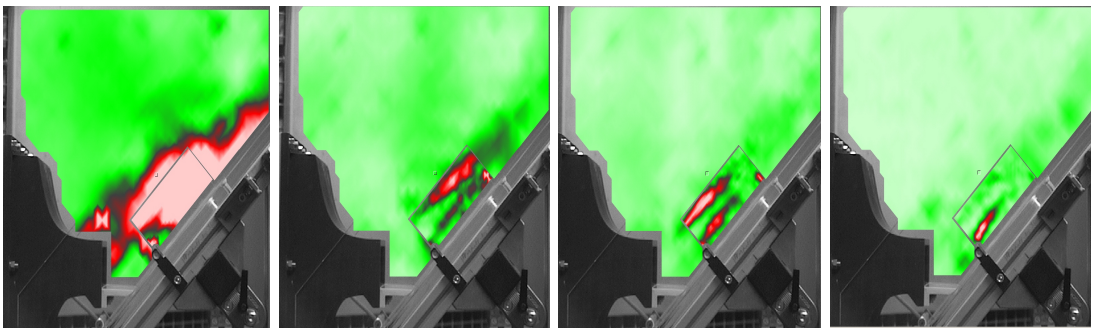

(a) 225 Hz (b) 450 Hz (c) 700 Hz (d) 1750 Hz

Figure 5.21: *Root mean square values of the pressure fluctuations made visible with laser interferometry for different frequencies, for a confined flow with rectangular obstacle. The variable plotted is the effective velocity. Iso-surfaces with same intensity are plotted in colors. Light red contours correspond to high levels of 5 $\mu m/s$.*

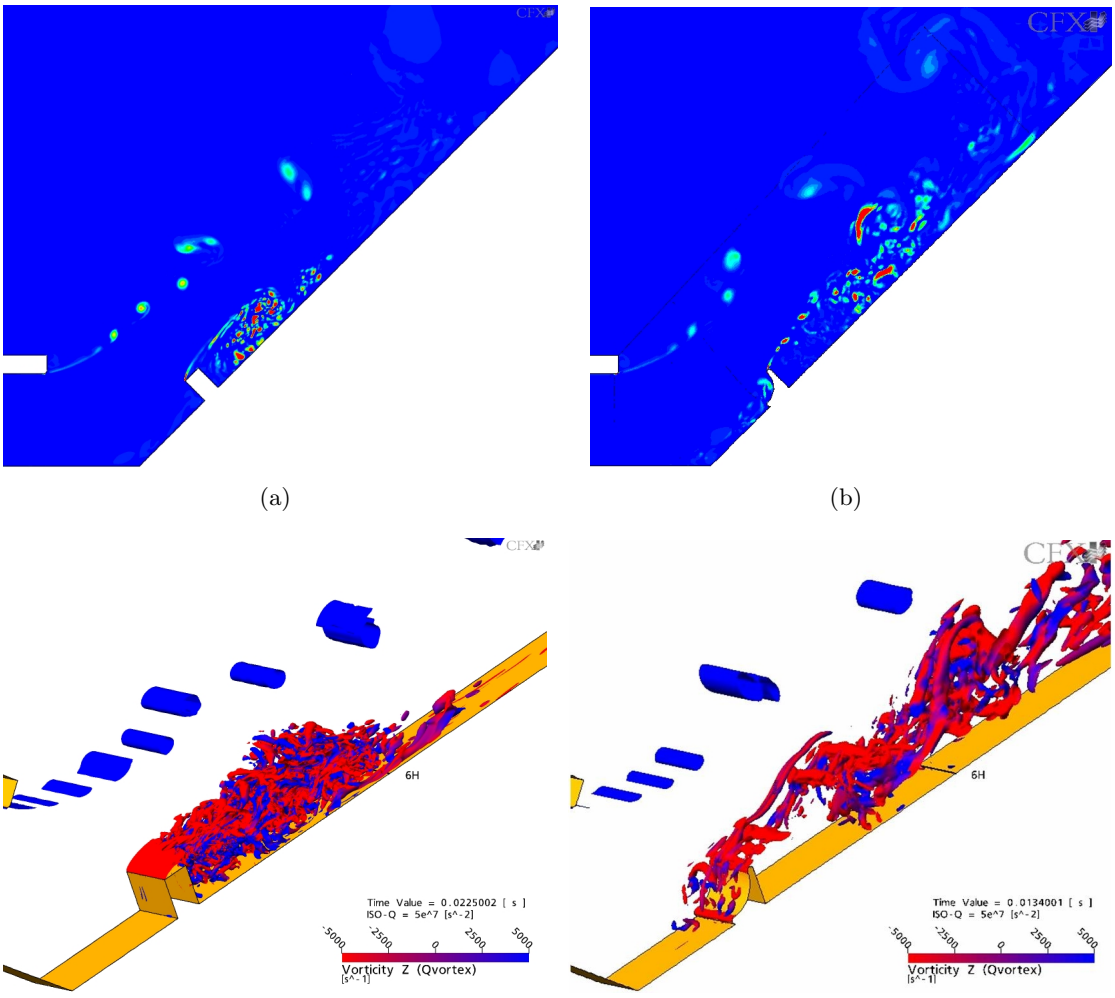

Figure 5.22: *Instantaneous snap-shot of vortex structures calculated with DES. The intensity of vortices is color coded for rectangular (a) and wiper profile (b). Iso-surfaces of stronger vortices ($5 \cdot 10^7 s^{-2}$) are plotted with color coded direction of rotation: red(clock-wise) and blue(anti clock-wise) for rectangular (c) and wiper profile (d).*

SNGR

We first compare the time integral scale of the velocity field calculated with RANS with those generated with SNGR (Section 3.3.3) in order to validate the data for the acoustic simulation.

Figure 5.23 shows the time scale for the rectangular test case, as derived from RANS calculation[5] (Section 3.3.3). Table 5.2 summarises the time scales at some points calculated with different RANS models and measured with HWA[6]. One notices, as expected, that the time scales increase flow downstream. Both models are equivalent and in relative good agreement with the measurements.

Using an own SNGR implementation[7] based on the same calculation (RANS-SST) one obtains a synthetic field, whose autocorrelation time is very similar to the calculated time scales. From figure 5.24 one reads for point 1 and 5, T=0.2 ms and T= 2 ms respectively.

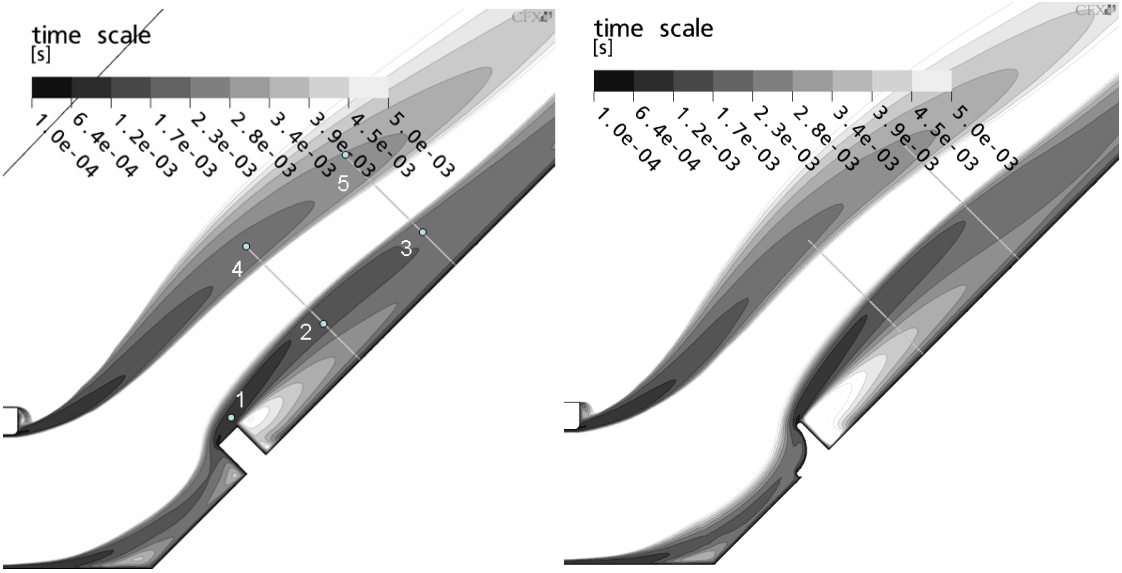

Figure 5.23: *Time scale ($\tau = \frac{k}{\epsilon}$) calculated with RANS-SST Model . Rectangular profile (left) and wiper profile (right).*

Table 5.2: *Comparison of time scales [ms] for confined jet impinging on wiper profile. Measurement with single probe hot wire anemometer. The measured time scale is the integral time scale calculated from the autocorrelation of the velocity signal.*

Point Number	Measurement (HWA)	RANS-SST (CFX)	RANS k-ϵ (Fire)
1	-	0.5 ms	-
2	0.5 - 3 ms	0.7 ms	0.8 ms
3	2.4 - 4 ms	1.3 ms	1.4 ms
4	1 - 1.4 ms	1.5 ms	1.3 ms
5	1.1 - 1.7 ms	2 ms	1.8 ms

[5]CFX; RANS-SST Model

[6]HWA is indicated for the measurement since all the locations are outside the reversed-flow region.

[7]3D, stand alone code with implementation of classical method (Section 3.3.2).

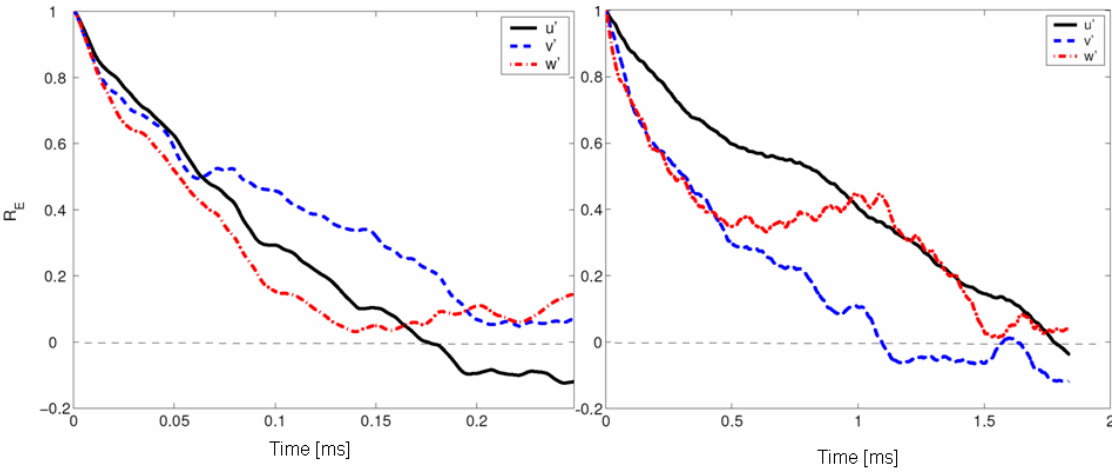

Figure 5.24: *Autocorrelation coefficient (R_E) for the velocity at point 1 (left) and 5 (right) for rectangular profile calculated with own implementation of SNGR method (RANS-SST Data)*

Besides that, the synthetic field shows statistical properties very similar to the isotropic field, as one can see from table 5.3. See Annex B.2 for the definition of the statistic moments and the properties of an isotropic field.

Table 5.3: *Statistic moments of synthetic velocity field at few sample points. SNGR with 500 modes and 20000 time samples. U is the time-averaged local speed and k the local turbulence kinetic energy.*

point number	(m1-U)/U	(M2-k)/k	skewness	flatness
1	2%	8%	-0.2/-0.6	2.9
3	5%	2%	-0.2/-0.9	2.4-3.1
5	5%	9%	-0.4/0.4	2.0-2.3

5.1.4.2 Separated Flow Regions

Figure 5.25 shows the typical separation bubbles which take place around the test objects at high Reynolds numbers using the rectangular profile for exemplification. For the rectangular object, along with the main region (C) with clockwise recirculation there is also an induced minor one (B) with anti-clockwise motion. Furthermore a minor region (A) in front of the object arises due to the high static pressure increase caused from the object. For the wiper the small region A is not detected.

Figure 5.26 shows the experimental result for the investigation of the separation lengths. Table 5.4 summaries and compares the numerical results and the experiment results. These results matches quite good.

5.1.4.3 Sound Pressure Level and Spectra

Figure 5.27 shows the location of the microphones used in the following measurements. For comparison between calculation and experiment, if not otherwise specified, one takes the orthogonal position (90°) on both spheres s1 and s2.

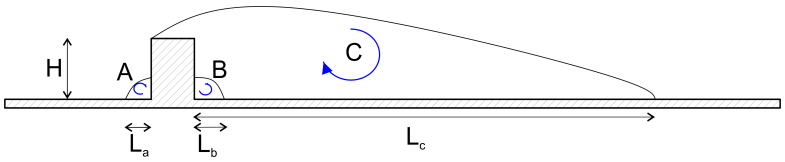

Figure 5.25: *Separation regions around the test-objects for high Reynolds number.*

Table 5.4: *Length of the streamline separation around two test objects for different bubbles. The flow is constrained with lateral sides. H is the height of the object.*

Object-Bubble	A	B	C
rectangle			
RANS (SST)		0.5 H	7.7 H
RANS (k-ε)	0.5 H	0.3 H	6.3 H
experiment		0.7 H	6.7 H
wiper			
RANS (SST)		1.0 H	9.5 H
experiment		0.9 H	8 H

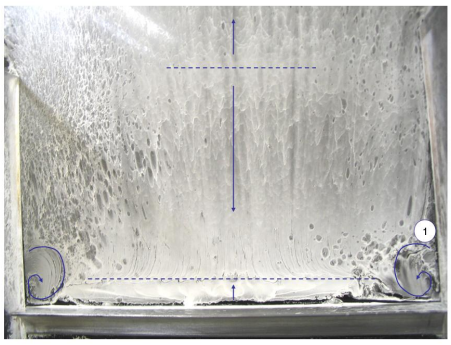

Figure 5.26: *Experimental visualisation of streamline near the wall with Oil-TiO_2 Mixture. Separation lines (dashed lines): 1) vortex due to the flow confinement.*

DES+EIF

The unsteady calculation with DES and the EIF source modeling reveals interesting physical phenomena such the one illustrated in Figure 5.29. Sound waves are mainly originated from a region behind the obstacle. The discretisation refinement and the resolution order can not be increased due to numerical instabilities. These instabilities are due to the numerical method itself (Euler equations) and are smoothed only due to numerical viscosity for relative coarse meshes. Using the 3D correction introduced in Chapter 5.1.2 one should average the sound sources on the z-direction for each position in space at each time step. This requires a big effort by exporting data between the CFD and the CAA solvers. We calculated therefore the average only on a reduced number of sections and evaluated a posteriori the effect on the sound source. The sound sources over the thickness are, as expected, not constant but one notices from table 5.5 that the differences (rms value) are relatively small even when using few positions for the average (Double rms value would increase the sound level by 3 dB). Therefore, only 3 sections have been used further for averaging. However we see as major problem the choice of the average length. In the original formulation (See chapter 5.1.2) , the length should correspond to an integral correlation length. Here, this length varies along the flow field.

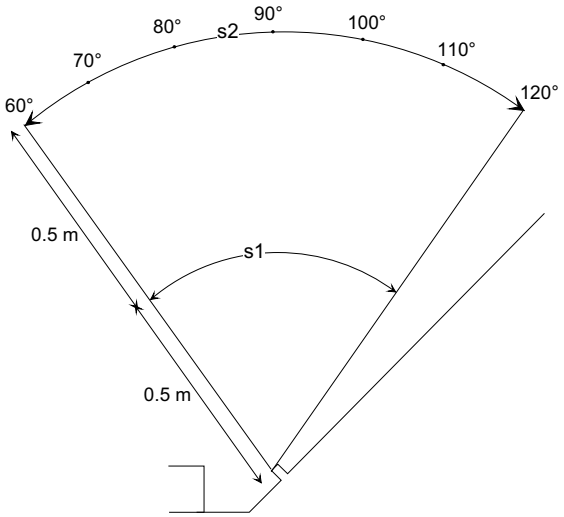

Figure 5.27: *Microphone positions. Two arcs of circle (s1, s2) with radius 0.5 and 1 m covers angles between 60 °and 120 °.*

Table 5.5: *Effect of the average on width direction (z) on the sound source. The value is the root mean square (rms) value of the source calculated with EIF method over 40 time steps (·10^6 Pa/s) at a fixed location. Width extension from -10 till 10 mm.*

number of samples in z-direction	nozzle	object	re-attachment
1 [a]	3.0	2.7	0.6
3 [b]	3.0	2.8	0.6
50 [c]	3.0	2.7	0.4

[a] at z= 0
[b] at z= 0, -9, +9 mm
[c] at each mesh element

Nevertheless, using the correction factor one obtains that OASPL matches quite well with experiments. The sound pressure level for increasing distances from a point-like source follows ($p^2 \propto \frac{1}{r^2}$ instead of $\propto \frac{1}{r}$). With the correction factor one obtains correctly a much stronger decay law than without. This is visible in table 5.6. One notices however a stronger decay than in the reality (-4 dB instead of -3 dB for 2D propagation and -8 dB instead of -6 dB for 3D propagation). This is probably due to the high numerical dissipation by using numerical methods of only 2nd order. Table 5.7 compares the OASPL obtained numerically (LEE+EIF), while table 5.8 shows the effect of a simulation with higher spatial discretisation order. The finer resolution causes instabilities which bring to divergence of the simulation for a longer simulation time.

Table 5.6: *Decay law for doubling the distance from the object. Measurement points on s1,s2 at 90 °. Values in dB. Measurement accuracy ± 0.5 dB.*

	2D	2D+correction	measurement
wiper	- 4	-8	-6
rectangle	-3	-4	-5

Table 5.7: *Directivity of numerical calculation (LEE+EIF). The values give the calculated OASPL in dB. A 3D correction with variable distance between observation points (sphere s1) and an idealised point source located at re-attachment (7 times the obstacle high) is used. Original values from 2D simulations are given in brackets.*

	60°	70°	80°	90°	100°	110°
wiper [a]	89 (107)	89 (107)	90 (108)	90 (108)	90 (108)	91 (108)
wiper [b]	87 (105)	88 (105)	90 (106)	90 (106)	91 (106)	92 (106)
wiper [c]				86 (102)		
rectangle [d]	84 (103)		84 (103)			
experiment		86-87		86-87		90

[a] F1 turbulence model, average over 3 points
[b] F1 turbulence model, symmetry plane
[c] F2 turbulence model, symmetry plane
[d] F2 turbulence model, average over 3 points

Table 5.8: *Effect of the acoustic mesh on OASPL for the same observation point (s1,90°). See Figure 5.9 for mesh geometry. Values are in dB for 2D calculation, with 3D correction factor and without (in brackets).*

	fine 2^{nd} Order	coarse 4^{th} Order
rectangular	84 (101)	95 (108)

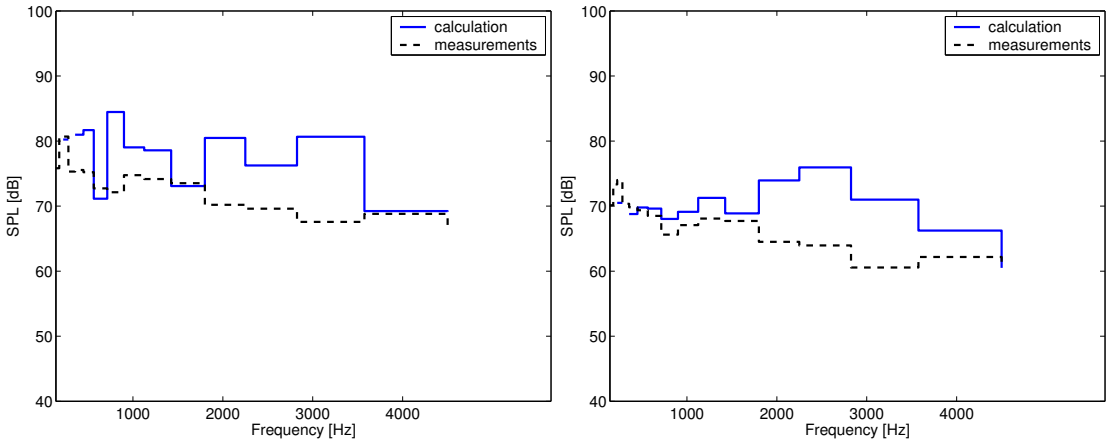

Figure 5.28: *Comparison numerical and experimental sound pressure levels for orthogonal position with distance 50 cm (left), 100 cm (right) for the wiper (LEE-EIF F1 turbulence model, integrated on 3 planes). The level is plotted in third octave bands.*

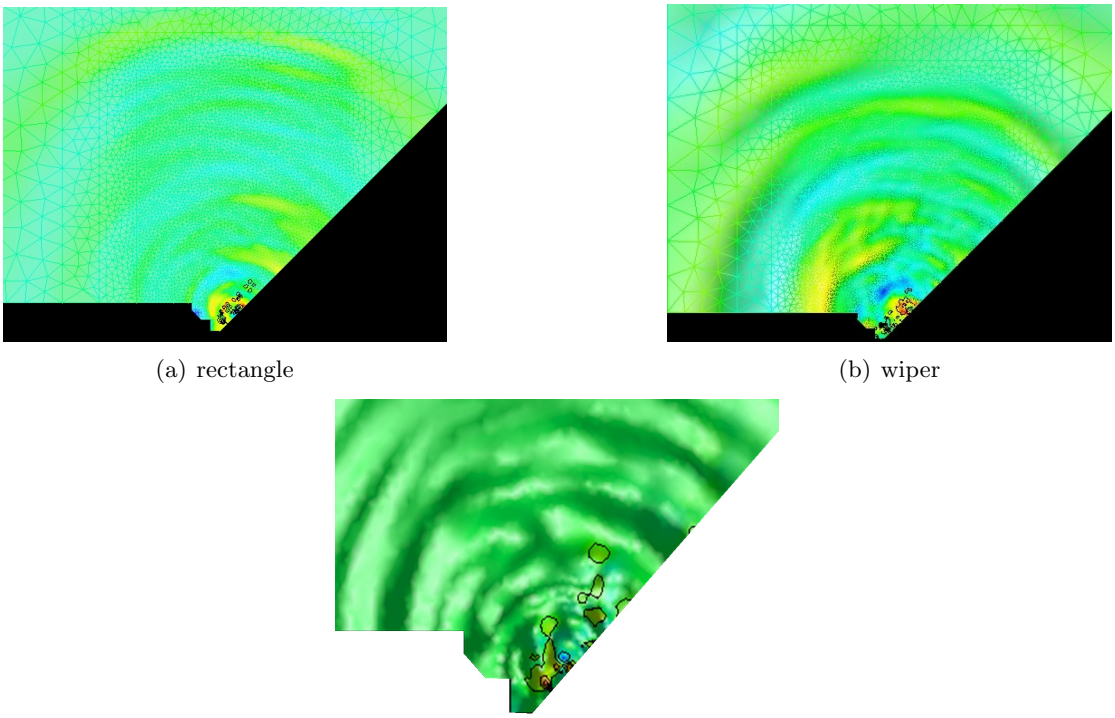

(a) rectangle

(b) wiper

(c) detail

Figure 5.29: *Acoustic results with DES-LEE method. The instantaneous sound pressure is color coded, the sound sources are plotted as black iso-lines. On the background is visible the calculation mesh (a-b). The detail c) shows the curvature of sound waves near to the obstacle and the instantaneous sound sources (colored iso-surfaces).*

SNGR

Calculations with own SNGR implementation (Section 3.3.3) show a large dependence from the discretisation. Figure 5.30 shows the grids and the instantaneous pressure field. Differences in the OASPL up to - 9 dB are presents. This is probably due to the low order derivatives used for the calculation of the sound source on the acoustic grid.

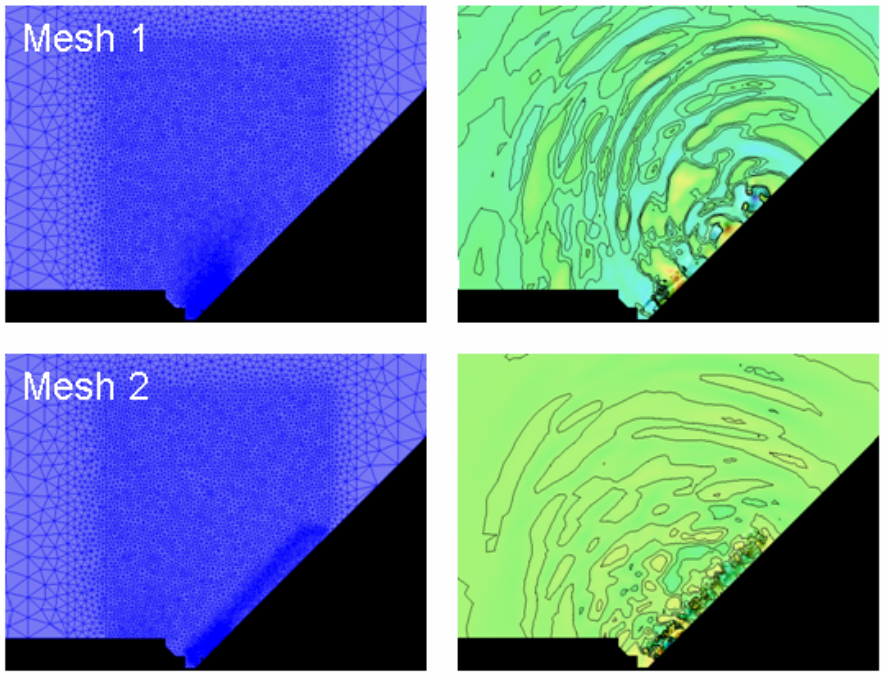

Figure 5.30: *Grids and instantaneous acoustic pressure field calculated with own SNGR implementation. Both 2D grids have about 15000 elements but the size of elements in the source (internal) region is 5-20 mm (mesh 1) and 7-10 mm (mesh 2). SNGR model with same parameters.*

This effect is also noticed in the implementation in the code *Fire*. Moreover, in SNGR, the integral length scale is deduced, with dimensional considerations, from the local turbulence energy and the dissipation rate A.5 and is valid a part from the factor K_Λ to be determined empirically. An experimental validation of this factor within this work was not possible[8]. As this factor influences the energy spectrum not only concerning the position of the maximum but also the level of the maximum itself, it is important to quantify the final effect on the acoustic simulation.

Figure 5.31 shows the OASPL calculated with the implementation in Fire for two different values of the factor K_Λ. The effect is very important: more than 10 dB.

Figure 5.32 compares the OASPL[9] for different SNGR implementations (Section 3.3.3) and K_Λ in few observation points in far field.

Even though the tendency over the observation points is maintained, it is evident a large sensitivity to the parameters and deviations from the measurements. Moreover, the calculation effort with those implementation is relevant and yields over 100 CPU

[8] A derivation from the integral time-scale calculated with HWA-measurement (Section 5.1.4.1) is limited to the Taylor-hypothesis of frozen turbulence.

[9] OASPL from 140 Hz up to 5000 Hz.

hours for simulation of 150 ms physical time on grid with about 500 K elements. This is in part given due to an inconvenient implementation of the synthetic source generation: in fact the sources are generated at each time step used for the LEE solution. This leads to frequencies up to 100 kHz which however can not be supported from grids for acoustic propagations.

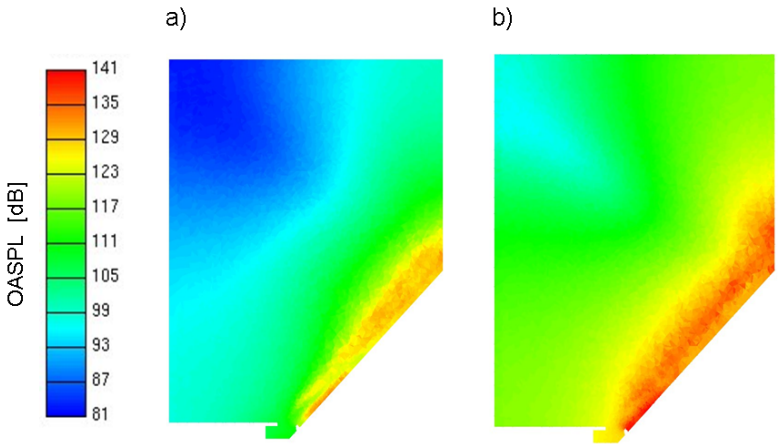

Figure 5.31: *Distribution of overall sound pressure level (OASPL) for different values of length scale parameter (K_Λ). a) K_Λ=1, b) K_Λ=15.*

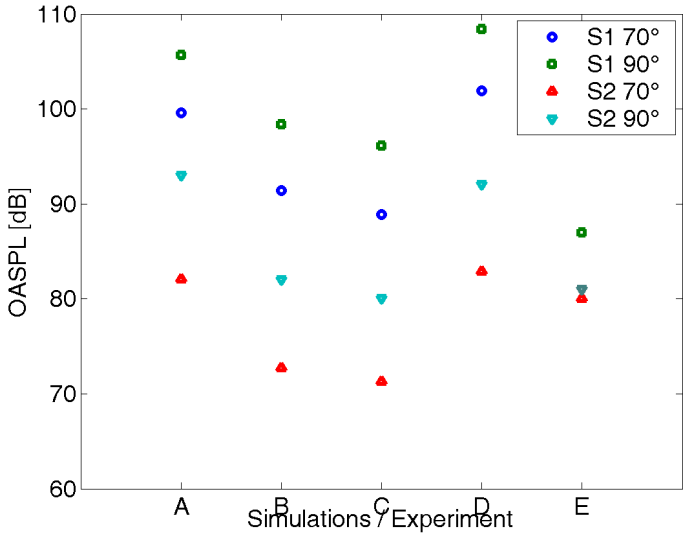

Figure 5.32: *Overall sound pressure level (OASPL) at 4 observation points (see figure 5.27 for the location) for simulation with* fire*(A-D) and measurements with microphones(E). A= standard implementation 'Bailly', B= implementation 'Billson' and K_Λ=1, C= as B but with reduced source domain, D= as B but with K_Λ=15.*

In conclusion, even though promising results have been achieved in the past for free jets [66],the SNGR approaches investigated so far seems not to be adapt for this class of aeroacoustic problems.

5.1.4.4 Sound Source and Sound Propagation

Figure 5.33 shows sound waves and hydrodynamic perturbations, measured with laser-scanning interferometry, for two different frequencies. Maxima and minima are highlighted respectively by red and green colors. One can notice a dipole like sound source in the obstacle region. On the other hand a localisation of all sound sources from the curvature of the sound waves is entirely possible. The picture 5.33-b suggests a broad sound source location in the region behind the obstacle for increasing frequencies.

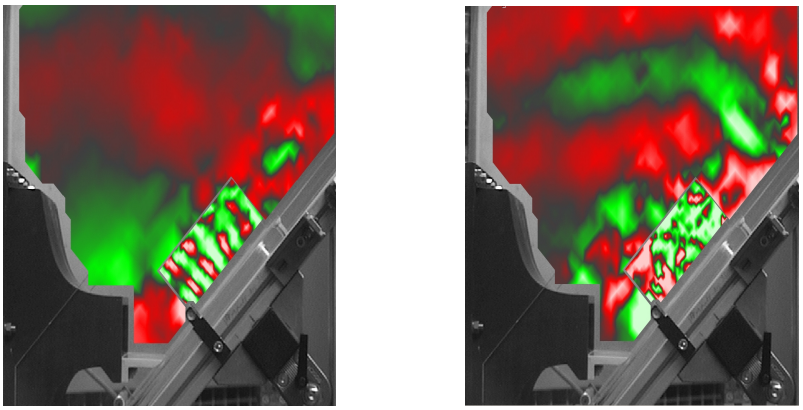

(a) 1100 Hz (b) 2350 Hz

Figure 5.33: *Instantaneous coherent pressure fluctuations made visible with laser interferometry (maxima in red, minima in green). Confined flow with rectangular obstacle with reference microphone at 50 cm from the obstacle at* 90°.

We attempt now to validate the location of sound sources calculated with EIF through measurement with the laser-scanning interferometry. For this purpose we use equation 2.19 and use $\frac{dn}{dp} \sim 2.72 \cdot 10^{-9} Pa^{-1}$. We suppose that the averaged dp/dt over the small thickness used for calculations (L=20mm) remains the same over the whole domain thickness (B=200mm) and consider the acoustic pressure in the source region negligible compared to the hydro-dynamic one. We obtain:

$$rms(v_{eff}) = 2|\frac{dn}{dp}|B \cdot rms(\frac{dp}{dt}) \tag{5.4}$$

The rms value of the sound source S, in its complete formulation for aeroacustic calculations (Equation 5.5) is also plotted alongside.

$$S = -\frac{\partial p}{\partial t} + \vec{U} \cdot \nabla p \tag{5.5}$$

with p the incompressible (hydro-dynamic) pressure perturbation and $\vec{U}$ the local time-averaged flow velocity.

Very similar patterns are noticed. On the other hand, the calculated absolute values of v_{eff} is one order of magnitude bigger than the measured one. We see many potential factors to be the cause: first, the reduced number of samples and the rough estimated integral over the domain width used in the calculation. As previously said the domain width is constant over the whole domain, the turbulence correlation length is not. Therefore one expects a greater discrepancy in the region where the correlation length becomes

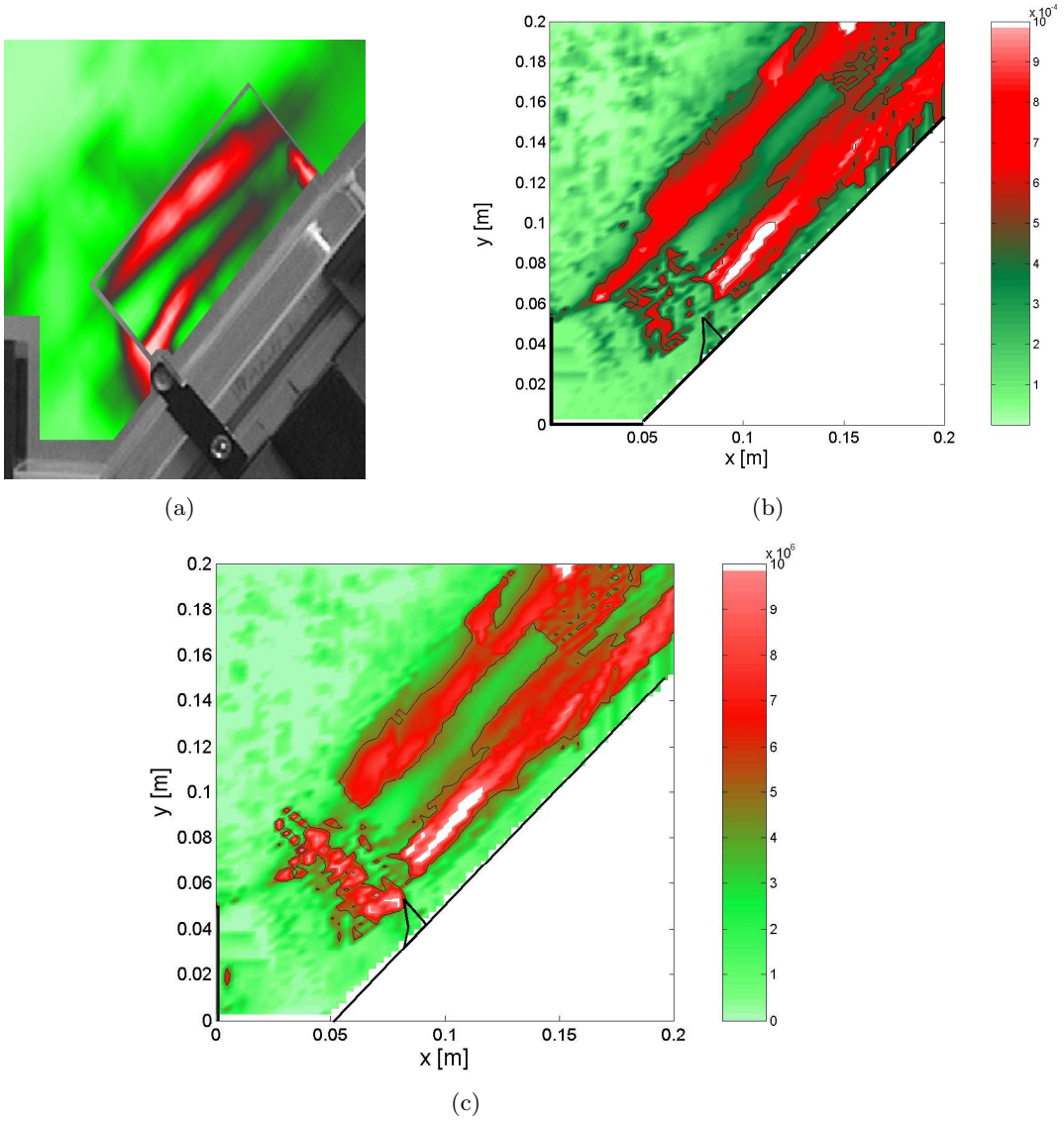

Figure 5.34: *Comparison of source terms. a) measurement v_{eff} (range 1-50 μm/s) b) calculation v_{eff} (range 20-1000μm/s) c) calculation EIF-source (range $0.04-2{\cdot}10^6$ Pa/s). Calculation over 7.5 ms (fs = 20 kHz) for the wiper geometry. Measurement over 40 ms averaged 200 times for rectangular geometry.*

larger (behind the object). That is observed, however the same intensity difference is noticed also in the shear layer from the nozzle, where small scale turbulence is present. We suppose therefore that the measurement itself could be underestimated. One reason could be due to the relatively large size of the reflected laser beam. This is expected to expose the perturbation over a larger area and therefore reduce the measured magnitude at the theoretical mesh point.

We see in this approach nevertheless the possibility to judge critically the numerical results obtained with EIF method at least for channel flows.

5.1.5 Mechanism of Sound Reduction for Separated Flows

We have seen so far that the reattachment region of separated flows acts as strong sound source. The reason is the highly turbulent fluctuations at the end of the recirculation bubble which impinge and 'wipe' the surface underneath.

We investigate now how this sound source can be reduced. *As long as* the separation is *inevitable* we see the following ways:

- De-correlation of the separation region
- Damping fluctuations at re-attachment
- Reducing lift and drag forces

De-correlation of the separation region The idea is to reduce the coherence at the separation in order to have de-correlated re-attachment regions. The aim is to reduce constructive interferences and therefore the sound emission at the re-attachment region. We implemented this idea on the basic form with a sinus profile top of the obstacle. See Figure 5.35).

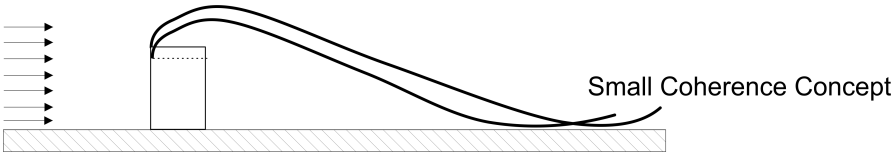

Figure 5.35: *Small coherence concept for the reduction of noise induced from flow separation.*

Damping fluctuations at re-attachment The idea is to reduce the buffeting intensity on the plate and therefore the sound emission at the flow re-attachment. One way to implement this idea is to create a high velocity air stream between the turbulent region and the plate. The air stream should reduce the fluctuation intensity perpendicular to the plate and postpone the re-attachment in a region where the turbulence energy is reduced. We will call this idea further on as '*air-pillow concept*'.

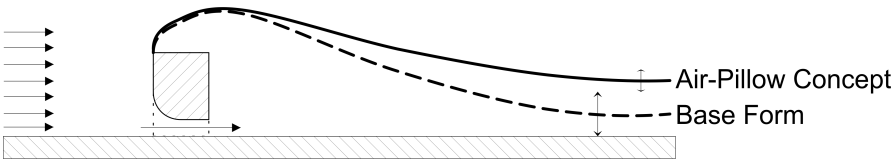

Figure 5.36: *Air Pillow concept for the reduction of noise induced from flow separation.*

Reducing lift and drag forces A flow separation induce fluctuations in the surface forces (lift and drag) generating dipole like sound sources. Therefore one can expect to reduce the sound intensity by reducing the pressure drag. The investigated objects are classed blunt bodies because the length-thickness ratio is very small (≤ 4). Using the equation of Curle for dipole-like sound sources, one find that the sound level in the far field depends on the time variation of lift and drag. We suppose that the time variation of lift and drag have a positive correlation to the lift and drag itself because of the vortex shedding. For blunt bodies the drag is primary pressure drag and it increases

when the ground clearance is reduced[6]. Moving the body away from the ground we expect therefore a reduction of the sound emission. On the other hand it is well known that blunt bodies in free flow shed periodically large vortices for a wide range of Reynolds numbers, thus inducing intense tonal noise.

Ideally these three solutions are distinct. In the practical implementation however we will see that they are partially combined with each other.

We consider now the implementation of the air-pillow concept using a rounded blunt body ('wedge') positioned with a gap to the plane d, but still having the same overall hight h from the plane. Figure 5.37 shows the flow predicted with a steady calculation around the base form and around the 'wedge' for d=5mm.

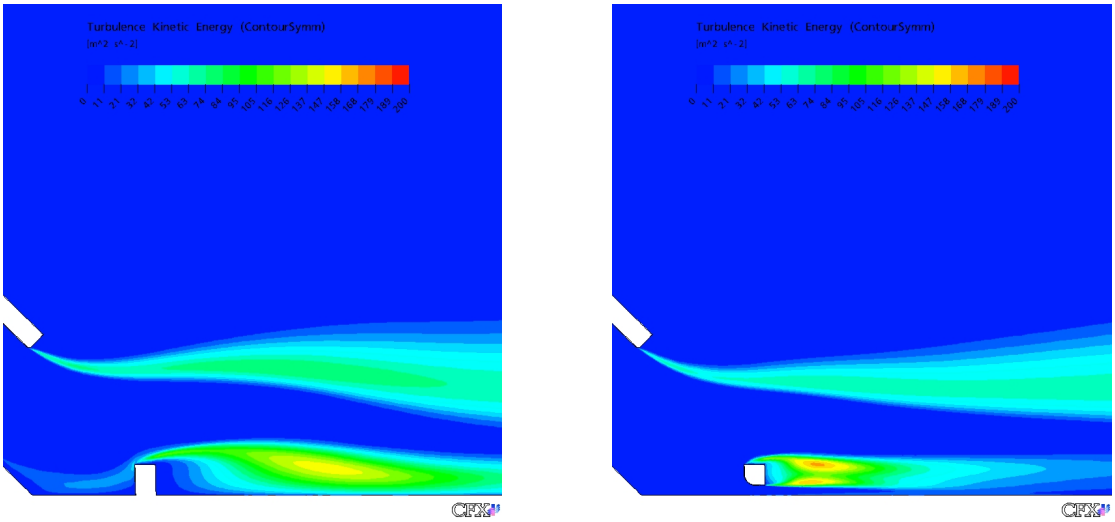

Figure 5.37: *Comparison of simulated turbulent kinetic energy (TKE) for flow impinging the base form (left) and the 'wedge' (right). Maximum TKE yields close behind the wedge ($\approx 170 m^2/s^2$).*

The turbulent bubble behind the obstacle is no longer attached to the ground. The obstruction effect at the nozzle is reduced so that a faster flow impinges the obstacle (+ 7% mass flow at outlet). Moreover, more turbulent kinetic energy is produced behind the obstacle (up to 15 % more). Using the definition of $C_D = \frac{2D}{\rho S U_\infty^2}$ and $C_L = \frac{2L}{\rho S U_\infty^2}$ with ρ density, D and L the pressure forces on the obstacle parallel and perpendicular to the plane, S the frontal surface, U_∞ the nominal outlet velocity (40m/s), we obtain $C_D = 1.3$, $C_L = 0.2$ for the 'wedge'. The drag and lift coefficients are respectively reduced -0.3, -0.1 compared to the base form. See the summary table 5.1.5.

Table 5.9: *Drag and lift coefficients for three basic geometries with steady numerical simulation (RANS-SST).*

	rectangle	wiper	'wedge' (h=5mm)
C_D	1.56	1.39	1.31
C_L	0.32	-0.84	0.18

We investigate now experimentally how two geometry factors influence the sound emission: the frontal area and the distance of the 'wedge' from the plane. The frontal area

is changed ± 13% (h=13-17 mm), and the distance from 1 to 4 mm. The measurements were repeated three times on different days obtaining the same tendency and very small differences in the OASPL (less than 0.1 dB). Therefore a very good measurement repeatability has been achieved.

Figure 5.38 shows the OASPL and spectra of the base form and air-pillow concept at a distance of 50 cm perpendicular to the obstacle.

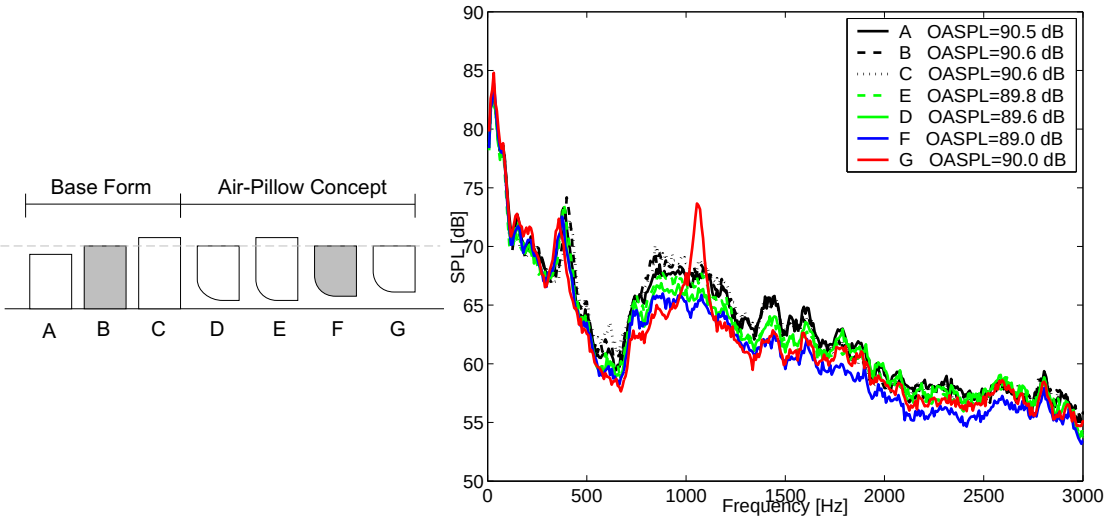

Figure 5.38: *Experimental result of the air-pillow concept. Spectra comparison for variation of the basic form (A-C) and of the realisation of the air pillow: wall distance of 2mm (D,E), 3mm(F) and 4mm(G). The gray dashed horizontal line on the left is the reference high (h=15 mm)*

As previously stated, the frontal area effects the obstruction at the nozzle inducing changes in the incoming velocity. However, the intensity of the acoustic source changes linearly with the surface area but with the 6th power of the velocity (dipole model), therefore we should expect a change in the OASPL. Despite of that the measurement shows no appreciable difference (± 0.1 dB). On the contrary, using a 'wedge' with the same frontal area (geometry E) one increases the mass flow and reduces at the same time the sound level (-0.8 dB). This supports the idea of the air-pillow. We notice a progressive reduction of sound level with increasing distance from the plane. The reason can be found either in a thicker damping stream according to the air-pillow concept or in the drag reduction due to greater ground clearance. At this point we can not separate the two mechanisms. The optimal sound reduction found for this configuration is 3 mm. By increasing the clearance more, vortices shed from both sides of the 'wedge' and produce a tonal noise at some 1000 Hz. The correspondent normalised frequency (Strouhal number $St = \frac{fD}{U_\infty}$) using D=h-d= 11 mm corresponds quite well to the value St= 0.25 typical for vortex shedding behind a bluff body (circular cylinder).

Figure 5.39 demonstrates that not only for one but systematically for every observation point, the OASPL of the rounded blunt body with a gap to the surface is smaller than for the base form. The maximum OASPL reduction is -2.4 dB when considering frequencies over 500 Hz. Considering that the base form itself increase the pressure level of the simple inclined plane by about 7 dB, the achieved result with the air-pillow concept shows a great potential.

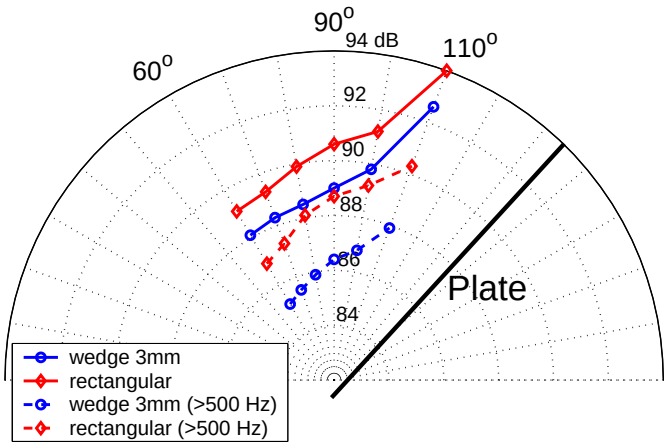

Figure 5.39: *Directivity plot of the basic form and of optimised air pillow (plane distance = 3mm). The OASPL is integrated over all frequencies (solid line) or from 500 Hz (dashed line) up.*

5.1.6 Conclusions

In this section we performed both fully unsteady and stochastic hybrid aeroacoustic calculations for two non trivial geometrical configurations. These configurations have been chosen to idealise typical obstacles impinged from subsonic flow occurring in the automotive industry. The present numerical results and experiments integrate each others and contribute to a better understanding of the physical phenomena for not trivial academic configurations.

The experimental validation of the fluid-dynamic properties of the flow shows discrepancies. Although steady turbulence models reproduce the time averaged flow very well, unsteady one show exuberant turbulence production. Moreover the frequency of the turbulence seems to be very sensitive to the properties of the mesh used to discretise the problem. Once the size of the domain requires to split the domain discretisation into more sub-domains, as here the case is, only connected sub-domains should be used, that is the domain interface should not have hanging nodes. Perfectly merged domains should prevent space interpolate of the numerical solutions between domains and therefore spurious reflections at the interface.

The acoustic calculation based on these unsteady fluid-dynamic results shows very good agreement of the overall sound pressure levels (OASPL) in far field after a correction for 3D sound propagation, even though the correction factor can be ideally used only for symmetric configuration where the sound sources are concentrated in a point. The uncertainty of the aeroacoustic results is difficult to estimate: because of the intrinsic instability of the underlying linearised Euler equations, the acoustic mesh can not be refined indefinitely in order to improve the accuracy of the results for the fluid-dynamic calculation. In particular: the finite element acoustic solution uses a sub-grid of the acoustic mesh in the sense that the solution is calculated over a number of so called Gauss points inside each mesh element, whose number depends on the accuracy order. Instabilities in the solution, triggered from the shear layers of the flow, could be observed starting from 4th order even on coarser meshes. We see therefore practicable only the 2 order space discretisation which on the other hand presents more dissipation.

There is evidence of several overlapped sound generation mechanisms: dipole type at the front side of the obstacle, supposed quadrupole-like in the nozzle shear layer and supposed dipole-like stretched sound source in the flow re-attachment region. A distinction of those source region have been tried which laser Doppler interferometry. A relative good qualitative agreement in the numerical and experimental source distribution is achieved even though the amplitudes differs one order of magnitude. One possible reason is seen in the actual limitation of the measuring technique. Nevertheless the source regions are localised with relative good precision and this method confirm its potential towards an other method used in previous aeroacoustic investigations (near field holography).

On the other side the SNGR aeroacoustic calculations show high sensitivity to the length scale factors and the relative high computational effort seems not to be justified.

5.2 Inclined Plate with Obstacles (unconfined flow)

5.2.1 Configuration and Models

This section is dedicated to the results obtained with LBM. Differently to cases of the previous section, the flow is here not confined by side planes and can develop three dimensionally (also time-averaged).

Figure 5.40 shows the profiles and their idealised geometrical environment.

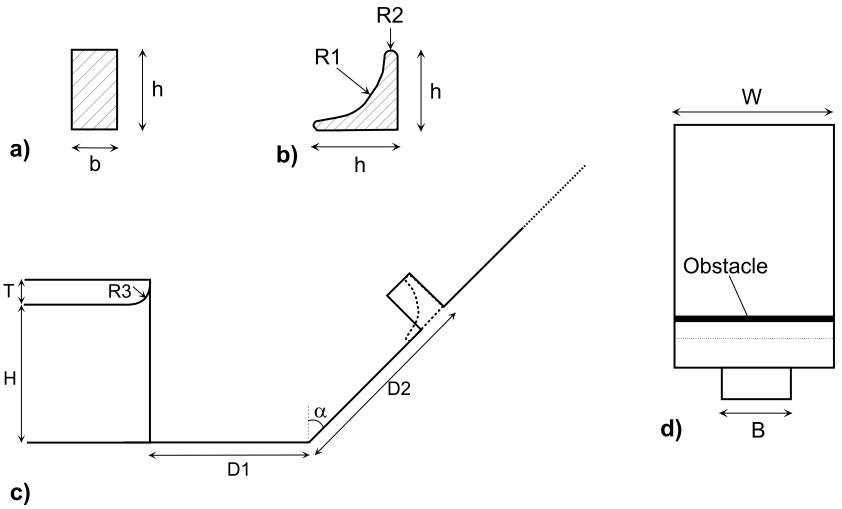

Figure 5.40: *a) rectangular profile, b) wiper profile, c) geometrical environment (profile), d) geometrical environment (top view).* $h = 15\,\text{mm}, b = 10\,\text{mm}, R1 = 13\,\text{mm}, R2 = 0.7\,\text{mm}, R3 = 1.75\,\text{mm}, D1 = 50\,\text{mm}, D2 = 60\,\text{mm}, H = 50\,\text{mm}, T = 10\,\text{mm}, B = 200\,\text{mm}, W = 800\,\text{mm}, \alpha = 45°$.

Figure 5.41 shows the domain discretisation used in this study (see also [105]). The domain is subdivided into 8 regions with voxel size doubling at each region crossing. The total number of elements is 21 millions. However, considering that the update rate of the voxels is proportional to the voxel size, the resulting computational effort corresponds to about 8 million cells of the same smallest size (fine equivalent voxels).

The time step was in the order of $\sim 1\mu s$. The calculation was run for $150ms$ after an initial phase of 40 ms which is necessary to obtain statistically steady data. The calculation took overall 2043 CPU hours on Opteron-type Machine.

5.2.2 Results

5.2.2.1 Separated Flow Regions

Figure 5.2.2.1 shows the typical separation regions which take place around the test objects at high Reynolds numbers. For the rectangular object, along with the main region (marked with C in the figure) with clockwise recirculation there is also an induced minor one (B) with anti-clockwise motion. Furthermore a minor region (marked A) in front of the object arises due to the high static pressure increase caused by the object. Moreover, the figures 5.43 and 5.44 show the separation and reattachment lines from time-averaged simulation and experiment in proximity of the wall. In the simulation

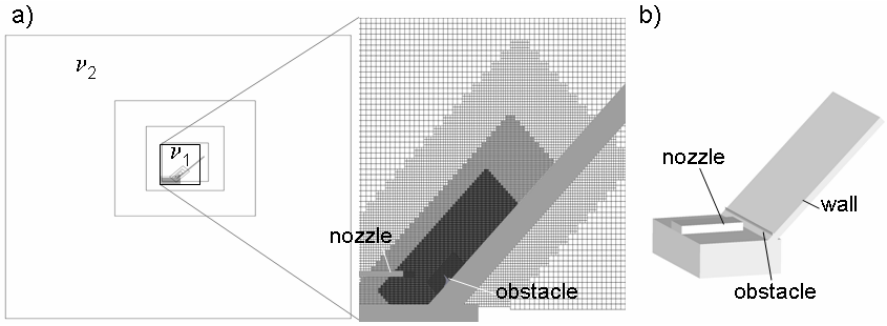

Figure 5.41: *Domain discretisation. a) Voxel size ranges from 0.6 (interior) to 76 mm. (exterior). The lines indicate doubling of Voxel size. The exterior has a fluid viscosity ν_2 100 times higher then the interior ν_1 b) three dimensional view of the geometry.*

the lines mark the sign change of the velocity parallel to the wall for the nodes of the first element-layer, whereas for the experiment those lines are interpreted from time averaged streamlines visualised with a Titanium dioxide mixture applied to the wall. The flow reattaches further behind the wiper profile than behind the rectangular geometry. Table 5.10 summaries and compares the maximum separation lengths for numerics and experiments. We observe apart from absolute values a good agreement in the trend between both test cases. Behind the body one finds two areas of swirling flow which are the footprints of an arch vortex and are localised about at the continuation of nozzle sides. In front of the body the flow is also separated. Simulation shows a large separated region starting at the plate inclination whereas the experiment seems to suggest an attached flow up to the minor region (marked A). Detailed analysis reveals that this is caused by a lack of resolution close to the wall in the numerical simulation.

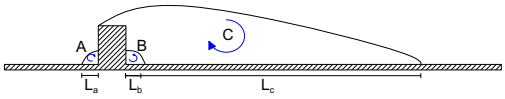

Figure 5.42: *separation regions. L_c is measured from the rear side of the obstacle*

Table 5.10: *Maximal length of the main separation region (C) for both profiles measured from the vertical rear side of the obstacle.*

	simulation	experiment
rectangular	6 H	7.6 H
wiper	7.6 H	8.3 H

5.2.2.2 Velocity and Turbulence Fields

The flow properties are investigated at several sections downstream the obstacle as indicated in figure 5.45. The computed mean velocity profiles agree very well with measurements just behind the obstacle (Section 3, Figure 5.46). Further downstream an offset between both with respect to the wall distance is noticed (Figure 5.46). As not only HWA but also LDA show the same behaviour we exclude measurement inaccuracy due to high turbulence levels.

Moreover figure 5.46 compares the in-plane turbulence kinetic energy (TKE). For the simulation TKE has been calculated from the solved velocity perturbations adding two third of the turbulence energy from the unresolved scales (turbulence model). At section 3 the turbulence is almost completely modelled while at section 5 the contibution of the

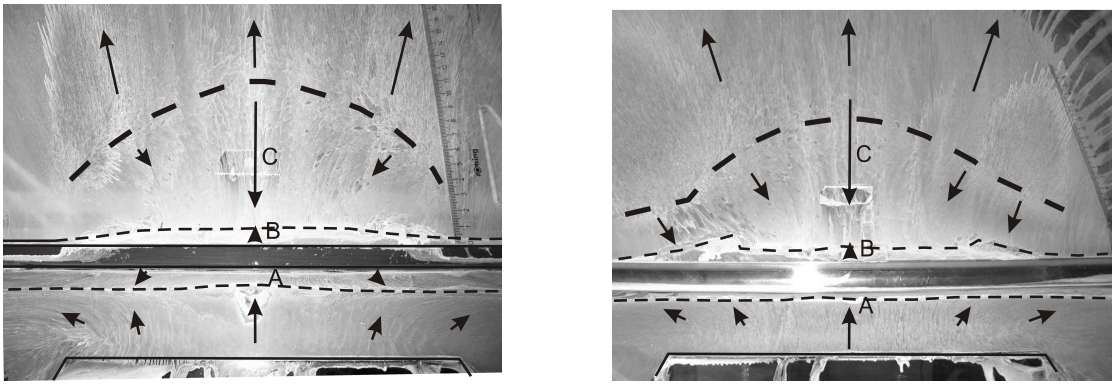

Figure 5.43: *Separation regions from experiment for the rectangular profile (left) and wiper profile (right). Due to the different perspective views, a comparison is possible only using the side reference.*

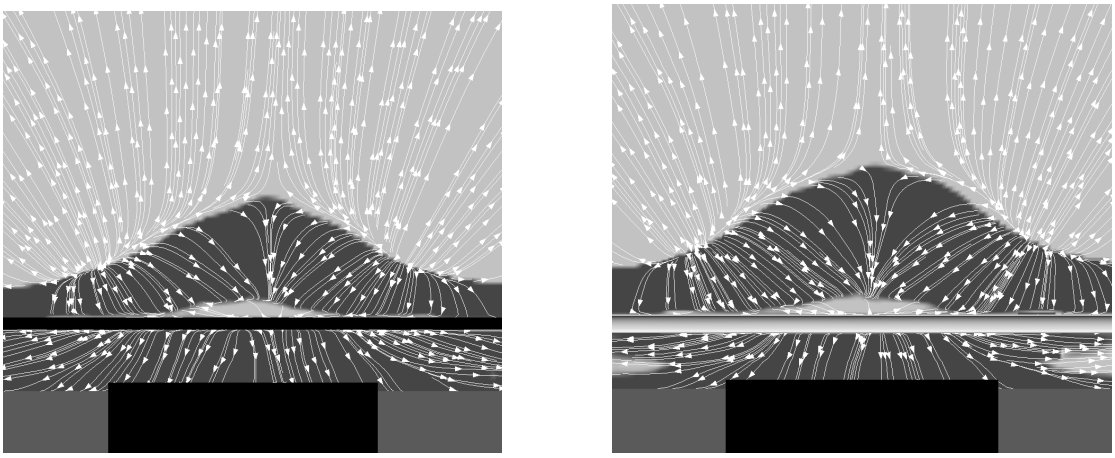

Figure 5.44: *Separation regions from the numerical simulation for the rectangular profile (left) and wiper profile (right). The nozzle is indicated in black, the reversed flow in dark gray.*

solved velocity perturbation is larger. We notice a large discrepancy between measurements and simulation further downstream. The absolute value of TKE is however not alone decisive for the sound emission, but frequency content and sources location.

5.2.2.3 Sound Pressure Level and Spectra

The sound pressure level and spectra are compared on two shells (s1,s2) at respectively 0.5 and 1 m from the obstacle, as indicated in figure 5.45-right. At those locations the highest sound frequencies expected to be solved are respectively about 5600 and 2800 Hz [10]. Only the locations on the second shell can be considered to approximate the far field condition (for frequencies larger than 1000 Hz). Figures 5.47, 5.48 and 5.49 show the one-third octave spectra and the overall sound presssure level (OASPL) from microphone measurements and from Lattice-Boltzmann simulation. Experimental measurements are carried out with a lowpassfilter with 25 kHz corner frequency. The spectra are processed

[10] highest frequencies due to the previously indicated requirement of 6 PPW and local grid resolution of respectively 10 and 20 mm

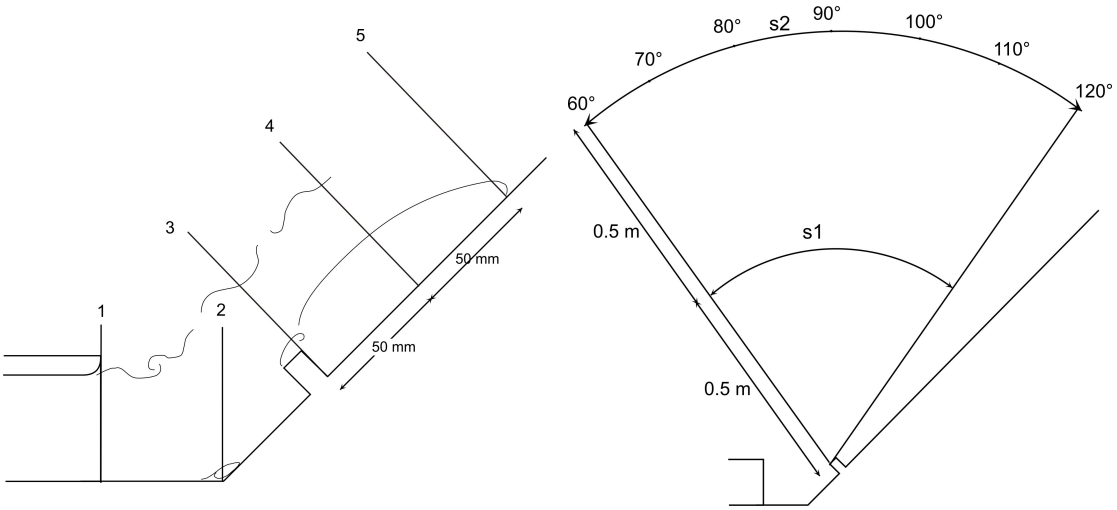

Figure 5.45: *Sections used for the comparison of the velocity field and turbulent kinetic energy between calculations and experiments. The separation regions of interest are also sketched (left). Microphone positions: Two circular arcs (further called shells s1, s2) with radius* 0.5 m *and* 1 m *covering angles between 60 °and 120 ° (right).*

with a Hanning-type window and averaged from 500 samples during a total of about 75 seconds. The OASPLs are obtained from integration of the spectra between 150 and 5000 Hz.

For the small distance (s1) and angles larger than $\sim 100°$, we can observe that the pressure fluctuations are affected by hydrodynamic fluctuations (pseudo sound), therefore the OASPLs are very large. In the region dominated by acoustic pressure fluctuations (s2 and s1 for angles smaller than $\sim 100°$) we observe a very good agreement of OASPL trend and a underestimation of typically 3-4 dB. Moreover the wiper profile shows a lower OASPL than the rectangular profile at all locations. This is confirmed experimentally. Globally the noise generated is broad band, showing however peaks in the low-middle frequencies. The analysis of the measured spectra reveals a different behaviour with the microphone angles: they show peaks at about 1400 Hz for 90° while they are under about 500 Hz for 70°. The comparison of measured spectra with simulated spectra show a relatively good agreement for both geometries (Figures 5.47 and 5.48).

5.2.2.4 Sound Sources and Sound Propagation

During a preliminary simulation it was noticed that the relatively quiet acoustic field was strongly affected by spurious reflections of pressure waves, almost orthogonal to the boundary. Therefore throughout this work a surrounding region with high viscosity has been used to damp these out. Moreover the role of this surrounding region has been investigated by changing its position relative to the voxel regions of different size (VR-transitions)(Fig.5.50).

Figure 5.51 shows the effects of this position on the pressure field. The pressure field seems to be less influenced by including or excluding the first orthogonal VR-transition into the high viscosity region. Therefore we deduce that the previously noticed strong reflections were originated by the boundary conditions and not intrinsically due to the VR-transitions.

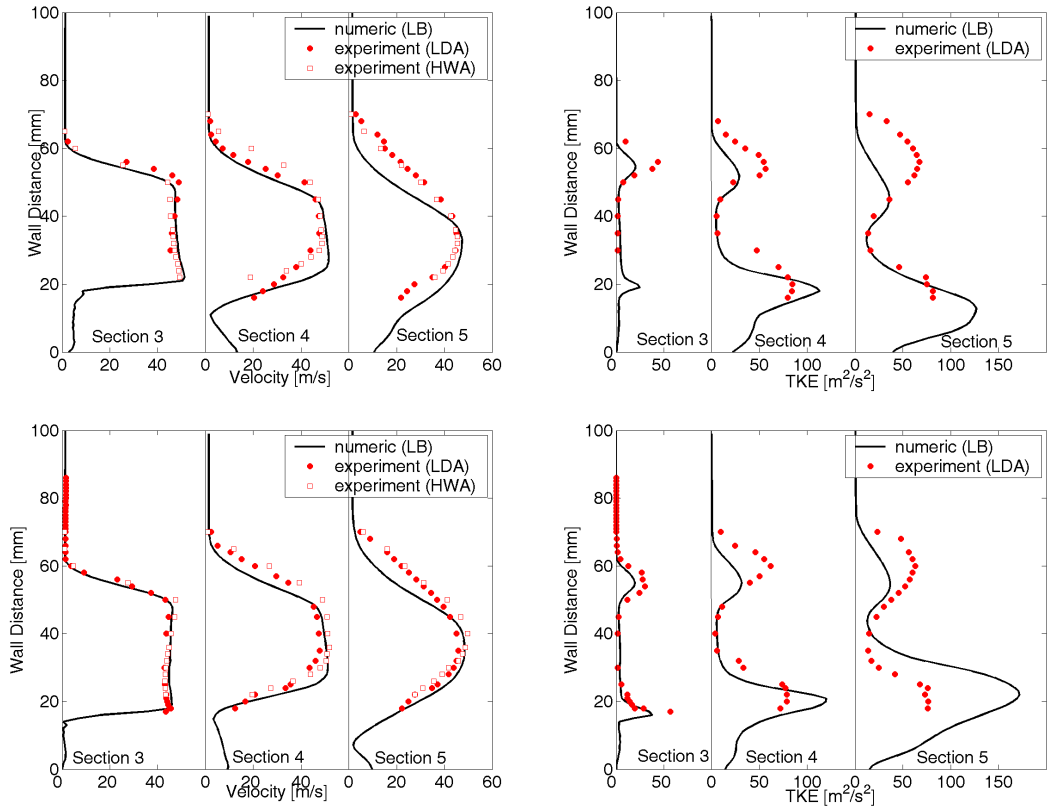

Figure 5.46: *Comparison for rectangular profile (top) and wiper profile (bottom) at different sections: velocity (left) and turbulent kinetic energy (right). The values are averaged on the grid cell, therefore they do not reach the expected value zero at the wall boundary. Number of samples at each location: 1K samples with sample frequency = 5 kHz (HWA) and 30K samples with variable sample frequency (LDA).*

The acoustic waves and the source regions are clearly visible by post-processing the simulated pressure field with band-pass filters (Figure 5.52) for 800 Hz the source is located near the obstacle, for 1700 Hz more in the reattachment region. The source region for frequencies around 1700 Hz can be easly localised in the region of flow-reattachment behind the obstacle. Laser interferometry shows qualitatively a similar behaviour (Figure 5.53). Moreover, both simulation and experiment show a region of interference close to the nozzle about between 70° and 90° (Figure5.45). This region is due to the nature of the main sound source due to the obstacle (dipole) and the reflections due to the nozzle itself.

5.2.3 Conclusions

The sound generation mechanisms for subsonic jets impinging on simplified not confined geometries have been investigated numerically and experimentally. The complexity of the physics has been modeled with a direct approach based on Lattice-Boltzmann Method (PowerFLOW). Surrounding region of increased viscosity together with non-reflecting pressure boundary conditions have been included in the simulation. In this

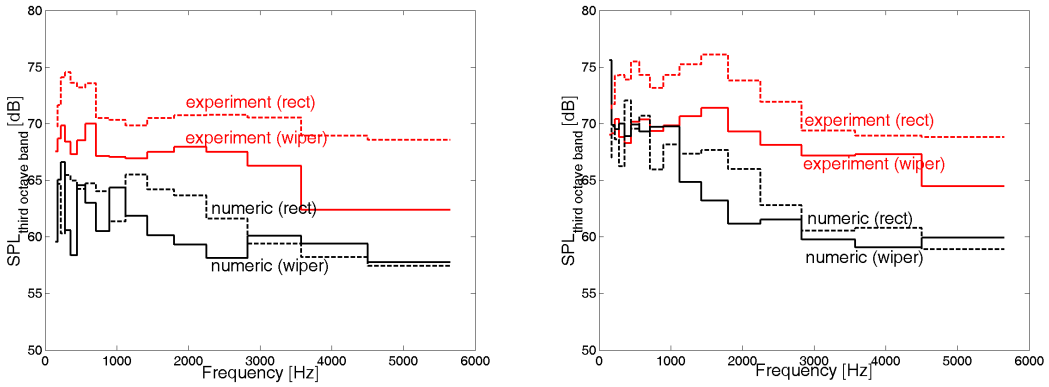

Figure 5.47: *Comparison spectra (third octave bands) for wiper and rectangular (rect) shape at distance s1 (70 ° and 90°) respectively from left to right.*

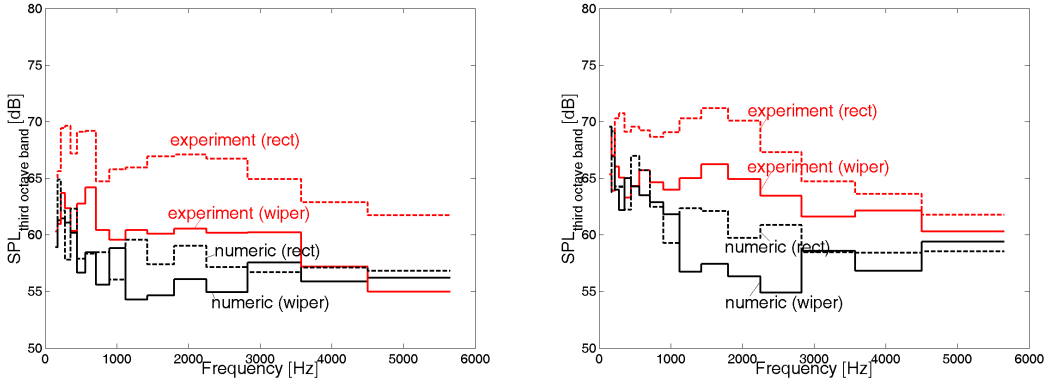

Figure 5.48: *Comparison spectra (third octave bands) for wiper and rectangular (rect) shape at distance s2 (70 ° and 90°) respectively from left to right.*

case artificial reflections of acoustic waves caused by numerical discontinuities, such as changes in the discretisation resolution and domain boundary condition, were suppressed. Although the turbulence levels for both investigated geometries are almost the same, experiments and simulations show differences in the OASPL and reveal that the shaped wiper profile is quieter than the rectangular one. In far field, at 1 m from the obstacle, this difference yields between 3 dB and 5 dB in the experiments and between 1 dB and 2 dB in the simulation. The sound directivity is predicted very well and shows a continuous but light level increase in flow downstream direction as in the experiments. It is also confirmed that the turbulence kinetic energy is not a measure for the OASPL: LBM overpredicts the turbulence level (more energy in the resolved turbulence scales, smaller separation regions) but underestimates about $3-4$ dB the OASPL levels. The selective frequency analysis shows the characteristic dipole-like sound propagation. Moreover, high frequency sound is mostly generated in the reattachment region behind the obstacle while the lower frequency sound has its origin at the obstacle. In conclusion, we have shown that the Lattice-Boltzmann approach is able to provide good trend predictions for subsonic aeroacoustic problems and to capture fundamental aeroacoustic physical phenomena.

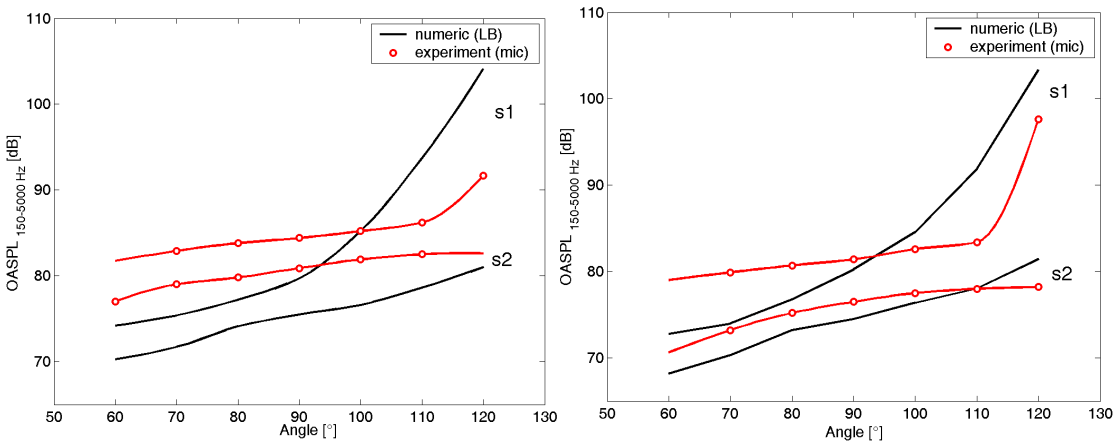

Figure 5.49: *Comparison of OASPL for rectangular profile (left) and wiper profile (right) at different positions and distances of microphones . s1 = 0.5 m distance, s2 = 1.0 m distance from profiles top back corner.*

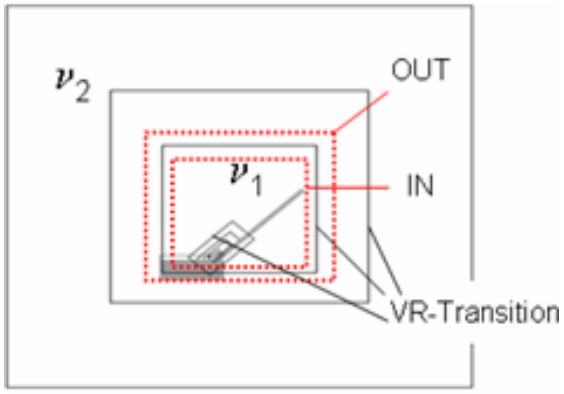

Figure 5.50: *Overview VR-Transitions.*

5.2.4 Two-Bodies Investigation

In this section we compare experimentally the sound level and spectra of different configurations in order to show the effect of small objects in the sound enhancement of subsonic impinging jets for the same flow-rate from the rectangular nozzle. Figure 5.54 shows a pronounced wide band maximum for the spectrum of the free jet at about 500 Hz. The inclined plane and particularly the obstacle increase the sound pressure level quite uniformly above about 1000 Hz (respectively about + 5 dB and + 20 dB) and smooth the maximum out. The pattern under 1000 Hz changes radically. Particularly in the low frequencies, under some 500 Hz, the obstacles cause peaks in the pressure level which persists also in far field and for different angles. Many sound sources are present in the test case with obstacle: dipole type at the front side of the obstacle, supposed quadrupole-like in the nozzle shear layer and supposed dipole-like stretched sound source in the flow re-attachment region. The peak at about 50 Hz is due to the acoustic room and to pseudo sound. From directivity analysis one extrapolates that the peak at about 200 Hz is due to the obstacle because the level in near field is constant over the arc of circle 70-100° centered in the obstacle. The sound sources due to reattachment seem to be more responsible for the level increase from about 1000 Hz.

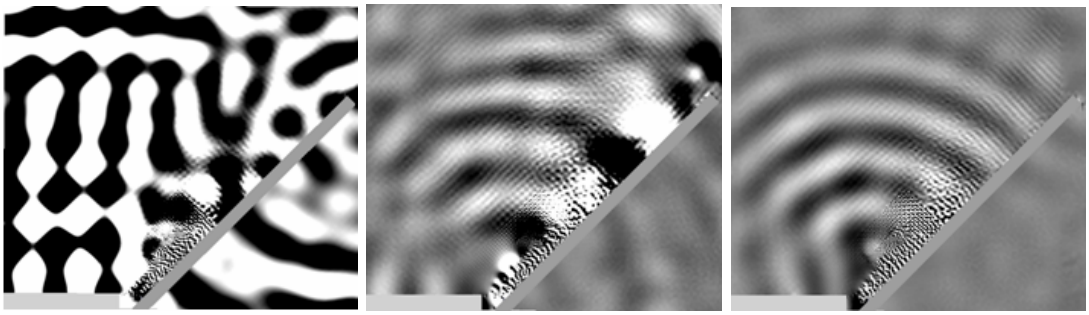

(a) (b) (c)

Figure 5.51: *Effect of high viscosity region on acoustic field (1700 Hz): without (a), outside first orthogonal VR transition (b), inside first orthogonal VR transition (c).*

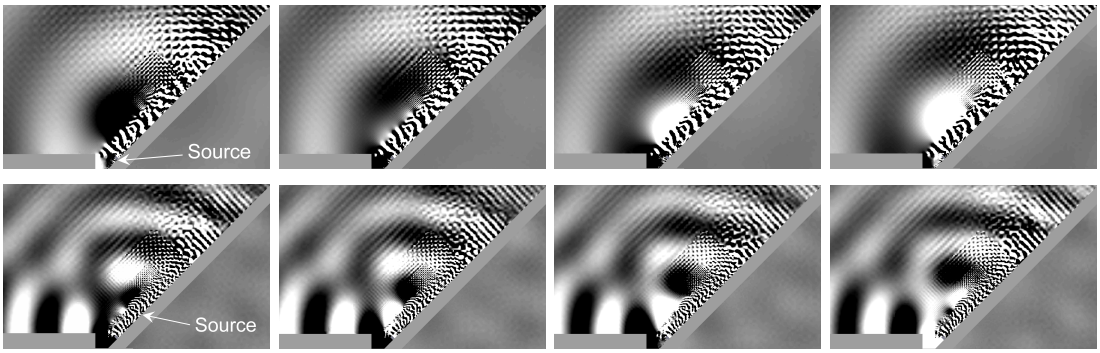

Figure 5.52: *Simulated instantaneous pressure field for 800 Hz (above) and 1700 Hz (underneath): sequence of 4 pictures over 0.2 ms.*

The flow confinement produces a small increase in the sound pressure level in the near field due, not to additional turbulence or flow modification, but to sound reflections originated from the lateral sides used to confine the flow. This has been proven by using a compact loudspeaker producing white noise in the re-attachment region instead of the impinging turbulent flow: one obtains an analogous level increase and frequency pattern.

For microphone positions at angles more than 110°, the pseudo sound dominates the sound pressure level in the near field (Figure 5.55). The sound pressure field is uniform in the z-direction as the OASPL measured at 50 cm distance (sphere s1) differs along the whole width of the plate (even for unconfined flow) by less than 1 dB.

The presence of an object in a separated wake increases the sound pressure level significantly (in our test case up to 11 dB). We found that the sound pressure level depends on the distance between the objects and that presents a maximum at a well defined location. As the location of the maximum does not depend on the microphone position, we exclude that the maxima occur because of the reducing length between sound source and microphones. Moreover, with the same motivation, the difference in the OASPL between microphones (2-5 dB) supports a strong directivity introduced by the second obstacle. This experimental investigation suggests some practical considerations: the obstacles placed in a separated flow enhance extremely the sound pressure level, however one can minimise it by positioning the obstacle away from a critical position. This

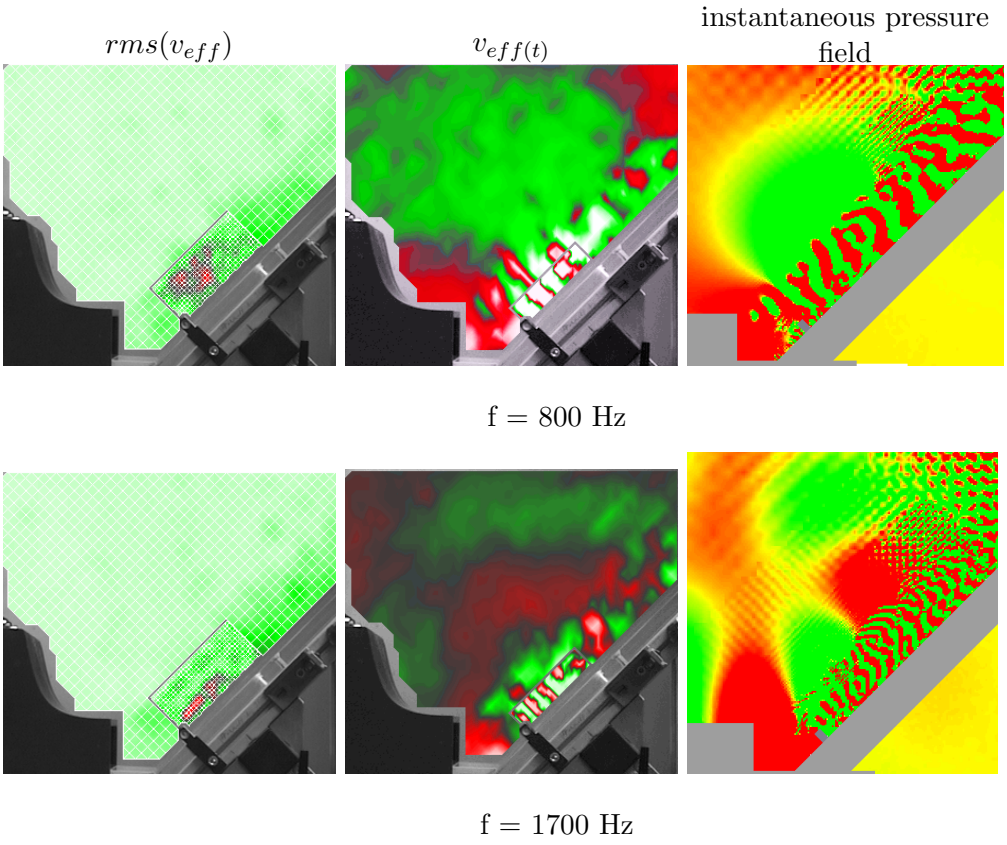

Figure 5.53: *Qualitative comparison of pressure fluctuation fields measured with laser interferometry and simulated with LBM for 800 Hz (top) and for 1700 Hz (down): root mean square field (left) and instantaneous field (center) of the measured variable V_{eff}. Simulated instantaneous band-filtered pressure field with LBM (right).*

critical position appears to be located before the re-attachment region, and therefore it is supposed to depend on the object high, which is in this case also its typical size. These considerations are valid as long as the obstacles are bluff bodies with small thicknesses. When the thickness is larger, the flow can reattach on the top of the obstacle itself, changing the size of the recirculation zone and probably the sound emission.

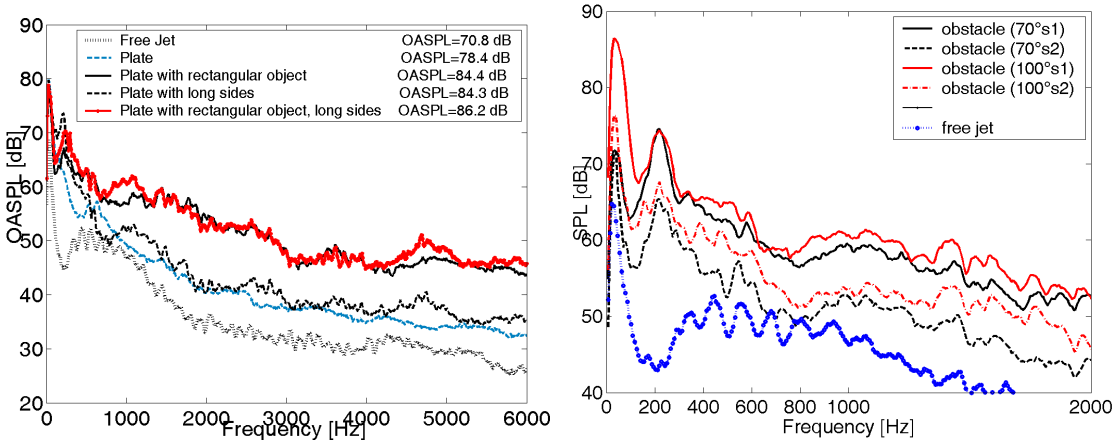

Figure 5.54: *Experimental spectra of sound pressure for different configurations: (left) free jet, jet impinging on a plate with and without obstacle with unconfined or confined flow (long sides). Measurement at 50 cm distance with 90° inclination. (right) free jet and jet impinging on a plate with wiper-like obstacle for different distances and observation angles.*

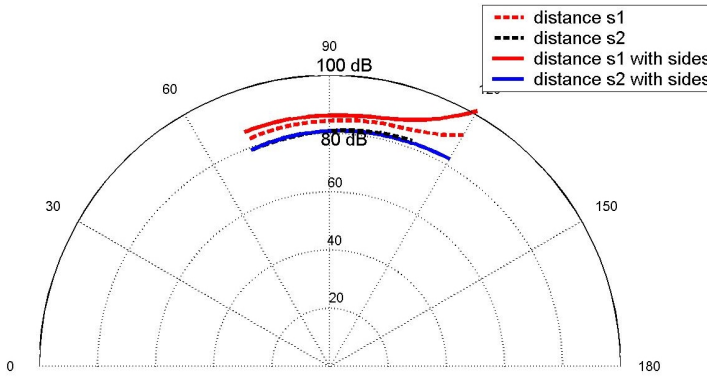

Figure 5.55: *Experimental directivity plot of sound pressure level for rectangular obstacle for different flow types (confined (*with sides*) vs unconfined) and distances (s1= 0.5m, s2= 1 m).*

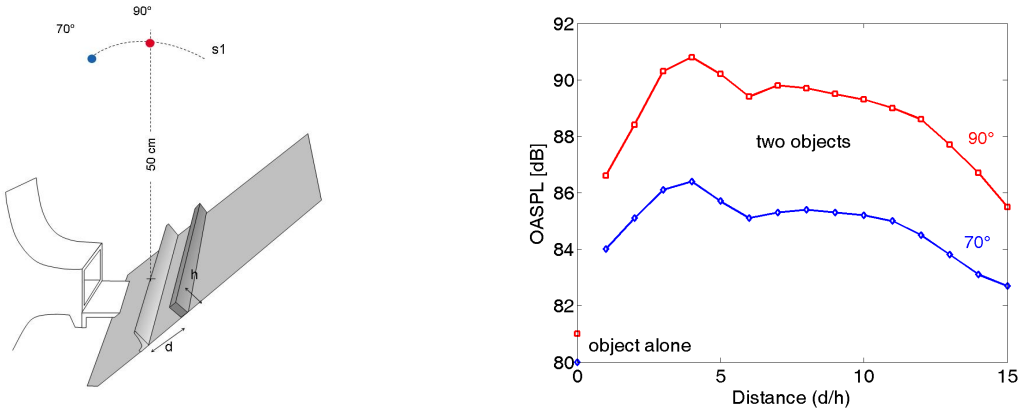

Figure 5.56: *Experimental sound pressure level of configuration with two obstacles. Measurement for increasing normalised distance (d/h) between obstacles at distance of 50 cm with inclination of 70 °(blue) and 90° (red). h is the obstacle hight. The flow is unconfined, and the obstacles are the wiper (front) and the rectangle (behind). The OASPL maximum occurs when the second object is in the separated region induced from the first one, approaching the re-attachment.*

Chapter 6

Experimental Investigation of Screen Wipers

Car noise is dominated at high speed, especially for comfortable sedan cars, by aerodynamic noise. Current development is conducted by car manufacturers and automotive suppliers in the area of a better cabin insulation [106], of improved design of cavities (sun roof, tyre compartment) and of large exterior parts (side mirror)[107],[108]. The interior of modern cars has reached high acoustic comfort thanks to these progressive noise optimisations but still many other optimisation areas exist. In particular certain sources which were previously masked are now brought out: the noise from screen wipers, for instance, can be very annoying because the wiping movement creates a time modulation of sound which eventually has a psychological impact on the passengers. Therefore car manufacturers requires a lower and lower impact to the overall sound level inside the car.

Screen wiper noise can have different origins, for example, mechanical origins: impulsive sound when turning the wiping direction or 'humming' sound[1] induced by wiper-lip grip [109]. In this section we investigate the aeroacoustic noise of screen wipers. As we will see further, it represents a distinctive and perceivable noise inside of modern cars. For the sake of completeness, the investigations are done with respect to the screen wiper as a whole system instead of the single screen wiper. Therefore we include the wiper strut and the supporting arm in the consideration as well. The problem is analysed experimentally, looking also for analogies to the simplified numerical simulations and experiments described in previous sections of this work.

In the past the aeroacoustic noise generated from wiper systems has been investigated by the automotive supplier Valeo [110]. In that work it has been tried to localise the sound sources experimentally using beam forming and to correlate their position to turbulent kinetic energy from steady simulations. However, the experimental localisation appears inaccurate, moreover the correlation to integral value of the kinetic energy is questionable.

In this section an experimental acoustic investigation of Bosch screen wipers is presented with following objectives:

- evaluation of the screen wiper contribution to the overall aeroacoustic noise of a modern car

[1] Low-frequency vibration (typically about 100 Hz).

- localisation of aeroacoustic sound sources induced by the screen wipers with respect to their frequency
- comparison of the acoustic emissions of a modern screen wiper (aerotwin) with those of a conventional model

This experimental work was conducted in the aeroacoustic wind tunnel of AUDI in Ingolstadt (Germany) on a serial model of the sedan car 'AUDI A6', right hand drive. The author acknowledges Dr. Wickern and Mr. Miehling [2] and Dr. Martin Fischer [3] for the organisation and the intensive co-operation before and during the measurements.

6.1 Configuration

Wind tunnel

The aeroacoustic AUDI wind tunnel is a closed-loop open test section wind tunnel with a nozzle size of 11 m^2. It is powered by a 2.6 MW fan and is capable of a maximum speed of 300 km/h. The minimum inflow turbulence yields $\sim$ 0.3 %. The test volume is embedded into a semi-anechoic chamber with a background noise (averaged over the chamber, outside the flow) of $\sim$ 60 dB at a speed of 160 km/h. Figure 6.1 shows the test car in the wind tunnel.

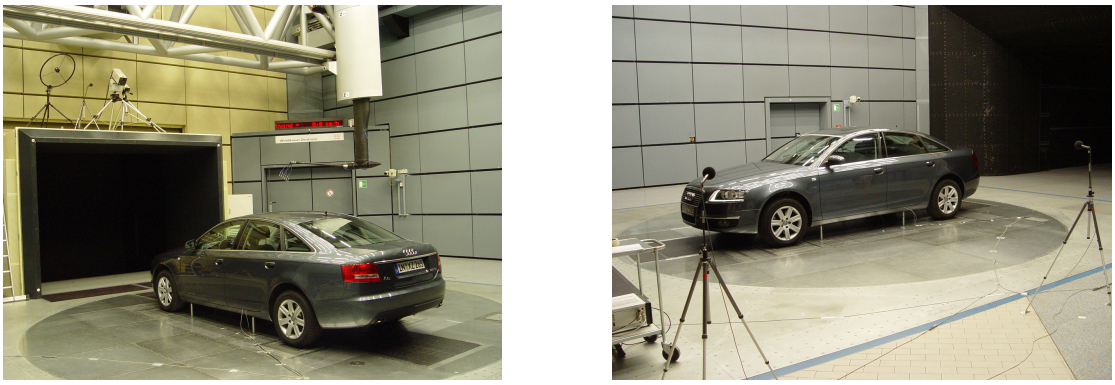

Figure 6.1: *Interior of the aeroacoustic wind tunnel (AUDI AG) and test car AUDI A6*

Measurement Systems

In order to reach the objectives stated previously, measurements of the sound pressure field outside and inside the car and of the vibrations of the wind screen have been carried out with the following systems:

- Acoustic camera (description of the measurement technique in section 2.3.2)
- Artificial Head Measurement System (HMS) [111] (not used in binaural recording modus)

[2] AUDI AG
[3] Robert Bosch GmbH

- Conventional capacitive microphones (0.5 inches) with wind-shield.
- Fixed and scanning laser vibrometers (Polytec PSV 300) (description of the measurement technique in section 2.3.3)
- Accelerometers

The microphones 1 and 2 are placed inside the car, respectively between driver and front passenger and close to the windscreen, while those numerated from 3 to 6 are placed outside around the car. The artificial head is placed at about the same position of the head of a typical adult driver. The acoustic camera and the lasers are located on the top of the wind tunnel nozzle and view the windscreen from outside. Figures 6.2 and 6.3 show the disposition of the measuring systems during the investigation.

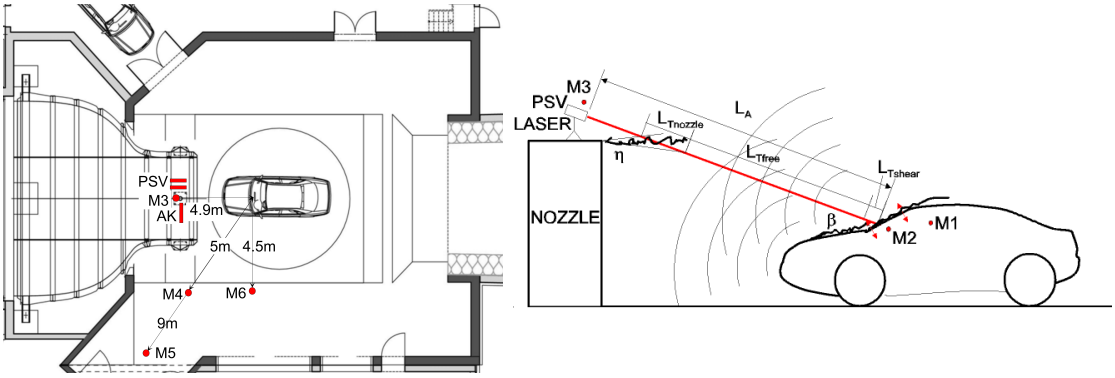

Figure 6.2: *Position of the measurement equipment: top view (left) and side view (right). Acoustic Camera (AK), Laser Vibrometer (PSV), reference Laser and Microphones (M1–M6). The distances crossed from the laser beam through the acoustic waves (L_A) and turbulence (L_T at nozzle, free jet and shear layer on the car) are also sketched.*

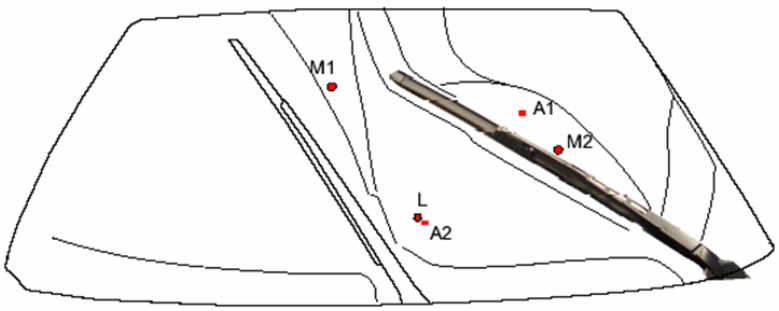

Figure 6.3: *Position of the measurement probes projected onto the windscreen: spot of reference laser (L), accelerometers glued on the interior side of the windscreen (A1, A2), and microphones (M1, M2) inside the car near the windscreen. Thin solid lines indicate particular streamlines around the screen wiper, further explained in figure 6.9.*

Measurement Campaign

Measurements are carried out at a nozzle speed of 140 km/h (≈ 39 m/s) and 200 km/h (≈ 56 m/s) for two screen wiper geometries during the wiping movements and for fixed

position.
The investigated wipers are modern 'aerotwin' wipers and common 'arch'-wipers (Figure 6.4). The investigations are carried out for single and double wiper configurations. Moreover the influence of a conventional spoiler on the arch-wiper has been tested.

Figure 6.4: *Geometry of the investigated Bosch screenwipers: conventional arch-wiper without spoiler(a), aerotwin wiper (b).*

The engine of the car was turned off and the wheels were standing still. The air temperature in the wind tunnel varied during measurements between 27 and 30 °C.

6.2 Screen Wiper Contribution to Overall Noise

The sound pressure during the wiping movement has been measured in the car interior (artificial head) for the highest flow speed of 200 km/h. The wiper at rest position under the hood has been taken as reference configuration for sound measurement. By plotting the spectra difference over the duration of the wiping movement (Figure 6.5) one discovers therefore the contribution of the screen wiper noise. First, the highest noise contribution arises in the downward movement. Second, for all wiper types on the present vehicle, the highest contribution yields at about 20-25 % of the cycle starting from the top (for single wiper)[4]. This corresponds to a inclination of the driver-side wiper of about 40° from the top of the A-Pillar. This position will be called 'critical position' in the following.
Moreover one notices that the sound level increase is very perceivable in two frequency domains:

1) 250 – 500 Hz (up to 2 dB)

2) 2500–7000 Hz (up to 4 dB)

In particular, the 'aerotwin' wiper system is louder in the first domain while the conventional one is louder in the second one (Figure 6.6).
This noise is assumed to be of purely aeroacoustic nature instead of mechanical one. In fact, it does not result from turning the wiper blade up and down at the end of the movement. Besides, it is not a 'humming' noise, due to cavity resonances induced from the wiper movement, which typically arises at about 100 Hz. Moreover, this noise is still present for the wiper fixed in the critical position.

[4]Using two wipers the aerodynamic resistance increases. Therefore it takes more time to reach the critical angular position indicated above. Compare cycle position in figure 6.5 a) and b).

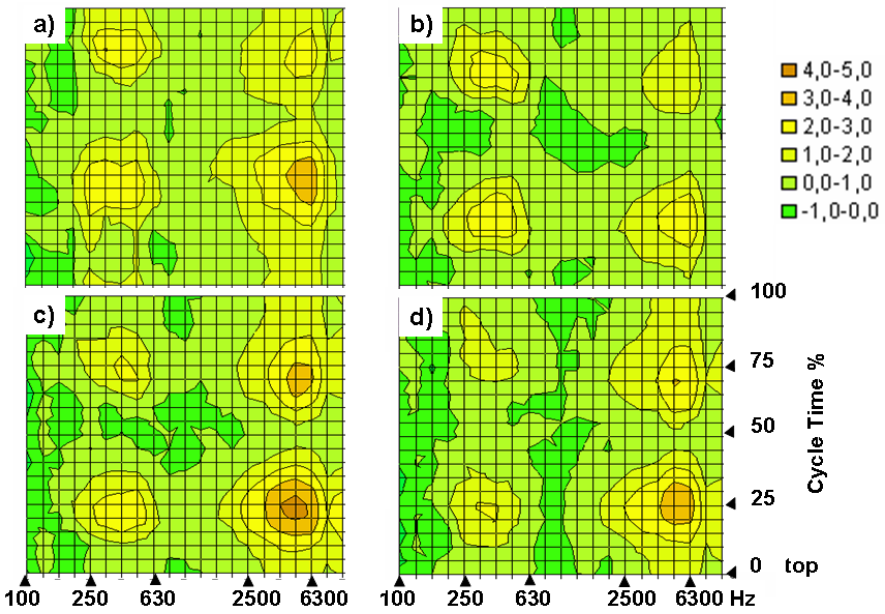

Figure 6.5: *Map of sound pressure differences from wiper in rest position under the hood for two aerotwins (a), aerotwin driver side (b), conventional wiper driver side with spoiler (c) and without (d). Speed $U =$ 200 km/h. Measurement with artificial head. Color legend in dB and third octave scaling for the x-axis. Plot courtesy of AUDI.*

The additional aeroacoustic noise due to the wipers in the critical position is perceivable although the aerodynamic noise level in the car interior is already high (at microphone 2 it yields about 79 dB for 200 km/h). This applies not just at selected frequencies but also as overall sound pressure level. The overall contribution yields + 1 dB for conventional wiper with spoiler and + 1.6 dB for 'aerotwin' (Figure 6.6). Moreover, plotting the spectra from the accelerometers placed on the windscreen over the time, one notices that the wiper, almost exclusively, is the source of high frequency noise. This can be seen in figure 6.8 as periodic stripes in the spectrum due the wiping movement. The contribution to the wind screen acceleration is quantified for the critical position of the wiper in figure 6.7. Outside (at microphone 3), the contribution of the screen wiper to the overall sound level is negligible (+ 0.4 dB), however, even here the frequency range above 1 kHz is still lightly increased (from 1 up to 1.5 dB).

The geometry of the screen wiper system effects also the sound spectrum. For high frequencies the conventional spoiler is more noisy than the aerotwin. The threshold depends on the measured point and measurement method and ranges here between 2 and 4 kHz. At this stage the cause for this difference is not clear. In the following other experimental methods are therefore used for a spatial mapping of the sound sources in order to answer this question.

6.3 Flow Visualisation

As we investigate sound sources of aerodynamic nature, the knowledge of the aerodynamic field around the screen wiper is necessary. The oil visualisation technique (Section 2.2.1) has been therefore used to visualise the flow field on the windscreen (Figure 6.9-a).

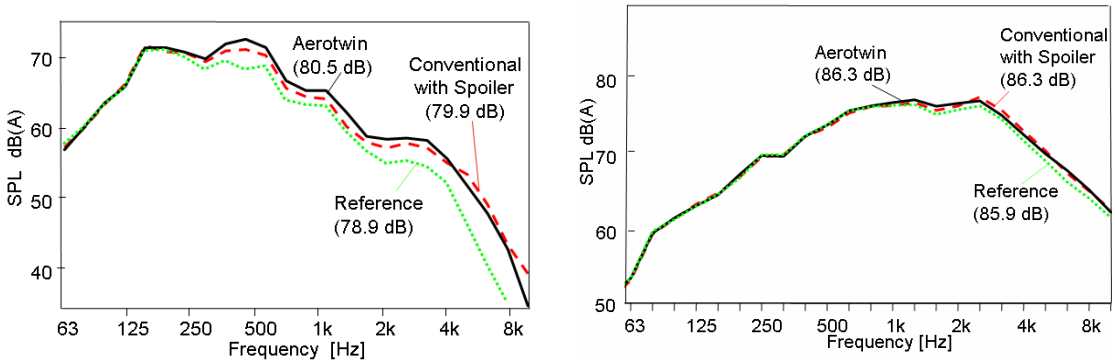

Figure 6.6: *Sound spectra for critical wiper position and for wiper at rest position (reference) for speed $U = 200\,km/h$ inside (microphone 2, left) and outside (microphone 3, right) the car. Third octave SPL. In bracket is the OASPL.*

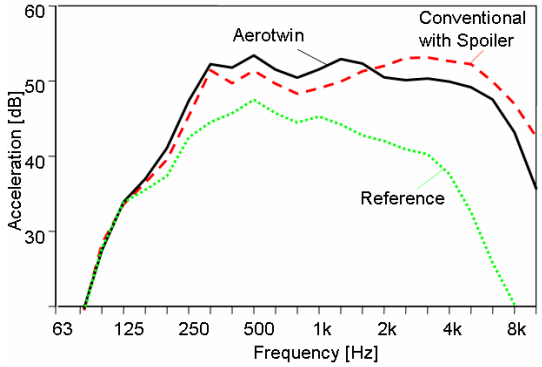

Figure 6.7: *Acceleration spectrum for critical wiper position and for wiper at rest position (reference) for speed $U = 200\,km/h$ at accelerometer 1. $0\,\mathrm{dB} = 1\,\mu\mathrm{m/s^2}$.*

For the critical position we distinguish recirculation regions off the hood edge (A1, A2) and the wipers (C1, C2), regions of parallel or slightly convergent streamlines (B1, B2) and of divergent streamlines (D1, D2). E1 and E2 indicate joining streamlines originating from different regions. F indicates the not-separated wake of the wiper. The largest separated region is located behind the driver wiper (C1). The three dimensional extension of this separation region is made visible with smoke in fig.6.9-b. The role of this separated flow region for noise source generation will become clear in the following section.

6.4 Localisation of Sound Sources

Once the contribution of aeroacoustic noise of the wiper to the overall sound pressure level of the car and its frequency spectrum is known (Section 6.2), the aeroacoustic sources can be localised spatially. This is done by selective filtering the signal from acoustic camera and laser interferometry.

The reconstruction algorithm of the acoustic camera is based on the assumption that the medium is at rest (Section 2.3.2). Therefore we expect an error in the localisation of the sources due to the flow convection in the wind tunnel. In order to quantify this effect, a punctual impulse generator was placed in the lower driver-side corner of the windscreen.

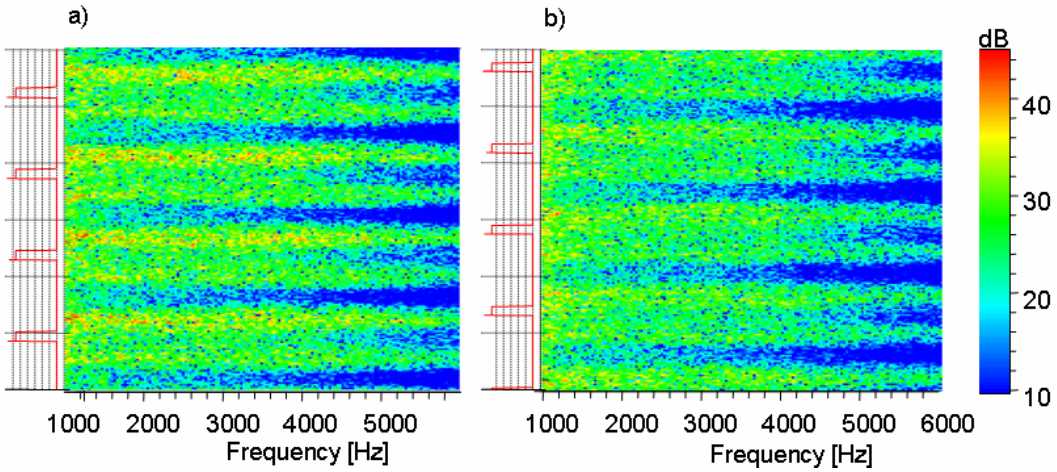

Figure 6.8: *Map of acceleration spectrum during four wiping movements; accelerometer position (1); conventional wiper with spoiler (a) and aerotwin (b); speed* $U = 140\,\mathrm{km/h}$. *Red diagrams show the direction change of the wiper at A-Pillar. Marks on vertical axis are spaced 1 second.* $0\,\mathrm{dB} = 1\,\mu\mathrm{m/s^2}$

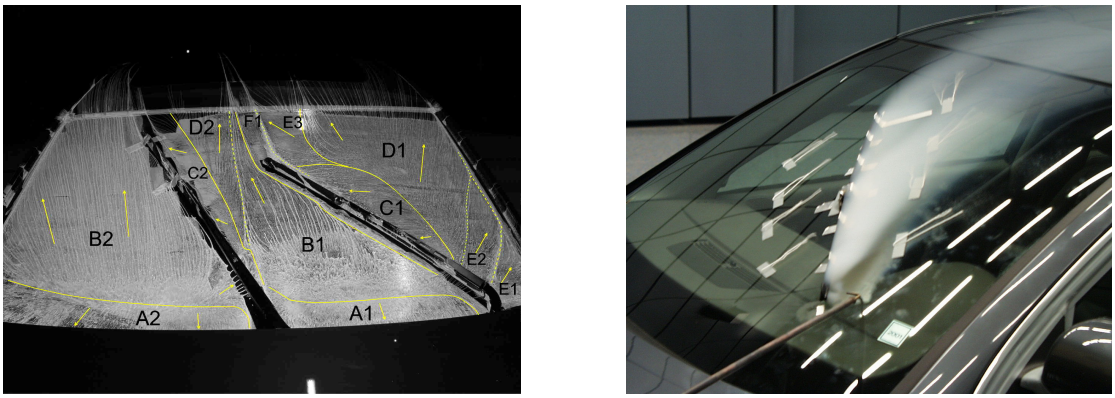

(a) (b)

Figure 6.9: *Flow visualisation for critical angle position of the screen wiper on the windshield and speed 200 km/h. a) streamlines along the windshield made visible with oil-film technique and topology: separating streamlines (solid lines) and joining streamlines (dashed lines). b) streaklines downstream the wiper made visible with smoke (Photo courtesy of AUDI).*

Figure 6.10 shows the position reconstructed from the acoustic camera without and with mean flow (140 km/h).

Once the convection effect is quantified it is possible to localise the aeroacoustic sound sources a posteriori. Here we assume that the convection effect remains the same for different positions on the screen wiper[5]. The localisation of aeroacoustic wiper sources is particularly effective for high frequencies because they are predominant. Even though the noise level captured at the acoustic camera (same level as microphone 3, in figure 6.6) is very low the position can be localised precisely.

[5]The assumption is acceptable as long as the thickness and the velocity of the flow, from the view point of the acoustic camera, over the windscreen is about constant.

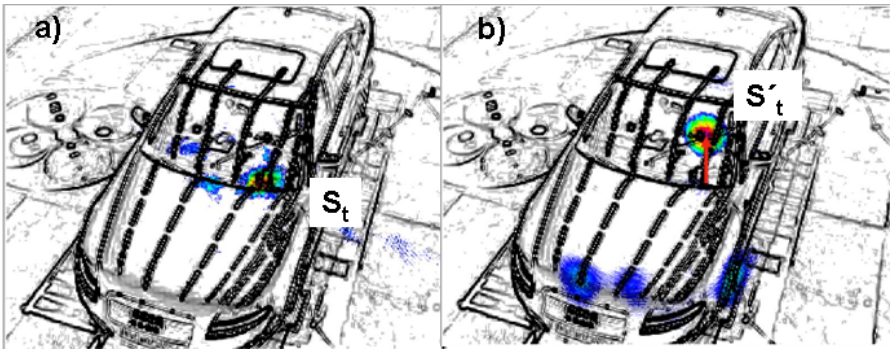

Figure 6.10: *Location of a test impulse source (S_t) by acoustic camera for a) air at rest and b) for 140 Km/h (S'_t). The displacement due to the wind tunnel speed is marked with a red arrow.*

Figure 6.11 shows the reconstructed position for this source.

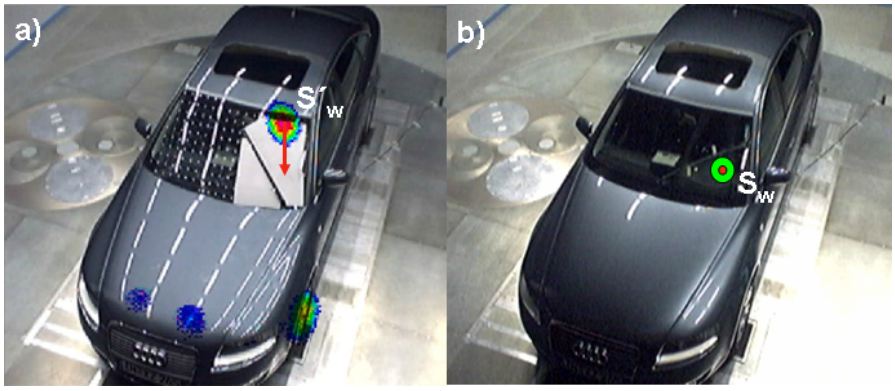

Figure 6.11: *Location of sound sources (frequencies above 5000 Hz) by acoustic camera for wind tunnel speed = 140 km/h (S'_w) in (a) and correction with respect to flow convection for the originating position (S_w) in (b).*

At lower frequencies it is more difficult to localise the aeroacoustic sound sources due to the screen wiper because they are less predominant within the overall aerodynamic noise. However laser interferometry can bring more insight here. The laser beam, pointed onto the windscreen from the outside, measures both windscreen vibrations and pressure fluctuations, as sketched in Figure 6.2-right. Differently from the preparatory investigation in section 4.2.1.2, where the laser beam was reflected from behind the transparent plate, here the reflectors are glued onto the surface (wiper screen), due to lack of space in the car interior, therefore vibrations can be detected.

Under the assumption that the acoustic pressure fluctuations can be neglected respect to the hydraulic pressure fluctuations, the measured effective velocity v_{eff} [6] is the sum of two contributions:

$$v_{eff} = v_{vib} + v_{turb} \tag{6.1}$$

$$\alpha(f) \stackrel{\text{def}}{=} \frac{v_{vib}}{v_{eff}} = \begin{cases} 1 & \text{(no turbulence)} \\ 0 & \text{(surface at rest)} \end{cases} \tag{6.2}$$

[6] See section 2.3.3

where v_{vib} is the contribution due to vibrations normal to the windscreen surface, v_{turb} the contribution due to flow turbulence and α a function of the frequency f.

The time derivative of the measured signal (v_{eff}) corresponds to an acceleration. In the following this quantity is compared to the acceleration measured by accelerometers in the same position (but on the interior side) as the laser measuring spots. The measured vibrations are caused, in general, by the flow around the whole car, not necessary due to the screen wiper alone. In Figure 6.12 we separate these contributions by comparing the signal at two points, whose fluid dynamic field is either significantly influenced from the wiper (1) or not (2).

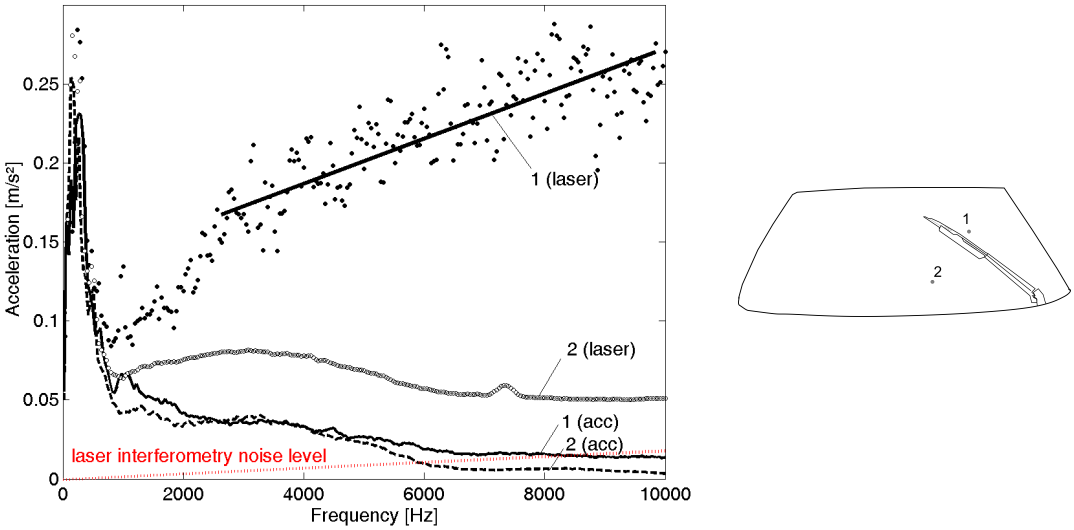

Figure 6.12: *Comparison of signals from accelerometer (acc) and laser interferometry (laser) for a conventional wiper at critical position and 140 km/h. The accelerations are measured in the points 1 and 2 (right).*

Upstream of the screen wiper (point 2) the spectra of accelerations measured with laser and accelerometers have similar shape with a quite constant offset above about 1500 Hz. Considering that downstream of the wiper (point 1), the spectra differ completely, particularly above about 1500 Hz again, we can exclude an offset in sensor calibration to be the cause. We see here more evident explanation in the turbulence induced from the wiper. Downstream of the wiper, the turbulence plays the largest role in the measured signal from laser ($\alpha \to 0$ in the model of Eq.6.1). From previous investigations in this work we know that this is definitely the source of noise. On the other hand, the acceleration on the screen represents not the cause but the *effect* of a pressure fluctuation on the wind screen structure. This is visible in the signal increase between the accelerometers: the vibrations downstream the wiper are larger. Also in the region upstream of the wiper the turbulence plays a role in the measured signal. It is however much smaller than downstream the wiper.

At lower frequencies the complete wind screen structure is excited. Here the acceleration amplitude is larger and the signal is dominated from vibration of the screen wiper.

One observes frequency peaks whose positions remain constant when increasing the velocity (a and b in picture 6.13). These are presumably structure resonances of the

wind screen. On the other hand, a frequency shift is visible for broad band accelerations (c in picture 6.13) whose origin is assumed to be a combination of shear layer turbulence from the wind tunnel nozzle and from the bonnet of the car.

The length of the laser beam crossing turbulent regions plays a large role in the absolute value measured with the laser: in fact it is an integral length (Section 2.3.3). This length is deduced easily from the figure 6.2: assuming the slope of shear layer expansion $\eta \sim \pm 0.15$(characteristic for medium Reynolds numbers up to $\sim 10^5$ [112]), a laser beam inclination of $\sim 30°$ and the given geometrical configuration, one obtains the length $L_{T_{nozzle}} \sim 1.2\,\mathrm{m}$. As $L_{T_{shear}}$ is much smaller (few centimeters), it can be concluded that the source of the offset between acceleration measured with laser interferometer and accelerometers at point 2 (Fig.6.11) is, at least partially, related to the shear layer of the wind tunnel nozzle rather than to the bonnet.

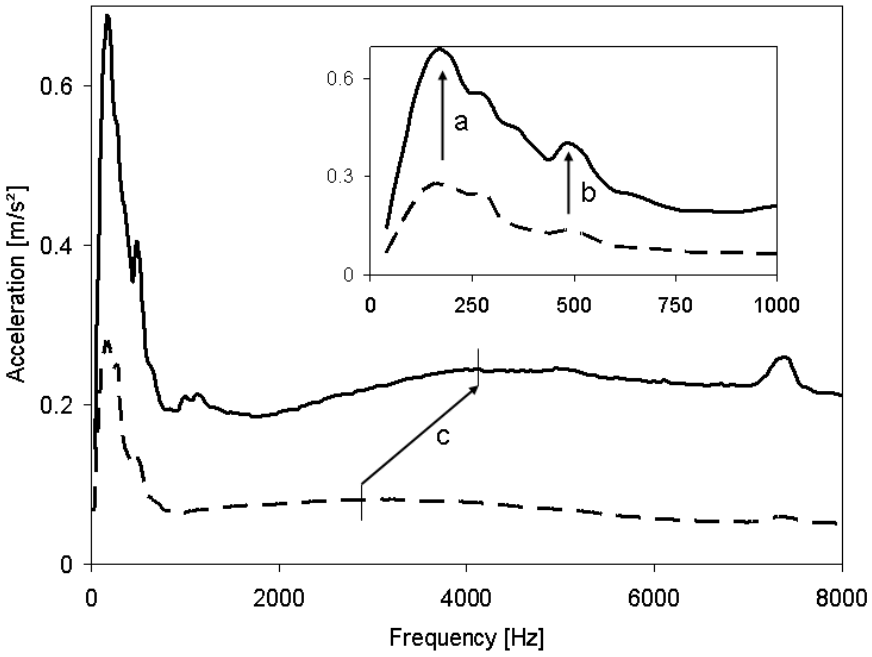

Figure 6.13: *Comparison of laser interferometry measurements at 140 (dashed line) and 200 km/h (solid line) for point 2. In the inset (top right) the frequency range up to 1000 Hz is enlarged.*

Increasing the speed the contribution of the turbulence is even more evident (Figure 6.14). A linear regression approximates well the acceleration signal from the laser interferometry in the frequency range 2000-10000 Hz (140 km/h) and 3000-10000 Hz (200 km/h).

The comparison of different wiper systems reveals the different location of the highest turbulent region: for aerotwin is near point 2, while it is near point 1 for conventional one. This is visible in figure 6.14. Moreover one sees that the signal is more intense for the conventional wiper at both positions in the range 2-8 kHz. This is an indicator of the sound source intensity and confirms the previous observation (fig. 6.6) that the conventional wiper is more noisy than aerotwin in this frequency range.

In figure 6.16 one can see the different distribution of the turbulent region over the windscreen. Here we see the direct consequence of the wiper strut of aerotwin and of the

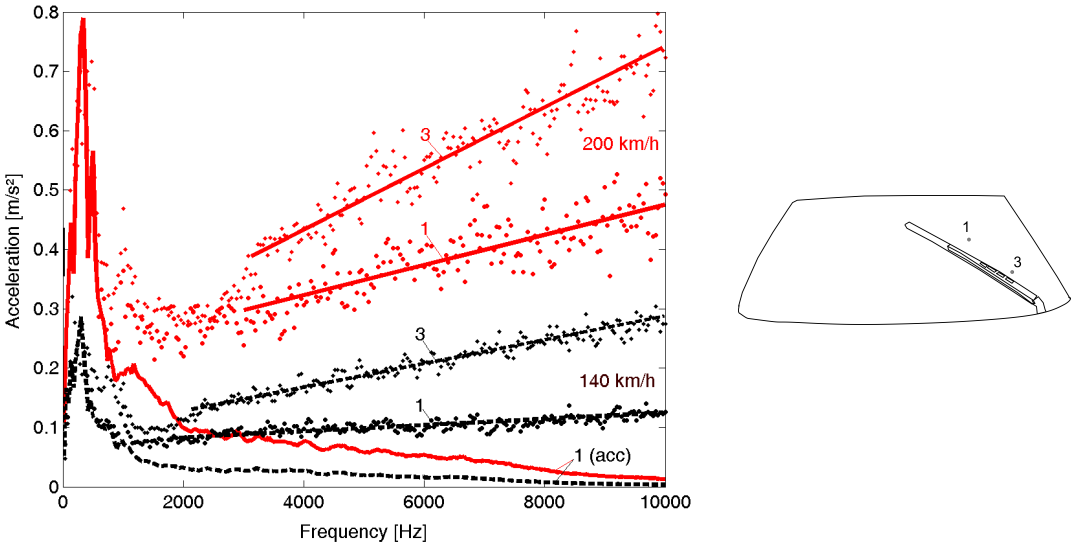

Figure 6.14: *Comparison of signals from accelerometer and laser interferometry for aerotwin wiper at critical position for 140 (black dashed line) and 200 km/h (red solid line). Measurement points are 1 (laser and accelerometer) and 3 (only laser).*

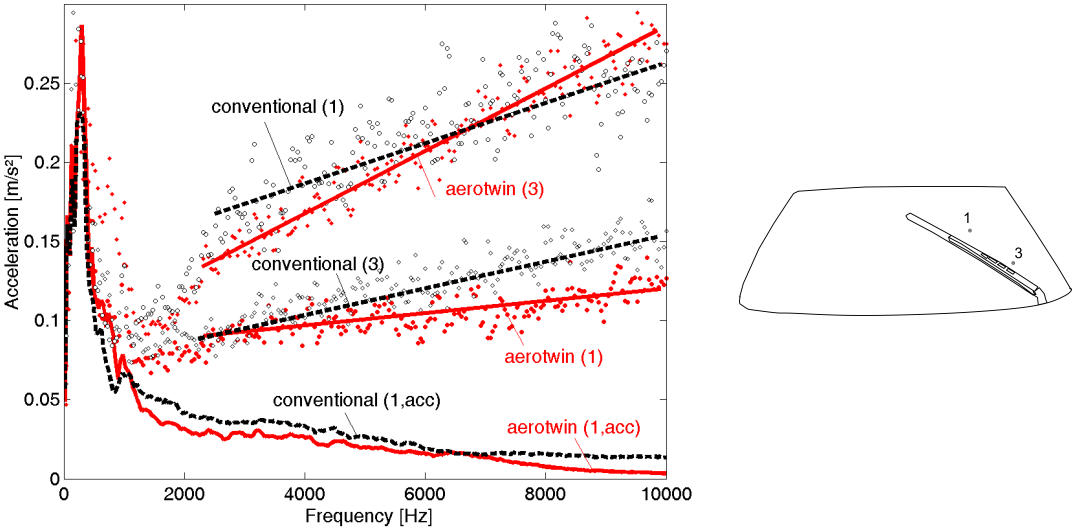

Figure 6.15: *Comparison of signals from accelerometer (acc) and laser interferometry for conventional wiper (dashed black line and unfilled symbols) and aerotwin wiper (solid red lines and filled symbols) at critical position for 140 km/h. Measurement points are 1 (laser and accelerometers) and 3 (only laser).*

spoiler of the conventional wiper. The turbulence distribution reflects the distribution of aeroacoustic sound sources. Furthermore one sees that the source for the conventional wiper is more extended than for the aerotwin for frequencies between about 4-8 kHz. This reinforces furthermore the previous observation that the conventional wiper is more noisy than aerotwin in this frequency range.

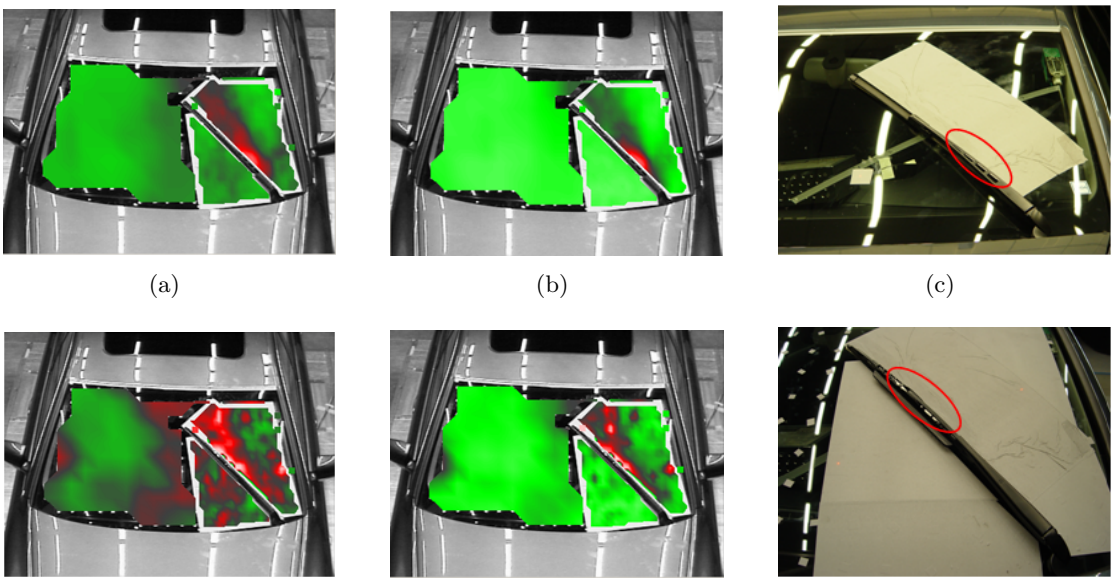

(a) (b) (c)

(d) (e) (f)

Figure 6.16: *Aeroacoustic measurement with Laser interferometry. Plot of rms value of signal v_{eff} for aerotwin (4000 Hz (a), 8000 Hz(b)) and conventional wiper (4000 Hz (d), 8000 Hz(e))for wind speed = 140 Km/h. Color coding: red (maximum) = 4 $\mu m/s$ (4 KHz). Localisation of maxima for aerotwin (c) and conventional wiper (d)*

The laser interferometry allowed also to localise shear waves in the windscreen originated from the wiper. For this, the variable measured is the product of v_{eff} and the pressure signal at the microphone 1 , in order to enhance particularly the excitations correlated with the sound inside the car.

Figure 6.17 shows shear waves at 400 and 3000 Hz from the bottom strut (a,c) and at 1400 Hz from the wiper (b).

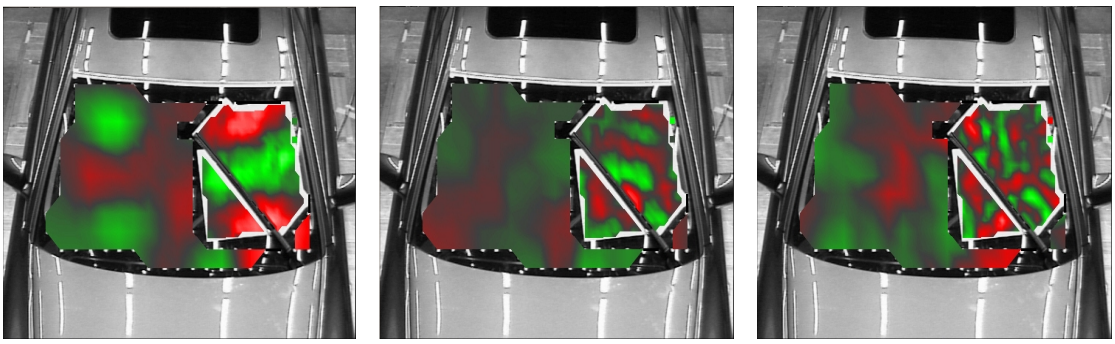

(a) 400 Hz (b) 1400 Hz (c) 3000 Hz

Figure 6.17: *Aeroacoustic measurement of aerotwin wiper on Audi A6 windshield with Laser Vibrometry. Instant value of a derived variable for wind speed = 200 Km/h. The variable is here the product of v_{eff} from laser interferometer and the pressure signal at microphone 1 [m/s*Pa].*

6.5 Conclusions

In this section it has been shown that the wiper strut and the supporting arm contribute to aeroacoustic noise perceivable from passengers mainly in two frequency domains. High-frequency sources (4000-8000 Hz) can be precisely located on the windscreen even during the wiping movement with the acoustic camera.

The comparison of this location to regions of high hydraulic pressure fluctuations, measured with laser interferometry, shows a very good agreement. This confirms the aeroacoustic nature of the source and suggests the recirculation region downstream of the wiper to be the cause. This position depends essentially from the supporting arm and spoilers applied on the wiper. The position does not change significantly by varying the flow speed (140-200 km/h). We assumed that the larger sound level of the conventional screen wiper (particularly for frequencies between 4 and 8 kHz) is a direct consequence of the extension and the intensity of the sound source on the wind screen.

We could show that the laser interferometry is an exceptional tool for the aerodynamic sound source localisation. The deviations in the acceleration measured with laser interferometer and accelerometers are in fact not a disturbance but rather a valuable information. From this we can derive an indicator for the sound source intensity.

At lower frequencies (250-500 Hz) the wiper system contributes to the overall sound level even more due to higher pressure levels. This contribution is however very difficult to localise spatially because it is masked from vibrations of the windscreen of other aeroacoustic nature. Here it is supposed that low-order modes of the windscreen are excited. For middle frequencies (1000-2000 Hz) the sound contribution of the wiper is limited nevertheless one can clearly see shear waves in the windscreen originating from it.

A comparison of this extremely complex configuration with the simplified geometries investigated previously in this work is difficult. However one assumes that, similar to the impinging jet on obstacles, the aeroacoustic noise generated from the wiper has two domains of interest: a strong and relatively small band at low frequency and one of broader band type at high frequency in the wiper downstream region.

For further investigation we stress the importance of pressure measurements on the exterior side of the wind screen in order to calculate the transmission properties of the wind screen. Moreover we suggest the use of reflectors inside the car for measurement with laser interferometry in order to separate more easily the contribution of the wind screen vibration from the turbulence in the measured signal.

Chapter 7

Conclusions and Outlook

This work presented a systematic validation and comparison of various numerical aeroacoustic prediction techniques for broad band noise. The investigation encompassed the fluid dynamic field, the source location and the propagation of sound for subsonic flow impinging on plates with or without obstacles (simplified screen wiper geometries).

In this context it was necessary to develop the coupling between codes (DES and LEE) and to implement own aeroacoustic approaches (SNGR).

Moreover a number of experimental methods and facilities have been selected, set up and in part developed for the validation of those numerical approaches. These include the co-design of a small aeroacoustic wind tunnel and the design of a traversing unit for automatic positioning of measurement probes. For the fluid dynamic measurements it was necessary to set up a laser Doppler anemometry and hot-wire anemometry system. For acoustic measurements, a near field holography system was utilised and laser interferometry systems were developed.

Within the preliminary investigations of section 4, we have shown the feasibility of the coupling between codes (DES and LEE). Moreover, the investigations presented in section 2.3.3.3 and particularly in section 4.2.1.2 indicated that laser interferometry is more precise in the localisation of aeroacoustic sound sources than, for instance, near field holography and is extraordinary helpful for the analysis of wave propagation. Moreover a relatively good qualitative agreement with the numerical source distribution has been achieved. However, this method suffers from the fact that the acoustic field is integrated over an optical path.

The turbulence level predicted with unsteady detached simulations showed large deviations from experimental results in the wake of the obstacles. Moreover it was shown that differences in the intensity and spectra of the turbulence between simulations and experiments were influenced by the topology of the numerical domains and, in particular, from the merging of the numerical domains. For symmetric configurations, the sound propagation calculated with a 2D code was corrected successfully to a 3D field.

Our investigation of section 5 have shown that the main sound sources are located at the obstacle itself and in the region where the flow reattaches to the wall. The latter has more intense emission in the higher frequency range, the former in the lower frequency range.

The stochastic modeling of the velocity fluctuations using the SNGR (Stochastic Noise Generation and Radiation) approach was investigated with a commercial implementation as well as the author's own implementation. The length scales of the turbulence

appeared to play a larger role than the absolute value of the turbulence. A parametric study indicated the sensitivity of the scales. An approach based on Lagrange multiplicators has been presented in order to reduce the spurious source terms which arise from the generation of stochastic turbulence (divergence of the turbulent field).

In this work the best numerical results have been achieved with a direct approach based on the Lattice-Boltzmann method. At present, the numerical efficiency and the accuracy of the acoustic solution is considered superior to the other methods for this class of aeroacoustic problems.

Moreover in this work several concepts have been presented to reduce the sound emitted by changing the obstacle geometry. In one realisation, an air pillow generated from an air jet created under the obstacle energises the recirculation region and avoids the buffeting in the impinging region. The efficiency of the concept has been demonstrated experimentally.

The last part of the thesis was dedicated to the experimental evaluation of screen wiper contribution to the overall aeroacoustic noise of a modern car, the localisation of the sound sources and the comparison between different constructive types. It was found that the sound generation mechanisms, investigated previously in this work on simplified geometries can be found also in real windscreen wipers in the full-scale automotive environment.

As outlook of this work we see the capability to perform efficient and reliable simulations of aeroacoustic noise generated from components (like screen wipers) on complete vehicles using lattice Boltzmann methods. Moreover, due to its great potential in the physical comprehension of sound mechanism, we see the interest of a further methodical development of laser interferometry for aeroacoustic applications.

Bibliography

[1] M.J. Lighthill, On Sound generated aerodynamically. I. General Theory. Proc.R.Soc.London A211, pp. 564-587, 1952

[2] M.E. Goldstein, *Aeroacoustics*, McGraw Hill, 1976

[3] R.C. Pankhurst, D.W. Holder, *Wind Tunnel Technique*, Sir Isaac Pitman and Sons, London, 1965

[4] A. Pope, *Wind-Tunnel Testing*, John Wiley and Sons, 2nd Edition, New York, 1964

[5] Emissionskennwerte technischer Schallquellen – Ventilatoren, VDI Richtlinien 3731, 1990

[6] Aerodynamics of Road Vehicles, edited by W.-H. Hucho, Butterworth-Heinemann Ltd, 1987

[7] R. Fernath, Inbetriebnahme eines Aeroakustik-Prüfstands, Diplomarbeit am Institut fuer Termische Strömungsmaschinen und Maschinenlaboratorium (ITSM), Universität Stuttgart, 2001

[8] W. Lips, *Stroemungsakustik in Theorie und Praxis*, Expert-Verlag, 2001

[9] R.D. Metha, P. Bradshaw, Design rules for small low speed wind tunnels, The Aeronautical Journal of the Royal Aeronautical Society, p.443-449, 1979

[10] M.J. Cohen, N.J.B. Ritchie, Low speed three-dimensional contraction design, Journal of the Aeronautical Society, Vol.66, pp.231-236, 1962

[11] G.-G. Boerger, Optimierung von Windkanaldüsen fuer den Unterschallbereich, ZfW, Vol.23, 1975, pp. 45-50

[12] T. Morel, Design of two-dimensional wind tunnel contractions, J. Fluids Eng., pp. 371-378, 1977

[13] E. Witoszynski in *Über Strahlerweiterung und Strahlablenkung, Vorträge über Hydro- und Aeromechanik*, Edited by Th.v. Karman, pp.245-251, Berlin 1924.

[14] A. Kaltenhauser, unpublished data from an aeroacoustic seminar hold at 'Haus der Technik', Essen 2002

[15] K.B.M.Q. Zaman, Flow field and near and far sound field of a subsonic jet, Journal of Sound and Vibration, 106,1-16, (1986)

[16] W.A. Olsen, J.H. Miles, R.G. Dorsch, Noise generated by impingement of a jet upon a large flat board, (NASA Report TN D-7075,1972)

[17] W.C. de Leeuw, H-G. Pagendarm, F.H. Post, B. Walter. Visual Simulation of Experimental Oil-Flow Visualization by Spot Noise Images from Numerical Flow Simulation , in: R. Scateni et al. (eds) Visualization in Scientific Computing '95, Springer Verlag, Vienna, 1995, pp.135-148

[18] H.H. Bruun, *Hot-Wire Anemometry - principles and signal analysis*, Oxford University Press, 1995

[19] A. Roshko, On the development of turbulent wakes from vortex streets, NACA Rep. 1191, 1954

[20] D.C. Collis and M.J. Williams, Two-dimensional convection from heated wires at low Reynolds numbers, Journal of Fluid Mechanics, Vol. 6, pp. 357-389, 1959

[21] F. Durst, A. Melling, J.H. Whitelaw, *Principles and practice of laser-Doppler anemometry*, Academic Press (1981)

[22] K.D. Jensen, Flow Measurements, in: J.of the Braz. Soc. of Mech. Sci. & Eng., Vol.26, No.4,2004 pp.400-419

[23] E.G. Williams, *Fourier Acoustics* (Academic Press,1999)

[24] G. Heinz, Wave Interference Technology - Übergaeange zwischen Raum und Zeit, 43rd International Scientific Colloquium, Technical University of Ilmenau, 1998

[25] M. Fink, Time-reversed acoustics, Physics Today, Vol.50, No.3, pages 34-40, 1997

[26] L. Zipser, S. Lindner, R. Behrendt, Interferometrische Messung und Visualisierung von Schallwellen und Turbulenzen, Technisches Messen, Oldenbourg Verlag, 6, 275-281 (2002)

[27] N. Mayrhofer, Optische Strömungsmessung im Turbomachinen mit Laser-Interferometern, Dissertation an der technischen Universität Graz, 2001

[28] N. Mayrhofer, J. Woisetschlaeger, Frequency analysis of turbulent compressible flows by laser vibrometry. Exp. Fluids 31, 153-161, (2001)

[29] G. Litfin, Technische Optik in der Praxis, Springer, 1997

[30] Nobel Lectures, Physics 1901-1921, Elsevier Publishing Company, Amsterdam, 1967

[31] H. Schlichting *Boundary-Layer Theory*, McGraw-Hill Classic Textbook Reissue Series, 1987

[32] E.F. Toro *Riemann Solvers and Numerical Methods for Fluid Dynamics: a practical introduction*, Springer-Verlag, Berlin Heidelberg, 1999

[33] S.B. Pope *Turbulent Flows*, Cambridge University Press, 2000

[34] D.G. Crighton, A.P. Dowling, J.E. Ffowcs Williams, M.Heckl and F.G. Leppington, *Modern Methods in Analytical Acoustics*, Lecture Notes, Springer-Verlag, 1992

[35] A. Powell, Aerodynamic noise and the plane boundary, Journal of the Acoustical Society of America, Vol.32, No.8,1960, pp.982-990

[36] C.L. Morfey, The role of viscosity in aerodynamic sound generation, International Journal of Aeroacoustics, 2(16), 225-240, 2003

[37] J.H. Ferziger, M. Peric, *Computational Methods for Fluid Dynamics* Springer-Verlag, 2002

[38] G.M. Lilley, in *Computational Aeroacoustics*, edited by J.C. Hardin and al., 'On the noise radiated from a turbulent high speed jet', (Springer-Verlag, 1992)

[39] T.W. Wu in *Boundary Element Acoustics* edited by T.W. Wu, 'The Helmholtz integral equation', WIT Press, 2000

[40] W.C. Reynolds, The potential and limitations of direct and large-eddy simulations, in *Whither Turbulence ? Turbulence at the Cross Roads*, J.L.Lumley ed., Springer Verlag, 1990

[41] U. Frisch, *Turbulence. The legacy of A.N. Kolmogorov*, Cambridge University Press, 1995

[42] F. Wu, A Survey of Numerical Methods for Computational Aeroacoustics Presentation at Cemracs Summer School, 2005

[43] J.C. Hardin, D.S. Pope, An Acoustic/viscous splitting technique for computational aeroacoustics, Theoret.Comput.Fluid Dynamics, 6(5-6),323-340 (1994)

[44] W.Z. Shen, J.N.Sorensen Comment on the Aeroacoustic Fomulation of Hardin and Pope, Readers' Forum, AIAA, Vol.37,1 pp.141-143 (1999)

[45] M. Strelets, Detached eddy simulation of massively separated flows, AIAA 2001-0879 (2001).

[46] J. Becker, Entwicklung eines effizienten Verfahrens zur Lösung hyperbolischer Differentialgleichung, Dissertation, Mathematische Fakultät Universität Freiburg, 2000

[47] M. Dumbser, Arbitrary High Order Schemes for the Solution of Hyperbolic Conservation Laws in Complex Domains, Dissertation, Institut für Aerodynamik und Gasdynamik der Universität Stuttgart, 2005

[48] V.A. Titarev, E.F. Toro, ADER: arbitrary high order Godunov approach, Journal of Scientific Computing, 17 (2002), 609-618

[49] F.Menter, Turbulenzmodellierung II- Zweigleichungs-Turbulenzmodelle, in *Kurzlehrgang Turbulenz, Grundlagen der Turbulenzmodellierung*, 2003

[50] P.G. Saffman, On the fine-scale structure of vector fields convected by a turbulent fluid. J.Fluid Mech. 16,545.

[51] R.H. Kraichnan, Diffusion by random velocity field, the physics of fluids, Vol.13-1,(1970),pp.22-31

[52] J.O. Hinze, Turbulence, McGraw-Hill (1975)

[53] M. Karweit, P. Blanc-Benon, D. Juve, G. Comte-Bellot, Simulation of the propagation of an acoustic wave through a turbulent velocity field: a study of phase variance, J.Acoust.Soc.Am. 89(1),1991 pp.52-62

[54] W. Bechara, C. Bailly, P. Lafon , Stochastic Approach to noise modelling for free turbulent flows, AIAA,Vol.32,3, 1994,pp.455-463

[55] W. Bechara, P. Lafon, C. Bailly, S.M. Candel, Application of a k-epsilon turbulence model to the prediction of noise for simple and coaxial free jets, Journal Acoust. Soc.Am. 97 (6),1995

[56] C. Bailly, P. Lafon, S.M. Candel, A Stochastic Approach to compute noise generation and radiation of free turbulent flows, CEAS/AIAA, 95-092,(1995)

[57] C. Bailly, P. Lafon, S.M. Candel, Computation of noise generation and propagation for free and confined turbulent flows, CEAS/AIAA, 96-1732,(1996)

[58] E. Longatte, Modelisation de la propagation et de la generation du bruit au sein des ecoulements turbulents internes, These de Doctorat, Ecole Centrale Paris, (1998)

[59] C. Bailly, D. Juve , A Stochastic Approach to compute subsonic noise using linearised Eulers equations, AIAA, 99-1872,(1999)

[60] N. Kalitzin, A. Wilde, Stochastic modelling of turbulence in CAA simulations of airframe noise, SWING proceedings, edited by H.Koerner,J.Delfs DLR Braunschweig (2000)

[61] C. Bailly, C. Bogey, D. Juve, Computation of flow noise using source terms in linearised Eulers Equations, AIAA, 00-2047,(2000)

[62] R. Ewert, M. Meinke, W. Schroeder, Comparison of Source Term Formulations for a Hybrid CFD/CAA Method. AIAA, 01-2200,(2001)

[63] C. Bogey, C. Bailly, D. Juve, Computation of flow noise using source terms in linearised Eulers Equations, AIAA, Vol.40,N.2,(2002)

[64] M. Bauer, Berechnung der Schallabstrahlung ueberstroemter Hinterkanten, Diplomarbeit, Technische Universitaet Dresden (2002)

[65] R. Ewert, W. Schröder, Acoustic Perturbation Equations based on flow decomposition via Source filtering, J.Comput.Phys,(2003)

[66] M. Billson, L.-E. Eriksson, L. Davidson, Jet Noise Prediction Using Stochastic Turbulence Modelling, AIAA, 03-3282,(2003)

[67] R. Ewert, Q. Zhang, W. Schröder, J. Delfs, Computation of trailing edge noise of a 3D lifting airfoil in turbulent subsonic flow, AIAA, 2003-3114 (2003)

[68] R. Ewert, M.Bauer, Towards the prediction of broadband trailing edge noise via stochastic surface sources, AIAA, 2004-2861 (2004)

[69] User Manual of CAA-Module for Software Fire Version 8.4,TNO TPD,(2005)

[70] R. Ewert, CAA Slat Noise Studies Applying Stochastic Sound Sources Based on Solenoidal Digital Filters AIAA Paper 2005-2862, 2005

[71] F. Kemm, C.D. Munz, Divergenzkorrektur als Fehlermodellierung; DFG-report, 2000

[72] A. Smirnov, S. Shi, I. Celik, Random Flow Generation Technique for Large Eddy Simulations and Particle-Dynamics Modeling Journal of Fluids Engineering, ASME, Vol.123, pp.359-371, (2001)

[73] P. Bhatnagar, E. Gross, M. Krook. A model for collision processes in gases. I. small amplitude processes in charged and neutral one-component system. Pys. Rev., vol.94, pp.511-525, 1954.

[74] S. Succi *The Lattice Boltzmann Equation - for Fluid Dynamics and Beyond*, Oxford University Press, 2001

[75] Y. H. Qian, D. d'Humieres and P. Lallemand, Lattice BGK models for Navier-Stokes equation. Europhys.Letters, 17(6):479-484, 1992 *The Lattice Boltzmann Equation - for Fluid Dynamics and Beyond*, Oxford University Press, 2001

[76] B. Crouse, Lattice-Boltzmann Stroemungssimulationen auf Baumdatenstrukturen, Dissertation, TU München (2003)

[77] M. Krafczyk, Gitter-Boltzmann-Methoden: Von der Theorie zur Anwendung, Habilitationsschrift, TU München (2001)

[78] J. Tölke, Gitter-Boltzmann-Verfahren zur Simulation von Zweiphasenströmungen, Dissertation, TU München (2001)

[79] X. Shan, X. He, Discretization of the velocity space in the solution of the Boltzmann equation, Phys.Rev.Lett. 80, 65-68 (1998)

[80] B. Crouse, S. Senthooran, G. Balasubramanian, D. Freed, S. Noelting, L. Mongeau, J. S. Hong, Sunroof Buffeting of a Simplified Car Model: Simulations of the Acoustic adn Flow-induced Responses. SAE-Paper No. 2005-01-2498 2005.

[81] E. Fares, Unsteady Flow Simulation of the Ahmed Reference Body using a Lattice Boltzmann Approach. submitted to Elsevier Science, 2004.

[82] J. Halliday, C. Teixeira, C. Alexander, Simulation of Engine Internal Flows using Digital Physics. Oil & Gas Science and Technology-Rev.IFP, vol.54, no.2, pp.187-191, 1999.

[83] S. Chen, G. Doolen. Lattice Boltzmann Method for Fluid Flows. Ann. Rev. Fluid Mech., vol.30, pp.329-364, 1998.

[84] D. Wolf-Gladrow. *Lattice-Gas Cellular Automata and Lattice Boltzmnn Models*. Springer Verlag, Germany, 2000.

[85] M.M. Pervaiz, C.M. Teixeira. Two Equation Turbulence Modeling with the Lattice-Boltzmann Method. Proc. o. ASME PVP Division Conference, Boston, 1999.

[86] Y. Qian, D. D'Humieres, P. Lallemand. Lattice BGK models for the Navier-Stokes equations. Europhys. Lett., vol.17, pp.479-484, 1992.

[87] B. Crouse, personal communication, 2006

[88] J.M. Buick, C.A. Greated, D.M.Campbell Lattice BGK simulation of sound waves Europhys.Lett., 43(3),pp. 235-240 (1998)

[89] A. Hölzer, Simulation der Bewegung nicht-sprischer Partikel in turbulenten Stroemungen mit dem Lattice-Boltzmann-Verfahren Diplomarbeit an der Universität Merseburg, 2002)

[90] P. Lallemand, L.-S. Luo Theory of the lattice Boltzmann method: Acoustic and thermal properties in two and three dimensions Physical Review E, vol.68, no. 3 (2003)

[91] S. Senthooran, B. Crouse, G. Balasubramanian, D. Freed, S. Noelting, M. Gleason, M. Puskarz. Simulation of Wall Pressure Fluctuations on Simplified Automobile Shapes using a Lattice Boltzmann Method ASME, IMECE2005-81877, 2005.

[92] C. M. Teixeira. Incorporating Turbulence Models into the Lattice-Boltzmann Method. Int. J. Modern Physics C, vol.9, no.8, pp.1159-1175, 1998.

[93] H. Chen, C. Teixeira, K. Molvig, Realisation of Fluid Boundary Conditions via discrete Boltzmann Dynamics. Int. J. Modern Physics C, vol.9, no.8, pp.1281-1292, 1998.

[94] V. Yakhot, S. A. Orszag. Renormalization Group Analysis of Turbulence. J.Sci.Comput. 1, 3 1986.

[95] V. Yakhot, S. A. Orszag, S. Thangam, T. B. Gatski, C. G. Speziale. Development of turbulence models for shear flows by a double expansion technique. Phys. Fluids A, vol.4, no.7, pp.1510-1520, 1992.

[96] H. Chen Volumetric formulation of the lattice Boltzmann method for fluid dynamics: basic concept Phys.Rev. E 58(3),3955, 1998

[97] R. Zhang, H. Chen, Y.H. Qian, S. Chen. Effective volumetric lattice Boltzmann scheme. Physical Review E, Vol. 63, 2001.

[98] A.V. Bobylev, The Chapman-Enskog and Grad methods for solving the Boltzmann equation, Soviet Physics Doklady, 27 (1), 1982.

[99] M. Fischer, M. Zucchini, *Application of Laser-Scanning Interferometry on Aeroacoustic Problems*, in Fortschritte der Akustik, DAGA (2004)

[100] Ffowcs-Williams in *Modern Methods in Analytical Acoustics: Lecture Notes*,edited by D.G. Crighton, A.P. Dowling et al., (Springer, 1992), Chapter 11

[101] M.S. Howe, Contributions to the theory of aerodynamic sound with application to excess jet noise and the theory of the flute, J.Fluid.Mech,71,pp.625-673 (1975)

[102] F.R. Menter, M. Kuntz, R. Bender, *A scale-adaptive simulation model for turbulent flow predictions*, AIAA paper 2003-0767 (2003)

[103] F.R. Menter, M. Kuntz, *Development and aapplication of a zonal DES turbulence model for CFX-5*, Internal Validation Report 17/0503, Ansys (2003)

[104] R. Ewert, Q. Zhang, W. Schröder, J.Delfs, Computation of Trailing Edge Noise of a 3D Lifting Airfoil in Turbulent Subsonic Flow, AIAA, 2003

[105] M. Zucchini, M. Fischer *Experimentelle und numerische Untersuchung der strömungsinduzierten Schallentstehung an 3D-Geometrien auf Oberflächen*, in Fortschritte der Akustik, DAGA (2006)

[106] M.D. Rao, Recent Applications of Viscoelastic Damping for Noise Control in Automobiles and Commercial Airplanes, Journal of Sound and Vibrations, Vol.262,(3),2003, pp.457-474

[107] R. Siegert, V. Schwarz and J. Reichenberger, Numerical simulation of aeroacoustic sound generated by generic bodies placed on a plate, AIAA Paper 99-1895, 1999

[108] F. Perot, J.M. Auger, H. Giardi, C. Bailly, D. Juve, Computation of the noise generated by low Mach number flows around a cylinder and a wall-mounted half-cylinder, AIAA Paper 2004-2859, 2004

[109] Bosch Research Info, Internet Ausgabe 3/2003, *http://researchinfo.bosch.com/-de/research/archive/*

[110] A. Sanon, S. Jallet, Acoustic Sources localization: Application to wiper aerodynamic noises, SAE 2003-01-1700, 2003

[111] Head Measurement System (HMS), *http://www.head-acoustics.de*

[112] P.G. Saffman, On the fine-scale structure of vector fields convected by a turbulent fluid. J.Fluid Mech. 16,545.

Appendix A

Fourier Analysis

A.1 Fourier Transforms

The Fourier transform $F(\kappa)$ of a continuous single-variable function $f(x)$ is defined as [23]:

$$F(k_x) \equiv \int_{-\infty}^{\infty} f(x) e^{-ik_x x}\, dx \tag{A.1}$$

and represented throughout this work as $\mathcal{F}[f(x)]$.
The inverse transform becomes:

$$f(x) = \frac{1}{2\pi} \int_{-\infty}^{\infty} F(k_x) e^{ik_x x}\, dk_x \tag{A.2}$$

Straightforward is the application to n-dimensional functions $f(x_1, \cdots, x_n)$:

$$F(k_1, \cdots, k_n) \equiv \int_{-\infty}^{\infty} \cdots \int_{-\infty}^{\infty} f(x_1, \cdots, x_n) e^{-i(k_1 x_1 + \cdots + k_n x_n)}\, dx_1 \cdots dx_n \tag{A.3}$$

$$f(x_1, \cdots, x_n) = \frac{1}{2^n \pi^n} \int_{-\infty}^{\infty} \cdots \int_{-\infty}^{\infty} F(k_1, \cdots, k_n) e^{ik_1 x_1 + \cdots + k_n x_n}\, dk_1 \cdots dk_n \tag{A.4}$$

Among the important derivation regarding the Fourier transform we remember the derivative, the shift theorem and the convolution theorem. Written in one variable they read:
Derivative

$$\mathcal{F}\left[\frac{df(x)}{dx}\right] = ik_x \mathcal{F}[f(x)] \tag{A.5}$$

Shift theorem

$$\int_{-\infty}^{\infty} f(x - x') e^{-ik_x x}\, dx = F(k_x) e^{-ik_x x'} \tag{A.6}$$

Convolution theorem

$$\int_{-\infty}^{\infty} \left[int_{-\infty}^{\infty} f(x - x') g(x')\, dx' \right] e^{-ik_x x}\, dx = F(k_x) G(k_x) \tag{A.7}$$

and denoting

$$f(x) * g(x) \equiv \int_{-\infty}^{\infty} f(x - x') g(x')\, dx' \tag{A.8}$$

in shorthand it reads:

$$\mathcal{F}\left[f(x) * g(x)\right] = F(k_x) G(k_x). \tag{A.9}$$

A.2 The Helmholtz equation

It is often useful to compute the Fourier transform of the homogeneous wave equation, in order to consider phenomena in the frequency domain. That yields the Helmholtz equation:

$$\nabla^2 \hat{p} + \kappa^2 \hat{p} = 0 \tag{A.10}$$

where the acoustic wavenumber is κ=ω/c_0, the frequency is given by $2\pi f = \omega$. and $\hat{p}$ is the complex function $\hat{p}(x, y, z, \omega)$.
The Fourier transform of Eulers equation becomes, in the frequency domain:

$$i\omega\rho_0\vec{\hat{u}} = \nabla\hat{p} \tag{A.11}$$

where ρ_0 is the fluid density and $\vec{\hat{u}}$ the Fourier-transformed velocity field.
The function $\hat{p}(\omega) = A(\omega)e^{i(k_x x+k_y y+k_z z)}$ is a solution of the equation as long as

$$\kappa^2 = k_x^2 + k_y^2 + k_z^2 \tag{A.12}$$

A.3 Wavenumber space

The propagation of a plane wave can be obtained from the inverse Fourier transform of Eq.A.10:

$$p(t) = Ae^{i(k_x x+k_y y+k_z z-\omega t)} \tag{A.13}$$

or in condensed form:

$$p(t) = Ae^{i(\vec{k}\cdot\vec{r})} \tag{A.14}$$

with k the wave direction and $\vec{r} = x\vec{i} + y\vec{j} + z\vec{k}$, the position vector of the observer.

A.4 Wave-field extrapolation

The wave-field extrapolation (Eq. 2.8) is easily demonstrated from the fact that multiple-variable Fourier transforms are related through exponential functions like that:

$$F_x F_y \left[p(x, y, z)\right] \equiv P(k_x, k_y, z) = P(k_x, k_y)e^{ik_z z} \tag{A.15}$$

$e^{ik_z z}$ allows to calculate the wave amplitude from one plane to another, therefore, it is called *propagation operator* for the pressure field. In a similar way, applying Eq.A.16 to the Euler equation (Eq.A.11) and by using Eq.A.5, one obtains:

$$U(k_x, k_y, z)\vec{i} + V(k_x, k_y, z)\vec{j} + W(k_x, k_y, z)\vec{k} = \frac{1}{\rho_0 c\kappa}(k_x\vec{i} + k_y\vec{j} + k_z\vec{k})P(k_x, k_y) \tag{A.16}$$

For the velocity component perpendicular to the z-plane, it reads:

$$W(k_x, k_y, z) = \frac{k_z}{\rho_0 c\kappa}P(k_x, k_y, z')e^{ik_z(z-z')} \tag{A.17}$$

here, $\frac{k_z}{\rho_0 c\kappa}e^{ik_z(z-z')}$ is called *propagation operator* for the velocity field.
The reconstruction performed in the near field holography is based on the propagation operators and the angular spectrum. Williams [23] showed that the exponential decay

of angular spectrum balances the inverse propagator, therefore the propagation of a i.e. pressure field is well behaved. In practice, however the success of the reconstruction - in particular its stability - depends on the quality of the measurement. Spatial noise and excessive distance between measurement points on the measurement grid can lead to the destruction of this cancellation process. It is therefore compulsory to use low-pass k-space filters on the measured angular spectrum, in order to have limited integrals. The cut-off frequency is dictated from aliasing reason (spacing of the measurement grid) and from the degree of corruption of the measured data.

A.5 Spectra of the Isotropic Turbulence

In the followings are listed the equations of the three dimensional energy spectra for isotropic turbulence:

- Von Karman spectrum: $E(\alpha) = A\frac{\overline{\vec{u}^2}}{\alpha_e}\frac{(\frac{\alpha}{\alpha_e})^4}{(1+(\frac{\alpha}{\alpha_e})^2)^{17/6}}$ with:
  - A is an adimensional experimental parameter
  - α_e is the wave number at which $E(\alpha)$ has a maximum
- Saffman-Pao spectrum: it bases on von Karman spectrum but considers the spectrum decreasing for smaller turbulence length, that is for wave numbers bigger than the Kolmogorov wave number α_ν. For flows with high Reynolds number ($\alpha_e \gg \alpha_\nu$), Saffman [112] and Pao (1965) proposed :
  $E(\alpha) = A\frac{\overline{\vec{u}^2}}{\alpha_e}\frac{(\frac{\alpha}{\alpha_e})^4}{(1+(\frac{\alpha}{\alpha_e})^2)^{17/6}}e^{-2(\frac{\alpha}{\alpha_\nu})^2}$
  - A become a constant ≈ 1.453
  - ν is the kinematic viscosity of the fluid
  - α_ν is the Kolmogorov wave number, $\alpha_\nu = (\frac{\varepsilon}{\nu^3})^{\frac{1}{4}}$
  - from the integral constraints $\rightarrow \alpha_e = 0.73\frac{\varepsilon}{\overline{\vec{u}^2}^{\frac{3}{2}}}$
- Liepmann spectrum: $E(\alpha) = \frac{8}{\pi}\overline{\vec{u}^2}\Lambda\frac{(\Lambda\alpha)^4}{(1+\Lambda^2\alpha^2)^3}$ with:
  - $\overline{\vec{u}^2} = \frac{2}{3}K$
  - Λ is the integral length scale of the turbulence

From adimensional considerations, $\Lambda = K_\Lambda \cdot \frac{(\frac{2}{3}K)^{3/2}}{\varepsilon}$ where K_Λ is a adimensional factor. As consequence, the value of the integral length scale (Λ) and the maximum of the spectral energy $E(\alpha)$ are very similar but not identical:

$$\alpha_e = \frac{0.747K_\Lambda}{\Lambda} \tag{A.18}$$

Figure A.1 compares the three shapes for the same mean flow data and same integral turbulence variables (ε, K) and shows a subdivision of the wave length into three typical regions. Values are taken from the shear layer out of the test case (impinging jet) investigated in this work.

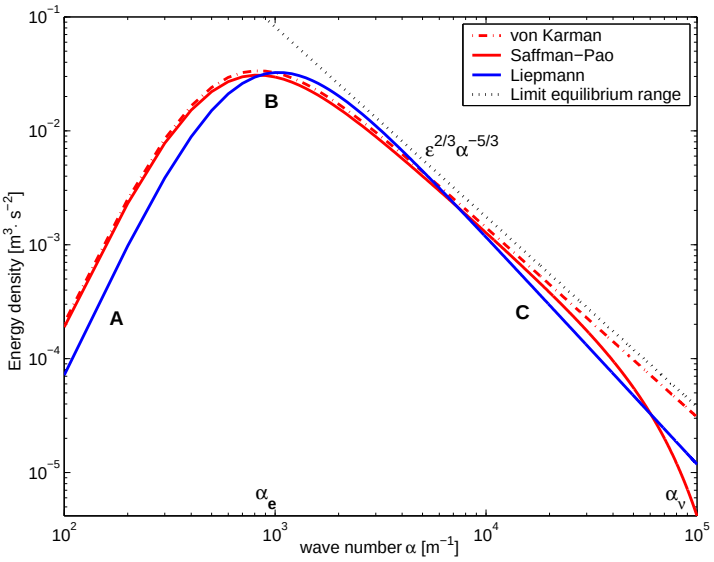

Figure A.1: *Comparison of three dimensional turbulence spectra. Values refers to exemplar point with* $K = 95\frac{m^2}{s^2}$ *and* $\varepsilon = 3.7 \cdot 10^5 \frac{m^2}{s^3}$ *with* α_ν *the Kolmogorov wave length and* α_e *the wave length for maximum energy. One distinguishes: a production region with largest eddies of permanent character (A), an inertial sub range (B) and a dissipative range (C).*

Appendix B

Experimental Facilities and Techniques

B.1 Nozzle Contours for the Wind Tunnel

A number of nozzles has been realised with rapid prototyping technique in the framework of this work. A contraction ratio of 5 for the 2D nozzle and of 6.9 for the axisymmetric nozzle has been used. Figure B.1 shows the contours used for two of the 2D nozzles. In this work only the nozzle with contour marked II has been extensively used for numerical validation. Both contours follows from the Witoszynski formula B.1:

$$y(x) = \frac{R_{out}}{\sqrt{1 - \frac{(1-(\frac{R_{out}}{R_{in}})^2)(1-\frac{x^2}{L^2})^2}{(1+\frac{x^2}{L^2})^3}}} \tag{B.1}$$

with R_{in} and R_{out} respectively the radius at nozzle inlet and outlet, L the length of the not rectilinear nozzle contour.

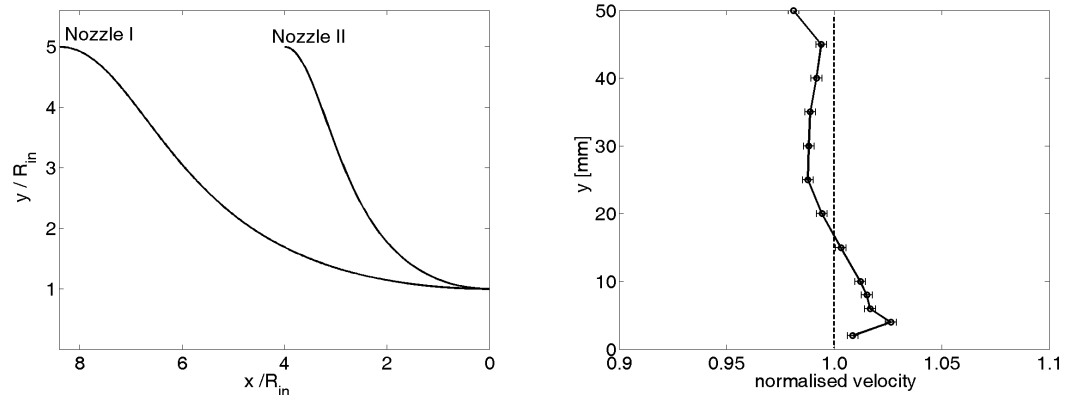

Figure B.1: *Contours for Windtunnel nozzles (left) and velocity profile measured at outlet of nozzle II, normalised with the mean velocity.*

Although the Nozzle II is extremely compact the velocity deviation from a block profile amounts only to ±2% (See Figure B.1) which is acceptable for the investigation of the present configuration.

B.2 Statistics

The first four statistical moments of a variable u, with p(u) the probability function, are defined as follows:

- $m_1(mean) = \int_{-\infty}^{\infty} up(u)du$
- $M_2(centraldeviation) = \int_{-\infty}^{\infty}(u - m1)^2 p(u)du$
- $M_3 = \int_{-\infty}^{\infty}(u - m1)^3 p(u)du$
- $M_4 = \int_{-\infty}^{\infty}(u - m1)^4 p(u)du$
  As alternative to M_3 and M_4 one can derive two coefficients:
- skewness $(\kappa) = \frac{M_3}{\sqrt{M_2^3}}$
- flatness $(\gamma) = \frac{M_4}{M_2^2}$

If u is the velocity, one call the turbulence *isotropic* when u is distributed as a Gaussian function, therefore $m_1 = 0$, $M_2 =$ turbulence kinetic energy, $\kappa = 0$ and $\gamma = 3$.

Curriculum Vitae

Angaben zur Person

Name:	Marco Zucchini
Geburtsdatum:	26.09.1971
Geburtsort:	Padua (Italien)
Staatsangehörigkeit:	italienisch

Ausbildung

1990	Abitur am Naturwissenschaftlichen Gymnasium in Ferrara (Italien) mit Auszeichnung *Francesco Viviani*
1997	Diplom in Luft- und Raumfahrttechnik an der Universität von Pisa (Italien) mit Auszeichnung (110/110 e lode) Diplomarbeit: *Neue Verfahren zur Maßkontrolle und Montage von Flugzeugen.* ECATA Junior, Aerospatiale, Toulouse (Frankreich)
1998	Abschluss in quantitativen Methoden für Managemententscheidung. SDA Bocconi, Mailand (Italien)

Berufserfahrung

1998-1999	Konstruktionsingenieur bei Visteon, Lille (Frankreich)
1999-2003	Entwicklungsingenieur im Geschäftsbereich Gasoline System bei Robert Bosch GmbH, Schwieberdingen
2003-2006	Doktorand in der Zentrale Forschung und Vorausentwicklung, Abteilung Angewandte Physik, bei Robert Bosch GmbH, Schillerhöhe
Seit 04.2006	Ingenieur in der Zentrale Forschung und Vorausentwicklung, Abteilung Angewandte Physik, bei Robert Bosch GmbH, Schillerhöhe